The variability of Lagrangian transport in the southern Benguela Current upwelling system

Moagabo Natalie Ragoasha

A thesis presented for the degree of

Doctor of Philosophy

Department of Oceanography

Faculty of Science

UNIVERSITY OF CAPE TOWN

July 2020

To my beloved aunt, Mmaphala Tsebehlane, sisters, Matsubu and Matsie Ragoasha and my nephew, Mampuru Ragoasha, I dedicate this work to you.

This work has been supervised by the following:

***Supervisor 1**

Prof. Chris Reason

Department of Oceanography

University of Cape Town

South Africa

***Supervisor 2**

Dr Steven Herbette

Laboratoire dOcéanographie Physique et Spatiale (LOPS), IUEM, Univ. Brest - CNRS - IRD - Ifremer, Brest, France

***Supervisor 3**

Dr Jenny Veitch

SAEON, Egagasini Node, Cape Town, South Africa

Nansen-Tutu Centre, Marine Research Institute, Department of Oceanography,

University of Cape Town

***Supervisor 4**

Dr Gildas Cambon

Laboratoire dOcéanographie Physique et Spatiale (LOPS), IUEM, Univ. Brest - CNRS - IRD - Ifremer, Brest, France

***Supervisor 5**

Dr Claude Roy

Laboratoire dOcéanographie Physique et Spatiale (LOPS), IUEM, Univ. Brest - CNRS - IRD - Ifremer, Brest, France

*Signatures are on file in the Science Faculty

I confirm that I have been granted permission by the University of Cape Towns Doctoral Degrees Board to include the following publication in my PhD thesis, and where

co-authorship is involved, my co-authors have agreed that I may include the publication:

Ragoasha, N., Herbette, S., Cambon, G., Veitch, J., Reason, C., and Roy, C., 2019. Lagrangian pathways in the southern Benguela upwelling system. *Journal of Marine Systems*, 195, pp.50-66. Doi: https://doi.org/10.1016/j.jmarsys.2019.03.008.

Declaration

I hereby declare that except where specific reference is made to the work of others, the contents of this dissertation are original and have not been submitted in whole nor in part for consideration for any other degree or qualification in this, or any other University. This dissertation is the result of my own work and includes nothing which is the outcome of work done in collaboration, except where specifically indicated in the text. This dissertation contains less than 80,000 words including appendices, bibliography, footnotes, tables and equations and has less than 150 figures.

Signature: Signed by candidate Date: July 2020

Acknowledgements

This has been a long roller coaster ride, with so many highs and low. However, the guidance, support and encouragement I had along the way made this journey enjoyable and this PhD a success. It is a pleasure to thank the people who made this thesis possible.

Firstly, I would like to express my immense gratitude to my supervisors: Prof. Chris Reason, Dr Steven Herbette, Dr Jenny Veitch, Dr Gildas Cambon and Dr Claude Roy, without their help this thesis would not have been possible. Chris, thank you for providing constructive feedback that helped to improve the writing of this thesis. Thank you Steven, without your guidance, patience, and training, I would not be nearly the person I am today. I am grateful to you Jenny, you were not only my supervisor but also a mentor. I am forever grateful for your motivation when I was down (You always had the right words of encouragement) and your honest feedback have been invaluable. I would like to thank Gildas for running the ocean model simulations and you were always available to help when I needed computational assistance. I am grateful for the training you gave me on ROMS and helping with to settle in LOPS and Brest. Claude, your extraordinary support and expert advice throughout this thesis process have been incredible.

I would like to acknowledge the funding by the South-African National Research Foundation (NRF, South Africa), the French Institute for Research and Sustainable Development (IRD, France) and ICEMASA for this thesis. This work was also supported by the French national program LEFE/INSU under the project's name Benguela Upwelling Innershelf Circulation (BUIC). This work was granted access to the HPC resources of [TGCC/CINES/IDRIS] under the allocation 2017- [DARI n°$A0020107443$] attributed by

GENCI (Grand Equipement National de Calcul Intensif).
To DAFF and DEA thank you for providing me with the in-situ data-sets used for the evaluation of the ocean model.

I also want to thank LOPS (UBO) for hosting me and making the completion of this thesis possible. To my colleagues who had become friends, Marion, Kenneth, Belinda, Ramontsheng, Juliano and Yurui, thank you for keeping my spirit high. Last but not least I would like to thank my family specially my aunt, two sisters and my nephew for their support and motivation throughout this journey. Thank you for believing in me.

Abstract

This study analyses the physical mechanisms that impact Lagrangian pathways and transport in the southern Benguela upwelling system (SBUS), an environment in which currents are key components of many important ecological processes, including the dispersal of marine larvae. Physical advection by currents is an important mechanism for egg and larvae transport success in the SBUS since the spawning areas and recruitment areas are separated by a long distance. Numerical model simulations of the SBUS coupled with particle tracking experiments are used to investigate Lagrangian pathways between the Cape Peninsula (34°S) and St Helena Bay (32°S) and how they are linked to the oceanic circulation. Transport success, given by the ratio of the number of particles that reach St Helena Bay (32°) over the total number of particles released, is used quantify the alongshore connectivity between the two regions.

Results of an interannual eddy-resolving (7 km) Coastal and Regional Ocean COmmunity (CROCO) model simulation, coupled with a Lagrangian particle-tracking model (Pyticles) reveal a strong seasonal cycle in transport success that is governed by the wind-induced Ekman drift as well as the complex three-dimensional structure of the alongshore jets and their variability. An efficient and fast inshore route taken by particles in spring (September-November). This period is the optimal window, as the jet is in its intensified state, close to the shore, and relatively stable. At this time of the year, offshore Ekman transport is still low enough to allow particles to remain on the inshore side of the jet. During the peak upwelling season, this inshore path becomes less efficient due to high offshore Ekman transport and also the Benguela Jet splits into multiple jets resulting in inshore and offshore routes. Particles advected in the offshore branch are exposed to

intense mesoscale variability and therefore are susceptible to chaotic trajectories, longer connection time and lower transport success.

The sensitivity of the alongshore connectivity to increasing ocean model horizontal resolution was investigated by developing a nested simulation based on a 3 km resolution grid. Increasing the model resolution from 7-km to 3-km reveals some changes in the intensity and the structure of the coastal circulation including the large-scale circulation associated with the Agulhas Current leakage. The increased resolution allows finer details of the coastal topography to be represented and this led to a Benguela Jet that is narrower and more coherent (less diffused). Moreover, the 3-km simulation resolves a nearshore poleward current that is not present in the lower resolution simulation. A more realistic topography also led to a reduced leakage of warm Agulhas Current waters and instabilities associated with it. Our results however show that at a seasonal time-scale, there is not much difference in the alongshore connectivity since the Benguela Jet that is responsible for this connectivity is present in both simulations.

The 3-km simulation is used to investigate the role of wind-driven coastal circulation and mesoscale variability on the interannual variability of transport success. This analysis reveals that the variability of transport success cannot be attributed to a single physical driver. The Benguela Jet is found to be the dominant driver of transport success variability for particles released on the shelf, while the removal of these particles occurs through offshore Ekman transport and the nearshore poleward current could contribute to negative anomalies of transport success. Cross-shore transport is shown to contribute to the variability in transport success through the activity of mesoscale eddies. An infrequent interaction of a passing Agulhas ring with the shelf led to a strong offshore advection of particles into the open ocean (a zone of highest EKE) and negative transport success. The influence of an Agulhas ring is dependent on two factors: (i) the duration of its interaction, and (ii) its distance from the shelf-edge and the origin of particles. A shorter and closer interaction tends to have a greater impact. There were only 18 interactions that occurred over the 20 years model simulation and 13 of them resulted in negative transport success

anomaly of particles that originated on the outer shelf-edge. In contrast, the shelf-edge cyclonic eddies favour the onshore transport of particles that originated on the outer shelf-edge and thus a positive anomaly transport success. This onshore transport mostly occurs in an event when these particles do not initially experience any offshore transport away from the shelf-edge by anti-cyclonic eddies.

The findings of this study will provide a valuable information for the future studies on the role of the physical drivers that impact transport of larvae and eggs.

Contents

Declaration **iv**

Acknowledgements **v**

Abstract **vii**

List of Figures **xxix**

List of Tables **xxx**

1 Literature Review **9**

1.1 Atmospheric forcing 9

1.1.1 Seasonal variability 9

1.1.2 Intra-seasonal and short-term variability 11

1.1.3 Interannual and long-term variability 11

1.2 Ocean circulation 13

1.3 Conclusion 18

2 The ROMS model **20**

2.1 The primitive equations 20

2.2 The vertical boundary conditions 23

2.2.1 Surface boundary condition at z=η(x,y,t) 23

2.2.2 Bottom boundary condition at $z = -H(x, y)$ 24

2.3 Surface fluxes forcing in the model 26

2.3.1 Momentum surface fluxes 26

2.3.2 Heat fluxes and fresh water flux 26

2.4 Vertical mixing and Turbulent closure scheme . . . 27
2.5 Horizontal mixing . . . 28
2.6 Lateral Boundary Conditions . . . 28
2.7 Time discretization . . . 29
2.8 Horizontal discretization . . . 30
2.9 Vertical discretization . . . 32
2.10 Advection schemes . . . 34
2.11 The ROMS model: summary . . . 35

3 A new simulation of the Southern Benguela Upwelling System 36
3.1 The regional model configuration developed: `BENGR15` . . . 37
3.1.1 Bathymetry . . . 37
3.1.2 Atmospheric surface forcing . . . 40
3.1.3 Lateral oceanic forcing . . . 44
3.1.4 Model spin-up . . . 45
3.1.5 Summary of the model configuration BENGR15 . . . 46
3.2 Model evaluation . . . 48
3.2.1 Mean Surface Circulation features . . . 48
3.2.2 Hydrography: Vertical currents and temperature . . . 54
3.2.3 The near-shelf thermal stratification . . . 55

4 Lagrangian pathways in the southern Benguela upwelling system 59
4.1 Introduction . . . 59
4.2 Lagrangian experimental set-up . . . 61
4.2.1 The Lagrangian particle-tracking model . . . 61
4.2.2 Statistical Lagrangian diagnostics . . . 62
4.3 Characteristics of the alongshore connectivity . . . 64
4.4 Alongshore Lagrangian pathways . . . 68
4.5 Inferring the role of the ocean circulation on the Lagrangian pathways . . . 70
4.5.1 Characteristics of the ocean surface circulation . . . 70
4.5.2 Characteristics of the ocean circulation at depth . . . 75

4.6 Discussion and conclusions 80

5 The impact of downscaling on SBUS circulation and Langrangian pathways 86

5.1 Introduction 86

5.2 A 3-km resolution simulation of the SBUS 89

5.2.1 The design of an offline nested grid: 89

5.3 Impacts of the horizontal resolution on the circulation 91

5.3.1 Reduction in the warm bias of the coastal waters 93

5.3.2 A narrower and smaller Benguela Jet 94

5.3.3 The presence of poleward jets 94

5.3.4 Impacts of the horizontal resolution on the mesoscale turbulence in the SBUS 96

5.3.5 An unexpected impact on the Agulhas leakage 101

5.4 Coastal circulation in the R3km simulation: summary 104

5.5 Sensitivity of the Lagrangian transport success to the downscaling 104

5.5.1 The Lagrangian setup 106

5.5.2 Comparison of the alongshore connectivity between R7km and R3km 106

5.6 Horizontal dispersion 112

5.6.1 Lagrangian pathways and Eulerian oceanic circulation 116

5.7 Summary and Conclusion 118

6 Interannual variability of transport success 122

6.1 Introduction 122

6.2 Transport success variability 127

6.3 The role of local dynamics 129

6.4 Inshore and offshore transport success 133

6.5 Cross-shore transport 137

6.5.1 Inshore particles 137

6.5.2 Offshore particles 141

6.6 The role of mesoscale eddies 144

6.7 Discussion and conclusions 152

7 Summary and future research **155**

7.1 Key Findings 160

7.2 Future work 162

A Abbreviations used for the description of the ROMS model **165**

B Eddy detecting and tracking algorithm **167**

List of Figures

1 A conceptual diagram of the life history of anchovy in the southern Benguela. From *Hutchings et al.* (1998). Fish eggs, spawned at the tip of Cape Agulhas are advected northward alongshore. They experience offshore losses along the way. Those that make it to the nursery area (St Helena Bay) are considered as recruits. In their early-stage, anchovy larvae have minimal swimming ability, which makes them behave as passive particles. Therefore, their dispersion and transport is directly dependant on the oceanic circulation (*Pagès et al.*, 1991). 2

1.1 Mean seasonal composite of 1000 mb geopotential height (m) over the South Atlantic ocean from NCEP (1980-2012) data: (a) summer (December-February), (b) autumn (March-May), (c) winter (June-August) and (d) spring (September-November). The contours shown are of the 100 m and 150 m geopotential height and represent the high and low pressure, respectively. The surface wind speed and direction is represented by the overlaid blue arrows. Data used was downloaded from NCEP website[1] 10

1.2 Surface synoptic pressure maps of the eastward propagating cyclones passing south of the continent obtained from South African Weather Services (from *Jury et al.* (1990)) and the formation of a trapped coastal low that can promote pulsed upwelling at 3-10 day intervals (*Hutchings et al.*, 2009). The H in each figure refers to the ridging high pressure cell, the bold line to the trailing edge of frontal system, and the arrow points the position of the coastal low. The three cases corresponds to days extending over 6-11 February 1981, 15-20 September 1985 and 18-23 April 1980, respectively. . . 12

1.3 Annual anomalies (1960-2010 period) of north/south wind component measured as wind-run (grey bars, km) and summer upwelling rates (cm day^{-1}) for Cape Point (taken from *Blamey et al.* (2015)). Positive/negative bars indicate a dominance of southerlies/northerlies. Positive/negative wind regime shifts and upwelling are denoted by grey and red arrows, respectively. There are some periods where the dominance of southerlies (northerlies) coincide with intensified (reduced) upwelling rates. The early 1980s to early 1990s period was predominately associated with reduced uwelling and northerlies and upwelling was intensified between 1997 and 2000. 12

1.4 Map of the South East Atlantic showing surface and near-surface currents, frontal zones, upwelling cells, major areas of freshwater input and bathymetry adapted from *Hardman-Mountford et al.* (2003). These are main oceanographic features that could impact biology in the Benguela upwelling system at different temporal and spatial scale (*Shannon et al.*, 1996). EUC, Equatorial Under Current; SEC, South Equatorial Current; SECC, South Equatorial Counter Current; AnC, Angola Current; BOC, Benguela Oceanic Current; BCC, Benguela Coastal Current; SAC, South Atlantic Current; AgC, Agulhas Current; ABF, Angola–Benguela front; STF, subtropical front; STG, subtropical gyre; ACC, Antarctic Circumpolar Current. The Benguela Current and Benguela Jet are labelled BOC and 'Cape Jet', respectively. 14

2.1 Schematic diagram of the KPP closure model used. The mixing coefficients computed by the KPP closure model are the vertical thermal diffusivity K_{Tv}, vertical haline diffusivity K_{Sv} and the vertical momentum viscosity K_{Mv}. 28

2.2 Schematic view of the ROMS predictor-corrector hydrostatic kernel. From (*Shchepetkin and McWilliams*, 2005). Ξ is here the free surface elevation (η in the text). 31

2.3 The placement of variables on the Arakawa-C grid used in the horizontal discretization of ROMS. From *Hedström* (2009). 31

2.4 Curvilinear horizontal coordinate 32
2.5 Vertical grid used in the vertical discretization of ROMS (from www.myroms.org). 32
2.6 An example of the BENGR15 vertical grid as prescribed by the σ-coordinate system. A zoom is made in the first 200 m of the water column in order to accentuate the distribution of the vertical grid in upper layer. Here the sigma coordinate parameters are $h_{cline} = 300$ m, $\theta_b = 6$, and $\theta_s = 5$ 34

3.1 Model year 2005, January average snapshot of sea surface temperature (SST) for the Benguela upwelling system configuration ("BENGR15"). The domain encompasses the region covering 2.5°W - 55.16°E and 54.5°S - 4.75°S. The box represents an extracted region over the southern Benguela (45.1°S to 22.1°S and from 5.0°E - 34.9°E) used in our study. 38
3.2 a) The original raw SRTM 30' bathymetry extracted over the BENGR15 domain. b) The bathymetry of the BENGR15 model configuration obtained after smoothing of the raw SRTM 30' batymetry. c) The difference between raw SRTM 30' and smoothed BENGR15 bathymetry 39
3.3 The difference between raw SRTM 30' and smoothed BENGR15 bathymetry (m). 40
3.4 Summer and winter mean meridional wind stress from (a,d) QuikSCAT, (b,e) CFSR (colors, in N m^{-2}, contour interval: 0.02 N m^{-2}) and (c,f) their differences (reanalysis - satellite winds) for the 2000-2008 period. Positive (negative) values in the difference maps are regions where the reanalysis is stronger (weaker) than satellite. The bold black line represent the zero difference and the contour interval is 0.005 N m^{-2}. 41
3.5 Summer and winter mean wind stress curl from (a,d) QuikSCAT and (b,e) CFSR (c,f) their differences (reanalysis - satellite wind stress curl) (colors, in Nm^{-3}). Cyclonic (anticyclonic) curl is negative (positive) and line bold black line represent the region of zero wind stress curl. 43
3.6 Summer and winter mean cross section of temperature taken from the southern boundary: (a,c) WOA13 and (b,d) SODA open boundary conditions with 1°C contour interval. The thick line represents the 16°C isotherm. . . 45

3.7 3-day mean volume anomaly, volume averaged kinetic energy and surface averaged kinetic energy for the 22 years (1989-2010) BENGR15 simulation. The red horizontal line represents the mean value of the data. 46

3.8 Maps of mean of the geostrophic surface eddy kinetic energy: a) computed from satellite (AVISO) data for the period between 1993 to 2015 and b) model-derived for the 1989-2010 period, both in $cm^{-2}\ s^{-2}$ (color). The contours represent the mean SSH, with a contour interval of 10 cm. The overlaid arrows indicate the sense of associated geostrophic currents. 49

3.9 Annual average of sea surface height (SSH) with corresponding surface geostrophic currents superimposed: a) model outputs averaged over 1989-2010; b) satellite absolute dynamic topography (ADT) data averaged over 1993-2010; c) across-shore profiles of model (solid) and satellite (dashed) annual averages of SST (red), ADT (blue) and alongshore geostrophic current (magenta) off Grotto Bay (black line in a) and b). The plotted model SSH was offset by +0.407 m so that the model and satellite spatially average fields matched over the domain of interest. 50

3.10 Annual average of Sea Surface Temperature (SST): a) satellite derived infrared data averaged over 2010-2017 (ODYSSEA); b) model data averaged over 1989-2010; c) Annual average of the SST bias (SST_{model} - $SST_{ODYSSEA}$). 51

3.11 Climatology of the summer and winter SST obtained from (a,d) CCI satellite, (b,e) model and (c,f) difference (model - observation) for the 1992-2010 period. The 16°C isotherm is superimposed in red. Positive (negative) values in the difference map are regions where the model overestimate (underestimate) observed SST. 52

3.12 Space-time plot of climatological mean cross-shore SST gradient at 33.15°S for: (a) CCI-satellite, (b) model , both with an interval of 0.01°C. (c) : model alongshore current with a contour interval of 0.05 $m\ s^{-1}$. The 200 m and 500 m isobaths are shown as white dashed lines. 54

3.13 Temperature transect off Grotto Bay (solid black line on Fig. 3.10) with the alongshore component of the geostrophic current superimposed (white contours). a) World Ocean Atlas annual average (WOA2013); b) Same as in a) for the model; c) Temperature bias (T_{model} - $T_{WOA2013}$). Geostrophic velocities is built with a reference level at 1000 m depth. Contours are plotted every with 0.05 m s^{-1} in the range [-0.05 0.25] m s^{-1}. Negative values are dashed. 55

3.14 Model derived bathymetry (black lines in metres) in blue with 100 m contour interval for shallower region than 500 m and 500 m interval for region deeper than 500 m. The red markers show the locations of the 12 CTD stations of the St Helena Bay Monitoring Line (SHBML). Stations 1-6 are located within the bay region (coastal region), stations 8-10 located over the mid-shelf region and stations 11-12 further offshore in the open ocean. . 56

3.15 Temperature transect along the SHBML CTD stations (location of station is shown in Fig. 3.14) with the alongshore component of the geostrophic current superimposed (white contours). a) SHBML annual average ; b) Same as in a) for the model; c) Temperature bias (T_{model}-T_{SHBML}). Geostrophic velocities is built with a reference level at 1000 m depth. Contours are plotted every with 0.05 m s^{-1} in the range [-0.05 0.25] m s^{-1}. 57

4.1 (a): Set-up of the Lagrangian experiments: particles are released over the SARP line (white circles), a cross-shore transect off Cape Point. They are counted as successfully transported particles if they reach, within 30 days, the St Helena Bay target area delineated by the red polygon. The bathymetry of the "BENGR15" model (in grey with white contours every 500 m) is also superimposed as well as two other cross-shore transects that particles will cross while being advected northward: the Grotto Bay line at 33.5°S (thick blue) and the Cape Columbine line at 33°S (thick black). (b): Initial distribution of particles over the SARP line for a given release event. σ layers are superimposed (black solid). 61

4.2 Monthly climatology of transport success TS_m (red dots) and alongshore wind-stress at the SARP line (black dots). The standard deviation of $TS_m$is also superimposed as errorbars. The wind stress is averaged over a box encompassing the southern Benguela from 12°E to 20°E and 26°S to 36°S. . 65

4.3 (a): Monthly distribution of successful particles by age when entering the target area. (b): Cumulated histogram of monthly climatology transport success with clusters of particles built according to their age of arrival: group I (age<10 days); group II (10<age≤15 days); group III: (15<age≤20 days); group IV: (20<age≤30 days). Probability have been normalised by the total number of particles released for each month m ($m = 1, \cdots, 12$) over the 22 years of the model run. 65

4.4 (a): Monthly distribution of successful particles by their depth of release. (b): Cumulative histogram of monthly climatology transport success with clusters of particles built according their initial isobath. Probability have been normalised as in Figure 4.3 67

4.5 Horizontal distribution of unsuccessful particles (plumes) 12 days after their release for the months of: (a) October; (b) January; (c) March; (d) June. The 200 m, 300 m (dashed), 500 m and 2000 m isobaths are superimposed. The colorbar shows the probability of finding a particle aged 12 days within the water column at a specific grid cell. 68

4.6 Same as Fig. 4.5 for the successful particles. The sum of probabilities over the grid gives the transport success plotted in Fig. 4.2. 69

4.7 Monthly climatology of the trajectory of successful particles by age of arrival into the target area τ (in days). Trajectories are plotted for particles released in: (a) October; (b) January; (c) March; (d) June. colors refer to the clusters of particles built according to their age of arrival τ. Group I: $\tau < 10$ (red); Group II: $10 < \tau \leq 15$ (blue); Group III: $15 < \tau \leq 20$ (green); Group IV: $20 < \tau \leq 30$ (magenta). The 200 m, 300 m (dashed), 500 m and 2000 m isobaths are superimposed (black). Note that the mean of the four trajectories at 12 days corresponds to the geometric centre of the plume plotted in Fig. 4.6. The SARP, Grotto Bay and Cape Columbine lines described in Fig. 4.1 are also superimposed (white dashed). 71

4.8 Monthly climatology of surface currents for: (a) October; (b) January; (c) March; (d) June. The magnitude of the current is shown in color (m s^{-1}) and current vectors are superimposed, as well as the 200 m, 300 m (dashed), 500 m and 2000 m isobaths (solid white). 72

4.9 Across-shore profile of normalised depth-integrated alongshore current (red), EKE (black), and probability of the occurrence of particles (blue solid) at the SARP line. The histogram of successful particles is also superimposed (blue dashed) as well as the histogram of all particles at any release events (green solid). Profiles are plotted for: (a) October; (b) January; (c) March; (d) June. The depth-integrated alongshore current and EKE are computed over the top 100 m and then normalised by their maximum value found among the 12 monthly climatology across-shore profiles for all three transects. For the EKE, this maximum (0.07 $m^2 s^{-2}$) occurred along the Grotto Bay transect in May. For the depth integrated current, this maximum (0.45 m s^{-1}) was found at the SARP line in January. The probability of occurrence of particles is normalised by its value on the SARP line when they are released. The colorbar shows the across-shore bathymetry, the enlarged circles mark the location of the 200 m, 500 m, 1000 m and 2000 m isobaths, respectively. 76

4.10 Same as Fig. 4.9 but for *Grotto Bay* (33.5°S). 77

4.11 Same as Fig. 4.9 but for *Cape Columbine* (33°S). 77

4.12 (Top): Grotto Bay vertical transect of alongshore velocities (color in m s^{-1}) and isotherms (white contours with contour spacing of 2°C). Contours of the current intensity are also superimposed (black) with a contour pacing of 1 cm s^{-1} and the zero contour in thick. (Bottom): The alongshore wind stress (blue) and z-component of the wind-stress curl (red) are superimposed for each across-shore transect, with the zero line (black dashed). Quantities are the monthly climatologies for: (a) October; (b) January; (c) March; (d) June. 79

4.13 (Top): Grotto Bay vertical transect of across-shore ageostrophic velocities (color in m s^{-1}) and isotherms (white contours with contour spacing of 2°C). Contours of the current intensity are superimposed (black) with a contour spacing of 1 cm s^{-1} (zero contour in thick). The depth of the Ekman layer (m), computed after matching the vertical integration of the ageostrophic velocity with the total across-shore Ekman transport ($\tau_{alongshore}/(\rho f)$) is also superimposed in red. (Bottom): The across-shore Ekman transport along each across-shore transect (red) , with the zero line (black dashed). Quantities are the monthly climatologies for: (a) October; (b) January; (c) March; (d) June. 81

4.14 Grotto Bay vertical transect of monthly climatology of EKE (color in m^2 s^{-2}) for: (a) October; (b) January; (c) March; (d) June. 82

5.1 Snapshot of SST (Year 2005, 1st of January). The black box delineates the boundaries of the nested 3-km child grid. Within the box, the SST of the 3-km simulation is superimposed upon the one of the 7-km simulation. . . . 88

5.2 Model bathymetry for the reference configuration (R7km) and the nested domain (R3km) 90

5.3 Cross-shore transects of vertical levels off Cape Point in the (a) R7km and (b) R3km model, plotted for every fifth level. 91

5.4 Annual average (2005-2012) of merged satellite CCI SST (left), model SST (centre), and SST bias [SST_{model} - SST_{CCI}] (right). SST contours are superimposed (black solid) with a 1°C contour interval. Top panels are for the R7km simulation whereas bottom panels are for the R3km simulation. . 92

5.5 Maps of the seasonally averaged alongshore component of surface currents for the R7km simulation (Top panel a-d) and R3km simulation (Bottom panel e-h). The colorbar represents the magnitude of the alongshore component of the velocity vector in m s^{-1}. Current vectors are superimposed, as well as the 200 m and 500 m isobaths (red solid line). 93

5.6 Hovmller plot of: satellite (left), model (middle) across-shore climatological mean SST gradient off Cape Point (34.15°S), and model monthly climatological mean of surface alongshore current (right panel) for the 7-km (top) and 3-km (bottom) simulations. The contour interval for the SST gradient and model velocity are 0.01°C km^{-1} and 0.05 m s^{-1} respectively. The location of the 200 m and 500 m isobaths are shown as white dashed lines. . 95

5.7 Vertical across-shore transects off Cape Point of the seasonally averaged alongshore component of the model current vector (colorbar in m s^{-1}) from the R7km (a) and R3km (b) simulation. Velocity/temperature iso-contours (black thin/red solid)are superimposed with a 0.1 m s^{-1}/2°C contour spacing. 97

5.8 Comparison of seasonally averaged surface Eddy Kinetic Energy (EKE) for the: R7km simulation (Top panel a-d) and R3km simulation (Bottom panel e-h). The 450 cm^2 s^{-2} contour is shown in black bold line to delimit the extension of the high values of EKE typically found in region affected by the Agulhas Current retroflection. The 200 m and 500 m isobaths are shown as white lines. 98

5.9 Snapshots of surface relative vorticity anomaly in the (a) R7km and (b) R3km simulation on the 1st of October 2010. 98

5.10 Same as Figure 5.7 but for EKE. Units in $cm^{-2}.s^{-2}$ and the contour interval is 50 cm^2 s^{-2}. Temperature contours are also superimposed in white with contour interval of 2°C. 100

5.11 Mean annual SSH (color, in metres) over the 2005-2012 period for a) R7km and b) R3km simulation. The bold dashed line show the model retroflection path of the Agulhas Current derived from the annual mean of the same period. The dashed black transect shows the SBUS southern boundary line (SBL) over which the meridional heat fluxes are estimated. CC stands for Cape Columbine and CP for Cape Point, the southernmost tip of the Cape Peninsula. the Black contours represent bathymetry shallower than 1000 m at 100 m depth intervals, with the grey lines representing bathymetry deeper than 1000 m at 500 m depth intervals. Letters label the main bathymetric features namely: **A**-Agulhas Bank, **B**-Protea and Argentina Seamounts, **C**-Erica Seamount and **D**-Agulhas Ridge. 102

5.12 Mean annual depth-integrated (upper 1000 m depth) heat fluxes (PW) across SBL (35°S) transect for the R7km (solid red line) and R3km (dashed red line) simulations. 1 PW=10^{15}W. 103

5.13 a): Set-up of the Lagrangian experiments: particles are released every 12 hours over the SARP line (white circles), a cross-shore transect off Cape Point. They are counted as successfully transported particles if they reach, within 30 days, the St Helena Bay target area delineated by the red polygon. The bathymetry of the R7km model (in grey with white contours every 500 m) is also superimposed. (b,c): Initial distribution of particles over the SARP line for a given release event for R7km and R3km, respectively. σ layers are superimposed (black solid). 105

5.14 Monthly climatology of transport success TS_m (red dots) and standard deviation of TS_m superimposed as error bars for a) R7km and b) R3km. c) Monthly climatology of transport success for R7km (red line) and R3km (black line). 107

5.15 Left: Monthly distribution of successful particles by age when entering the target area. Right: Cumulative histogram of monthly climatology transport success with clusters of particles built according to their age of arrival: group I (age<10 days); group II (10<age≤15 days); group III: (15<age≤20 days); group IV: (20<age≤30 days). For R7km (a) and R3km (b). Probability have been normalised by the total number of particles released for each month m ($m = 1, \cdots, 12$) over the 20 years of the model run. 110

5.16 Monthly cumulative contribution of the (a): inshore particles and (b): offshore particles to transport success for the R7km (grey bars) and R3km (cyan bars). The monthly transport success of the particles originating over the inner shelf (0-200 m isobath) is also superimposed on (a) for the R7km (red dashed line) and R3km (black dashed line). The red and black lines respectively represent the transport success for particles from the mid-shelf (200-500 m isobaths) in the R7km and R3km. 111

5.17 Seasonal plume dispersion pattern of unsuccessful particles at a) 6 days and b) 12 days after their release for 7 km (panel a-d) and 3 km (panel e-h). The density (colorbar) is obtained by dividing the sum of particles located in a defined grid box by their respective grid box area. The density of particles is shown in log scale to capture the large dispersion of particles in the higher resolution and a reference contour (blue line) of 3.5 m^{-2} is superimposed. The 200 m and 2000 m isobaths are also superimposed. 114

5.18 Same as in Figure 5.17 but for successful particles. 115

5.19 Seasonal cross-shore profile of normalised depth-integrated alongshore current (red), EKE (black), and probability of particles' occurrence (blue solid) at Cape Point for (a) R7km and (b) R3km. The histogram of successful particles is also superimposed (blue dashed). The enlarged circles mark the location of the 200 m, 500 m, 1000 m and 2000 m isobaths, respectively. . . 117

5.20 Snapshot of SST (Year 2005, 1st of January) for the (a) 7-km and (b) 3-km simulation. The black box delineates the 1-km simulation boundaries and the SST of the 1-km is superimposed within the box. (c) Monthly climatological transport success of R1km_EXP1 (red line) and R1km_EXP2 (blue line) over the 2005-2011 period. 120

6.1 (a): Map showing anchovy spawning area on the Agulhas Bank (dashed lines) that extends from 18°E to 26°E and the nursery area located off the west coast between Cape Columbine and the Orange River on the west coast (dotted lines). The arrow indicates the approximate location of the shelf-edge jet current (Benguela Jet), the star indicates the location of Cape Point. The SARP monitoring line is represented by the cross-shore transect (black solid line) off Cape Point. The map has been adapted from *Huggett et al.* (2003). (b): SBUS recruitment strength of anchovies in billions (1985-2012) (black line) and adults biomass (bar graph) in tons (1984-2012). Updated from *van der Lingen and Huggett* (2003). 124

6.2 (a): Map of the R3km model simulation bathymetry (in grey with a contour interval of 500 m). Particles are released between the surface and -100 m along the across-shore transect off Cape Point (white circles). The target are is defined offshore St Helena Bay and is delineated by the red polygon. A particle is considered successful if it reaches the target area within 30 days (b): One random initial vertical distribution of particles off Cape Point during a release event (blue circles). Terrain following Sigma levels of the R3km model are superimposed in black. 128

6.3 Monthly climatology of transport success $\overline{TS_m}$ (red dots) and their standard deviation σTS_m (error-bars) 129

6.4 Normalised monthly transport success anomalies (TS′) over the 1992-2011 period. 129

6.5 (a) Annual mean sea surface alongshore current velocities (m s^{-1}) of the R3km simulation. 200 m and 500 m isobaths are shown in black. (b) Scatterplots of normalised transport success anomalies against the Benguela Jet index anomalies averaged between Cape Point (34°S) and St Helena Bay (32°S) over the 200-500 m isobaths. A positive (negative) Benguela Jet anomaly suggests a stronger (weaker) than average northward jet 131

6.6 (a) January alongshore wind stress (m s^{-1}) climatological mean of the R3km simulation. 200 m and 500 m isobaths are shown in black. Same as in Fig. 6.5b but for transport success anomalies against alongshore wind stress anomalies averaged over at the transect off Cape Point (black line on the map (a)). A positive (negative) alongshore wind anomaly suggests a stronger (weaker) equatorward winds. 132

6.7 Annul mean surface EKE ($cm^{-2}s^{-2}$) of the R3km simulation. 500 m and 3000 m isobaths are superimposed in white. (b) Same as in Fig. 6.5b and Fig. 6.6b, but for normalised transport success anomalies against EKE anomalies. The EKE anomalies are averaged between Cape Point (34°S) and Cape Columbine (33°S), from the shelf edge (500 m isobath) to the 3000 m isobath. A positive (negative) EKE anomaly suggests a stronger (weaker) mesoscale turbulence. 132

6.8 Same as in Fig. 6.4 but it is plotted in cumulated bars of inshore (TSI′: blue) and offshore (TSO′: orange) transport anomalies such that TSI′ + TSO′ = TS′ 134

6.9 Standardised time-series of monthly inshore transport anomalies (bar graph) and superimposed is: (a) Benguela Jet anomalies (black line), (b) Alongshore wind stress anomalies (green line), (c) Coastal poleward flow (cyan) plus the nearshore southward transport of particles (dashed black line) and, (d) the offshore EKE anomalies. 135

6.10 Standardised time-series of monthly offshore transport anomalies (bar graph) and EKE anomalies are superimposed as a black line. 136

6.11 An example of the two individual trajectories plotted from their initial position on the SARP line (black line) to their entry into the target area (blue dashed polygon) corresponding to the groups of cross-shore displacement of particles originating from the inshore section: TSII in cyan and TSIO in magenta. 139

6.12 Standardised time-series (bar graph) of monthly successfully transported: (a) inshore particles that were displaced less than 50 km offshore from their initial distance from the 500 m isobath (TSII′) and, (b) inshore particles that were displaced more than 50 km offshore from their initial distance from the 500 m isobath (TSIO′) anomalies. Anomalies of inshore transport success (TSI′) are superimposed in a black line. 140

6.13 Inshore transport success anomalies (TSI′) shown as cumulative bars of successful particles that were not displaced beyond 50 km of their initial distance from the 500 m isobath (TSII′: blue) and inshore particles that were displaced more than 50 km of their initial distance from the 500 m isobath (TSIO′: yellow) such that $TSI' = TSII' + TSIO'$. 141

6.14 Same as Fig. 6.11 but corresponding to the groups of cross-shore displacement of particles originating from the offshore section: TSOI in purple and TSOO in green 143

6.15 Normalised time-series (bar graph) of monthly: (a) offshore particles that were never displaced during their journey more than 50 km offshore from their initial distance from the 500 m isobath (TSOI′) and, (b) offshore particles that were displaced at least once, more than 50 km offshore from their initial distance from the 500 m isobath (TSOO′) anomalies. Anomalies of offshore transport success (TSO′) are superimposed in a black line. . . . 143

6.16 Offshore transport success anomalies (TSO′) shown as cumulative bars of successful particles that were not displaced beyond 50 km of their initial distance from the 500 m isobath (TSOI′:blue) and inshore particles that were displaced more than 50 km of their initial distance from the 500 m isobath (TSOO′:yellow) such that $TSO' = TSOI' + TSOO'$ 144

6.17 A map showing the distribution of eddies by their generation site indicated by the circles and their mean diameter (in color) during their duration in the region 36°S - 32°and 14°E - 20°E for: (a) cyclonic eddies and, (b) anti-cyclonic eddies. The background contours are the 500 m isobath in black and in grey is the 1000 m, 2000 m and 3000 m isobaths 146

6.18 Left: trajectories of Agulhas rings (different colors) tracked into the south-eastern Cape Basin following the Northern route (blue) defined by *Dencausse et al.* (2010a) between January 1992 and December 2011. The black solid circles indicate where the rings were first detected. The black across-shore line off Cape Point represents the SARP line and grey lines are the 500 m, 1000 m, 2000 m and 3000 m isobaths. Right: the three routes - Northern, Central and Southern defined by *Dencausse et al.* (2010a) 147

6.19 (a) Monthly mean SSH anomalies (m) in color and vectors superimposed corresponds to monthly mean surface current velocities. (b) The location of the detected Agulhas ring (black circles) during their interaction duration and the red circle represents size of the eddy at $1.5\times R_{eddy}$. (c-d) shows the trajectories of inshore particles and offshore particles characteristic of the anticyclonic circulations. The black contour represents the 500 m isobath. The top row represents the scenario which is associated with an Agulhas ring was passed further south (January 2000) and whereas, the bottom row represents the scenario associated an Agulhas ring passing north near the SARP line (January 2002). 149

6.20 (a) April 1992 monthly mean SSH anomalies (m) in color and vectors superimposed corresponds to monthly mean surface current velocities. (b) The number of cyclonic eddies (blue circles) detected between Cape Point and Cape Columbine with their position at each time-step during their life-time is indicated by individual circles. (c-d) shows the trajectories of inshore particles and offshore particles characteristic of the cyclonic circulations. . . 150

6.21 Correlation map showing only the significant correlation at 95% confidence level between monthly transport success time-series and EKE anomalies: (a) total transport success anomalies (TS′), (b) inshore transport success anomalies (TSI′) and, (c) offshore transport success anomalies (TSO′). The 500 m isobath separating the inshore and offshore region is superimposed as the red line. 151

B.1 Snapshot (01 January 1992) of eddies detected by the eddy detection algorithm in the R3km SSH field, contoured at 5 cm. Red (blue) circles indicate anti-cyclones (cyclones) and their trajectories throughout their lifetime are shown by red and blues lines, respectively. All eddies are tracked irrespective of their lifetime and the number shown on each eddy represents their identifiers (ID numbers). The yellow line traces the 500 m isobath. 170

List of Tables

3.1 BENGR15 configuration, at 7.5 km spatial resolution main parameters . . . 47

5.1 Summary of model configuration for the R7km and R3km simulations. . . . 92

6.1 Summary of mean (1992-2011) cyclonic and anticyclonic eddy properties in the R3km simulation in the region 36°S - 32°and 14°E - 20°E. 146

6.2 A summary of the occurrence of an Agulhas Ring interaction with the 3000 m isobath in the vicinity of the SARP in terms of years, months, days of influence, its minimum distance (km) and mean distance (km). Their associated offshore transport success anomaly is also presented. The instances when the ring had a interaction with the shelf-edge (500 m isobath) is denoted by *. 148

General Introduction

Eastern Boundary coastal Upwelling Systems (EBUS) are some of the most productive marine systems. They cover less than 1% of the world's ocean surface but supports 20% of the marine fish catch (*Alves and Miranda*, 2013). The Benguela Current Large Marine Ecosystem (BCLME), situated off the west and south-west coasts of southern Africa, is one of the four major EBUS of the world's ocean (*Hill*, 1998). It extends from the Angola-Benguela Frontal Zone (ABFZ) situated between 15-17°S to 37°S in latitude and from 0°E to 20°E in longitude. This study focuses on the Southern Benguela Upwelling System (SBUS), a sub-region within the BCLME generally defined as bounded to the north by the Lüderitz cell (26.6°S), the largest and most perennial upwelling cell (*Shannon and Nelson*, 1996; *Weeks et al.*, 2006), and to the south by the warm Agulhas Current.

Equatorward alongshore winds blow predominantly in summer along the west coast of South Africa, inducing an offshore transport of the coastal surface waters through Ekman dynamics. The no-inflow condition at the coast creates a divergence of the offshore Ekman transport that induces a vertical velocity directed towards the surface. This upwelling of deep, cold and nutrient-rich waters enriches the euphotic zone with nutrients, which stimulates and sustains a high primary production and a rich ecosystem and provides a suitable environment for small pelagic fish. Catches of sardines and anchovy are abundant in the region which drives an essential socio-economic activity.

In the EBUS, the abundance of small pelagic fish populations is regulated by a combination of several physical and biological processes (*Bakun*, 1996). Since 1983, repeated hydro-acoustic surveys have been carried out in the SBUS to monitor the populations

of sardines and anchovies. Their analysis shows significant interannual variability in the anchovy abundance and catches (*van der Lingen et al.*, 2002; *Huggett et al.*, 2003). Subsequently, extensive research has been undertaken focusing on the early life history of small pelagic fish and on how this variability could be linked to changes in the environmental conditions (*Boyd et al.*, 1998; *Hutchings et al.*, 1998; *Huggett et al.*, 2003; *Mullon et al.*, 2003; *Parada et al.*, 2003; *Lett et al.*, 2006; *Miller et al.*, 2006; *Parada et al.*, 2008; *Koné et al.*, 2013).

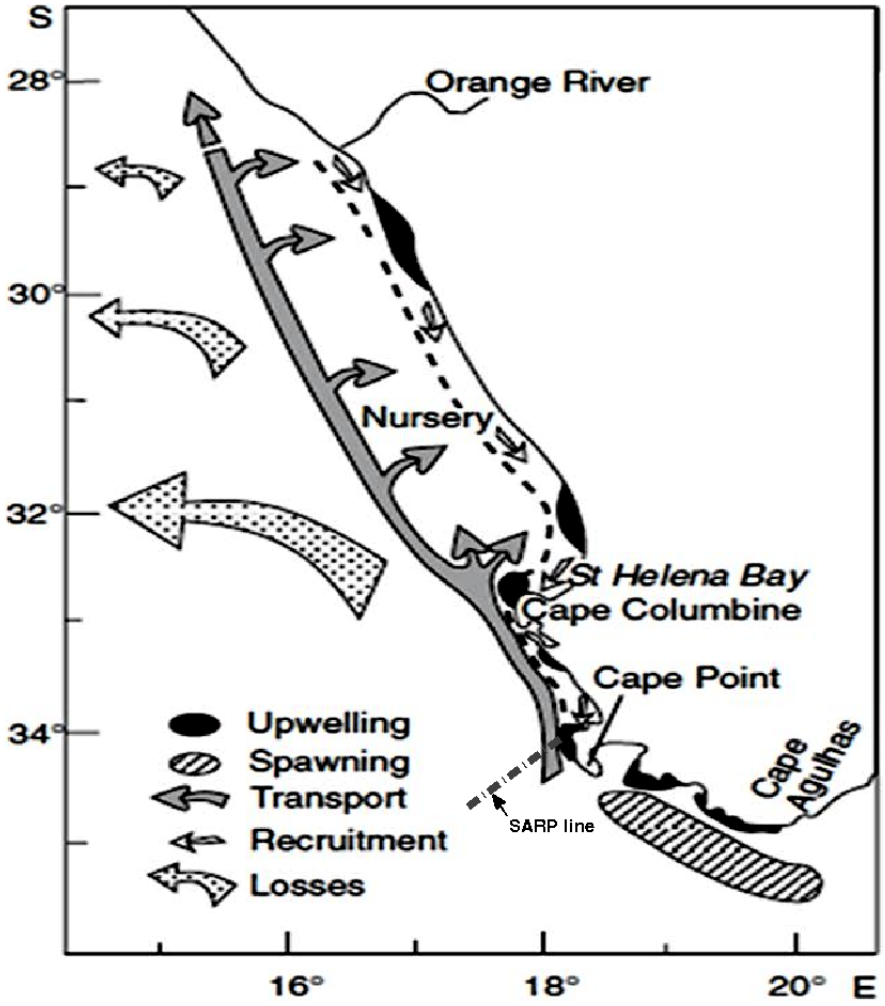

Figure 1: A conceptual diagram of the life history of anchovy in the southern Benguela. From *Hutchings et al.* (1998). Fish eggs, spawned at the tip of Cape Agulhas are advected northward alongshore. They experience offshore losses along the way. Those that make it to the nursery area (St Helena Bay) are considered as recruits. In their early-stage, anchovy larvae have minimal swimming ability, which makes them behave as passive particles. Therefore, their dispersion and transport is directly dependant on the oceanic circulation (*Pagès et al.*, 1991).

Anchovy eggs are spawned during the spring and summer season, in the western Agul-

has Bank (WAB), a 200 m depth large coastal plateau that extends up to 400 km offshore at the south tip of the South African continent (*Hutchings*, 1992; *Hutchings et al.*, 1998; *Huggett et al.*, 2003) (Fig. 1). Since 1997, an eastward extension of the spawning ground has been observed at the eastern side of the bank (*Roy et al.*, 2007) but with the west coast being the main nursery. In order to survive, eggs and larvae must be transported from the spawning to the nursery grounds in less than 30 days. Nevertheless, in the SBUS, the latter is situated more than 400 km away, off the southern African west coast, between Cape Columbine and the Orange River. This makes the SBUS distinctive from its northern Benguela counterpart and the other major Eastern Boundary Upwelling Systems (EBUS) where spawning and nursery grounds overlap. The success of transport to the nursery ground is considered to be critical for the anchovy stock, and one of the main drivers of the recruitment variability of anchovy (*Shelton and Hutchings*, 1982; *Hutchings*, 1992; *Hutchings et al.*, 1998). However, in their early-stage, anchovy larvae have minimal swimming ability, which makes them behave as passive particles. Therefore, their dispersion and transport, from the Agulhas Bank to the nursery area, are directly dependant on the oceanic circulation (*Pagès et al.*, 1991).

Hutchings (1992) presented a schematic picture of the major processes impacting the eggs and larvae journey from the western Agulhas Bank to the west coast upwelling region (Fig. 1). This scheme was based on knowledge of the coastal circulation and numerous observations of eggs and larvae distribution (*Bang and Andrews*, 1974; *Shelton and Hutchings*, 1982; *Shannon*, 1985; *Armstrong et al.*, 1987; *Shelton and Hutchings*, 1990). A coastal current flowing northward and following the shelf, namely the Benguela Jet, is considered as the major conveyor belt linking the western Agulhas Bank and the west coast upwelling area. According to *Nelson* (1989), the Benguela Jet is a narrow current ($\sim$ 20 km) that flows northward along the South African west coast between Cape Point (34.15°S, 18.4°E) and Cape Columbine (33°S, 17.5°E). The jet can sustain high velocities, ranging from 25 cm s^{-1} to 75 cm s^{-1} (*Bang and Andrews*, 1974; *Gordon*, 1985). It lies over a poleward undercurrent (*Nelson and Hutchings*, 1983), that flows over the shelf edge and occasionally reaches the surface. The jet varies in position and strength and responds

rapidly to changes in wind stress magnitude and direction. It follows the seasonal cycle of the upwelling (*Armstrong et al.*, 1987) and intensifies in summer when coastal upwelling of cold waters contributes to reinforcing the across-shore density gradient (*Veitch et al.*, 2006, 2017). In winter, when the wind direction reverses, this across-shore density gradient weakens but persists due to the intrusions of warm Agulhas waters from the south (*Twatwa Mhlongo et al.*, 2005).

Hutchings' (1992) scheme for Lagrangian transports of fish eggs and larvae has been widely used to set-up numerous Lagrangian modelling studies in the southern Benguela (*Mullon et al.*, 2003). *Huggett et al.* (2003), followed by *Parada et al.* (2003; 2008), carried out pioneering work demonstrating that the dominant anchovy spawning patterns in the southern Benguela could be reproduced when combining a 3-D hydrodynamic model with a Lagrangian particle-tracking tool. They also quantified the impact, on eggs and larvae transport success, of parameters such as the initial location, density and patchiness of eggs, as well as behavioural processes such as diurnal vertical migration, mortality due to lethal temperatures or predation. However, neither the local pathways nor the physical processes responsible for the transport of particles was studied in detail, even though the success of their experiments was obviously linked to the capacity of the hydrodynamical model to reproduce the main characteristics of the currents in the region.

The modelling works of *Veitch et al.* (2006) and *Blanke et al.* (2009) provided insights on the importance of the Benguela Jet for the connectivity between the western Agulhas Bank and the west coast upwelling area. More recently, in a detailed modelling study of the shelf edge currents, *Veitch et al.* (2017) described the bifurcation of this jet between Cape Point and Cape Columbine into a weak, narrow branch flowing over the shelf edge and a strong offshore branch flowing in the north-westward direction. A bifurcation of the jet, as well as other physical processes such as induced offshore Ekman transport and occasional entrainment by Agulhas rings, have been suggested as important physical processes impacting the alongshore transit of fish eggs and larvae (*Hutchings et al.*, 1998; *Skogen et al.*, 2003; *Veitch et al.*, 2006; *Garavelli et al.*, 2012).

This thesis builds upon these recent physical modelling studies to investigate in details how the horizontal and vertical structure of the shelf edge jets and the presence of mesoscale turbulence impact the alongshore trajectory of passive particles in the SBUS. The approach consists in a set of Lagrangian particle tracking experiments based on a robust hydrodynamical model capable of simulating the dominant physical processes influencing the along-shore transport of particles, *i.e.* a realistic seasonal coastal circulation, a realistic mesoscale eddy field, Agulhas leakage bringing warm Agulhas waters offshore of the southern Benguela shelf. While our study remains motivated by questions related to the dynamics of anchovy reproductive patterns and recruitment variability, it distinguishes from the others as it focuses on the physical transport processes that impact the survival of individuals at early stages. We are convinced that an important step for improving our understanding of the functioning of marine ecosystems is first to gain a detailed understanding of the physical processes that impact the life cycle. We believe that this understanding is of primary importance before adding other biological compartments, such as predation and mortality.

The Lagrangian experiments are built upon the pioneering work of *Huggett et al.* (2003) to focus exclusively on the northward alongshore portion of the hypothesised trajectory of anchovy larvae from the Agulhas Bank to St Helena Bay, *i.e.* the portion between Cape Point and St Helena Bay. If the Benguela Jet is assumed to play a dominant role in the transport of fish larvae, the success of this route should be in theory more predictable than the cross-shelf transport in the vicinity of the turbulent Agulhas retroflection. Compared to the model used by *Huggett et al.* (2003) and *Parada et al.* (2003, 2008), the simulations used for this study were created using a more recent version of Regional Ocean Modelling System (ROMS) and a regional configuration with higher vertical and horizontal resolutions to allow an accurate representation of the mesoscale and sub-mesoscales structures generated by the Benguela Jet instabilities, as well as the inner shelf (less than 100 m depth) poleward jets.

This study is dedicated to assessing the role of locally generated physical processes on the alongshore pathways. Our analysis is focused on the physical processes related to (i) the wind surface forcing (Ekman drift, Benguela Jet, coastal poleward current) and (ii) the role of the mesoscale dynamics at play in the area. Remotely forced ocean physics, such as southward propagating coastal Kelvin waves, that have been demonstrated to be of minor importance in the southern Benguela (*Illig et al.*, 2018) or large scale interannual variability of Agulhas leakage into the South Atlantic Ocean (*Loveday et al.*, 2014) is neglected. On the other hand, the full spectrum of atmospheric forcing variability is considered in order to correctly represent the locally generated physical processes (upwelling and Ekman dynamics forced by the local wind) and its interaction with the intense mesoscale dynamics at play in this region. Keeping the full variability of the atmospheric forcing to run a 20-year simulation allows deriving a much more realistic seasonal cycle than if an average surface forcing from a climatology was used. This is a major difference between our set-up and those used by studies published in the early 2000s. In our set-up, the local wind-forced physical processes (such as Ekman drift, upwelling cells, poleward undercurrent) are different and much more realistic.

The outline of the thesis is as follows: Chapter 1 presents a literature review of the dynamics of the SBUS. A brief description of the circulation in the SBUS is given, focusing on the main oceanographic and atmospheric features that may influence the transport of anchovy larvae during their early stages. Chapter 2 provides a detailed description of the numerical model used for this study and Chapter 3 describe the reference numerical simulation designed, and its validation. Our reference simulation is based on a 7.5 km horizontal resolution grid, with 100 vertical levels, and it encompasses all the Benguela Upwelling System, the Southern Ocean up to 54°S and the Mozambique Channel. Unlike the climatologically forced model of *Veitch et al.* (2017), our ocean model is forced by 6-hourly surface forcing (wind, heat and freshwater fluxes) over the 1989-2010 period. A careful assessment of this reference simulation against available in-situ and satellite datasets is presented.

Chapter 4 focuses on the physical processes that influence the seasonal cycle of the

alongshore connectivity between the southernmost portion of the SBUS (Cape Point at 34°S) and St. Helena Bay (32°S). The Lagrangian experiments aim at addressing the following: (1) the identification of the dominant pathways that ensure this connectivity; (2) their characteristics and robustness, and (3) the ocean dynamics that are responsible for the seasonal alongshore transport success variability. Results are based on the 7.5 km horizontal resolution reference simulation. The details of the Lagrangian experimental set-up used in the subsequent chapters are also presented here.

Chapter 5 discusses the sensitivity of these results to the resolution of the hydrodynamical model. For this purpose, one nested simulation based on 3 km resolution grid is developed and also run for 20 years. Increasing the spatial resolution allows some fine-scale shelf dynamical features, such as the very inshore poleward coastal jet, to be modelled. Furthermore, the Agulhas leakage was also unexpectedly changed in the higher resolution model, with some important implications on the stratification of the region. These gains of realism have an impact on the alongshore connectivity, in particular on its variability. However, they confirm the significant role of the Benguela Jet in modulating the seasonal cycle of the alongshore connectivity.

Having identified the mechanisms that drive the seasonal cycle allows us to investigate how the interannual variability of each of these processes individually impact the interannual variation of transport success. This is the focus of Chapter 6. This study is based on the 3 km simulation nested within the 7.5 km simulation. The 7.5 km simulation considers a monthly climatology at lateral boundaries, which filters out the interannual signal, but keeps the seasonal one. It is important to stress that the objective of this work is not to study the impact of remotely generated interannual variability, but rather to identify the significant local dynamical processes influencing the seasonal cycle of transport between Cape Point and St Helena Bay, i.e. a realistic Benguela Jet, coastal poleward current, offshore Ekman drift, and off-shelf eddy field.

Finally, conclusions and future directions of this research are discussed in Chapter 7. A better understanding of the processes controlling Lagrangian transport dynamics in the SBUS allows for better connections to be made between the physics and the biology of both lower (primary productivity) and middle trophic-levels (pelagic fish eggs and larvae).

183 It also enlightens some potential implications for the understanding of the propagation of
184 harmful algal blooms and/or oil spills and pollutants.

Chapter 1

Literature Review

This chapter presents a literature review of the current knowledge on the ocean circulation of the southern Benguela upwelling system (SBUS). The literature review will first focus on the atmospheric forcing that drives the upwelling dynamics, and then the main regional circulation.

1.1 Atmospheric forcing

1.1.1 Seasonal variability

The primary atmospheric forcing of the southern Benguela upwelling system is the semi-permanent South Atlantic Anticyclone (SAA), the presence of continental low-pressure systems and the eastward propagating mid-latitude cyclones south of the continent at 2-8 day periods (*Risien et al.*, 2004; *Shillington et al.*, 2006; *Burls and Reason*, 2008). The SAA, denoted by the 150 m isoline in Figure 1.1, undergoes a seasonal latitudinal migration. It moves southward (northward) during austral summer (winter). It also shifts longitudinally such that it is found closer to the coast in spring (Fig 1.1d) and moves offshore in summer and autumn (Fig 1.1a,b). This migration results in the variability of the upwelling favourable winds in the region between the 25°S-35°S. The presence of a continental low-pressure trough over the south of the African continent results in the strengthening of the alongshore equatorward winds in summer. On the other hand, the presence of the continental high and the northward movement of SAA in winter weakens

the upwelling-favourable winds and results in the dominance of westerlies over the region (Fig 1.1c) (*Shelton et al.*, 1985). As a result, the upwelling-favourable winds reach a maximum during summer and downwelling favourable winds occur in winter with spring and autumn being transition periods.

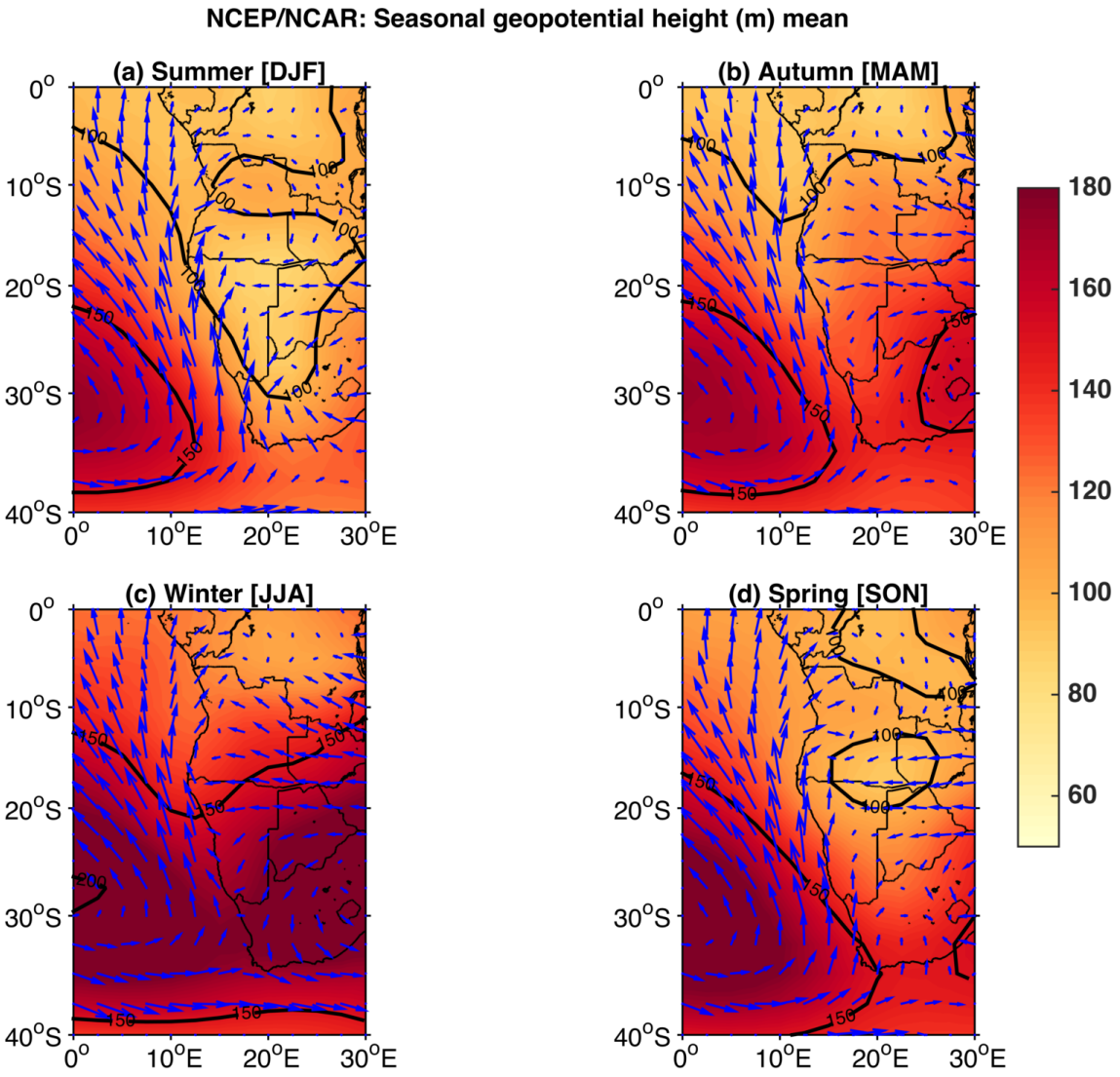

Figure 1.1: Mean seasonal composite of 1000 mb geopotential height (m) over the South Atlantic ocean from NCEP (1980-2012) data: (a) summer (December-February), (b) autumn (March-May), (c) winter (June-August) and (d) spring (September-November). The contours shown are of the 100 m and 150 m geopotential height and represent the high and low pressure, respectively. The surface wind speed and direction is represented by the overlaid blue arrows. Data used was downloaded from NCEP website[1]

[1]https://www.esrl.noaa.gov/psd/cgi-bin/data/composites/printpage.pl

1.1.2 Intra-seasonal and short-term variability

The large-scale seasonal variability of the atmospheric forcing over the SBUS region co-exists with some short-term and intra-seasonal atmospheric features. The equatorward upwelling favourable winds that blow predominantly during summer are subject to substantial intra-seasonal variability. Synoptic features such as the passage of cold fronts, cut-off lows and mesoscale features such as the Berg winds[2], coastal lows and diurnal sea breeze (*Shillington et al.*, 2006) can disrupt the favourable upwelling winds at different temporal and spatial scale (*Shillington et al.*, 2006) and can promote specific upwelling or downwelling events (*Fennel*, 1999).

The eastward passage of cyclonic storms south of South Africa, may generate winds with poleward and onshore components driving downwelling events (Fig. 1.2) (*Bakun*, 2001). On the other hand, the occurrence of coastal lows are characterised by the poleward propagation of a low pressure system along the west coast of South Africa (*Jury et al.*, 1990). This phenomenon causes the strengthening (weakening) of favourable upwelling winds in its leading (trailing) edge (*Jury and Brundrit*, 1992; *Shillington et al.*, 2006) and this in turn may induce more/less upwelling (*Payne et al.*, 1992).

1.1.3 Interannual and long-term variability

Blamey et al. 2012 analysed in detail the Cape Point anemometer time series over the period 1965-2011. Figure 1.3, extracted from their paper, shows the annual average time series of the north-south component of the wind speed responsible for the coastal divergence of Ekman transport. The south-easterlies vary on the interannual time scale. Although the signal has some chaotic behaviour, some clear periods of positive/negative upwelling index can be distinguished. *Blamey et al.* (2012, 2015) identified these periods and characterised some of the regime shifts. The period of interest of this study goes from 1990 to 2012. During this period, a net amplification of the upwelling favourable winds occurred during the 1990s, followed by a net decrease in the early 2000s.

Large scale patterns of atmospheric variability may explain partly these regime shifts. At interannual time scales, the Benguela atmospheric circulation is influenced by large-

[2]Berg winds are offshore directed and blow mostly during winter when a high-pressure system over the continent co-exists with a low-pressure system along the coastal area.

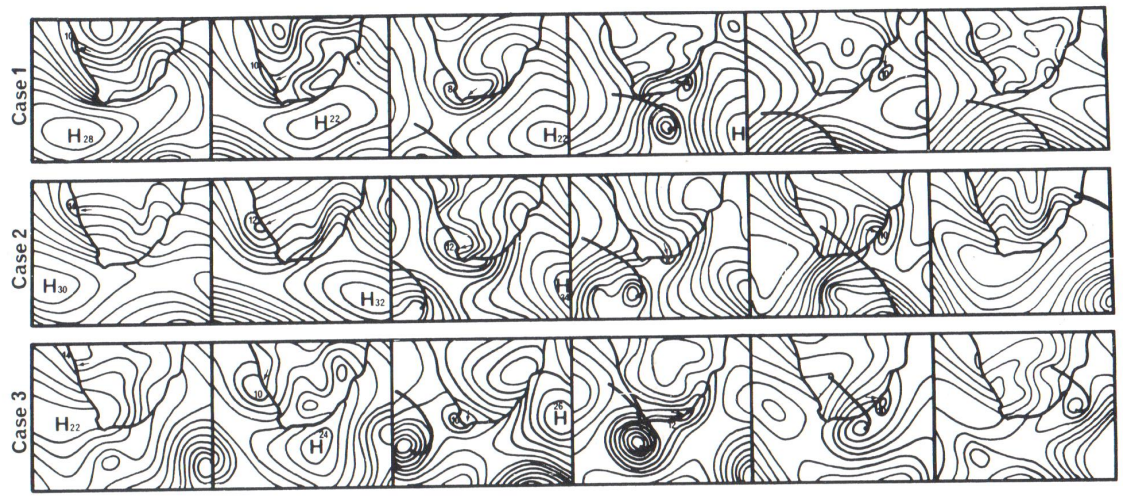

Figure 1.2: Surface synoptic pressure maps of the eastward propagating cyclones passing south of the continent obtained from South African Weather Services (from *Jury et al.* (1990)) and the formation of a trapped coastal low that can promote pulsed upwelling at 3-10 day intervals (*Hutchings et al.*, 2009). The H in each figure refers to the ridging high pressure cell, the bold line to the trailing edge of frontal system, and the arrow points the position of the coastal low. The three cases corresponds to days extending over 6-11 February 1981, 15-20 September 1985 and 18-23 April 1980, respectively.

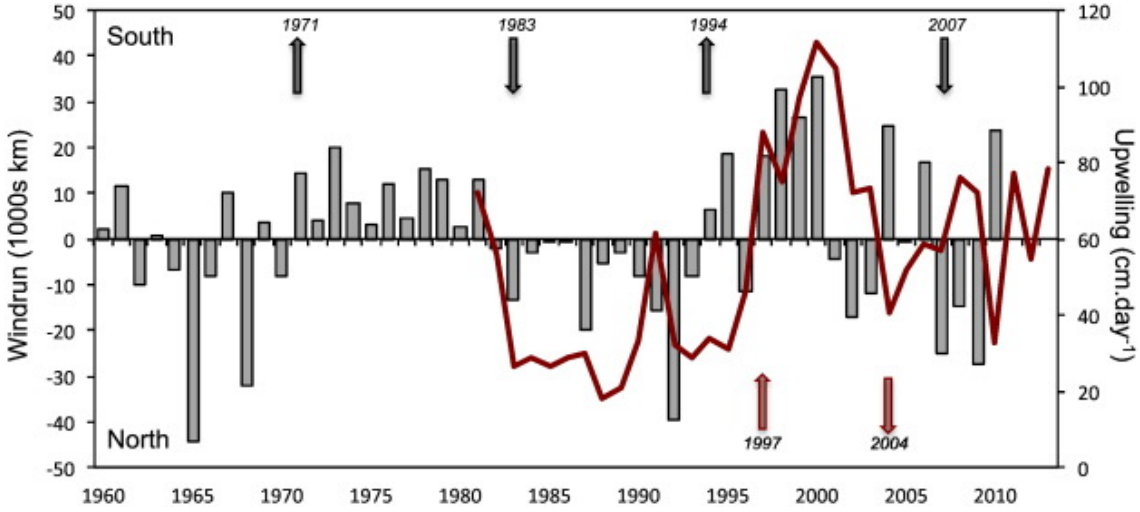

Figure 1.3: Annual anomalies (1960-2010 period) of north/south wind component measured as wind-run (grey bars, km) and summer upwelling rates (cm day^{-1}) for Cape Point (taken from *Blamey et al.* (2015)). Positive/negative bars indicate a dominance of southerlies/northerlies. Positive/negative wind regime shifts and upwelling are denoted by grey and red arrows, respectively. There are some periods where the dominance of southerlies (northerlies) coincide with intensified (reduced) upwelling rates. The early 1980s to early 1990s period was predominately associated with reduced uwelling and northerlies and upwelling was intensified between 1997 and 2000.

scale interannual variability of the El Niño-Southern Oscillation (ENSO) and the Southern Annular Mode (SAM) (*Pitcher and Pillar*, 2010; *Tim et al.*, 2015). According to *Tim et al.* (2015), these climate modes of variability influence upwelling through the modulation of local atmospheric conditions.

Seasonal composites of sea-level pressure (SLP) anomalies indicated that La Niña/El Niño events are characterised by positive/negative SLP anomalies over the South Atlantic mid-latitudes (*Colberg et al.*, 2004). Because higher SLP over the South Atlantic mid-latitudes enhance the strength of the south easterly upwelling favourable winds, this positive/negative correlation between an ENSO index and SLP anomalies over the South Atlantic suggests that stronger/weaker south easterlies may be expected during El Niño/La Niña years (*Risien et al.*, 2004; *Dufois et al.*, 2012)).

The SAM is the dominant mode of climate variability in the extra-tropical Southern Hemisphere (*Hall and Visbeck*, 2002) and results in meridional shifts of the mid-latitude westerlies on various time scales. These shifts can be monitored using the Marshall Index, defined as the meridional differences in normalised sea level pressure between the Antarctic (65°S) and the southern hemisphere mid-latitudes (40°S) (*Marshall*, 2003). Positive SAM indices are associated with a poleward shift of the atmospheric jet stream, which in turn leads to a weakening of the westerlies between 45° S and 20° S (*Hall and Visbeck*, 2002). Several studies suggest that this weakening of the westerlies is accompanied by a strengthening of the south-easterly upwelling favourable winds (*Hall and Visbeck*, 2002; *Hutchings et al.*, 2009). In fact, positive correlations exist between upwelling favourable wind anomalies over the SBUS and summer averages (December-February) of the SAM index (*Tim et al.*, 2015).

1.2 Ocean circulation

The mean regional circulation in the SBUS and its seasonal cycle are described in *Nelson and Hutchings* (1983). Its main features are summarised in Figure 1.4 extracted from *Hardman-Mountford et al.* (2003).

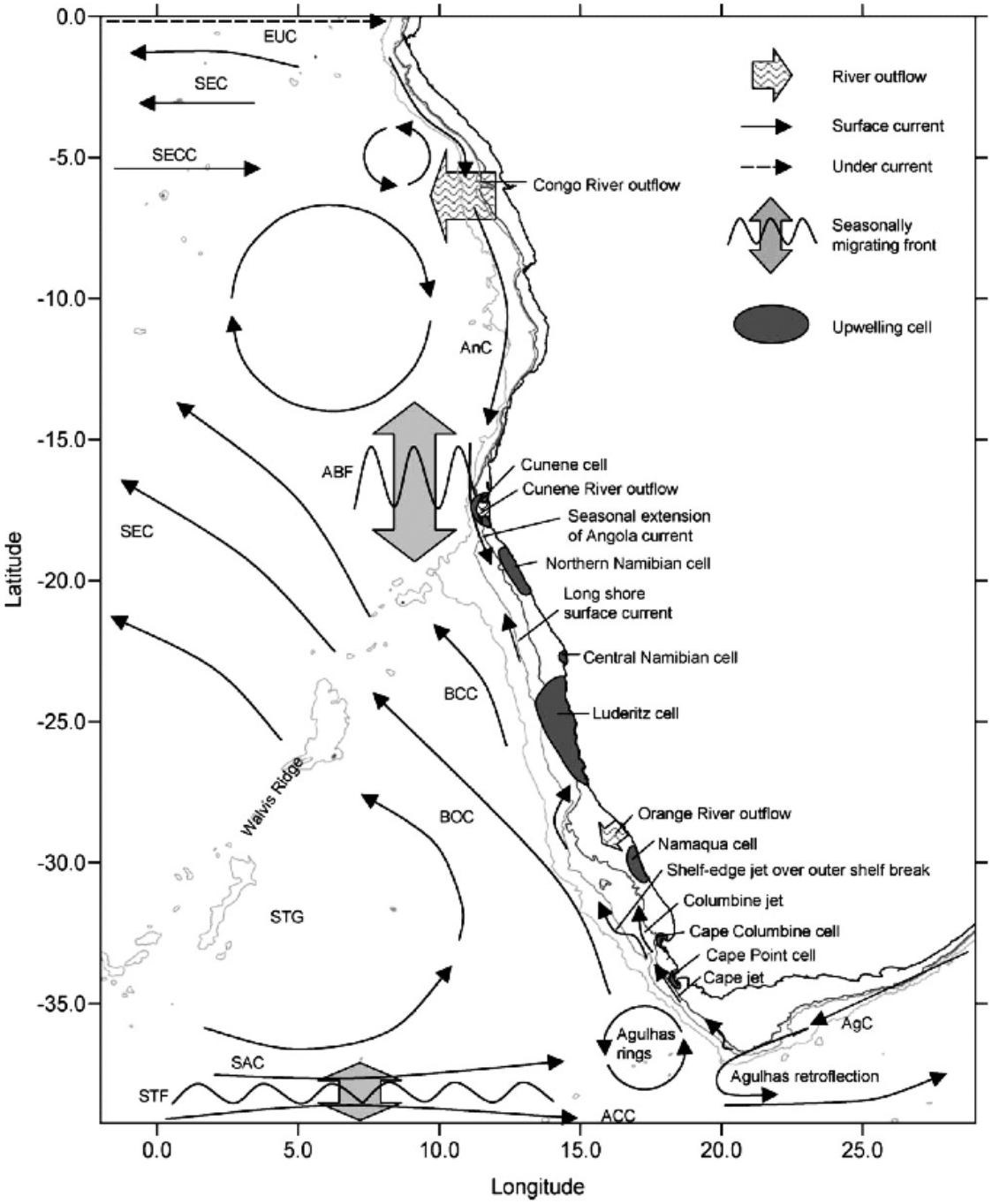

Figure 1.4: Map of the South East Atlantic showing surface and near-surface currents, frontal zones, upwelling cells, major areas of freshwater input and bathymetry adapted from *Hardman-Mountford et al.* (2003). These are main oceanographic features that could impact biology in the Benguela upwelling system at different temporal and spatial scale (*Shannon et al.*, 1996). EUC, Equatorial Under Current; SEC, South Equatorial Current; SECC, South Equatorial Counter Current; AnC, Angola Current; BOC, Benguela Oceanic Current; BCC, Benguela Coastal Current; SAC, South Atlantic Current; AgC, Agulhas Current; ABF, Angola–Benguela front; STF, subtropical front; STG, subtropical gyre; ACC, Antarctic Circumpolar Current. The Benguela Current and Benguela Jet are labelled BOC and 'Cape Jet', respectively.

Some intense alongshore surface and sub-surface currents

The surface circulation in the region is mainly dominated by equatorward currents. The broad (100 km) Benguela Current that constitutes the eastern limb of the South-Atlantic Subtropical Gyre (*Peterson and Stramma*, 1991) is located offshore beyond the shelf edge. Over the shelf edge, another northward along-shore flow co-exists, namely the Benguela Jet. The latter flows northwards along South Africa's west coast between Cape Point and Cape Columbine. It is much narrower (a few tens of kilometres) than the Benguela Current, but has higher velocities ranging from 25 cm s^{-1} to 75 cm s^{-1} (*Bang and Andrews*, 1974; *Gordon*, 1985). It is in thermal wind balance with the cross-shore density front that results from the upwelling of cold waters inshore and the presence of warmer waters offshore (*Blanke et al.*, 2009; *Veitch et al.*, 2017). Even though the Benguela Jet gets intensified in summer (*Armstrong et al.*, 1987), when the coastal upwelling of cold waters occurs, it can be observed throughout the year thanks to the leakage of warm Agulhas waters into the SBUS (*Nelson and Hutchings*, 1983; *Strub et al.*, 1998). Another feature of the SBUS mean circulation is the presence of a poleward undercurrent (PUC) that flows over the continental shelf edge underneath the Benguela Jet (*Shelton and Hutchings*, 1982; *Nelson and Hutchings*, 1983). This is a common feature between all main four EBUS of the world ocean. It is worth noting that this undercurrent may occasionally reach the surface. The surfacing of the poleward undercurrent is not specific to the SBUS. When it happens, it can either split the surface equatorward jet, or shift it offshore (*Song et al.*, 2011). This leads to the co-existence of a complex network of alongshore multi-core jets in most EBUS.

A theoretical study by *Fennel et al.* (2012) shows that the cross-shore horizontal and vertical structure of these jets is governed by the bathymetry, the alongshore wind-stress, and the curl of the wind stress. The latter results mainly from the coastal wind drop-off. Its signature is the presence of an along-shore 300 km width coastal band of cyclonic negative wind stress curl (WSC). Increasing the cyclonic WSC over the shelf edge strengthens the poleward undercurrent, which in turn displaces the surface equatorward jet offshore. As expected, in the absence of WSC, the shelf edge equatorward jet relocates closer to the coast (*Song et al.*, 2011). However, the poleward undercurrent is always present with or without WSC. A study by *Junker et al.* (2015) suggests that the poleward undercurrent

may be modulated by remotely generated coastal Kelvin wave signals.

An intense mesoscale eddy activity

Eddies and filaments are general mesoscale features of the SBUS (*Rubio et al.*, 2009). They can be generated either locally from mixed barotropic/baroclinic instabilities of the density fronts (*Veitch et al.*, 2010), or remotely in the Agulhas retroflection region. Their presence modulates the schematic picture of the circulation given by the mean flow and potentially play a large role in structuring the ecosystem (*Hutchings et al.*, 1998; *Rubio et al.*, 2009).

In EBUS, mesoscale eddies play a significant role in the cross-shore transport of buoyancy, balancing the net surface heat losses and gains (*Marchesiello et al.*, 2003; *Capet et al.*, 2008b; *Colas et al.*, 2013). Their ability to generate cross-isobaths flow breaks the dynamical barrier set up by the shelf slope and facilitates cross-shore exchanges of water masses between the coastal upwelling zone and the adjacent open ocean. Eddies and filaments may thereby entrap coastal shelf biological material and drag it out into the open ocean, impacting the overall cumulative cross-shore mass transport of biota (*Hernández-Carrasco et al.*, 2014; *Veitch et al.*, 2010). In addition, vertical velocities are triggered on their lateral boundaries when horizontal density gradients are enhanced by frontogenesis (*Capet et al.*, 2008b; *Lévy et al.*, 2012).

A unique location in the vicinity of a western boundary current

The SBUS is distinct by having the warm Agulhas Current with its ring shedding as its southern boundary, unlike any other Eastern Boundary Upwelling Systems. The Agulhas Current forms the western branch of the South Indian Ocean subtropical gyre and flows southward along the east coast of South Africa. As it reaches the southern tip of the African continent at 20°E, it turns back and flows eastward into the South Indian Ocean. This process results in the generation of intense mesoscale activity including the generation of shelf-edge cyclonic eddies as it interacts with the Agulhas Bank (*Penven et al.*, 2001). The retroflection of the Agulhas current is also accompanied by a leakage (18 Sv) of warm

and salty waters of Indian Ocean origin into the South Atlantic Ocean (*Loveday et al.*, 2014). This leakage occurs through the shedding of large (radius> 100 km) anticyclonic Agulhas Rings, smaller (radius < 50 km) cyclonic eddies and filaments. Agulhas rings are shed at a rate of 5-6 per year when the Agulhas Current retroflects eastward. They then propagate into the South Atlantic. Each of them transports large volumes (0.5-1.5 Sv) of Indian Ocean waters (*Schouten et al.*, 2000; *van Aken et al.*, 2003; *Doglioli et al.*, 2006). This leakage is partly responsible for the enhanced cross-shore density gradient observed in the SBUS, which explains why the Benguela Jet is such a narrow and intense current, squeezed onto the shelf edge in between the 200 m and 500 isobaths. In addition, this leakage also explains why the SBUS is characterised by a strong offshore mesoscale variability reflected by high EKE values in excess of $\sim$500 $cm^{-2}s^{-2}$ that extends to -600 m depth in contrast to the nearshore region (EKE $\sim$ 100 $cm^2.s^{-2}$) and the $\sim$ 120 $cm^{-2}s^{-2}$ in the offshore California Current System (*Capet et al.*, 2008b; *Veitch et al.*, 2009; *Veitch and Penven*, 2017).

The presence of this very intense mesoscale turbulent activity in the coastal transition zone can also drive a strong intra-seasonal variability of the shelf circulation. There are also some rare observations of Agulhas rings interacting with the Benguela upwelling front (*Duncombe-Rae et al.*, 1992), triggering mesoscale instabilities leading to the formation filaments of cold water that extends further offshore in the open ocean (*Payne et al.*, 1992).

The coastal poleward current

Shelf and nearshore currents vary in response to the short-term fluctuations of the atmospheric forcing (*Nelson*, 1989). Variations of the nearshore negative cyclonic wind stress curl associated with atmospheric boundary layer dynamics and orographic effects may modulate the intensity and occurrence of poleward surface flow in the first 200 m depth coastal band (*Brown and Hutchings*, 1987; *Marchesiello et al.*, 2003; *Veitch et al.*, 2009). The presence of cyclonic wind stress curl on the innershelf may induce a poleward counter current consistent with the Sverdrup relation (*Vallis*, 2006). This innershelf counter current may sometimes merge with the offshore poleward undercurrent located on the shelf slope (*Junker et al.*, 2015).

In addition, periodic current reversals can also occur during episodes of relaxation of favourable upwelling wind stress and are characteristic of all EBUS. In the California mid-shelf (depths over 100 m), they have been extensively documented (*Send et al.*, 1987; *Winant et al.*, 1987; *Huyer and Kosro*, 1987; *Kosro*, 1987; *Largier et al.*, 1993). In-situ observations of the California mid-shelf region, show that these episodes generate a complex inner shelf circulation characterised by a strong counter-current (*Cudaback et al.*, 2005; *Roughan et al.*, 2006) and poleward flow of warm waters that can accumulate inside bays (*Gan and Allen*, 2002b; *Melton et al.*, 2009; *Washburn et al.*, 2011).

In the SBUS, there is also evidence of current reversals associated with the poleward propagation of warm waters on the innershelf (*Fawcett et al.*, 2008). They can lead to a large increase of temperature up to 5°C day^{-1} in the very nearshore region and inside of St Helena Bay. This occurs when the equatorward wind stress relaxes and the nearshore upwelling circulation is no longer in geostrophic balance resulting in a counter-current that flows around the headlands and transports some warm waters (*Gan and Allen*, 2002a).

In EBUS, the response of the shelf-circulation to the short-term variability of the atmospheric forcing has been investigated using regional ocean models. The importance of using a realistic, time-varying surface forcing was demonstrated by *Blanke et al.* (2005) who found that a daily wind product is more efficient in simulating the observed nearshore interannual variability of sea surface temperature anomalies (warm and cold events) and short-term upwelling events than a weekly product (*Blanke et al.*, 2002).

1.3 Conclusion

The literature review presented in this chapter on the southern Benguela ocean circulation has identified complex physical features with different temporal and spatial scales. The Benguela Jet plays a role as a vehicle for fish eggs and larvae from the southern tip of the SBUS to St Helena Bay on the west coast. However due to lack of longer in-situ measurements, the variability of the jet in terms of its structure and intensity has not been thoroughly studied. Hence, it is not fully known how this variability in the jet and mesoscale variability influences the alongshore transport of fish eggs and larvae. Therefore, other tools such as numerical models can be used to provide us with desired spatially and

temporally cohesive outputs in order to study the ocean circulation of the SBUS. The next chapter deals with the ROMS model that is used in this thesis to simulate the ocean circulation of the SBUS.

Chapter 2

The ROMS model

This chapter focuses on the description of the ocean model employed in this study to simulate the ocean circulation in the Benguela Upwelling System. Here, we focus on the numerical details of the Regional Oceanic Modeling System (ROMS; Shchepetkin and McWilliams 2005; Shchepetkin 2015) in its Coastal and Regional Ocean Community (CROCO[1]) version (*Debreu et al.*, 2012).

Readers who are familiar with the ROMS model may skip this chapter and move directly to chapter 3 in which the reference simulation is described. However, readers who wish to learn more about the components necessary to develop a numerical ocean circulation model may find here some relevant information about the equations that are time integrated, the vertical and lateral boundary conditions, the numerical schemes, and the horizontal and vertical discretization.

2.1 The primitive equations

The primitive equations are a set of partial differential equations. They result directly from the very general momentum conservation Navier-Stokes equations for Newtonian rotating fluids (*Kundu et al.*, 2015), when one considers together the flow to be incompressible, hydrostatic, of Boussinesq type (*Vallis*, 2006). This set of equations is completed by an equation of state that provides the fluid density as a function of pressure, temperature and salinity. Therefore, two tracer conservation equations are added for temperature and

[1] `http://www.croco-ocean.org/`

salinity respectively. After combining all together, we obtain the following set of equations, here written in Cartesian coordinates:

- 2 prognostic equations for u and v derived from the conservation of horizontal momentum

$$\frac{\partial u}{\partial t} + \vec{v}.\vec{\nabla}u - fv = -\frac{\partial \phi}{\partial x} + D_u \tag{2.1}$$

$$\frac{\partial v}{\partial t} + \vec{v}.\vec{\nabla}v + fu = -\frac{\partial \phi}{\partial y} + D_v \tag{2.2}$$

- 1 diagnostic equation for the pressure derived from the vertical momentum conservation equation with the hydrostatic assumption

$$\frac{\partial \phi}{\partial z} = -\frac{\rho g}{\rho_o} \tag{2.3}$$

- 2 prognostic equations for potential temperature T and salinity S derived from the conservation of tracer content

$$\frac{\partial T}{\partial t} + \vec{v}.\vec{\nabla}T = D_T \tag{2.4}$$

$$\frac{\partial S}{\partial t} + \vec{v}.\vec{\nabla}S = D_S \tag{2.5}$$

- 1 diagnostic equation for w derived from for the continuity equation (mass conservation + incompressible flow)

$$\frac{\partial u}{\partial x} + \frac{\partial v}{\partial y} + \frac{\partial w}{\partial z} = 0 \tag{2.6}$$

- 1 diagnostic equation for the water density derived from for the equation of state for seawater (*Shchepetkin and McWilliams*, 2005)

$$\rho = \rho(T, S, P). \tag{2.7}$$

x, y, z are the independent variables related to the east-west, north-south, vertical directions respectively, and t the time independent variable. The prognostic variables are the

zonal (u), meridional (v) and vertical (w) components of the velocity vector $\vec{v}$, the potential temperature (T) and the salinity (S). ρ is the seawater density, $\rho_0 = 1025$ kg m^{-3} the reference seawater density, $f = 4\pi/86400 \ \sin(\lambda)$ the Coriolis parameter, λ the latitude, ϕ the dynamic pressure, $\vec{g}$ the constant of gravity. D_u, D_v, D_T and D_S are the diffusive terms for momentum, temperature and salt respectively.

The hydrostatic assumption neglects the vertical acceleration terms, and the Boussinesq assumption neglects the variation of density in the horizontal momentum equations. The diffusive terms of the primitive equation include second order partial derivatives according to x, y and z and some knowledge of the diffusion coefficients for momentum and heat and water fluxes. They can be decomposed into a vertical part (_v suffix) and an horizontal part (_h suffix).

$$D_u = D_{uh} + D_{uv} \tag{2.8}$$

$$D_v = D_{vh} + D_{vv} \tag{2.9}$$

$$D_T = D_{Th} + D_{Tv} \tag{2.10}$$

$$D_S = D_{Sh} + D_{Sv} \tag{2.11}$$

For the momentum equations , we have

$$D_{uh} = \frac{\partial}{\partial x}\left(K_{Mh}\frac{\partial u}{\partial x}\right) + \frac{\partial}{\partial y}\left(K_{Mh}\frac{\partial u}{\partial z}\right) \tag{2.12}$$

$$D_{uv} = \frac{\partial}{\partial z}\left(K_{Mv}\frac{\partial u}{\partial z}\right) \tag{2.13}$$

$$D_{vh} = \frac{\partial}{\partial x}\left(K_{Mh}\frac{\partial v}{\partial x}\right) + \frac{\partial}{\partial y}\left(K_{Mh}\frac{\partial v}{\partial z}\right) \tag{2.14}$$

$$D_{vv} = \frac{\partial}{\partial z}\left(K_{Mv}\frac{\partial v}{\partial z}\right) \tag{2.15}$$

where K_{Mh} and K_{Mv} are the coefficients of horizontal and vertical eddy viscosity for

momentum. For the tracers equations , we have

$$D_{Th} = \frac{\partial}{\partial x}\left(K_{Th}\frac{\partial u}{\partial x}\right) + \frac{\partial}{\partial y}\left(K_{Th}\frac{\partial u}{\partial z}\right) \tag{2.16}$$

$$D_{Tv} = \frac{\partial}{\partial z}\left(K_{Tv}\frac{\partial u}{\partial z}\right) \tag{2.17}$$

$$D_{Sh} = \frac{\partial}{\partial x}\left(K_{Sh}\frac{\partial v}{\partial x}\right) + \frac{\partial}{\partial y}\left(K_{Sh}\frac{\partial v}{\partial z}\right) \tag{2.18}$$

$$D_{Sv} = \frac{\partial}{\partial z}\left(K_{Sv}\frac{\partial v}{\partial z}\right) \tag{2.19}$$

where K_{Th}/K_{Sh} and K_{Tv}/K_{Sv} are the coefficients of horizontal and vertical eddy diffusivity for heat/salt.

The presence of first order and second order spatial derivatives in the primitive equations implies the use of boundary conditions. These boundary conditions are used to specify the fluxes of momentum, heat and fresh-water at the lateral and surface boundaries. In the presence of hard boundaries (bottom, land), the no-flux condition across the boundary is used.

2.2 The vertical boundary conditions

The presence of vertical partial derivatives in the primitive equation requires surface and bottom boundary conditions to be specified. These conditions are of particularly importance because they control the inputs and losses of momentum, heat and fresh-water fluxes through the surface and bottom boundaries.

2.2.1 Surface boundary condition at z=η(x,y,t)

At the surface, at z=η(x,y,t) where η is the free surface elevation, the ocean receives input of momentum through wind stress, as well as inputs or losses of heat/salt trough heat/fresh-water surface fluxes. These fluxes relate to either the local atmospheric components of the wind stress, or the heat and freshwater surface fluxes:

$$K_{Mv}\frac{\partial u}{\partial z} = \frac{\tau_x^s}{\rho_o}(x,y,t) \tag{2.20}$$

$$K_{Mv}\frac{\partial v}{\partial z} = \frac{\tau_y^s}{\rho_o}(x,y,t) \tag{2.21}$$

$$K_{Tv}\frac{\partial T}{\partial z} = \frac{Q_{net}}{\rho_o C_p} \tag{2.22}$$

$$K_{Sv}\frac{\partial S}{\partial z} = \frac{(E_v - P_r)\ SSS}{\rho_o} \tag{2.23}$$

τ_x^s, τ_y^s are the surface wind stress in x and y directions respectively, where as Q_T is the net surface heat flux, $(E_v - P_r)SSS$ is the net fresh-water flux, with E_v the net evaporation rate, P_r the precipitation rate freshwater flux and SSS the sea surface salinity.

A quadratic law is used to express the surface wind stress components as a function of the atmospheric wind velocity components (u_{10}^a and v_{10}^a) 10 m above sea level, the air density ρ_{air}, and the surface drag coefficient C_D^s.

$$\tau_x^s = \rho_{air} C_D^s \sqrt{u_{10}^2 + v_{10}^2}\ u_{10} \tag{2.24}$$

$$\tau_y^s = \rho_{air} C_D^s \sqrt{u_{10}^2 + v_{10}^2}\ v_{10}. \tag{2.25}$$

In addition a dynamical condition is imposed on the vertical velocity so that the free surface behaves as a material derivative:

$$w = \frac{\partial \eta}{\partial t} + u\frac{\partial \eta}{\partial x} + v\frac{\partial \eta}{\partial y} \tag{2.26}$$

2.2.2 Bottom boundary condition at $z = -H(x,y)$

At the bottom of the ocean, a condition of no flow is imposed, as well as zero heat and freshwater fluxes across the seafloor:

$$w = -\left(u\frac{\partial H}{\partial x} + v\frac{\partial H}{\partial y}\right) \tag{2.27}$$

$$K_{Tv}\frac{\partial T}{\partial z} = 0 \tag{2.28}$$

$$K_{Sv}\frac{\partial S}{\partial z} = 0. \tag{2.29}$$

Momentum is dissipated through bottom friction and the bottom boundary conditions are

$$K_v \frac{\partial u}{\partial z} = \frac{\tau_x^b}{\rho_o}(x, y, t) \tag{2.30}$$

$$K_v \frac{\partial v}{\partial z} = \frac{\tau_y^b}{\rho_o}(x, y, t), \tag{2.31}$$

with τ_x^b, τ_y^b the bottom stress in the in x and y directions respectively. The expression for bottom stress uses a combination of linear, quadratic, or logarithmic terms (*Hedström*, 2009):

$$\tau_x^b = (-r + C_D^b \sqrt{u^2 + v^2}).u_b \tag{2.32}$$

and

$$\tau_y^b = (-r + C_D^b \sqrt{u^2 + v^2}).v_b \tag{2.33}$$

where r is a friction velocity and C_D^b bottom a non dimensional **bottom** drag coefficient.

- "Linear friction",

  Linear friction can be implemented by setting $\mathbf{C_D^b = 0}$, which implies:

$$(\tau_b^x, \tau_b^y) = -r\,(u_b, v_b)$$

  .

- "Quadratic friction",

  Quadratic friction can be implemented by setting $\mathbf{r = 0}$, which implies:

$$(\tau_b^x, \tau_b^y) = C_D^b \sqrt{u_b^2 + v_b^2}\,(u_b, v_b)$$

  .

- "Quadratic friction using a Von Karman Prandtl logarithmic layer "

  The "Von Karman Quadratic Friction" has the same formulations as the "classic" quadratic friction ($\mathbf{r = 0}$). The only difference lies in the the parameterization of

the drag coefficient C_d^b:

$$C_D^b = (\frac{\kappa}{\log[\Delta z_b/z_r]})^2 \quad \text{if} \quad C_D^{min} < C_D^b < C_D^{max}, \text{otherwise} \tag{2.34}$$

$$C_D^b = C_D^{min} \quad \text{or} \quad C_D^b = C_D^{max} \quad \text{if} \quad C_D \quad \text{is outside this range} \tag{2.35}$$

$\kappa = 0.41$ represents the Von Karman constant and Δz_b, the thickness from the first level to the bottom. C_D^b becomes variable and depends on the thickness of the first vertical level, reaching its maximum value if the vertical resolution near the bottom is close to the scale of roughness z_r.

2.3 Surface fluxes forcing in the model

2.3.1 Momentum surface fluxes

The wind forcing is imposed in the form a surface stress τ^s (Eqs. 2.24 and 2.25) in the surface boundary conditions of the horizontal momentum equations. τ^s is calculated at each point on the model grid from the wind speed components 10 m above sea level u_{10}^a, v_{10}^a, the air density and the drag coefficient C_D^s. Several parametrizations exist to estimate C_D^s. The latter is usually calculated using a so-called "bulk" parametrization. In the following, we chose the one proposed by *Fairall et al.* (1996). All the atmospheric data required to calculate the surface wind stress are provided by the 6 hourly Climate Forecast System Reanalysis (CFSR) atmospheric reanalysis(*Saha*, 2010).

2.3.2 Heat fluxes and fresh water flux

The surface boundary conditions in the two prognostic equations for temperature and salinity require the specification of a net heat and fresh-water flux at each grid point of the model grid. The net heat flux is the sum of four components:

$$Q_{net} = Q_{solar\_net} + Q_{long-wave\_net} + Q_{latent} + Q_{sensible}, \tag{2.36}$$

where Q_{solar_net} is "short wave" radiative flux due to solar radiation penetrating into the ocean's surface top layers, $Q_{long-wave\_net}$ the "long wave" infrared flux emitted from the

Earth to the atmosphere, Q_{latent} the latent heat flux due to condensation/evaporation processes at the ocean-atmosphere interface and $Q_{sensible}$ the sensitive heat flux due to heat conduction at the ocean-atmosphere interface. It is worth noting that the latent and sensitive heat fluxes are "turbulent" heat fluxes.

The formulation of the net fresh water fluxes EmP_{net}has already been presented in Eq. 2.23 and is computed as :

$$EmP_{net} = (E_v - P_r)\ SSS \tag{2.37}$$

with E_v the net evaporation rate, $Prate_{net}$ the precipitation rate and SSS the sea surface salinity.

To be consistent with the wind stress parameterization described above, the explicit calculation of Q_{net} and EmP_{net} are based on the "bulk" parametrization of *Fairall et al.* (1996), and all the necessary atmospheric data required in calculations are provided by the 6 hourly CFSR reanalysis atmospheric reanalysis (*Saha*, 2010).

2.4 Vertical mixing and Turbulent closure scheme

Sub-grid unresolved turbulent processes are parametrized using a downgradient diffusive law. The vertical turbulent diffusivity coefficient is calculated using the non-local K-profile planetary (KPP) scheme (*Large et al.*, 1994). In the interior, vertical mixing is mainly due to shear instabilities associated with internal wave activity, as well as double diffusion. Shear instabilities occur when the Richardson number becomes higher than 0.25. The KPP mixing scheme consists in calculating the boundary layer depth (h) at each grid point as a function of a bulk Richardson number, and the surface/bottom wind stress and buoyancy forcing. The vertical diffusivity coefficient is then increased artificially within these boundary layers. Some special functions are used to insure smooth transitions between the interior and surface/bottom vertical mixing coefficients. The KPP scheme has proven to work well at mid-latitudes and in the tropics. There, it allows a fair realistic representation of the surface mixed layer during convective and storm events, as well as its diurnal cycle (*Large et al.*, 1994).

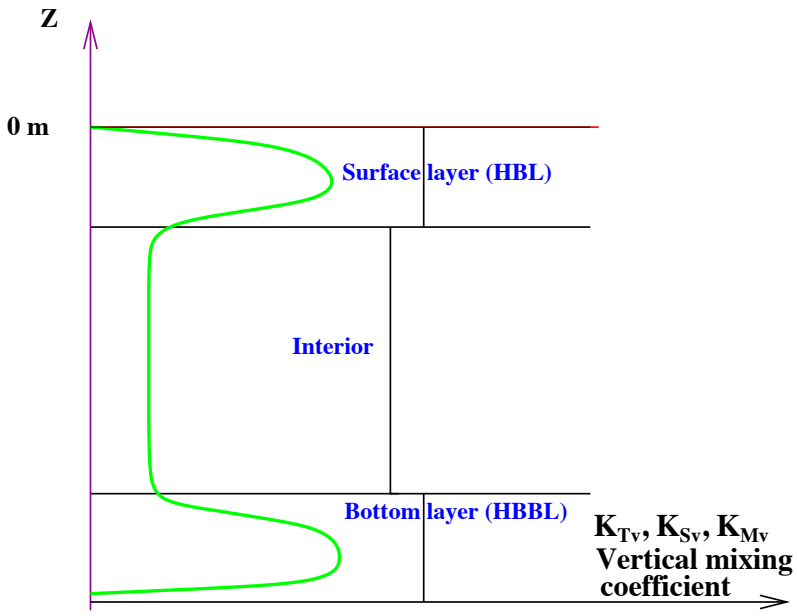

Figure 2.1: Schematic diagram of the KPP closure model used. The mixing coefficients computed by the KPP closure model are the vertical thermal diffusivity K_{Tv}, vertical haline diffusivity K_{Sv} and the vertical momentum viscosity K_{Mv}.

2.5 Horizontal mixing

Horizontal turbulent mixing processes occur through the diffusive terms of the primitive equations, generally in the form a laplacian or bilaplacian operator. The values of the diffusive coefficients for momentum K_{Mh}, heat K_{Th}, and salt K_{Sh} are "turbulent" values. Their expression should result from a parametrization of the turbulent sub-grids non resolved processes. Nevertheless, in practise, they are set to a minimum value chosen to be high enough so that numerical artefacts are dissipated. This minimum value is generally higher then the real value, and very fine scale dynamics tend to be over-dissipated in the simulations, resulting in over-smoothed solutions. In ROMS, the use of third-order advection scheme with implicit dissipation theoretically prevents the user from adding horizontal viscosity.

2.6 Lateral Boundary Conditions

The presence of horizontal partial derivatives in the momentum equations requires specifying some lateral boundary conditions for u, v, T and S.

The case of land-boundary

In the case of land-boundary, conditions are similar to some extent to the conditions imposed at the seabed, *i.e.* no inflow and zero heat and freshwater flux across the land boundary:

$$u_\perp = 0 \tag{2.38}$$

$$K_{Th}\frac{\partial T}{\partial x_\perp} = 0 \tag{2.39}$$

$$K_{Sh}\frac{\partial S}{\partial x_\perp} = 0 \tag{2.40}$$

where $x_\perp$ is the direction perpendicular to the land boundary. For the velocity component parallel to the land-boundary, a no-slip or free-slip condition (*Hedstrom*, 1997) is imposed.

The case of open boundary

In the case of open ocean borders, boundary conditions are slightly different. One wishes to impose the surrounding ocean known temperature, salinity and velocities at the boundary, as well as to allow disturbances and waves originating from the domain to leave without influencing the interior solution. In ROMS, open boundary conditions are implemented with a method that combines outward oblique radiation and adaptive nudging towards a known external data (*Marchesiello et al.*, 2001). "Sponge" layers, within which the lateral viscosity coefficient is smoothly increased from the background interior value towards a maximum value at the boundary are also implemented. Their role is to smooth out model-boundary inconsistencies, prevent spurious reflection of the external/internal solution and maintain long-term model stability. The width of the sponge layer is typically 10 grid cells. The external values of temperature, salt and velocity components at the boundary are either specified from observations or models with larger domains.

2.7 Time discretization

To limit computational cost, ROMS uses a split-explicit time-stepping integration technique that decomposes the three-dimensional fields into a fast barotropic and a slow baro-

clinic mode (*Shchepetkin and McWilliams*, 2005). The primitive equations are vertically integrated to provide the prognostic variables of the barotropic mode: η, $\overline{u}$, $\overline{v}$. The vertically integrated two-dimensional (2-D), momentum equations are solved using a time-step typically 10 times smaller than the baroclinic step used to solve the three-dimensional (3-D) baroclinic momentum and tracer equations (Fig. 2.2). Before being re-injected into the into the three-dimensional equations, the barotropic variables are time-averaged over the baroclinic time-step in order to limit aliasing errors that may result from high frequencies dynamics present in the barotropic 2-D equations (*Shchepetkin and McWilliams*, 2005).

The time stepping numerical scheme for the 2-D and 3-D equations follows a robust plan that combines a Leap-Frog predictor scheme and a corrector Adams-Moulton scheme. This technique allows the use of larger time-steps by a factor of about four (*Shchepetkin and McWilliams*, 2005).

This method was found to be more robust because it is more efficient to resolve two-dimensional than three-dimensional equations over a short-time step. It also allows to overcome the limitations imposed by the Courant-Friedrichs-Levy (CFL) stability condition (*Ezer et al.*, 2002; *Shchepetkin and McWilliams*, 2005).

2.8 Horizontal discretization

In the horizontal direction, the model variables are discretized on a numerical staggered Arakawa-C grid (Figure 2.4). This grid is well suited for models with resolution finer than the internal Rossby radius (*Arakawa and Lamb*, 1977). The density (ρ), depth (h), Coriolis parameter (f), vertical velocity (ω), sea surface height and tracers (temperature and salinity) are defined at the centre of the grid-cell, while the horizontal velocity components $(u)/(v)$ are defined at the middle of its eastern/northern and western/southern boundary.

Note that ROMS uses an orthogonal curvilinear coordinate system (Figure 2.4). This system can follow an irregular lateral boundary (grid rotation, increased resolution toward the coast, etc..). It is advantageous because the computational grid placing is quite flexible and can be optimised for a given problem.

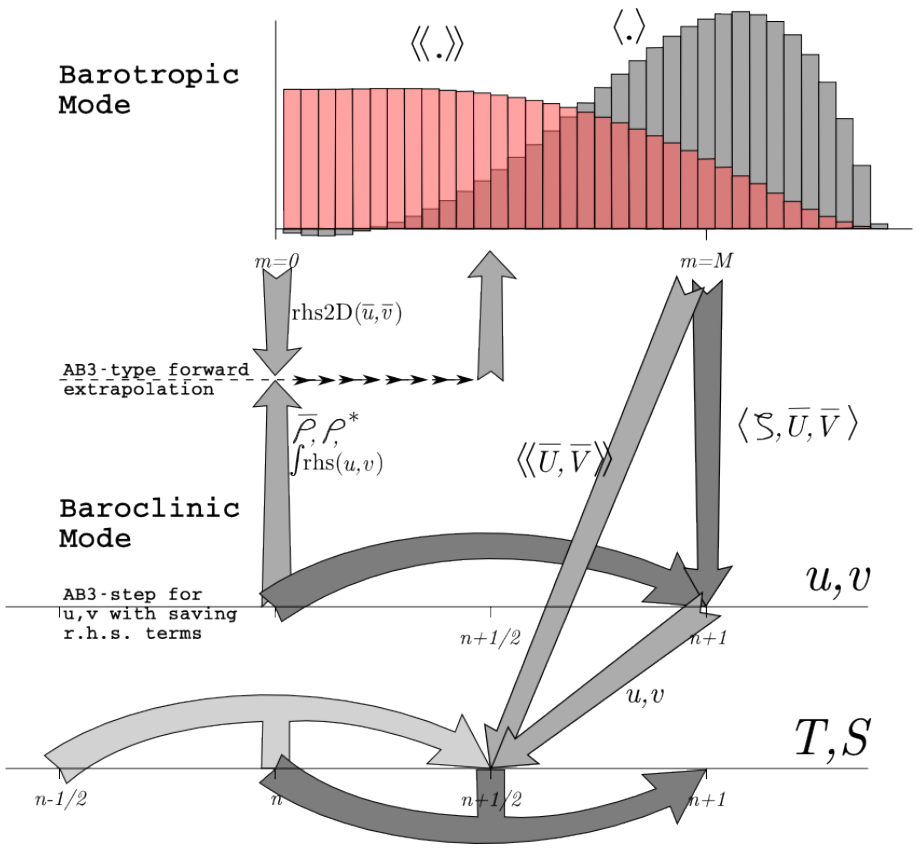

Figure 2.2: Schematic view of the ROMS predictor-corrector hydrostatic kernel. From (*Shchepetkin and McWilliams*, 2005). Ξ is here the free surface elevation (η in the text).

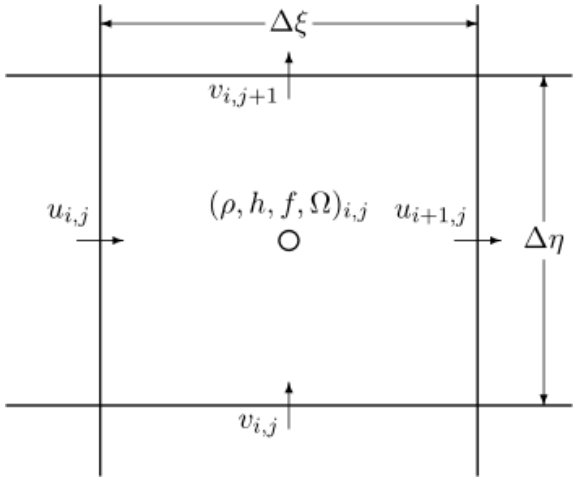

Figure 2.3: The placement of variables on the Arakawa-C grid used in the horizontal discretization of ROMS. From *Hedström* (2009).

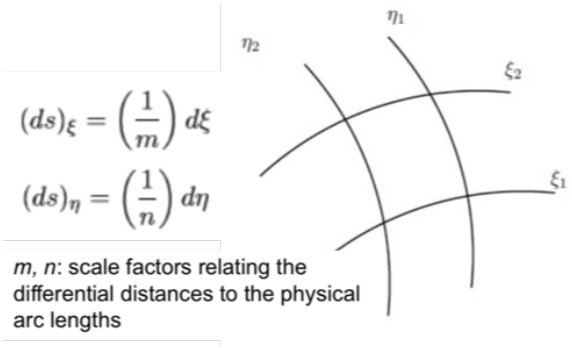

Figure 2.4: Curvilinear horizontal coordinate

2.9 Vertical discretization

In the vertical direction, ROMS uses a staggered grid (Fig. 2.5) where ρ points are interposed between two vertical velocity Ω points.

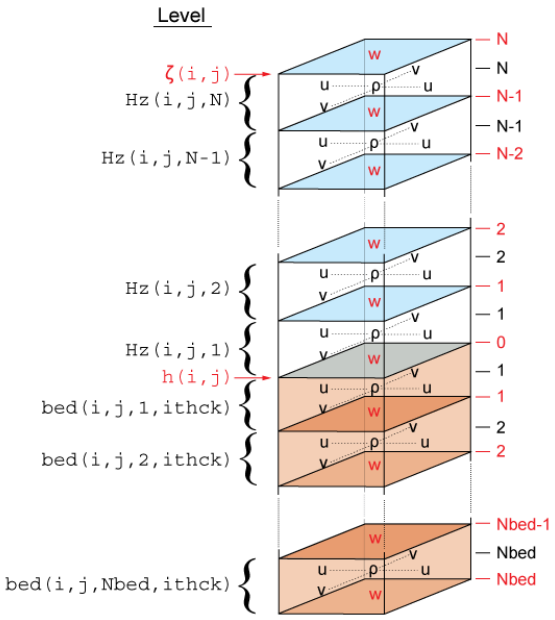

Figure 2.5: Vertical grid used in the vertical discretization of ROMS (from www.myroms.org).

ROMS follows a sigma or terrain-following stretched coordinate system which improves the representation of the topography, increasing the vertical resolution over the continental shelf (*Song and Haidvogel*, 1994). Sigma coordinates are particularly adapted to study shelf dynamics and to enhance resolution in the surface mixed layer and at the bottom for the proper representation of bathymetry-flow interaction (*Veitch et al.*, 2006).

The calculation of the depth of sigma layers at each grid point takes into account the

free surface elevation and the bathymetry (*Shchepetkin and McWilliams*, 2005) : [2]

$$z(x,y,\sigma,t) = \zeta(x,y,\sigma) + [\zeta(x,y,t) + h(x,y)]\, z_0(x,y,\sigma) \tag{2.41}$$

$$z_0(x,y,\sigma) = \frac{h_c\sigma + h(x,y)Cs(\sigma)}{h_c + h(x,y)} \tag{2.42}$$

where $\zeta(x,y,t)$ is the free-surface elevation, h(x,y) the ocean bottom depth, σ a fractional vertical stretching coordinate ($-1 \leq \sigma \leq 0$), h_c a positive thickness controlling the stretching, $Cs(\sigma)$ a non-dimensional monotonic vertical stretching parameter ($-1 \leq Cs(\sigma) \leq 0$),$z_0$(x,y,$\sigma$) a nonlinear vertical transformation.

$$sc = \frac{\sigma - N}{N} \tag{2.43}$$

$$csf = \frac{1. - cosh(\theta_s\ sc)}{cosh(\theta_s) - 1.} \quad \text{if } \theta_b > 0, \quad csf = -sc^2 \quad \text{otherwise} \tag{2.44}$$

$$Cs(\sigma) = \frac{e^{\theta_b csf} - 1.}{1. - e^{-\theta_b}} \qquad \text{if } \theta_s > 0, \quad Cs(\sigma) = csf \quad \text{otherwise} \tag{2.45}$$

The parameters, θ_s, θ_b and h_{cline} control the vertical grid resolution and stretching.

- h_{cline} thus defines the thickness at which to increase the resolution in vertical grid surface
- θ_s ($\theta_s > 0$), θ_b defines the rate of resolution increase in the surface layer.
- θ_b ($0 < \theta_b < 1$) controls the resolution increase in the bottom layer, $\theta_b = 1$ correspond to the same stretching than the surface. $\theta_b = 0$ correspond to no refinement of resolution at the bottom.

Figure 2.6 illustrates the sigma levels through a vertical section in the model configuration that was developed and that is presented in chapter 3.

[2] For simplicity we only present the latest transformation available in ROMS, NEW_S_COORD option, others are still available and can be found in the online documentation http://www.croco-ocean.org

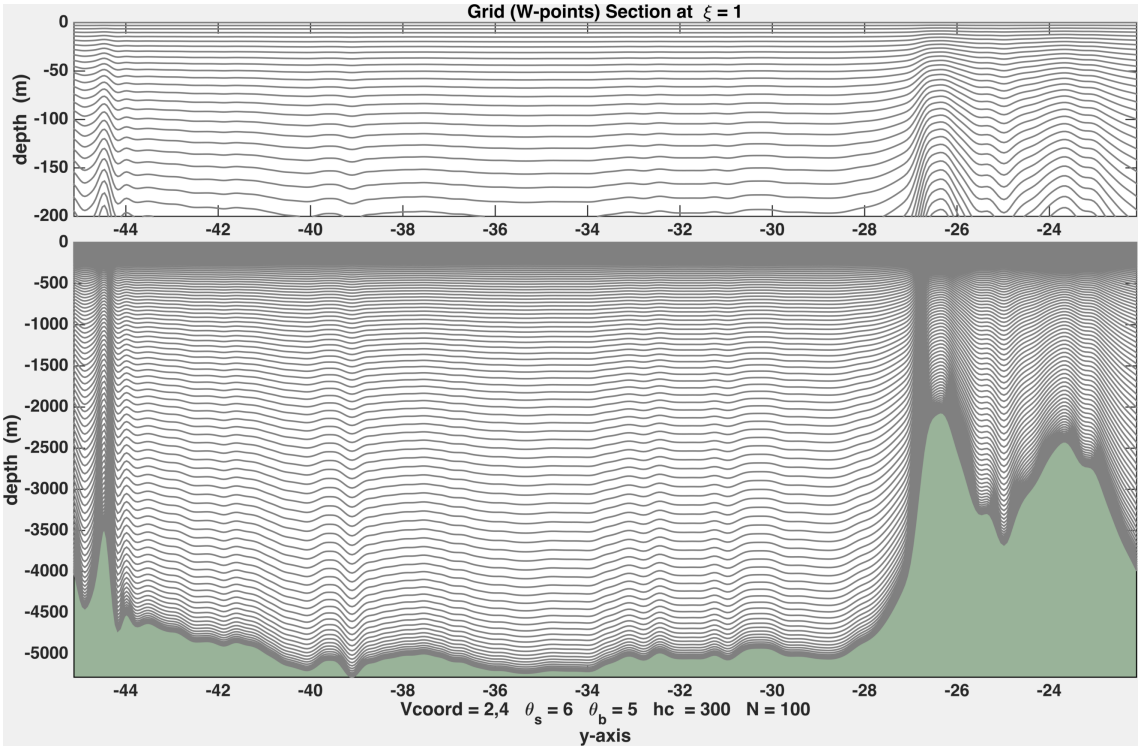

Figure 2.6: An example of the BENGR15 vertical grid as prescribed by the σ-coordinate system. A zoom is made in the first 200 m of the water column in order to accentuate the distribution of the vertical grid in upper layer. Here the sigma coordinate parameters are $h_{cline} = 300$ m, $\theta_b = 6$, and $\theta_s = 5$

2.10 Advection schemes

The advection scheme is third-order upstream biased which reduces dispersion errors necessary to maintain smoothness. This scheme enhances precision for a given grid resolution (*Shchepetkin and McWilliams*, 1998). However, the implementation of the third-order advection-diffusion scheme has lead to the development of spurious diapycnal mixing in σ-coordinate models. A solution to this problem was addressed by *Marchesiello et al.* (2009) and involves the split of advection and diffusion for the tracer equation, and the latter appears as a biharmonic operator. This solution was implemented in our configuration to preserve the low diffusion and dispersion benefits of the original scheme while maintaining water mass characteristics.

2.11 The ROMS model: summary

ROMS is a free-surface, terrain-following σ-coordinate model with split-explicit time stepping. It integrates in time the primitive equations with state of the art numerical methods and with Boussinesq and hydrostatic approximations. The advection scheme is third-order upstream biased, which reduces dispersion errors, essentially enhancing precision for a given grid resolution (*Shchepetkin and McWilliams*, 1998). The diffusive part of the advection scheme is rotated along the isopycnal surfaces to avoid spurious diapycnal mixing (*Marchesiello et al.*, 2009; *Lemarié et al.*, 2012). Adaptive open boundary conditions combine outward radiation and nudging towards prescribed external boundary conditions (*Marchesiello et al.*, 2001). Additional eddy viscosity is added in the sponge layer at open boundaries, where it increases smoothly over several grid points. Subgrid-scale vertical mixing is governed by a non-local, K-profile parametrization (KPP) scheme (*Large et al.*, 1994). A quadratic bottom drag is applied.

Chapter 3

A new simulation of the Southern Benguela Upwelling System

This chapter focuses on the description of the new eddy resolving simulation that is used to study the along-shore connectivity in the SBUS. The latter is based on the analysis of Lagrangian trajectories advected by oceanic currents produced by this simulation. Our first goal is to build a robust hydrodynamical model with the major ingredients, *i.e.* a realistic mesoscale eddy field, a realistic Agulhas leakage that brings warm waters off the Benguela shelf and enhances the offshore turbulence, and a realistic wind field with its full (seasonal+ intraseasonal + interannual) variability. To satisfy these needs, the horizontal resolution of this simulation was chosen to be $1/15^\circ$ (7.5 km), over a domain that encompasses large portions of the ocean adjacent to the whole South African continent. In order to reproduce a "statistically" realistic representation of the Agulhas Current and its retroflection, the domain was extended as far 54° S and also includes the southern part part of the Mozambique Channel where the Agulhas Current initiates. Throughout this manuscript, this simulation will be thereafter considered as our reference simulation. It will be used in all subsequent chapters, either directly in chapter 4 to study the physical processes impacting the seasonal cycle of the along-shore connectivity, or indirectly in chapter 5 and 6 to provide lateral boundary conditions for higher resolution nested models.

A monthly climatology of heat, fresh-water and momentum fluxes will be used at the lateral boundaries, and 22 years of 6-hourly atmospheric conditions (winds, moisture, tem-

perature, infrared and short wave radiations) will be used as surface boundary conditions. As a result, the inter-annual variability produced by this simulation over the Benguela region will come from the local forcing and the turbulent eddy field, not from the lateral boundaries. Therefore, the influence of remote dynamical features such as equatorial coastal Kelvin waves will be neglected. However, the contribution of remote forcing to the local dynamics is much less important in the Southern Benguela than in the northern Benguela and north of the Angola-Benguela front (*Illig et al.*, 2018). Our priority is to focus on the role dynamical processes occurring locally, or nearby like for example eddies generated during the Agulhas retroflection.

The chapter is constructed as follows. Section 3.1 provides a description of model reanalysis, in-situ and satellite data sets used either to build and force our simulation, or to compare the results of our simulation against. The configuration itself and its modelled oceanic circulation is described in section 3.2.

3.1 The regional model configuration developed: `BENGR15`

A regional configuration of the ocean surrounding the Southern African region, including the Mozambique Channel, the Agulhas retroflection, and the Benguela, is developed specifically to study ocean circulation patterns of the SBUS. It is composed of a $1/15°$($\sim$ 7.5 km) grid resolution extending from 54.5°S to 4.75°S and 2.5°W to 55.16°E (Fig. 3.1) and has 909×866 grid points. The vertical resolution consists of 100 vertical terrain-following levels (sigma coordinate) that are stretched to obtain a vertical resolution from 1 m in the surface layers to 100 m in the bottom layers. The vertical grid uses stretching surface and bottom parameters of $h_{cline} = 300$ m, $\theta_b = 6$, and $\theta_s = 5$.

3.1.1 Bathymetry

The bottom bathymetry used in this configuration is derived from the Shuttle Radar Topography Mission (SRTM 30 plus) product (available at `http://topex.ucsd.edu/WWW.html/srtm30.plus.html`) based on the 1-min *Smith and Sandwell* (1997) global datasets and higher-resolution surveys when available. It is interpolated on the model grid. To avoid pressure gradient errors induced by terrain-following (sigma) coordinates in shallow

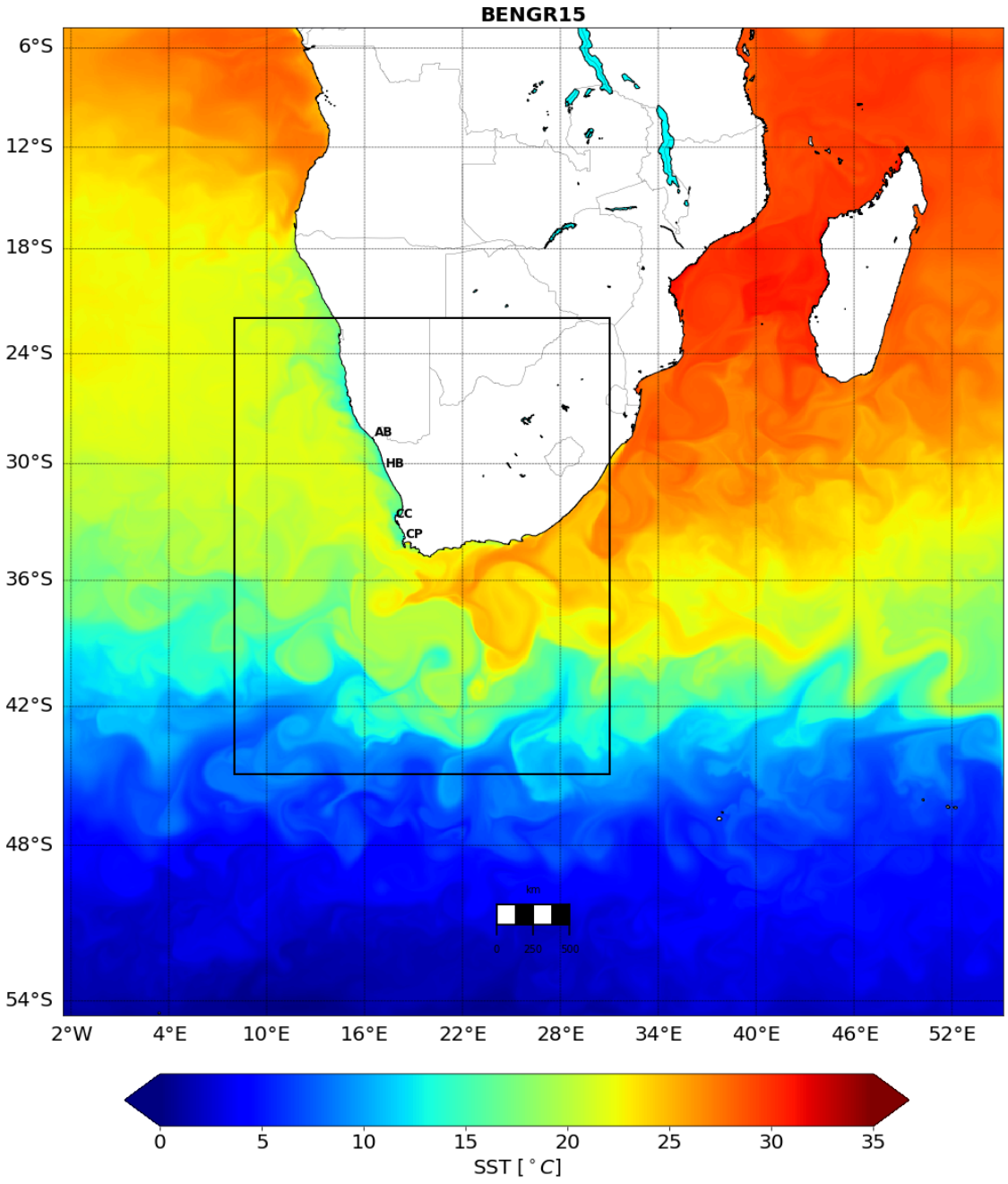

Figure 3.1: Model year 2005, January average snapshot of sea surface temperature (SST) for the Benguela upwelling system configuration ("BENGR15"). The domain encompasses the region covering 2.5°W - 55.16°E and 54.5°S - 4.75°S. The box represents an extracted region over the southern Benguela (45.1°S to 22.1°S and from 5.0°E - 34.9°E) used in our study.

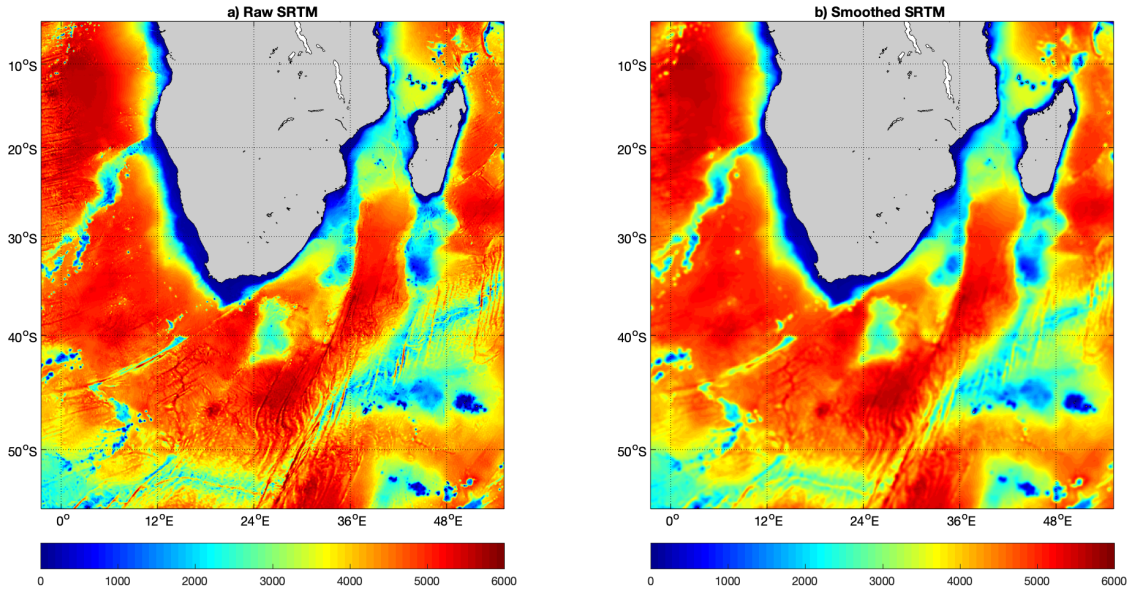

Figure 3.2: a) The original raw SRTM 30' bathymetry extracted over the BENGR15 domain. b) The bathymetry of the BENGR15 model configuration obtained after smoothing of the raw SRTM 30' batymetry. c) The difference between raw SRTM 30' and smoothed BENGR15 bathymetry

regions with steep bathymetry, the model bottom topography is smoothed where the steepness of the topography ($r = \frac{\delta h}{2h}$) exceeded 0.2 (*Beckmann and Haidvogel*, 1993). When the depth is shallower than 10 m, it is reset to 10 m.

A comparison between the smoothed bathymetry interpolated on the model grid and the original SRTM30' bathymetry is presented on Fig. 3.2a,b. Despite some obvious smoothing of some small scale bathymetric features (Fig. 3.3), one sees that the main topographic features of the region are reproduced in the BENG15 topography. On the eastern flank of South Africa, where the Agulhas Current flows southward, the shelf is very narrow. It widens at the tip of the African Continent to form a large plateau, the Agulhas Bank, that extends south, up to 400 km offshore at the longitude of Cape Agulhas. On the South-East Atlantic side, the Agulhas ridge delimits the entrance of the South Atlantic. It stretches along the South-West/North-East direction. It forms the southern boundary of the Cape basin, an abyssal plain that lies offshore the SBUS and extends as far north as 20°S. Some isolated seamounts are present on its eastern flank. In between these seamounts, and the South-African west coast, there is a narrow passage that allows Agulhas leakage into the South Atlantic. At 20° S, the Walvis Ridge forms the northern boundary of the

Cape Basin. It also stretches along the South-West/North-East direction. The SBUS is characterised by a narrow shelf between Cape Point and Cape Columbine. The latter widens slightly north of St Helena Bay.

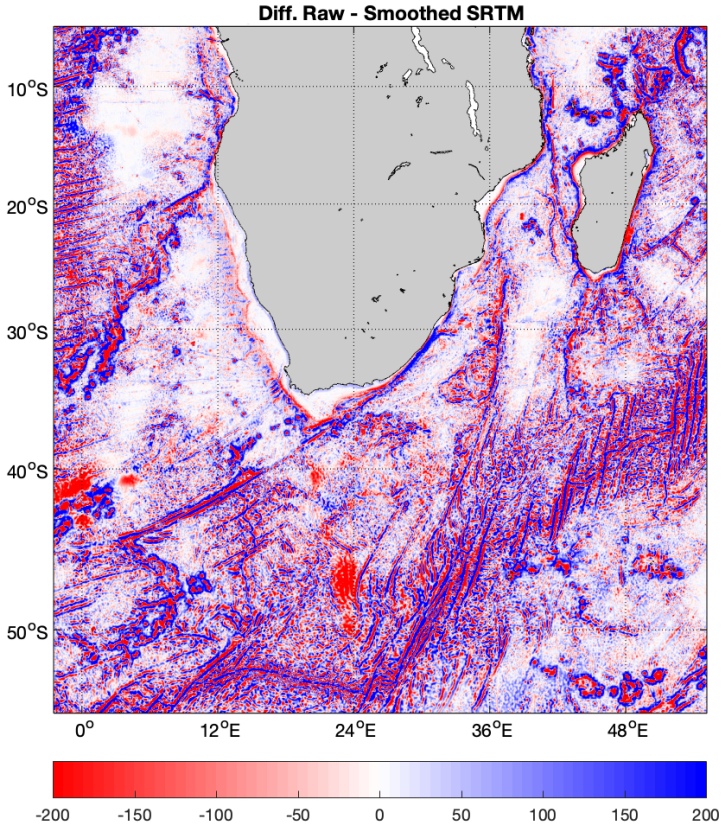

Figure 3.3: The difference between raw SRTM 30' and smoothed BENGR15 bathymetry (m).

3.1.2 Atmospheric surface forcing

In EBUS, the alongshore wind forcing is the main ingredient that forces the circulation. It is therefore essential to force our model with a wind product that reproduces the main observed patterns of the wind forcing; i.e. its seasonal cycle and its spatial variability. A good representation of the wind stress curl is of particular importance because it relates dynamically to the Ekman pumping and can therefore enhance upwelling (*Colas et al.*, 2011). It also plays a role on the dynamics of the poleward undercurrent (*Capet*, 2004). In EBUS, it is not rare to observe some intensification of the wind forcing around capes that coincide with enhanced upwelling cells.

At the surface, atmospheric forcing (heat, fresh water and momentum fluxes) are calcu-

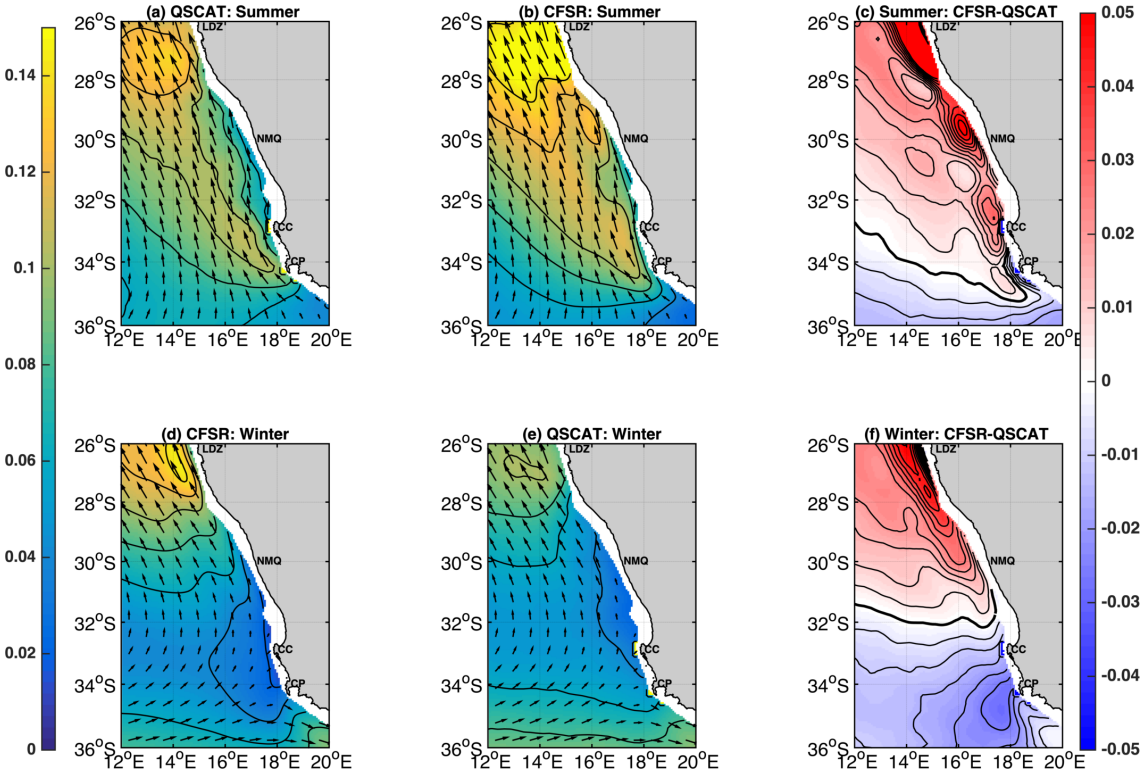

Figure 3.4: Summer and winter mean meridional wind stress from (a,d) QuikSCAT, (b,e) CFSR (colors, in N m^{-2}, contour interval: 0.02 N m^{-2}) and (c,f) their differences (reanalysis - satellite winds) for the 2000-2008 period. Positive (negative) values in the difference maps are regions where the reanalysis is stronger (weaker) than satellite. The bold black line represent the zero difference and the contour interval is 0.005 N m^{-2}.

lated using bulk formulae (*Fairall et al.*, 1996) from the NCEP Climate Forecast System Reanalysis (CFSR) with a 6-hourly sampling and a spatial resolution of 0.3°(*Saha*, 2010). CFSR is a global coupled ocean-atmosphere-land-sea ice modelling system that uses the NCEP Global Data Assimilation System, and it is available over 31 years from 1979 to the end of 2017. To evaluate the CFSR reanalysis in SBUS, the wind stresses and wind-stress curl computed using the bulk formule are compared to wind stresses observed from the NASA scatterometer QuikSCAT sattelite. QuikSCAT wind used here are homogeneous temporal series of daily mean wind stress fields, on a global 0.5° x 0.5° resolution grids, generated from L2B product distributed by the French ERS Processing and Archiving Facility CERSAT[1]. It is worth noting that near-coastal regions QuikSCAT wind stress data are masked due to land contamination and are not available within 25 km off the

[1]http://www.ifremer.fr/cersat/en/data/overview/gridded/mwfqscat.html

coast.

Wind stress

Comparing the summer and winter climatology of wind stress from the CFSR reanalysis and QuickSCAT satellite observations show some good agreements between the two over the SBUS (Figure 3.4). The summer and winter seasons are defined to encompass the upwelling period from October to March, and the non-upwelling period from April to September.

As expected, in summer, the direction of the alongshore wind stress is directed equatorward. The maximum wind stress core corresponds with the Cape Point upwelling cell at 34°S and the Lüderitz cell at 26°S (*Hutchings et al.*, 2009, *Weeks et al.*, 2006) (Fig. 3.4 a,b). In winter, the equatorward winds weaken and become predominately westerlies south of Cape Point (Fig. 3.4 d,e) consistent with the northward movement of South Atlantic cyclone. Favourable upwelling winds persist year-round at Lüderitz cell, but they are much weaker in winter. Although CFSR winds seem to be overestimated in regions coinciding with the major upwelling cells of the SBUS (Fig. 3.4c), the upwelling favourable winds are reproduced with a good degree realism.

Wind stress curl

The seasonal distribution of the wind stress curl over the southern Benguela is presented in Figure 3.5. There is an alongshore coastal band of negative (cyclonic) wind-stress curl associated with the along-shore wind drop-off. The position and local maximum of the cyclonic wind stress curl varies seasonally according to the seasonal cycle of the atmospheric forcing. It is maximum and moves poleward during summer months whereas it retreats northward during winter months. It then becomes weaker south between Cape Point and Cape Columbine. There are some areas where the alongshore wind stress is locally enhanced, therefore enhancing the cyclonic wind stress curl (*Bakun and Nelson*, 1991). In the SBUS, three of these specific regions can be distinguished clearly: between Cape Columbine (33°S) and Cape Point (34°S), off Namaqua shelf (30°S) and nearby Lüderitz (*Weeks et al.*, 2006). Although, the CFSR wind stress cyclonic curl appears stronger than

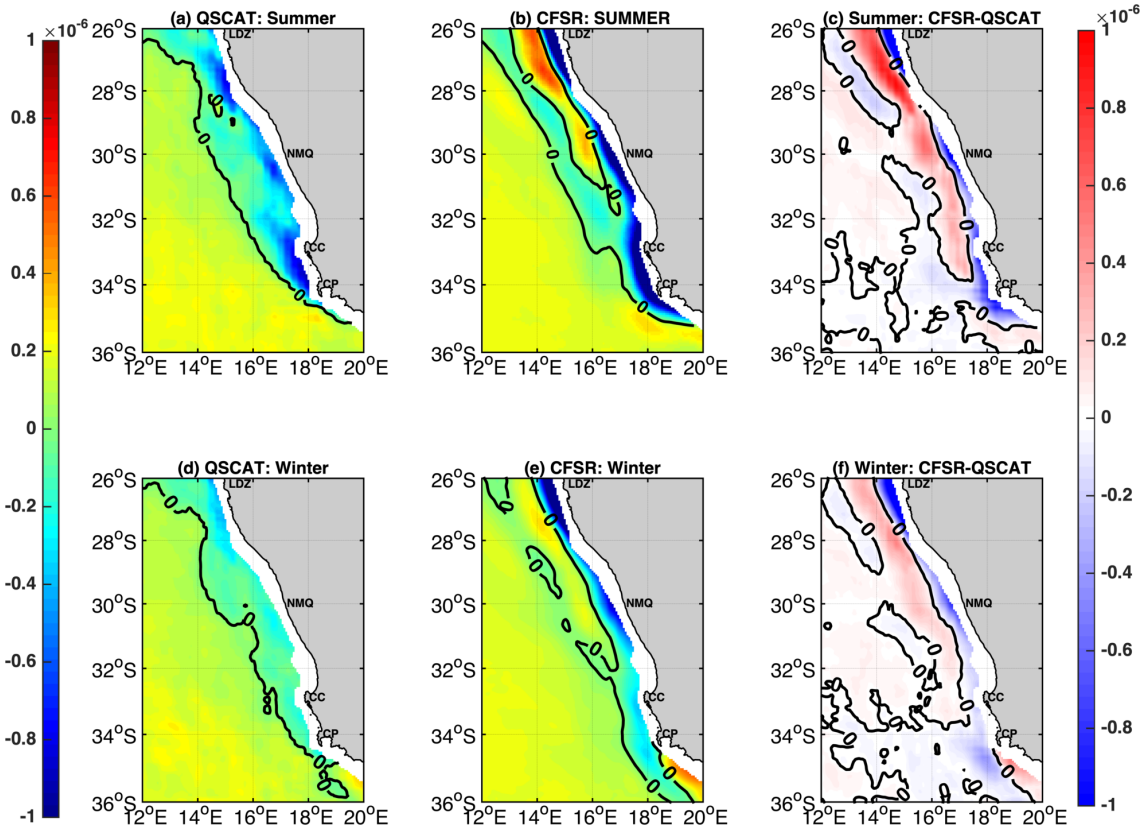

Figure 3.5: Summer and winter mean wind stress curl from (a,d) QuikSCAT and (b,e) CFSR (c,f) their differences (reanalysis - satellite wind stress curl) (colors, in Nm^{-3}). Cyclonic (anticyclonic) curl is negative (positive) and line bold black line represent the region of zero wind stress curl.

the one derived from QuickSCAT observations (Fig. 3.5c,f), the three upwelling cells are consistently represented and match with the observations.

3.1.3 Lateral oceanic forcing

The conditions for temperature, salinity, horizontal velocity and sea level at the lateral boundaries were provided by a monthly seasonal climatology (1958-2005) derived from the SODA 2.3.2 reanalysis. SODA is a global ocean model with a horizontal resolution of 0.25° in longitude and 0.4° in latitude. It has 40 vertical levels with a 10-m spacing near the surface (*Carton and Giese*, 2008). This reanalysis covers the period 1958-2005 and assimilates observational data in a general circulation model based on the Parallel Ocean Program (*Smith et al.*, 1992). The ROMS model was initialised from January 1979 using 3-D current, temperature, salinity and SSH derived from SODA climatology with a 10-year spin-up.

The SODA reanalysis is evaluated with World Ocean Atlas 13 (WOA13). The World Ocean Atlas 2013 provides objectively analysed fields of temperature, salinity as well as several nutrients. The spatial resolution of these data are from 1°to 0.25°globally, and the data is distributed between the surface and 5500 m (*Locarnini et al.*, 2013). In contrast to the previous WOA09 (2009) that consisted of 32 depth levels, the WOA13 has increased vertical resolution of 102 levels. The data are provided at a temporal resolution of annual, seasonal or monthly climatologies. WOA13 is used to compare temperature sections based on SODA open boundary conditions data used in the model.

The SODA vertical structure of temperature taken at the southern boundary of the domain during summer and winter is examined and compared with the one obtained from WOA13. The thermal gradient in the surface layers is stronger in summer (Fig. 3.6a,b) indicative of higher stratification than in the winter (Fig. 3.6c,d) and the layer of temperatures >16°C is thicker in winter. This layer is warmer (∼18°C) towards the east, near the Agulhas Current region in WOA13 during this period. The seasonal vertical position of the 16°C isotherm and the V-shaped structure of the isotherms are consistent in both WOA13 and SODA. Since we apply SODA at the boundaries ∼1500-2000 km away (see full domain in Fig. 3.1) from the interior of the domain, the discrepancies, although minor,

will have reduced effect on the ocean model solution in the SBUS region. Hence we are confident with using SODA at the lateral boundaries.

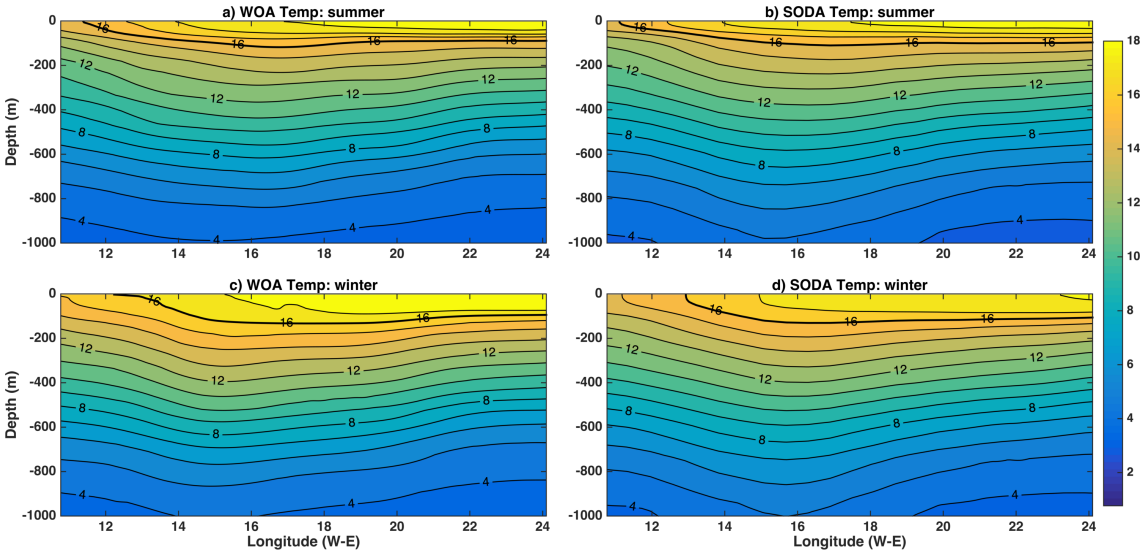

Figure 3.6: Summer and winter mean cross section of temperature taken from the southern boundary: (a,c) WOA13 and (b,d) SODA open boundary conditions with 1°C contour interval. The thick line represents the 16°C isotherm.

3.1.4 Model spin-up

The BENGR15 simulation is initialised with the January 1979 conditions given by the SODA reanalysis, and it is run for a total of 33 years (1979-2011). A 10-year spin-up is carried out for the model to reach a statistical equilibrium. To minimise storage requirements, we only downloaded model outputs from model year 11 to year 33 (1989 – 2010). Therefore the diagnostic analysis presented in Figure 3.7 was done on the 1989 – 2010 output variables averaged and stored every three days. Figure 3.7b,c shows that the change in kinetic energy is minimal and it fluctuates around its mean, which is indicative that the model has reached a statistical equilibrium.

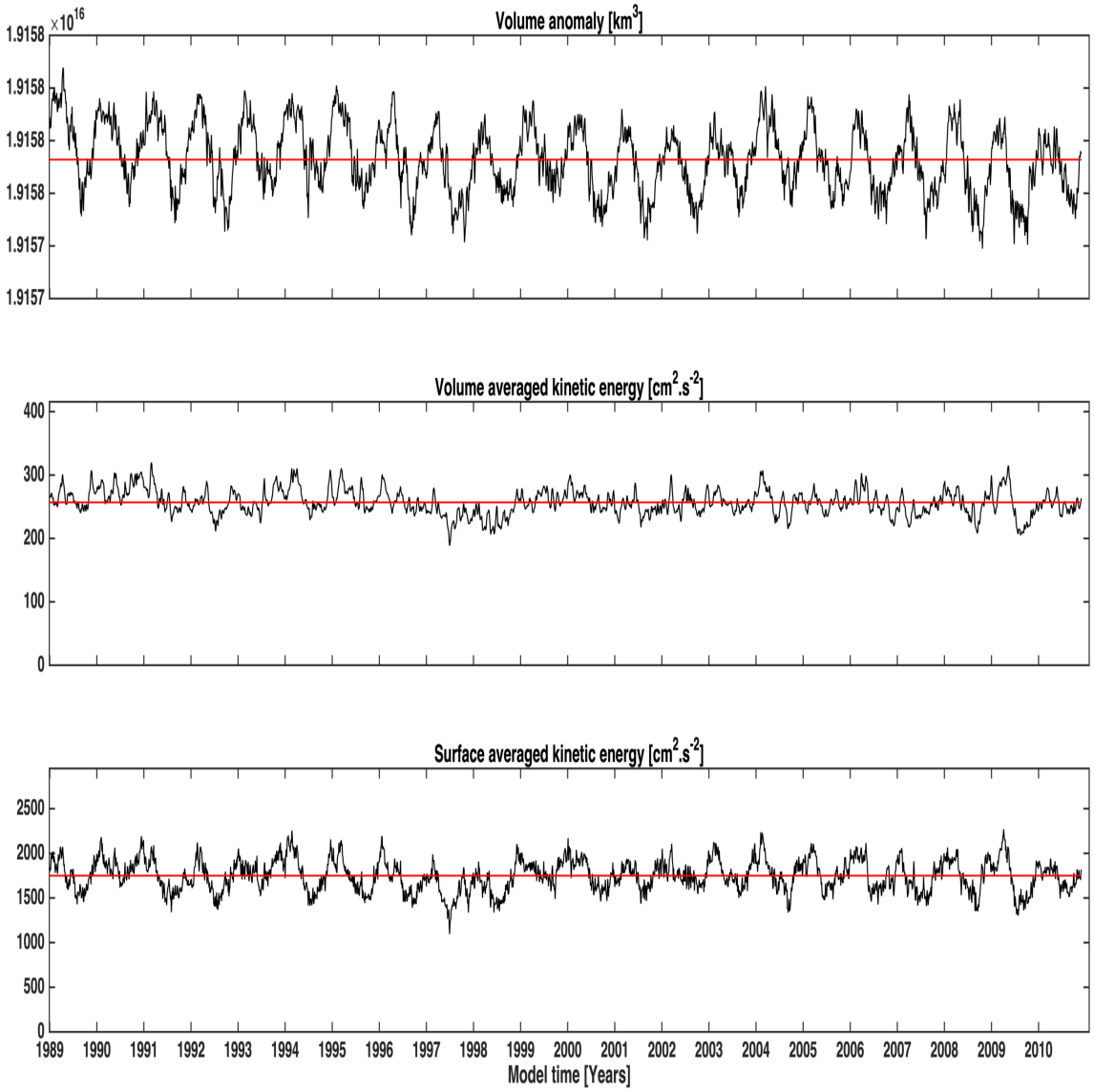

Figure 3.7: 3-day mean volume anomaly, volume averaged kinetic energy and surface averaged kinetic energy for the 22 years (1989-2010) BENGR15 simulation. The red horizontal line represents the mean value of the data.

3.1.5 Summary of the model configuration BENGR15

Parametrizations and main characteristics of the BENGR15 model configurations are presented Table Tab. 3.1 below.

Parameters and Unit	**Values**
Horizontal rid size (N_x N_y)	$N_x = 909$ et $N_y = 866$
Number of vertical levels N_z	$N_z = 100$
Vertical resolution refinement σ-coordinate parameter at surface [$0 < \theta < 8$]	$\theta = 6$
Vertical resolution refinement σ-coordinate parameter at depth $0 \leq b \leq 1$	$b = 5$
Minimal depth h_{min} in m	$h_{min} = 10$
Thick of the maximum refinement layer	$h_c = 300$ m
Slow 3D-baroclinic time step (s) $0 < \Delta t_{bc} < \min(\frac{N_{bt} L_x}{N_x \sqrt{g h_{max}}}, \frac{L_x^2}{N_x^2 A_h^{sp}}, \frac{\Delta z_B}{r})$	$\Delta t_{bc} = 540$ s
Number of barotropic iterations during one baroclinic time step ($N_{bt} = \frac{\Delta t_{bc}}{\Delta t_{bt}}$)	$N_{bt} = 60s \rightarrow \Delta t_{bt} = 9$s
Bottom friction ($m^2.s^{-2}$)	Quadratic logarithmic parametrisation, $z_r = 0.001$, $C_d^{min} = 1e^{-4}$ and $C_d^{max} = 2.5e^{-3}$
Nudging time (in days) for tracers	$\tau_{in}^T = 1$ & $\tau_{out}^T = 360$
Nudging time (in days) for momentum	$\tau_{in}^M = 3$ & $\tau_{out}^M = 360$
Sponge layer	Sponge layer width $L^{sp} = 10$ grid points Viscosity $K_M h^{sp} = XX$ [automatic computation] Diffusivity $K_T h^{sp} = XX$ "
Bathymetry	SRTM30' + smoothing at $r = \frac{\delta h}{2h} \leq 0.2$
Surface Atmospheric forcing	Bulk formulation *Fairall et al.* (1996) based on the 6-hourly CFSR atmospheric reanalysis
Lateral Oceanic forcing	Initial and open boundary conditions computed from monthly climatology of the oceanic reanalysis SODA 2.3.2
Outputs frequency	Averaged outputs every 3 days
Period cover by the simulation	1979-2011 (33 years, spin-up over 1979-1989), analysis period of 23 years

Table 3.1: BENGR15 configuration, at 7.5 km spatial resolution main parameters

3.2 Model evaluation

In order to study the variability of passive particles' transport, it is essential that our model reproduces the seasonal cycle of the main currents within the region, before analysing intraseasonal and interannual time scales.

3.2.1 Mean Surface Circulation features

Surface Eddy Kinetic Energy (EKE)

To estimate mesoscale activity in the upper-ocean, surface geostrophic eddy kinetic energy (EKE) is computed using geostrophic velocities derived from sea level anomaly (SLA). In the model, sea level anomaly (η') is computed by subtracting the monthly climatology sea surface height ($\bar{\eta}$) from the 3-daily sea surface height model outputs to remove the seasonal cycle. The SLA (η') is then used to calculate the non-seasonal surface geostrophic velocity anomalies as follows:

$$u'_g = -\frac{g}{f}\frac{\partial \eta'}{\partial y} \tag{3.1a}$$

$$v'_g = -\frac{g}{f}\frac{\partial \eta'}{\partial x} \tag{3.1b}$$

where g is the acceleration due to gravity (9.80 m s^{-2}), f is the Coriolis parameter, x and y are the longitude and latitude positions, respectively.

The u'_g and v'_g are then used to calculate the non-seasonal surface geostrophic EKE:

$$EKE = \frac{1}{2}(u'^2_g + v'^2_g) \tag{3.2}$$

Regarding the observations, the delayed-time absolute dynamic topography (ADT), sea level anomalies (SLA) and geostrophic velocities obtained from a gridded data product produced by DUACS are used to evaluate simulated surface geostrophic flows and eddy kinetic energy. AVISO supplies the Data Unification and Altimeter Combination System (DUACS) gridded product (CLS, Toulouse, France, available at http://www.aviso.altimetry.fr/duacs/) from 14 October 1992 to 27 December 2001, with a nominal resolution of 1/3 ^{o} every week. These measurements are obtained from merged TOPEX, POSEIDON, ERS and

Jason gridded data (*Ducet et al.*, 2000).

Figure 3.8 shows a comparison between simulated, and altimetry derived EKE. Both the simulated spatial pattern of the mean surface large-scale circulation and its variability compare well with the EKE derived from satellite altimetry. In general, the most significant EKE values (>2000 cm^{-2} s^{-2}) coincide with the energetic Agulhas Current, the Agulhas retroflection and the return current. The position of the Agulhas retroflection in the model (Figure. 3.8b) also appears to agree with satellite data. This retroflection drives an intense mesoscale activity that leaks into the south-eastern Atlantic Ocean (*Veitch et al.*, 2006) reflected by high values of EKE (∼300-500 cm^{-2} s^{-2}) in the offshore side of the upwelling region between 36°S and 33°S. However, the simulated and observed EKE are qualitatively similar in their spatial patterns but not in magnitude, as the model underestimates EKE values in the Agulhas retroflection. It is important to note that the simulated coastal geostrophic EKE minima off the west coast are not captured in the altimetry due to the incapability of the satellite to retrieve data close to the coast.

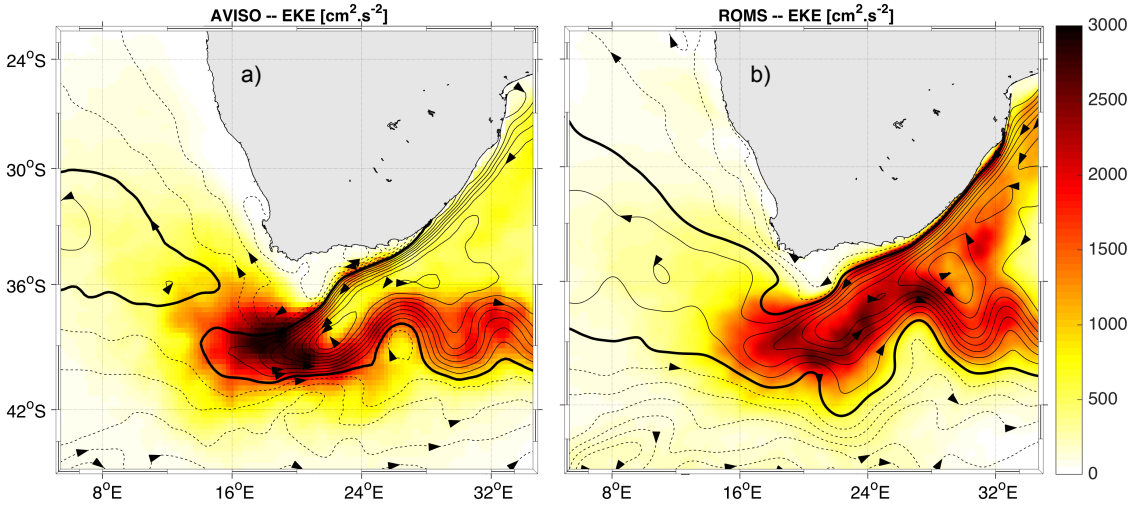

Figure 3.8: Maps of mean of the geostrophic surface eddy kinetic energy: a) computed from satellite (AVISO) data for the period between 1993 to 2015 and b) model-derived for the 1989-2010 period, both in cm^{-2} s^{-2} (color). The contours represent the mean SSH, with a contour interval of 10 cm. The overlaid arrows indicate the sense of associated geostrophic currents.

Sea surface heights from the model and altimetry show that the general climatological characteristics of the large-scale ocean circulation are well reproduced in our simulation (Fig. 3.8). The complex and chaotic dynamics of the Agulhas Current and its retroflection,

that in turn leads the leakage of warm Indian ocean waters into the Atlantic, is well represented. The Agulhas Current flows south-westward following the east coast of South Africa. When it passes the tip of the Agulhas Bank, it abruptly veers eastward and forms the Agulhas return Current. Although the simulated retroflection tends to occur 100 km east from the observed position, the levels of mean eddy kinetic energy (EKE) found in the model and observations are similarly high within this region. The retroflection is in fact accompanied by the shedding of large anticyclonic eddies and filaments, some of which enter into the South Atlantic Ocean and form the Agulhas leakage (*Loveday et al.*, 2014). The signature of this leakage in the form of a tongue of high EKE values, spreading northwestward into the Atlantic, can be seen in the model as in the observations. Finally, the long term average of this mesoscale eddy field propagating northwestward into the South Atlantic results in the eastern branch of the South Atlantic subtropical gyre.

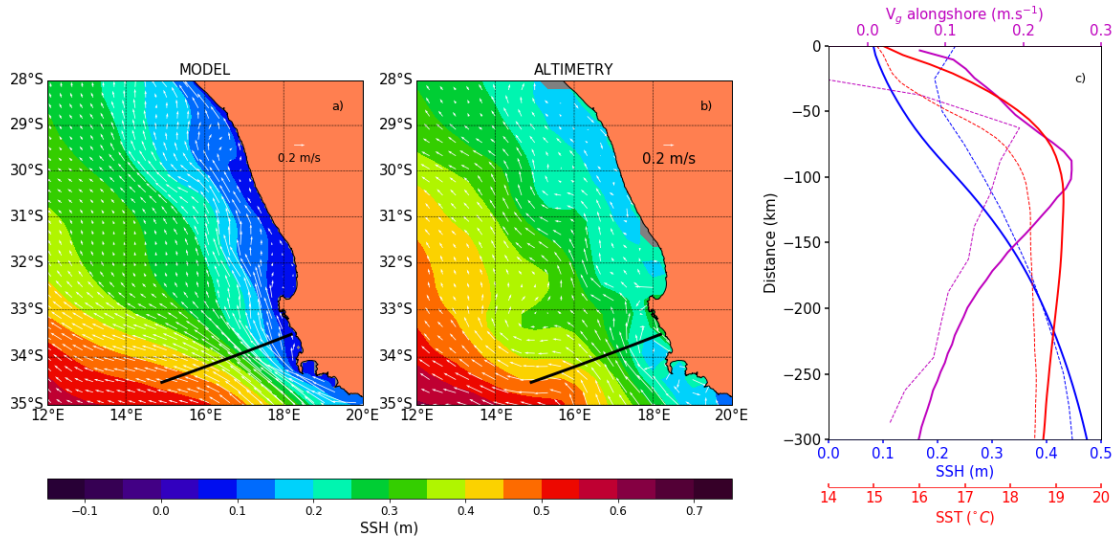

Figure 3.9: Annual average of sea surface height (SSH) with corresponding surface geostrophic currents superimposed: a) model outputs averaged over 1989-2010; b) satellite absolute dynamic topography (ADT) data averaged over 1993-2010; c) across-shore profiles of model (solid) and satellite (dashed) annual averages of SST (red), ADT (blue) and alongshore geostrophic current (magenta) off Grotto Bay (black line in a) and b). The plotted model SSH was offset by +0.407 m so that the model and satellite spatially average fields matched over the domain of interest.

Zooming in Fig. 3.8 over the SBUS to get a closer view of the alongshore current shows that the modelled surface geostrophic currents display similar characteristics to the observations (Fig.3.9 a,b). The eastern branch of the South Atlantic subtropical gyre

flows northwestward. There is an intensified inshore branch, between the 200 and 500 m isobaths, the Benguela Jet, with average velocities reaching 20 cm s^{-1} in the model, and slightly less (15 cm s^{-1}) in the observations (Fig.3.9 c). However, this bias could be linked to the coarse resolution of altimetry near the coast. Additionally, negative surface alongshore geostrophic current is observed within 50 km offshore distance in the altimetry which was not captured by the model simulation. The presence of a coastal poleward current is consistent with current meter measurements of *Nelson* (1989).

Sea surface temperature (SST)

The comparison of the modelled and infrared ODYSEA (*Piollé and Autret*, 2011) sea surface temperature (SST) shows that the cooling of coastal waters in summer consistently occurs in the model and observations (Fig. 3.10). There is an inshore warm bias of roughly 1.5^{o}C in the simulation, but such bias in regional models of EBUS is quite common [2].

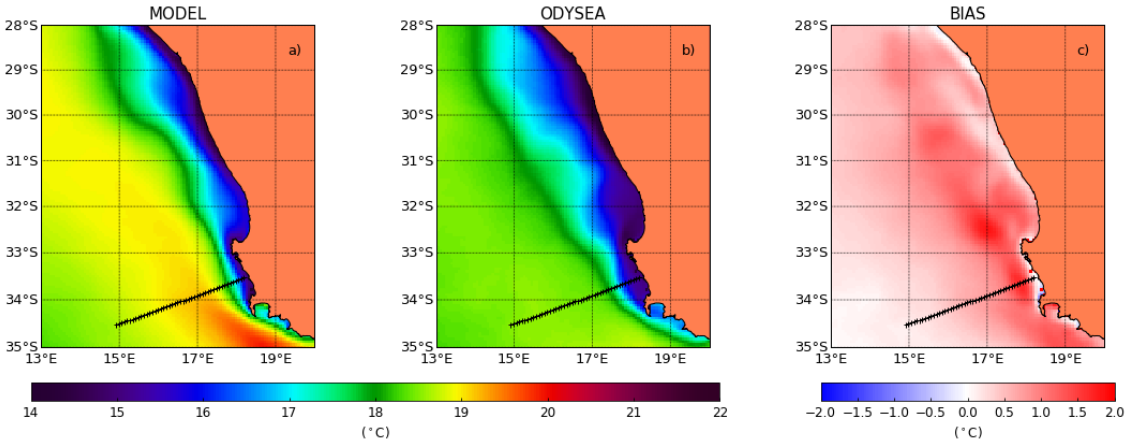

Figure 3.10: Annual average of Sea Surface Temperature (SST): a) satellite derived infrared data averaged over 2010-2017 (ODYSSEA); b) model data averaged over 1989-2010; c) Annual average of the SST bias (SST_{model} - $SST_{ODYSSEA}$).

A second satellite observed SST product, ESA-CCI SST, has been used to evaluate the model SST bias trough the strong seasonal cycle encountered in the regions. CCI-SST is a daily satellite SST from the European Space Agency's Climate Change Initiative (CCI; `http://www.esa-sst-cci.org/`) launched by European Space Agency (ESA). The CCI data has a ∼0.05°resolution and spans from 1991 to 2010 with a 0.1 K accuracy (*Hollmann*

[2]Misrepresentation of surface heat fluxes, wind-stress and vertical mixing in the coastal region could partially explain this bias.

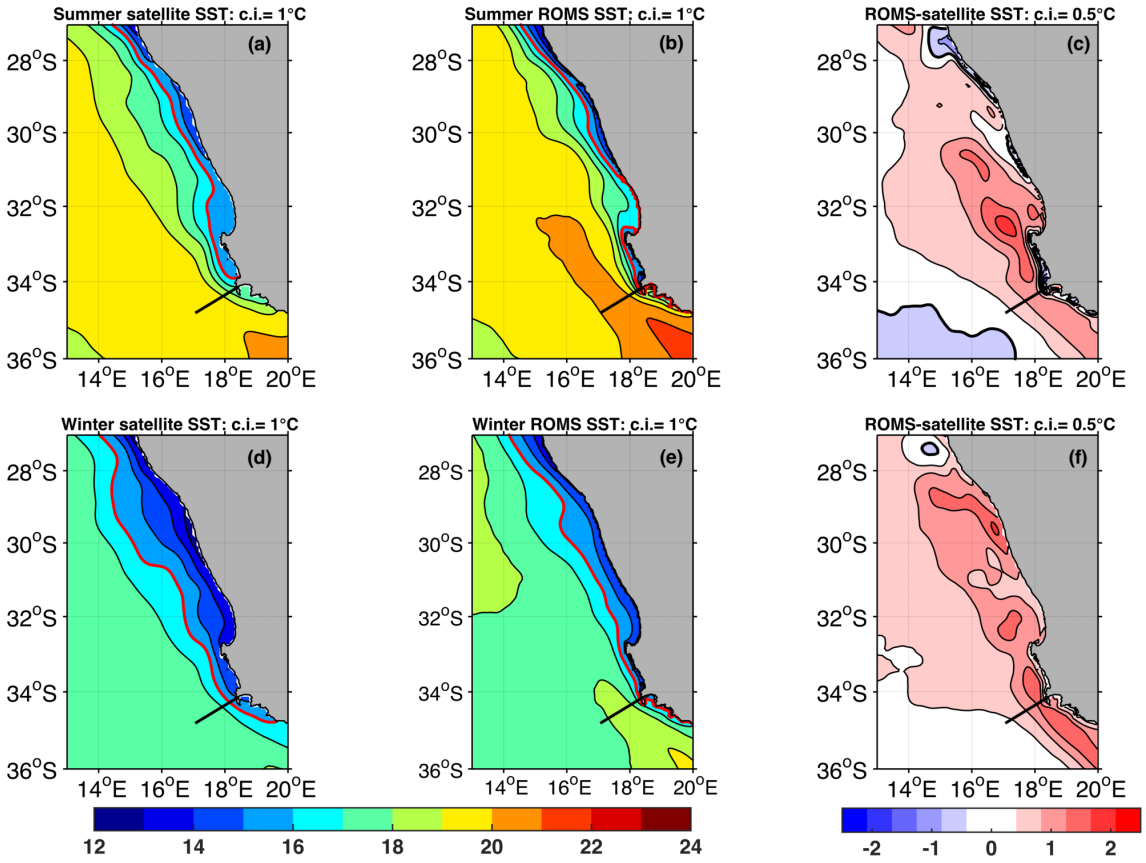

Figure 3.11: Climatology of the summer and winter SST obtained from (a,d) CCI satellite, (b,e) model and (c,f) difference (model - observation) for the 1992-2010 period. The 16°C isotherm is superimposed in red. Positive (negative) values in the difference map are regions where the model overestimate (underestimate) observed SST.

et al., 2013). The daily data were then averaged to obtain monthly data.

In summer, SST varies from about 15°C at the coast to 21-22°C offshore (Fig. 3.11a,b). Lower temperatures are observed in winter where the temperature drops down to 13-14°C near the coast, and maximum temperatures of 16-17°C are found offshore (Fig. 3.11d,e). Some notable differences are also observed. The cold coastal water bounded by the 16°C isotherm (red line) appears to meander further offshore in the observations than that in the model. The model is ∼1°C warmer in the offshore region, and the warm bias increases to 1-2°C in the coastal region (Fig. 3.11c,f). Its origin stems from the warm Agulhas Current water leakage overestimation into the South Atlantic indicated by the warm SST tongue coming from the southern boundary. This introduces a warm bias in our simulation extending as far north as Cape Columbine, and this was similarly found in *Veitch et al.* (2006).

Zonal SST gradient

Since the model overestimates temperatures both in the offshore region and coastal region, we believe that the cross-shore SST gradient could still be correctly represented. The cross-shore temperature gradient ($\Delta\mathrm{SST}_{x_i}$) can be used as a proxy for the density gradient that drives the alongshore equatorward jet (*Veitch et al.*, 2017). This SST gradient ($\Delta\mathrm{SST}_{x_i}$ in °C km^{-1}) is here calculated as a zonal difference between adjacent model grid points or satellite data pixels as follows:

$$\Delta SST_{x_i} = \frac{SST_{(i+1)} - SST_{(i-1)}}{X_{(i+1)} - X_{(i-1)}} \tag{3.3}$$

where ΔX is the zonal distance in km between the neighbouring grid points. The seasonal climatology of this SST gradient, based on the model and satellite data (CCI-SST), is plotted on cross-shore distance versus time Hovmuller diagram at 34.14°S (Fig. 3.12). The SST gradient has a marked seasonal cycle, with maximum gradient during the upwelling season (October-March). The model is able to capture its seasonal pattern: it intensifies in summer (-0.01°C km^{-1}) and extends further offshore during the late upwelling season (January to March). There is a good correspondence between the positions of the Benguela Jet and the SST gradient as shown in *Veitch et al.* (2017). This equatorward geostrophic

jet is observed throughout the year between the 200 m and 500 m isobaths. The jet's velocities can be greater than 0.45 m s^{-1} during the early upwelling season (October-November). In the late upwelling season, the jet also moves offshore. This suggests that the jet may be driven by the cross-shore SST gradient.

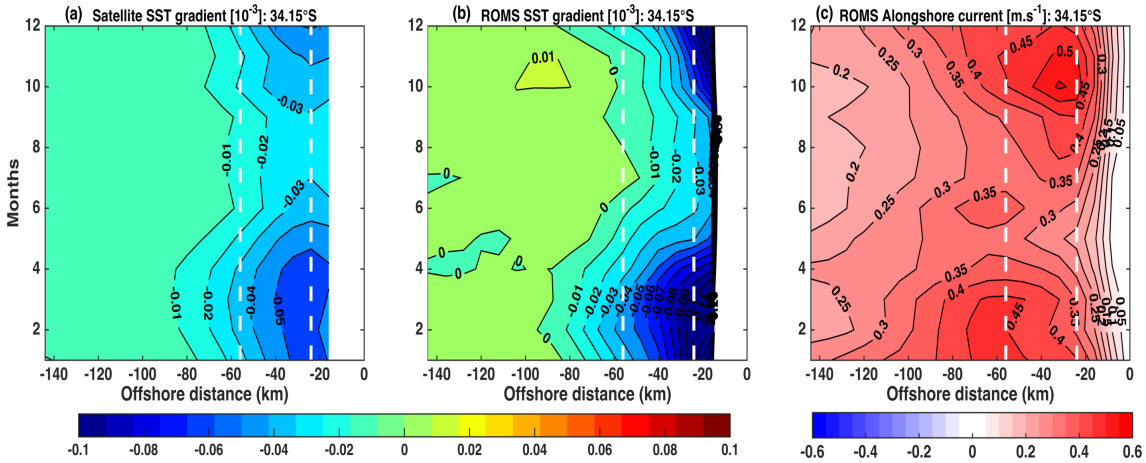

Figure 3.12: Space-time plot of climatological mean cross-shore SST gradient at 33.15°S for: (a) CCI-satellite, (b) model , both with an interval of 0.01°C. (c) : model alongshore current with a contour interval of 0.05 m s^{-1}. The 200 m and 500 m isobaths are shown as white dashed lines.

3.2.2 Hydrography: Vertical currents and temperature

The cross-shore section of the simulated and observed (WOA2013) alongshore geostrophic velocities taken at a transect off Grotto Bay (33.5°S), extending 300 km offshore is presented in figure 3.13. The geostrophic velocities are calculated using the thermal wind relation using the 1000 m depth as a reference level from which to perform the vertical integration. Figure 3.13a,b shows a well-defined, broad and strong northward coastal jet corresponding to the Benguela Jet that extends to the depth of 300 m. Its core is located about 120 km offshore, and its intensity weakens with depth.

A subsurface poleward undercurrent can be observed on the shelf break in agreement with current meter measurements of *Nelson* (1989). Poleward velocities can reach up to 0.1 m s^{-1} during summer. A thermal warm bias reaching up to 1-2°C can be observed in the model. However, this bias is homogeneous in its across-shore (≃200 km) and vertical (≃100 m) extension (Fig. 3.13c). Therefore, the surface layers across-shore density gradients are expected to reasonably well reproduced in the simulation, and, consequently, the

modelled alongshore geostrophic currents derived from the hydrography also match the observations.

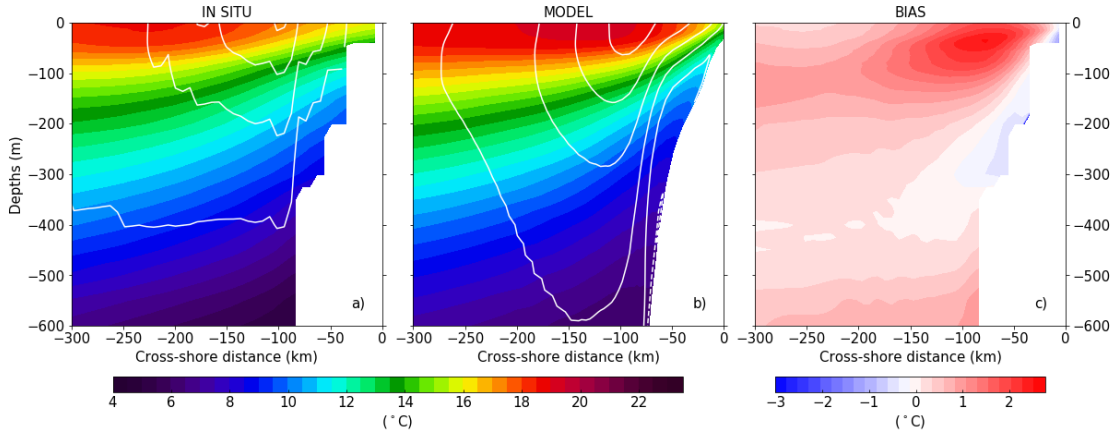

Figure 3.13: Temperature transect off Grotto Bay (solid black line on Fig. 3.10) with the alongshore component of the geostrophic current superimposed (white contours). a) World Ocean Atlas annual average (WOA2013); b) Same as in a) for the model; c) Temperature bias (T_{model} - $T_{WOA2013}$). Geostrophic velocities is built with a reference level at 1000 m depth. Contours are plotted every with 0.05 m s^{-1} in the range [-0.05 0.25] m s^{-1}. Negative values are dashed.

3.2.3 The near-shelf thermal stratification

The St Helena Bay Monitoring Line (SHBML) consists of 12 stations located in St Helena bay just offshore Elands Bay (32.30°S, 18.31°E) (Figure 3.14). Conductivity-Temperature-Depth (CTD) profiles go from the surface to a maximum depth of 1466 m, and stations have been monitored monthly by the South African Department of Environmental Affairs from April 2000 to December 2011 (*Lamont et al.*, 2015). Seasonal climatology of these data provide a unique dataset to estimate the thermal structure of the model in the nearshore region.

Differences between model-derived and in-situ based temperature for the SHBML confirm that there is a positive warm bias (>3°C) in the upper 100 m in the offshore region (Fig. 3.15). Nevertheless, the modelled across-shore temperature variations are very similar to the observed ones. Temperatures inside the bay are much cooler than in the offshore region, and the thermocline is shifted upward consistent with the presence of coastal upwelling.

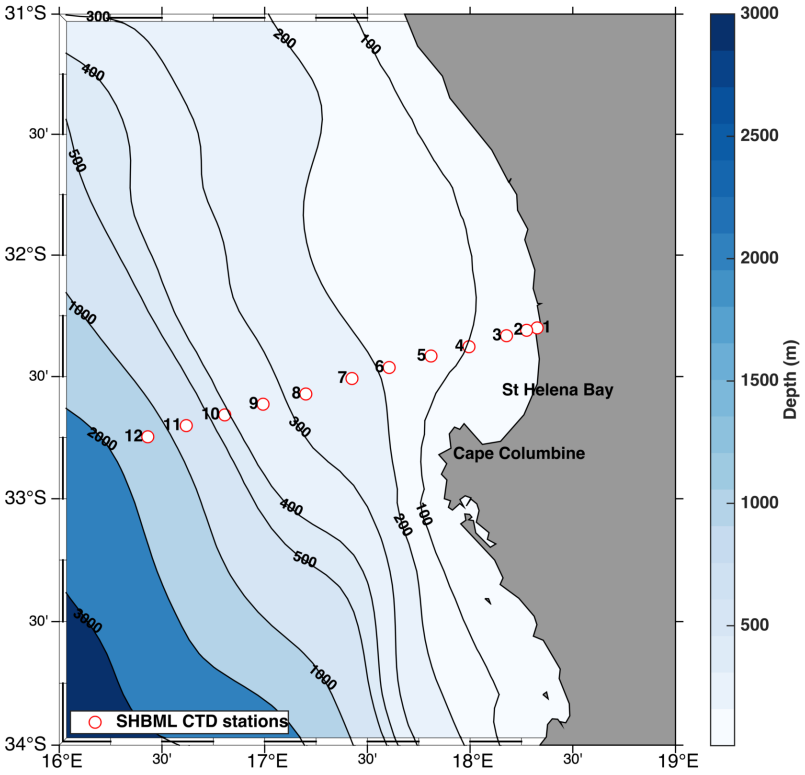

Figure 3.14: Model derived bathymetry (black lines in metres) in blue with 100 m contour interval for shallower region than 500 m and 500 m interval for region deeper than 500 m. The red markers show the locations of the 12 CTD stations of the St Helena Bay Monitoring Line (SHBML). Stations 1-6 are located within the bay region (coastal region), stations 8-10 located over the mid-shelf region and stations 11-12 further offshore in the open ocean.

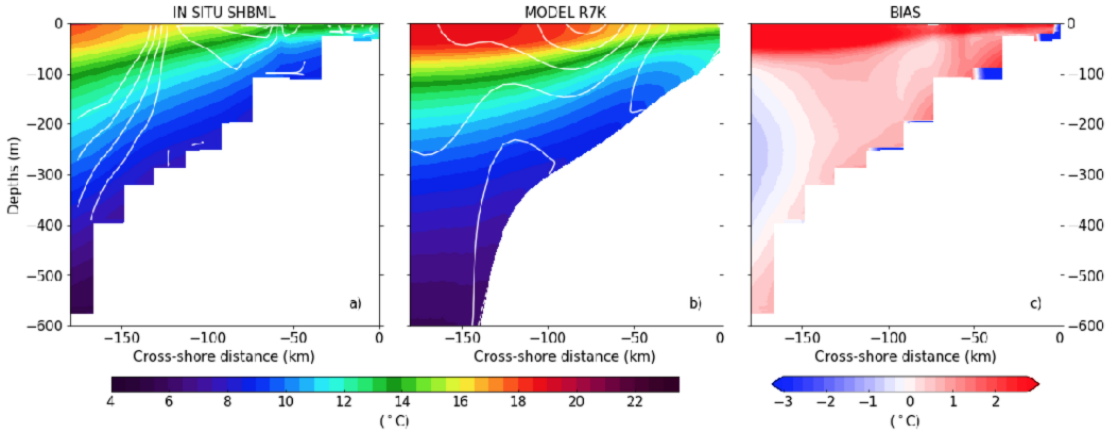

Figure 3.15: Temperature transect along the SHBML CTD stations (location of station is shown in Fig. 3.14) with the alongshore component of the geostrophic current superimposed (white contours). a) SHBML annual average ; b) Same as in a) for the model; c) Temperature bias (T_{model}-T_{SHBML}). Geostrophic velocities is built with a reference level at 1000 m depth. Contours are plotted every with 0.05 m s^{-1} in the range [-0.05 0.25] m s^{-1}.

Summary of the model evaluation

The oceanic circulation of the SBUS is studied with a mesoscale-resolving interannual (1989-2010) simulation and evaluated with available satellite and in-situ data. Despite the warm bias, the results from the model evaluation show that the model is capable of reproducing many of the physical features typical of a coastal upwelling system:

- A surface northward density-driven current located on the shelf in between the 200 m and 500 m isobath, namely the Benguela Jet;
- A poleward undercurrent confined to the slope-edge in a 250-1000 m depth range.
- The presence of intense mesoscale field just off the shelf.

However, the 7-km horizontal resolution was also not sufficient to accurately represent the observed innershelf poleward current. It is, however, important to note that the evaluation of the coastal circulation is a challenge due to a limitation of available observational data. When available, the observational data have a coarse resolution, especially within the 50 km coastal band, and this is not adequate to resolve coastal processes. Consequently, some of the model bias found in the coastal region could be explained by the low resolution of the satellite measurements. Additionally, misrepresentation of surface heat

fluxes, wind-stress and vertical mixing in the coastal area could partially explain some the warm coastal bias.

Chapter 4

Lagrangian pathways in the southern Benguela upwelling system

The content of this chapter is extracted from a paper entitled *Lagrangian pathways in the southern Benguela* published in the Journal of Marine Systems in 2019 (*Ragoasha et al.*, 2019):

Ragoasha, N., Herbette, S., Cambon, G., Veitch, J., Reason, C., and Roy, C., 2019. Lagrangian pathways in the southern Benguela upwelling system. *Journal of Marine Systems*, 195, pp.50-66. Doi: https://doi.org/10.1016/j.jmarsys.2019.03.008.

4.1 Introduction

The effect of ocean currents on fish eggs and larvae during their journey from spawning to nursery grounds in the southern Benguela upwelling system is poorly understood. The survival and successful transport of fish eggs and larvae, at early-stage, results from complex biological and physical processes. This study focuses on the physical processes that impact the connectivity between the western edge of the Agulhas Bank and the west coast upwelling. A set of Lagrangian experiments are conducted with particles being released within the top 100 m of the water column along an across-shore transect off Cape Point

(34° S). The Lagrangian experiments aim at addressing the following: (1) the identification of the dominant pathways that ensure this connectivity; (2) their characteristics and robustness; (3) the ocean dynamics that link to the alongshore transport success seasonal variability. Results are based on the 7.5 km horizontal resolution reference simulation.

Results presented within this chapter are based on the reference mesoscale eddy resolving interannual (1989-2010) simulation of the region, with a horizontal resolution of 7.5 km. Unlike the climatologically forced model of *Veitch et al.* (2017), our ocean model is forced by 6-hourly surface forcing (wind, heat and freshwater fluxes) over the 1989-2010 period. The use of a realistic, 22 years-long, eddy-resolving simulation that gives robustness to the seasonal cycle that we computed and to our conclusions regarding the role of the Benguela Jet, Ekman drift and mesoscale eddies in the advection of particles between Cape Point and Cape Columbine.

A first step towards elucidating the role of the jet consists of identifying the different physical processes that control the seasonal cycle of this northward alongshore connectivity between Cape Point and St Helena Bay, just north of Cape Columbine. The Lagrangian experiments aim at addressing the following: (1) the identification of the dominant pathways that ensure this connectivity; (2) their characteristics and robustness; (3) the ocean dynamics that link to the alongshore transport success seasonal variability.

The Lagrangian experiments designed for the purpose of this study, are described in section 4.2. Section 4.3 then characterises the seasonal cycle of the alongshore connectivity in terms of duration of travel and initial positions. The Lagrangian pathways taken by particles are identified in section 4.4, while section 4.5 investigates the link between the observed Lagrangian dispersal patterns and the across-shore structure of the ocean circulation, mainly the alongshore currents and the mesoscale turbulent eddy field. Finally, a summary and discussion of our results highlight the complexity of the across-shore structure of alongshore jet currents in the region.

4.2 Lagrangian experimental set-up

In our experiment, particles are released over the Sardine and Anchovy Recruitment Program (SARP) line, which is a cross-shore transect situated off Cape Peninsula. The section extends from (34.15°S, 17.55°E) and (34°S, 18.4°E) and is located between the coastal land and the offshore region defined by the 3000 m isobath (Fig. 4.1a). For each vertical profile, particles are randomly distributed over the first 100 m depth (Fig. 4.1b) with a density of 1.125 particles per metre. This transect is considered as a transition zone separating the spawning area and the recruitment area for small pelagic fish (*Garavelli et al.*, 2012).

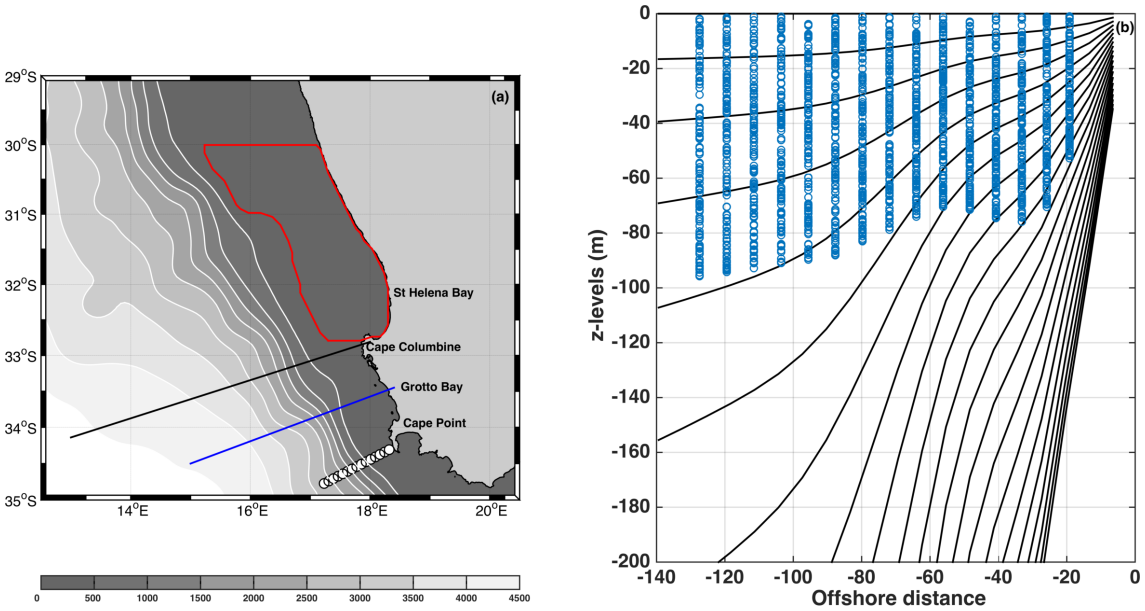

Figure 4.1: (a): Set-up of the Lagrangian experiments: particles are released over the SARP line (white circles), a cross-shore transect off Cape Point. They are counted as successfully transported particles if they reach, within 30 days, the St Helena Bay target area delineated by the red polygon. The bathymetry of the "BENGR15" model (in grey with white contours every 500 m) is also superimposed as well as two other cross-shore transects that particles will cross while being advected northward: the Grotto Bay line at 33.5°S (thick blue) and the Cape Columbine line at 33°S (thick black). (b): Initial distribution of particles over the SARP line for a given release event. σ layers are superimposed (black solid).

4.2.1 The Lagrangian particle-tracking model

In the present study, ROMS outputs of velocity fields are coupled to a Lagrangian particle-tracking model. The Lagrangian experiments are performed off-line based on an algorithm

called Pyticles developed by *Gula et al.* (2014). Pyticles is a Python/Fortran hybrid parallelized code. The 4th order RungeKutta (RK4) scheme is used to integrate time between particle positions with the ROMS simulated velocity fields interpolated to the particle locations at each integration time step. RK4 method uses the interpolated velocity information at four increments between time steps t_n and $t_n + 1$ (*van Sebille et al.*, 2018). This interpolation is necessary to account for the time interval differences between consecutive stored velocity field and the time step ($\triangle t$) required for particle displacement. The only dispersion process considered is the advective flow according to the hydrodynamic model with no additional diffusive terms implemented in Pyticles. Parameters such as the number of particles released in time and in space as well as the values for the forcing frequency and time step can be defined. Particles can be released with a continuous injection or once-off release.

4.2.2 Statistical Lagrangian diagnostics

• Transport success (TS) diagnostics

For each release event, transport success (TS_e) is given by the ratio of the number of particles that have reached St Helena Bay (red polygon) target area (Fig. 4.1a) over the total number of particles released (N_e) (*Huggett et al.*, 2003). This polygon extends between 32.8°S and 30°S and from the coast to 300 m isobath. Each particle was counted only once during its first entry into the polygon at any time within their 30 days life span.

$$\mathrm{TS}_e = \frac{n_e}{N_e}, \tag{4.1}$$

where n_e is the number of particles entering St Helena Bay during event e. N_e, the number of particles released during event e is kept constant during the Lagrangian experiment. TS_e can be seen as a proxy for the SARP line/St Helena Bay connectivity.

The monthly transport success TS_m is computed by averaging over the simulation all events specific to each individual month:

$$\mathrm{TS}_{m\{m=1,\ldots,12\}} = \sum_{e(m)} TS_{e(m)} \times \frac{1}{N_{e(m)}}, \tag{4.2}$$

were $e(m)$ is the event index chosen to correspond to all the release events occurred during month m.

For every monthly transport success, we estimate its standard deviation (σ_{TS_m}). This could be used as an estimation for the amplitude of the interannual variability.

$$\sigma_{TS_m\{m=1,\ldots,12\}} = \sqrt{\sum_{e(m)} [TS_{e(m)} - TS_m]^2} \tag{4.3}$$

• **Diagnostics of particle dispersion patterns**

In order to get a general view of the routes taken by the released particles, maps of particle distribution are plotted according to their age (given in days after their release). The density of particles aged t_l within a given grid cell centred at x_i, y_j is calculated as follows:

$$d(x_i, y_j, t_l) = \frac{n(x_i, y_j, t_l)_e}{n_p} = d_{ijl}, \tag{4.4}$$

where $n(x_i, y_j, t_l)_e$ is the number of particles aged t_l found within the grid cell centred at x_i, y_j, and n_p the total number of particles released. Here, grid cells correspond to the horizontal grid of the ROMS model. The above definition insures a consistent normalisation of the particle distribution. The density would be one if all particles at the SARP line would be advected within the grid cell when they are aged t_l. Note that this density is calculated for some specific released events, here grouped monthly.

Maps of the density distribution can be understood as plume of particle dispersion. The geometric centre of the plume represents the mean position of particles aged t_l and is computed as follows:

$$X_c, Y_c(t_l) \quad = \quad \sum_p X_p(t_l), Y_p(t_l) \times \frac{1}{n_p} \quad = \quad \sum d_{ijl}(X_i, Y_j) \tag{4.5}$$

where X_p, Y_p are the position of a Lagrangian tagged p at an age t_l. n_p is the number of particles released, and X_i, Y_j are the ROMS grid coordinates.

4.3 Characteristics of the alongshore connectivity

The following section intends to characterise the seasonal cycle of the alongshore connectivity between the SARP line and St Helena Bay in terms of: i) transport success, ii) time taken by successful particles to travel northward, iii) initial vertical and across-shore position of successful particles.

Fig. 4.2 plots the monthly climatology of the alongshore wind stress at the SARP line together with transport success TS_m and its standard deviation. Both monthly alongshore transport success and its standard deviation show a strong seasonal cycle, that does not strictly superimpose with the upwelling. Upwelling favourable winds prevail in austral spring and summer from October to March, whereas transport success peaks in November-December (late spring), at the beginning of the upwelling season. Our results show that, on average, during this period, particles have a 30% chance of reaching St Helena Bay with a standard deviation as high as 10%. The likelihood of particles making it northward decreases during the peak of the upwelling season (January-February), and reaches its lowest value (13%) in autumn. At this time of the year, the variability of the transport success also appears to be the lowest.

The age of arrival into the target area also varies seasonally (Fig. 4.3a). There is a peak in the age distribution around 7 days for particles released between July and October. For the rest of the year, the age distribution flattens and gradually shifts towards higher values during the upwelling season. From February to June, it is homogeneously spread between 10 and 25 days. The cumulative histogram of monthly transport success for 4 groups of particles built according to their age of arrival (group I: age$<$10 days; group II: 10$<$age$\leq$15 days; group III: 15$<$age$\leq$20 days; group IV 20$<$age$\leq$30 days) reveals that particles arriving within 10 days account for more than 50% of the successful particles between August and November (Fig. 4.3b). Particles having short connection time are found all year round but are a minority in late summer and autumn. This suggests the existence of a "fast route" between the SARP line and St Helena Bay, which could be the dominant pathway in late winter and spring. Nevertheless, other routes could exist. There might even be a "slow route" from January to June, when the majority of particles belongs to group IV.

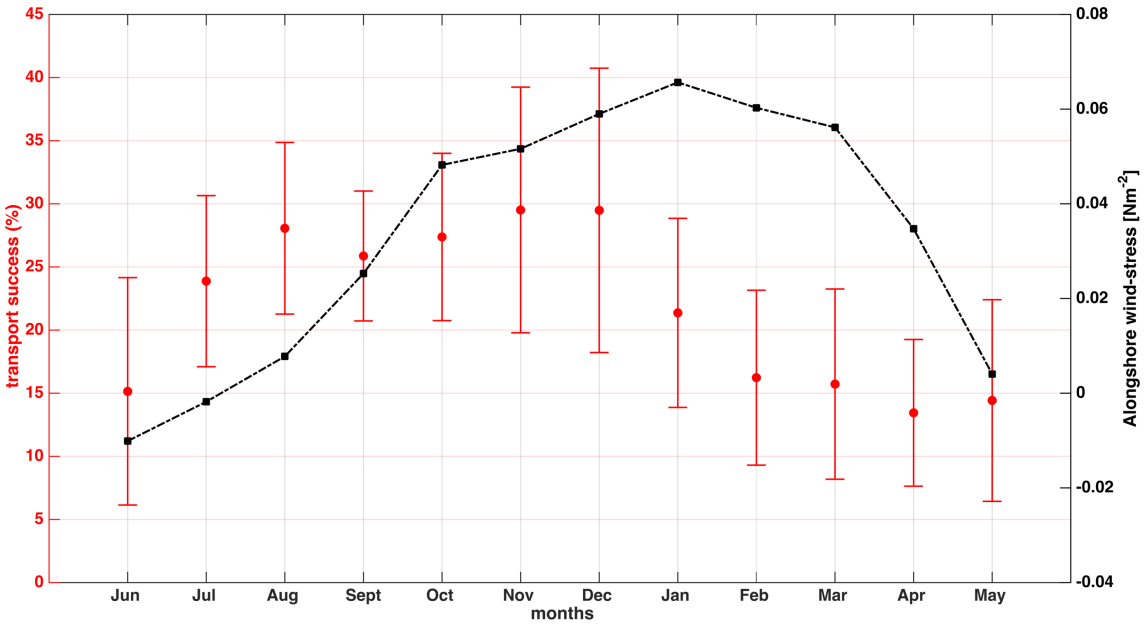

Figure 4.2: Monthly climatology of transport success TS_m (red dots) and alongshore wind-stress at the SARP line (black dots). The standard deviation of $TS_m$is also superimposed as errorbars. The wind stress is averaged over a box encompassing the southern Benguela from 12°E to 20°E and 26°S to 36°S.

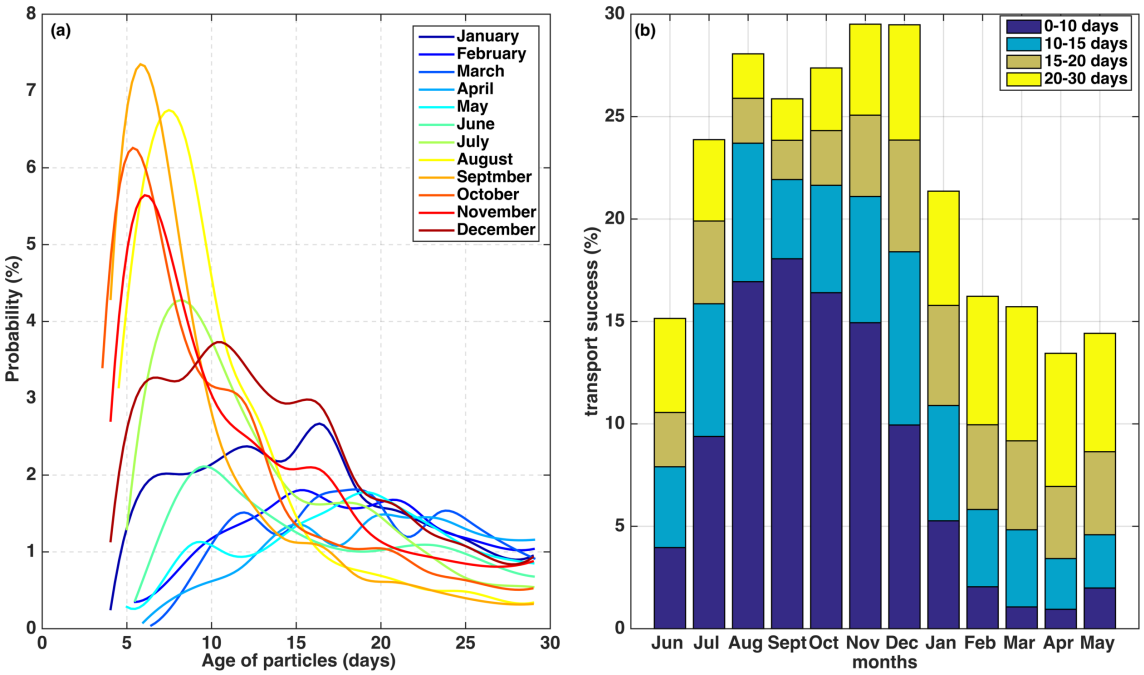

Figure 4.3: (a): Monthly distribution of successful particles by age when entering the target area. (b): Cumulated histogram of monthly climatology transport success with clusters of particles built according to their age of arrival: group I (age<10 days); group II (10<age≤15 days); group III: (15<age≤20 days); group IV: (20<age≤30 days). Probability have been normalised by the total number of particles released for each month m ($m = 1, \cdots, 12$) over the 22 years of the model run.

The initial vertical and across-shore positions of particles are also important parameters affecting transport success. The majority (∼90%) of particles arriving in St Helena Bay are released between 0 m and 70 m depth (Fig. 4.4a). There is a peak in the distributions around 55 m depth, whose intensity varies seasonally and intensifies in between October-March. Within this depth range, there is a pronounced seasonal contrast. During austral winter, particles released in the top surface layer (0 to 35 m depth) have a higher probability of reaching St Helena Bay than during the rest of the year (∼ 3.7% in July versus 1.7% in January). If only particles successfully transported are counted in the calculation, 50% of those arriving in St Helena Bay in July are those initially released within the top surface layer. The proportion drops to 25% for those released in January. During spring and summer, the opposite pattern is observed with particles released in the subsurface layers having a higher transport success. These results are consistent with the general assumption that, in eastern boundary upwelling systems (EBUS), upwelling favourable winds usually enhance the offshore advection of surface particles.

Grouping particles according to the isobath on which they have been released is a way to investigate how the contrasted across-shore structure of the circulation at the SARP line impacts transport success. Particles released over the continental shelf (between the coast and the 300 m isobath) account for more than 50% of the successfully transported particles, although they only represent one sixth of the total number of particles released (Fig. 4.4b). Their probability of reaching St Helena Bay gets as high as 75% (not shown) in late winter and early spring. Further investigations (not shown) indicate that being released inshore not only increases the particles' probabilities to reach St Helena Bay, but also decreases their travel durations.

These results suggest the existence of an efficient "fast" inshore route connecting the western edge of the Agulhas Bank to the west coast upwelling region. However, this analysis is only based on the final and initial positions of the particles. The identification of the pathways taken by these particles is done in the following section by considering the northward progression of particles during their 30 day life span and their average trajectories.

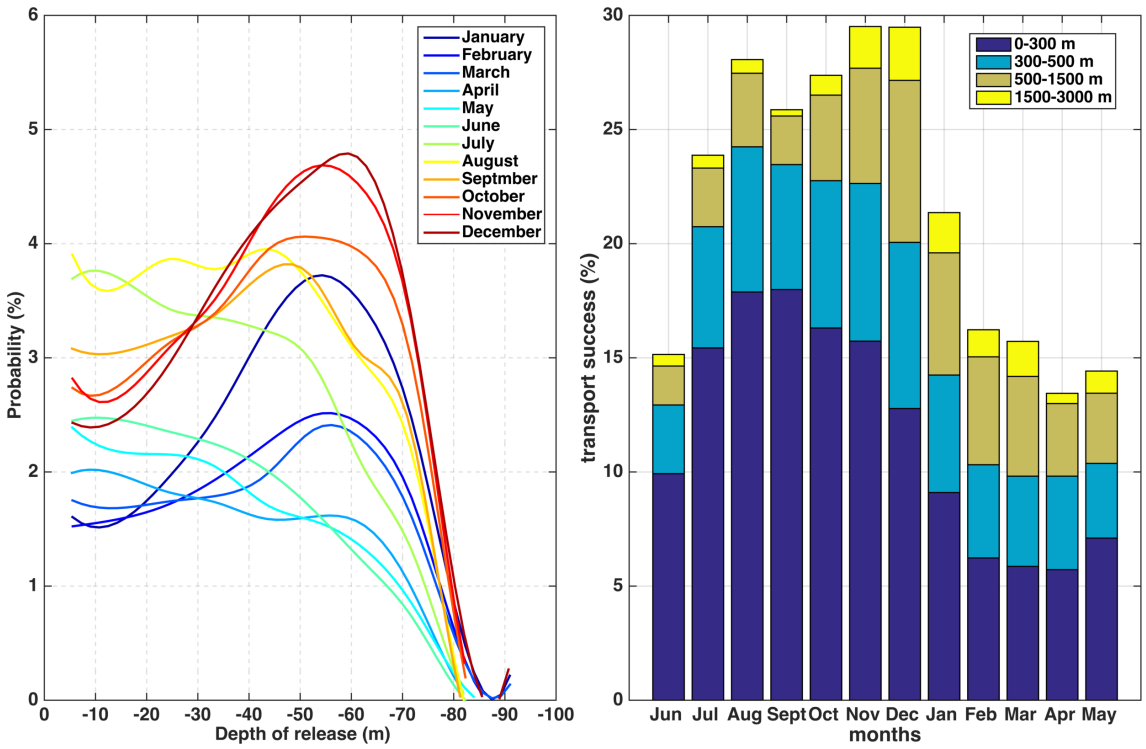

Figure 4.4: (a): Monthly distribution of successful particles by their depth of release. (b): Cumulative histogram of monthly climatology transport success with clusters of particles built according their initial isobath. Probability have been normalised as in Figure 4.3 .

4.4 Alongshore Lagrangian pathways

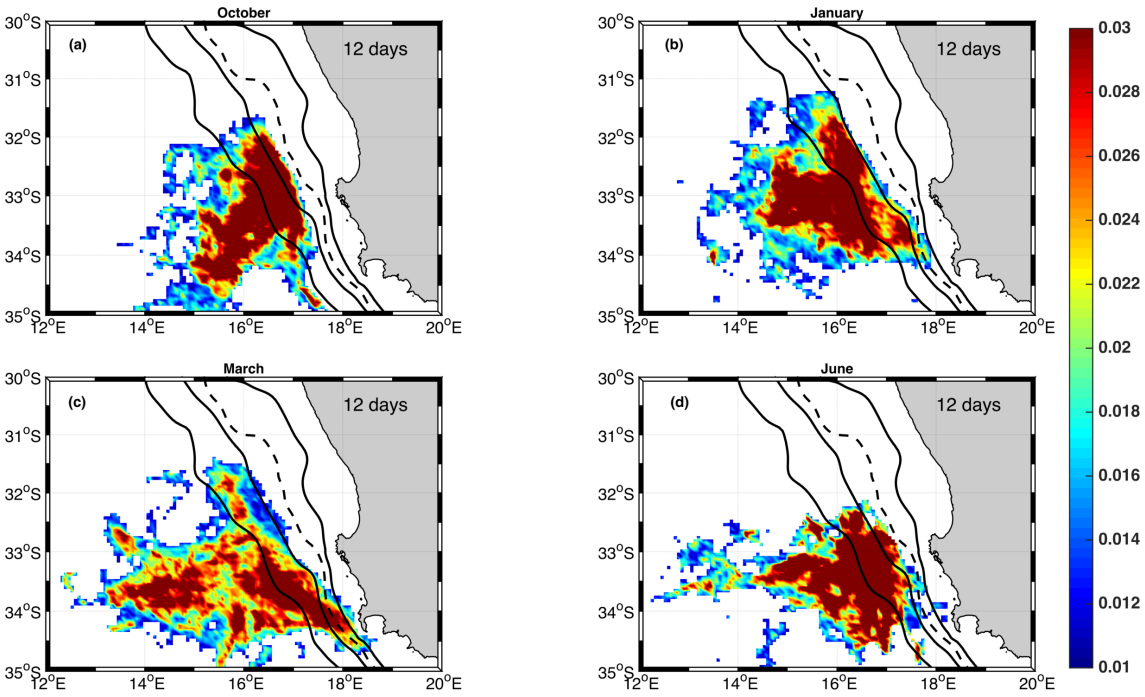

Figure 4.5: Horizontal distribution of unsuccessful particles (plumes) 12 days after their release for the months of: (a) October; (b) January; (c) March; (d) June. The 200 m, 300 m (dashed), 500 m and 2000 m isobaths are superimposed. The colorbar shows the probability of finding a particle aged 12 days within the water column at a specific grid cell.

In order to get a general view of the routes taken by Lagrangian particles, maps of particles' spatial distribution (plumes) are plotted according to their age τ (in days) on the horizontal grid of the "BENGR15" simulation. The age of particles is zero when they are released. For a series of release events, we count all particles aged τ found within the water column of the grid cell located at position (x, y) in Cartesian coordinates. After dividing this by the total number of particles released during this list of events, we obtain the probability $d(x, y, \tau)$ of finding a particle aged τ at location (x, y). We also build a monthly climatology of this probability. For example, the monthly probability of January is obtained by considering all release events that occurred in January over 1989-2010.

Maps of the spatial distribution of the particles show that, once released on the SARP line, successful and unsuccessful particles take distinct routes. 12 days after their release, unsuccessful particles have been largely spread offshore beyond the 500 m isobath (Fig. 4.5), whereas successful particles remain trapped on the shelf edge between the 200 m

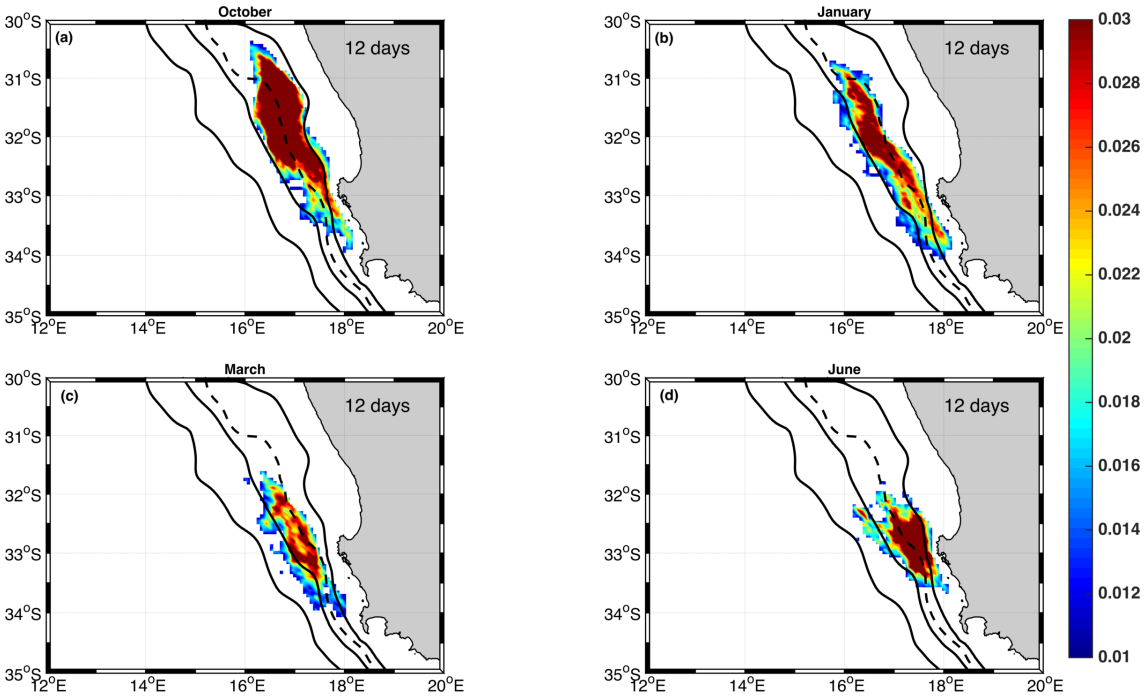

Figure 4.6: Same as Fig. 4.5 for the successful particles. The sum of probabilities over the grid gives the transport success plotted in Fig. 4.2.

and 500 m isobath (Fig. 4.6). The characteristics of the plume change seasonally. In October, successful particles get dispersed in a compact and elongated plume, that stretches quickly towards the equator following the shelf edge. Additionally, most of these particles make their journey in less than 10 days after being released inshore of the 300 m isobath. From January to June, the northward extension of the plume progressively reduces.

The fate of unsuccessful particles is to be dispersed offshore, following a northwestward orientated cone that extends throughout the coastal transition zone (Fig. 4.5). They experience a widespread dispersion into the open ocean as they leave the shelf slope region and are advected through the coastal transition zone, an area known for intense mesoscale turbulence in EBUS (*Marchesiello et al.*, 2003; *Capet et al.*, 2008a). The north-westward spreading of unsuccessful particles is maximum in March. The low values of transport success found at this time of the year (Fig. 4.2) confirm the general idea that passive particles, once advected offshore, struggle to come back inshore. From January to June, the plume also shows a V-shape, past Cape Columbine, which suggests a branching of the route. One branch seems to follow the slope whereas the other bifurcates offshore, as was already pointed out in the work of *Garavelli et al.* (2012) and *Veitch et al.* (2017).

A monthly climatology of the successful particles' trajectories is presented in figure. 4.7. The latter is computed after joining together the geometric centre of the plume of successful particles every 12 hours from 0 to 30 days. This figure highlights the seasonal changes of the pathways taken by successful particles during their transit to St Helena Bay. In January and March, the trajectory of particles is shifted offshore. It starts bending westward at the latitude of the SARP line, crosses the 500 m isobath, and finally veers back inshore towards the 500 m isobath at Cape Columbine. The majority of successful particles make their journey in more than 20 days (Fig. 5.15) and follow an offshore path. In October, the offshore route to St Helena Bay is no longer active. The majority of particles make their journey in less than 10 days following an inshore route that almost overlies the 300 m isobath. In June, the few particles reaching St Helena Bay also follow an inshore route, but the latter is slower than during October. Our findings on the seasonality of the pathways and their locations can be summarised as follows. The inshore route is the dominant pathway in late winter and early upwelling season, when offshore Ekman transport is moderate and particles are able to remain inshore. This inshore route is characterised by short connection times (< 10 days). During the peak of the upwelling season, this inshore route persists, but becomes less efficient, as it mainly concerns subsurface particles located below the Ekman layer (about 40 m in the Benguela upwelling system). Connection times also tend to be longer (> 10 days). A slower offshore route, with connection times in the 20-30 days range, exists for particles either initially released on the shelf slope (from the 300 m to the 1500 m isobaths) or advected offshore by Ekman transport during their early age. This offshore route becomes the dominant pathway in summer.

4.5 Inferring the role of the ocean circulation on the Lagrangian pathways

4.5.1 Characteristics of the ocean surface circulation

The Lagrangian experiments show that a "fast" inshore route and a "slow" offshore route co-exist and bring particles from Cape Point to St Helena Bay. The following section

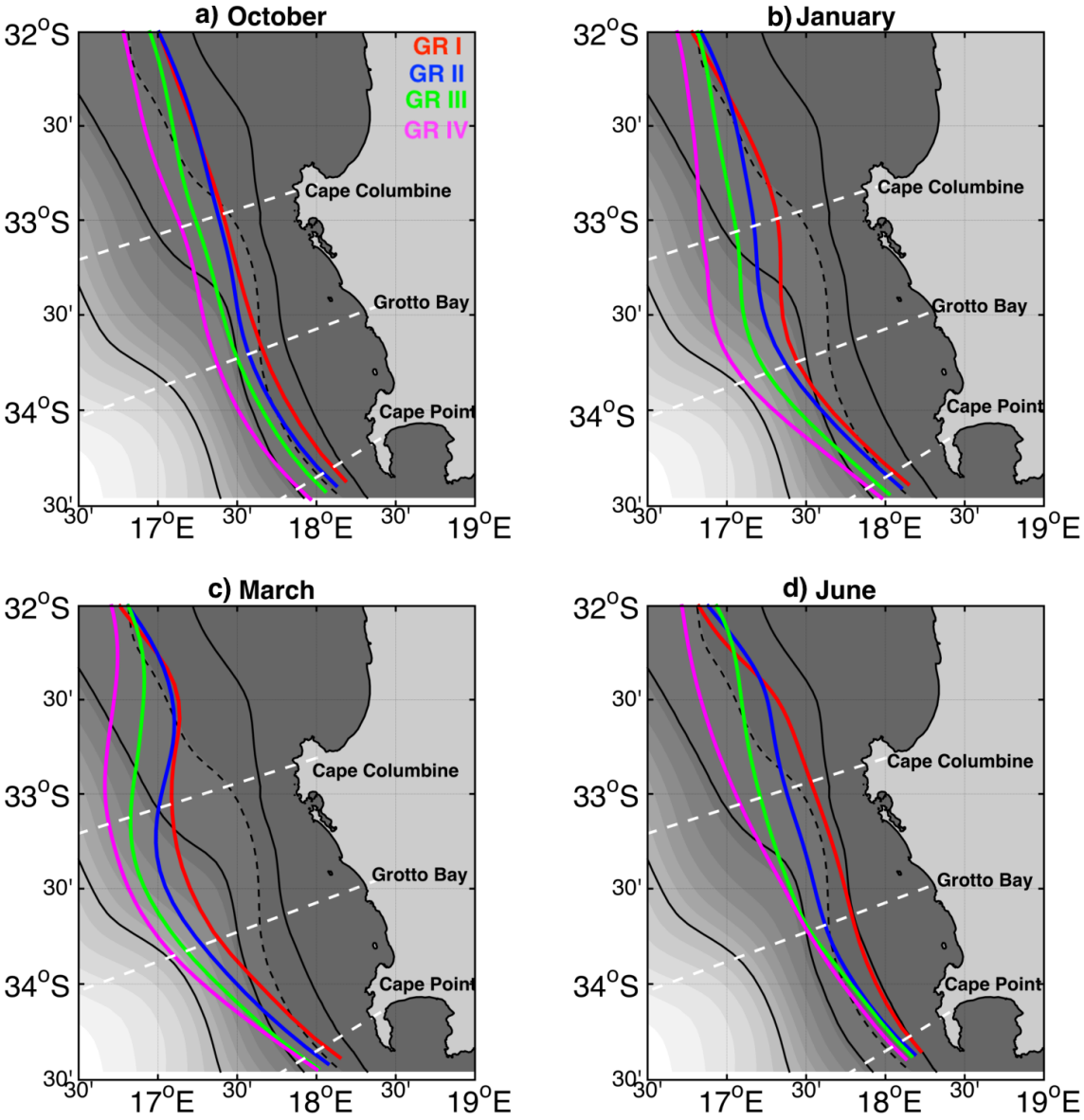

Figure 4.7: Monthly climatology of the trajectory of successful particles by age of arrival into the target area τ (in days). Trajectories are plotted for particles released in: (a) October; (b) January; (c) March; (d) June. colors refer to the clusters of particles built according to their age of arrival τ. Group I: $\tau < 10$ (red); Group II: $10 < \tau \leq 15$ (blue); Group III: $15 < \tau \leq 20$ (green); Group IV: $20 < \tau \leq 30$ (magenta). The 200 m, 300 m (dashed), 500 m and 2000 m isobaths are superimposed (black). Note that the mean of the four trajectories at 12 days corresponds to the geometric centre of the plume plotted in Fig. 4.6. The SARP, Grotto Bay and Cape Columbine lines described in Fig. 4.1 are also superimposed (white dashed).

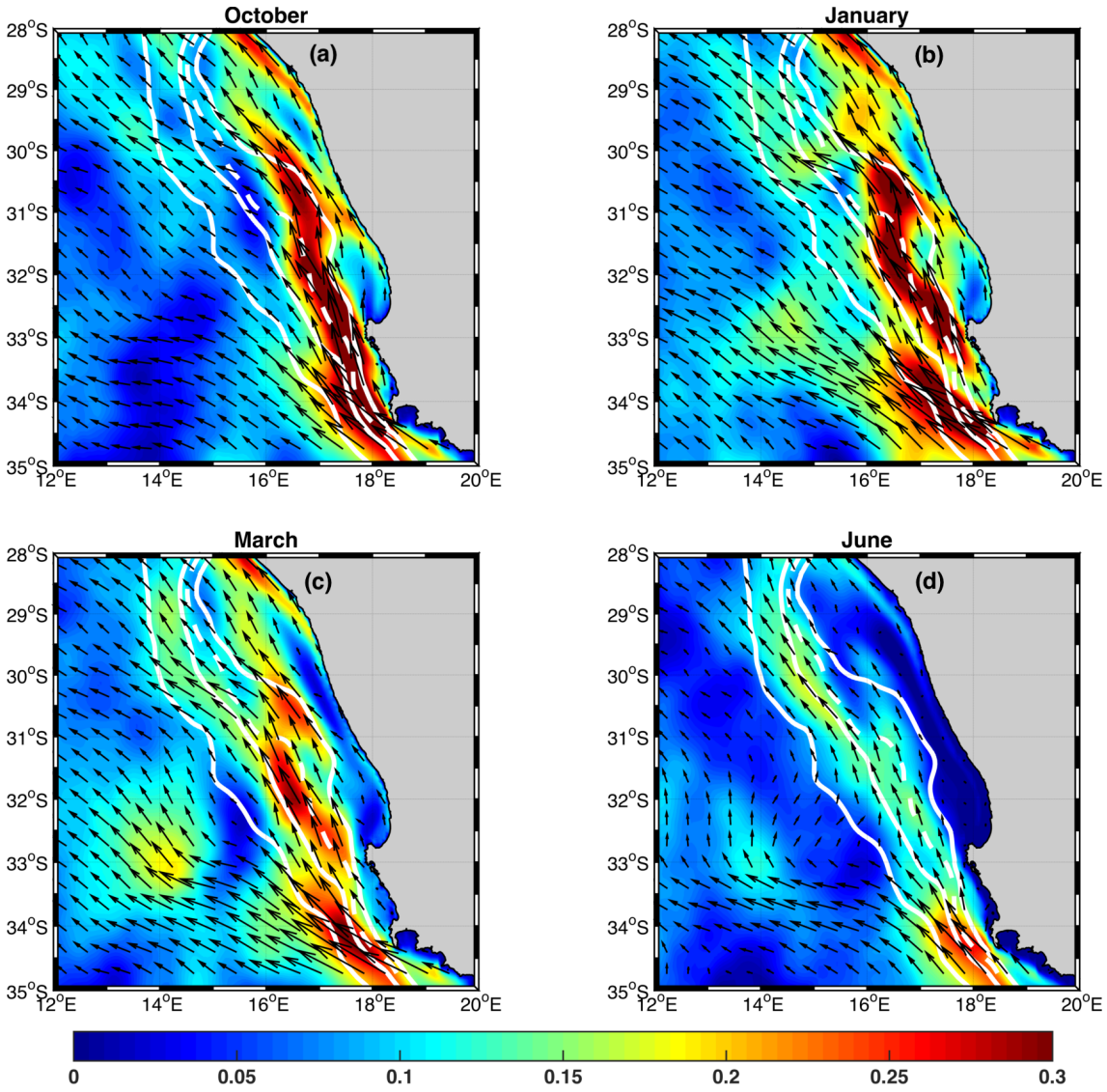

Figure 4.8: Monthly climatology of surface currents for: (a) October; (b) January; (c) March; (d) June. The magnitude of the current is shown in color (m s^{-1}) and current vectors are superimposed, as well as the 200 m, 300 m (dashed), 500 m and 2000 m isobaths (solid white).

investigates how the Eulerian oceanic circulation of the model relates to these identified pathways.

Maps of monthly climatological surface currents show a nearshore equatorward jet, namely the Benguela Jet (Fig. 4.8). This jet can be observed all-year round, with a marked seasonal variability. In October, it is intensified and spatially coherent. In January, at the vicinity of 33.5°S, it separates into two branches: i) an offshore branch that flows northwestward beyond the 2000 m isobath; ii) a coastal branch that flows alongshore in between the 200 m and 500 m isobaths and intensifies north of Cape Columbine. During the late upwelling season and early winter (March-June), the jet is still separated into two branches, but weakens, except off Cape Point (34°S).

Considering that the Benguela Jet dynamically connects the south and the west coasts of South Africa (*Garavelli et al.*, 2012; *Veitch et al.*, 2017), we superimpose, along three across-shore transects, the across-shore profiles of the: i) distribution of the particles; ii) depth-integrated (top 100 m) alongshore velocity; iii) depth-integrated (top 100 m) eddy kinetic energy (EKE). The across-shore profiles are plotted for the SARP line along which particles are released (Fig. 4.9), for the transect off Grotto Bay that intersects particles' trajectory at midway (Fig. 4.10) and for the transect off *Cape Columbine* (Fig. 4.11) that intersects particles' trajectory just before they enter the target area. The across-shore profile of the distribution of particles is obtained by counting particles crossing the transects. Quantities are normalised by their maximum value found among the 12 monthly climatology across-shore profiles of all three transects (Fig. 4.7).

Off Grotto Bay and Cape Columbine, the peak in the across-shore distribution of all particles (blue solid) almost superimposes with the peak in the jet's alongshore intensity (red solid). As expected, all year round, particles leave the SARP line and propagate northward embedded within the Benguela Jet. A different pattern is observed when only successful particles are considered. During their northward progression, successful particles (blue dashed) always remain on the inshore (cyclonic) side of the jet, following roughly the 300 m isobath. This area generally coincides with low values of surface EKE. The EKE can be interpreted as a proxy for the intensity of mesoscale oceanic turbulence. One would expect a particle that goes through an area of strong EKE to be more likely caught within

mesoscale turbulent oceanic features, such as eddies and filaments. An exception to this pattern is the occurrence of a secondary peak of EKE nearby the peak of successful particles in October off Grotto Bay (Fig. 4.10a). However, it does not have a negative effect on transport success because the alongshore jet and/or the topographic slope may be strong enough to counteract the turbulence dispersive effect in the near-shore region. In January and March, when the jet shifts offshore, presumably to conserve its potential vorticity as it gains cyclonic relative vorticity from the wind stress curl (*Castelao and Barth*, 2007), the peak in all particles also shifts offshore. This results in more particles entering a region where the surface EKE increases from low values at the coast to high values offshore.

At this stage of the analysis, the ability for particles to remain on the inshore side of the jet seems to be a necessary ingredient for transport success. Consequently, one would expect physical processes like wind-induced offshore/inshore Ekman transport during the upwelling/non-upwelling season to have a negative/positive effect on transport success. However, the picture is not as simple. This analysis brings to light that the broadening, the cross-isobath shift and the branching of the jet are other important processes that impact the alongshore connectivity between Cape Point and Cape Columbine, together with wind-induced Ekman transport. During the upwelling season, in January and March, despite intensified offshore Ekman transport, the broadening of the jet allows most particles to remain embedded within its core up to Grotto Bay (Fig. 4.10). Off Cape Columbine, multiple alongshore narrow jets exist all year round (Fig. 4.11). Ekman transport may either make particles follow one particular branch (January) or push them out of any branch (March). In March, the few successful particles are those trapped within the intensified inshore branch of the jet. In June, the distribution of the particles is disconnected from the jet (Fig. 4.10d). This can result from the inshore Ekman transport induced by prevailing westerly winter winds. It allows successful particles to remain trapped within the cyclonic inshore side of the jet up to Grotto Bay. Further north, when the jet divides into several branches, only the few most inshore particles manage to remain trapped within the inshore branch. The other ones get ejected from any branch, not even reaching the second less offshore branch. The across-shore position of particles at the location of the

jet's division seems to be a crucial parameter that determines which branch particles may follow. Wind-induced Ekman velocities may set up this position.

Finally, our results underline the importance of intrusions of Agulhas waters. Off Cape Point, where particles are released, there is a strong variability in the across-shore structure of the alongshore jet (not shown). A significant proportion of particles (30%) is advected southward just after being released, and then advected back northward through the transect. During their return northward path, they may cross the transect at a more offshore position than their initial position, which explains the mismatch (Fig. 4.9) between the initial distribution of all particles (green solid) and the distribution of all particles crossing the transect (blue solid).

In summary, we have shown that the efficient and fast inshore route taken by the particles in late winter and spring corresponds to particles being advected within an intense northward laminar nearshore jet. In summer and autumn, the route to St Helena Bay becomes less efficient and slower because of the offshore drift of the jet and its branching at Cape Columbine. Wind induced offshore Ekman transport contributes to particles being trapped within the offshore branches of the jet.

4.5.2 Characteristics of the ocean circulation at depth

Surface alongshore currents have a complex across-shore structure (multiple jets), and show pronounced latitudinal contrasts in the intensity and position of the jets. In the following, we investigate how the vertical structure of the flow, associated with the multiple jets observed at the surface, may explain the sensitivity of transport success to the initial depth of particles (Fig. 4.4).

Vertical transects off Cape Point (not shown), Grotto Bay (Fig. 4.12) and Cape Columbine (not shown) all show the existence of a poleward undercurrent lying over the shelf slope. This poleward undercurrent seems to persist all year round, but has a strong seasonal cycle. In winter (June), it is weak ($\sim$5 cm s^{-1}), narrow ($\sim$40 km) and located deeper than 100 m depth. During the upwelling season, it is strong ($\sim$25 cm s^{-1}), wider ($\sim$100 km); its core extends in the offshore direction and towards the surface ($\succeq$50 m

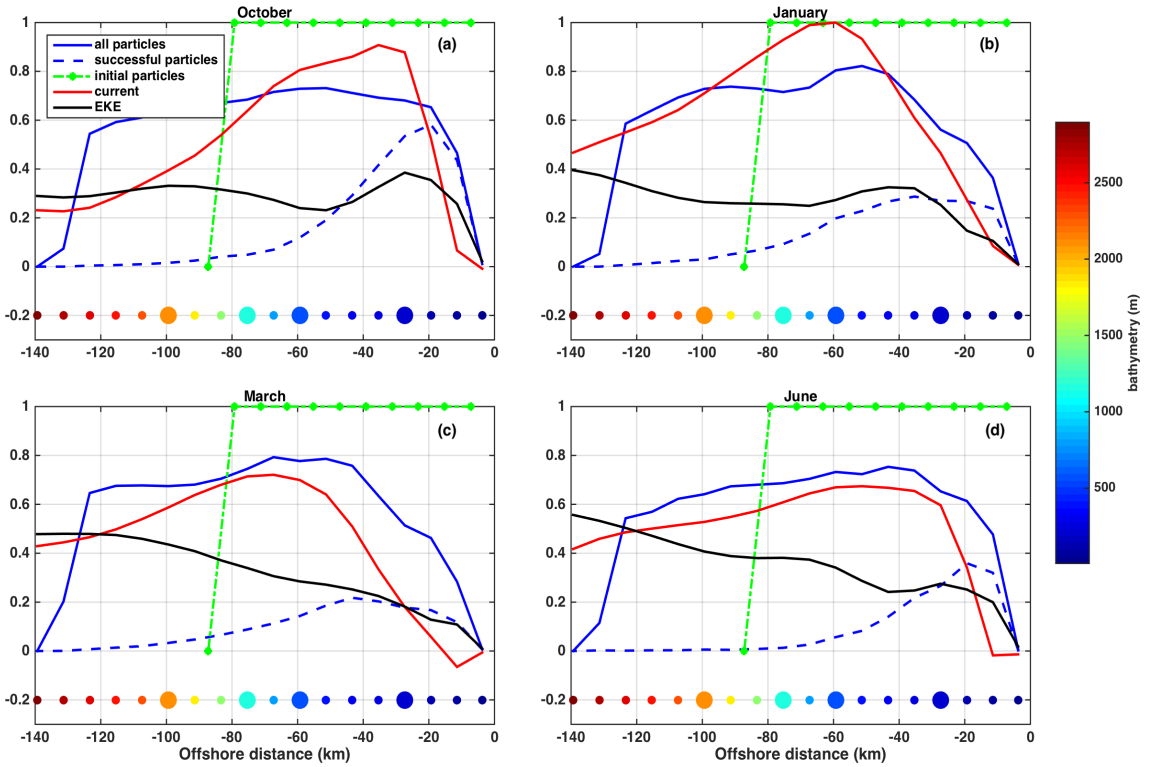

Figure 4.9: Across-shore profile of normalised depth-integrated alongshore current (red), EKE (black), and probability of the occurrence of particles (blue solid) at the SARP line. The histogram of successful particles is also superimposed (blue dashed) as well as the histogram of all particles at any release events (green solid). Profiles are plotted for: (a) October; (b) January; (c) March; (d) June. The depth-integrated alongshore current and EKE are computed over the top 100 m and then normalised by their maximum value found among the 12 monthly climatology across-shore profiles for all three transects. For the EKE, this maximum (0.07 m^2s^{-2}) occurred along the Grotto Bay transect in May. For the depth integrated current, this maximum (0.45 m s^{-1}) was found at the SARP line in January. The probability of occurrence of particles is normalised by its value on the SARP line when they are released. The colorbar shows the across-shore bathymetry, the enlarged circles mark the location of the 200 m, 500 m, 1000 m and 2000 m isobaths, respectively.

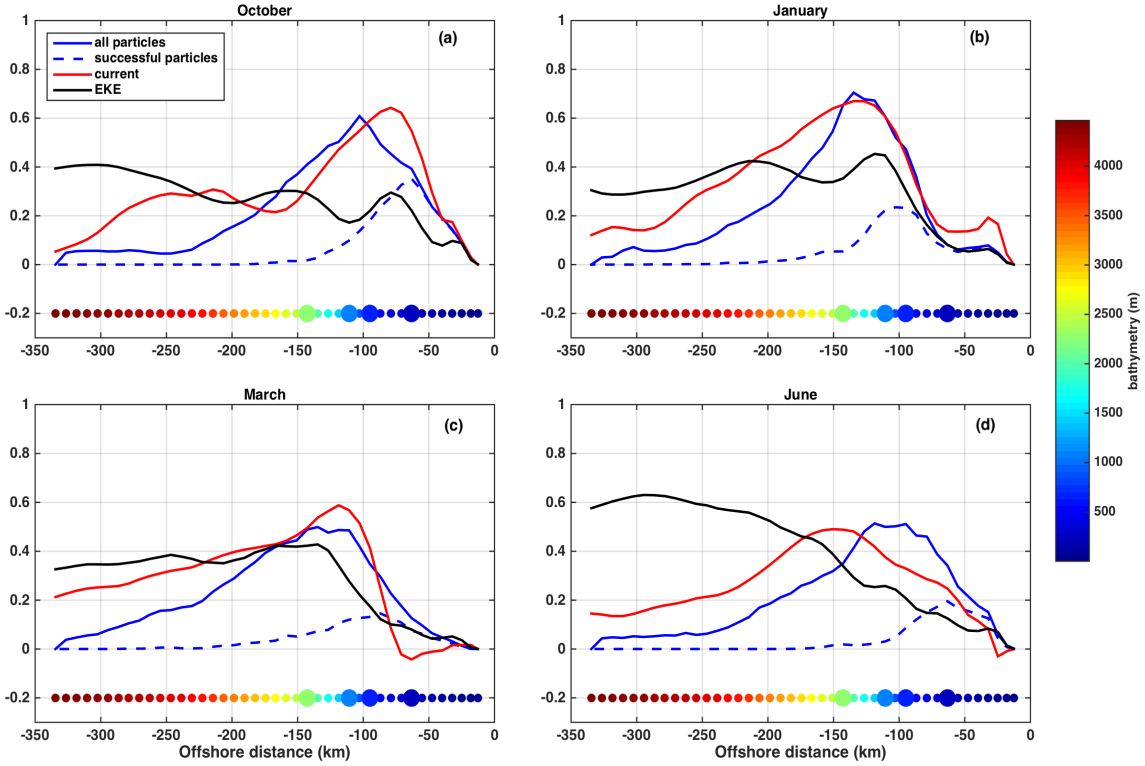

Figure 4.10: Same as Fig. 4.9 but for *Grotto Bay* (33.5°S).

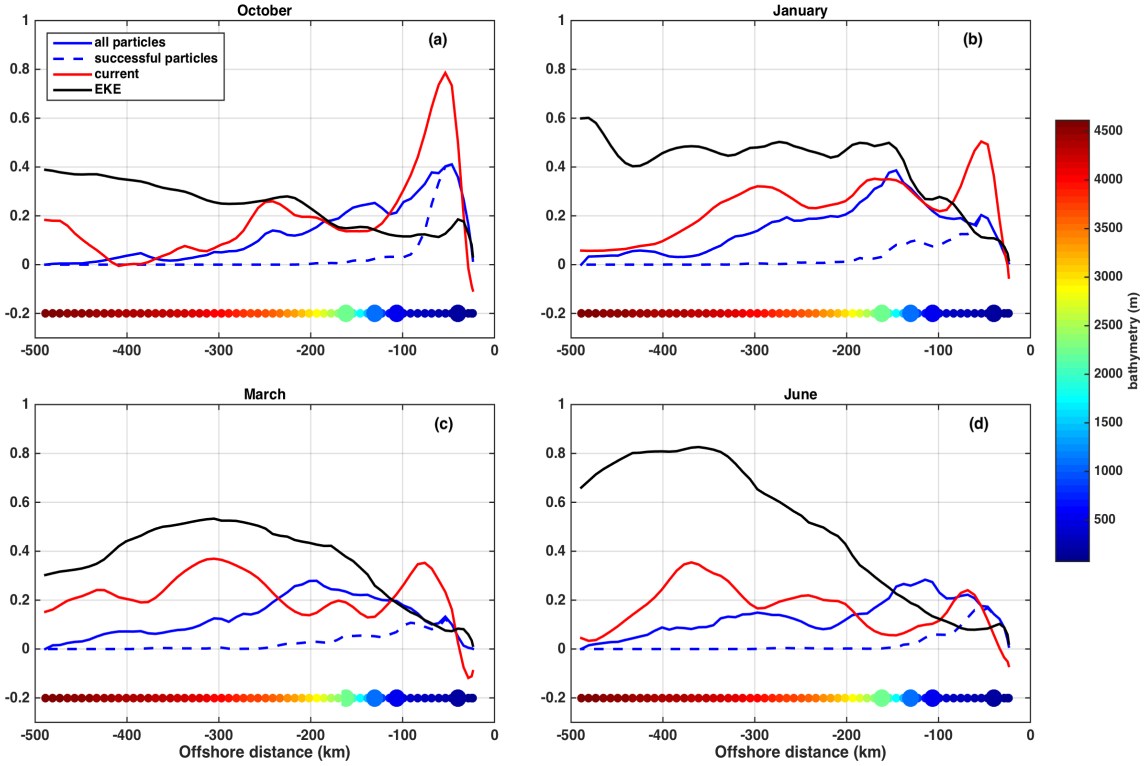

Figure 4.11: Same as Fig. 4.9 but for *Cape Columbine* (33°S).

depth). The strengthening of the poleward undercurrent and its uplifting to the surface during austral summer is induced by the development of a negative (cyclonic) wind-stress curl within the 100 km nearshore band in relation to the coastal wind drop-off (Fig. 4.12).

The shoaling and strengthening of the poleward undercurrent impacts the surface currents. At the SARP line, it mainly induces an offshore shift of the alongshore northward jet, which leads to the occurrence of a surface counter current in the nearshore area. North of Cape Point, the strengthening of the poleward undercurrent comes with the vertical pinching and weakening of the surface current. Off Grotto Bay, in January, the core of the undercurrent domes so sharply that it almost outcrops the surface 100 km from the coast. This mechanism is responsible for the bifurcation and separation of the surface current into multiple jets. While the main branch of the northward surface jet remains located offshore and extends as deep as 500 m depth, the coastal branch is squeezed between the surface and 50 m depth and follows the 300 m isobath. This squeezing of the surface jet should cause particles released below 50 m depth to be embedded within the poleward undercurrent. Consequently they would fail to reach St Helena Bay. The cumulated transport success according to the depth of release (not shown) shows the opposite. It turns out that the successful particles progress northward after getting trapped within the core of the thick offshore branch of the current.

The processes impacting the particles located in the top 50 m of the water column can be explored by considering the ageostrophic velocities in the vertical across-shore transects off the west coast (Fig. 4.13). The latter are computed after subtracting the geostrophic velocity (derived from the hydrography) from the total velocity. As expected, ageostrophic currents are found in the surface and bottom boundary layers. When the upwelling favourable winds prevail in summer, intense offshore velocities are found in the top 40 m due to the Ekman drift. Surface particles get advected offshore into a region of intensified mesoscale activity. In EBUS, surface EKE generally increases as one goes offshore through the coastal transition zone but remains low at depths (*Capet et al.*, 2008b). In the SBUS, intrusions of warm waters from the Agulhas Current in the form of eddies and filaments sustain high levels of EKE at depths (*Veitch et al.*, 2009; *Veitch and Penven*, 2017). This high EKE pattern is generated by eddies and filaments being

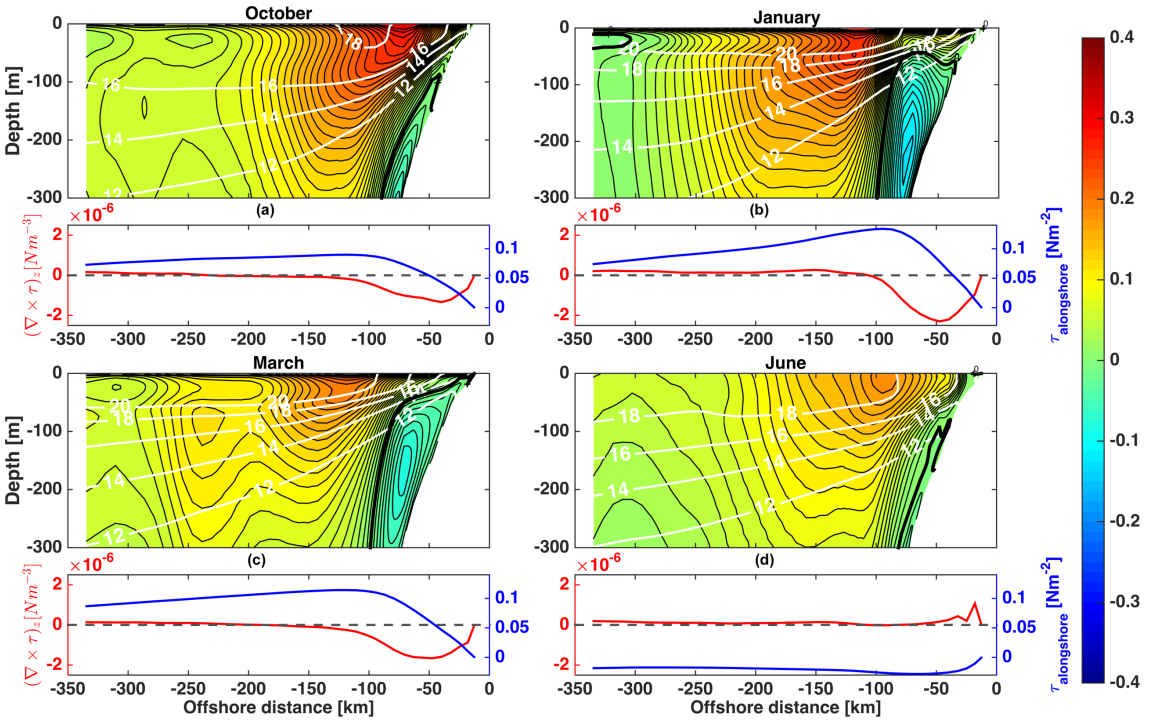

Figure 4.12: (Top): Grotto Bay vertical transect of alongshore velocities (color in m s^{-1}) and isotherms (white contours with contour spacing of 2°C). Contours of the current intensity are also superimposed (black) with a contour pacing of 1 cm s^{-1} and the zero contour in thick. (Bottom): The alongshore wind stress (blue) and z-component of the wind-stress curl (red) are superimposed for each across-shore transect, with the zero line (black dashed). Quantities are the monthly climatologies for: (a) October; (b) January; (c) March; (d) June.

directly injected in the system from the Agulhas retroflection region and/or being formed from baroclinic/barotropic instabilities of the jet itself. This is clearly observable off Grotto Bay in winter, when the absence of upwelling allows these intrusions to progress near the coast (Fig.4.14). In summer, these intrusions still happen but progress more offshore, beyond the upwelling density front. However, peaks of surface EKE can still be observed within the top 100 m of the water column in the first 200 km nearshore band. These peaks are linked to barotropic/baroclinic instabilities of the different branches of the jet. One peak coincides with the offshore anticyclonic part of the surface jet, whereas the inshore peak coincides with the poleward undercurrent.

4.6 Discussion and conclusions

Lagrangian experiments, based on a 22 years (1989-2010) interannual simulation of the oceanic circulation in the SBUS, are used to describe the alongshore connectivity between Cape Point and St Helena Bay. *Hutchings* (1992) had previously pointed out the existence of an alongshore corridor followed by fish eggs and larvae that were spawned on the Agulhas Bank. A series of Lagrangian studies had then linked this corridor with the existence of the Benguela Jet, a shelf edge equatorward current (*Blanke et al.*, 2009; *Veitch et al.*, 2017).

This study confirms that successful particles leave the SARP line, *i.e.* the transect off Cape Point, and progress northward embedded within the Benguela Jet. Nevertheless, the latter intensifies during the upwelling season, while transport success decreases during this period. This brings to light that other dynamical processes impact Lagrangian transports. Wind-induced across-shore Ekman transport, offshore mesoscale instabilities, Agulhas intrusions in the form of eddies and filaments combine together with the complex structure of the alongshore jets to transport particles towards St Helena Bay. The across-shore position of the jet, its intensity, its orientation relative to the coast and its bifurcation also play a key role and need to be taken into account when quantifying the alongshore connectivity.

We have shown that there is an efficient fast inshore route during late winter and early spring that is facilitated when the surface equatorward alongshore jet is in the form of one

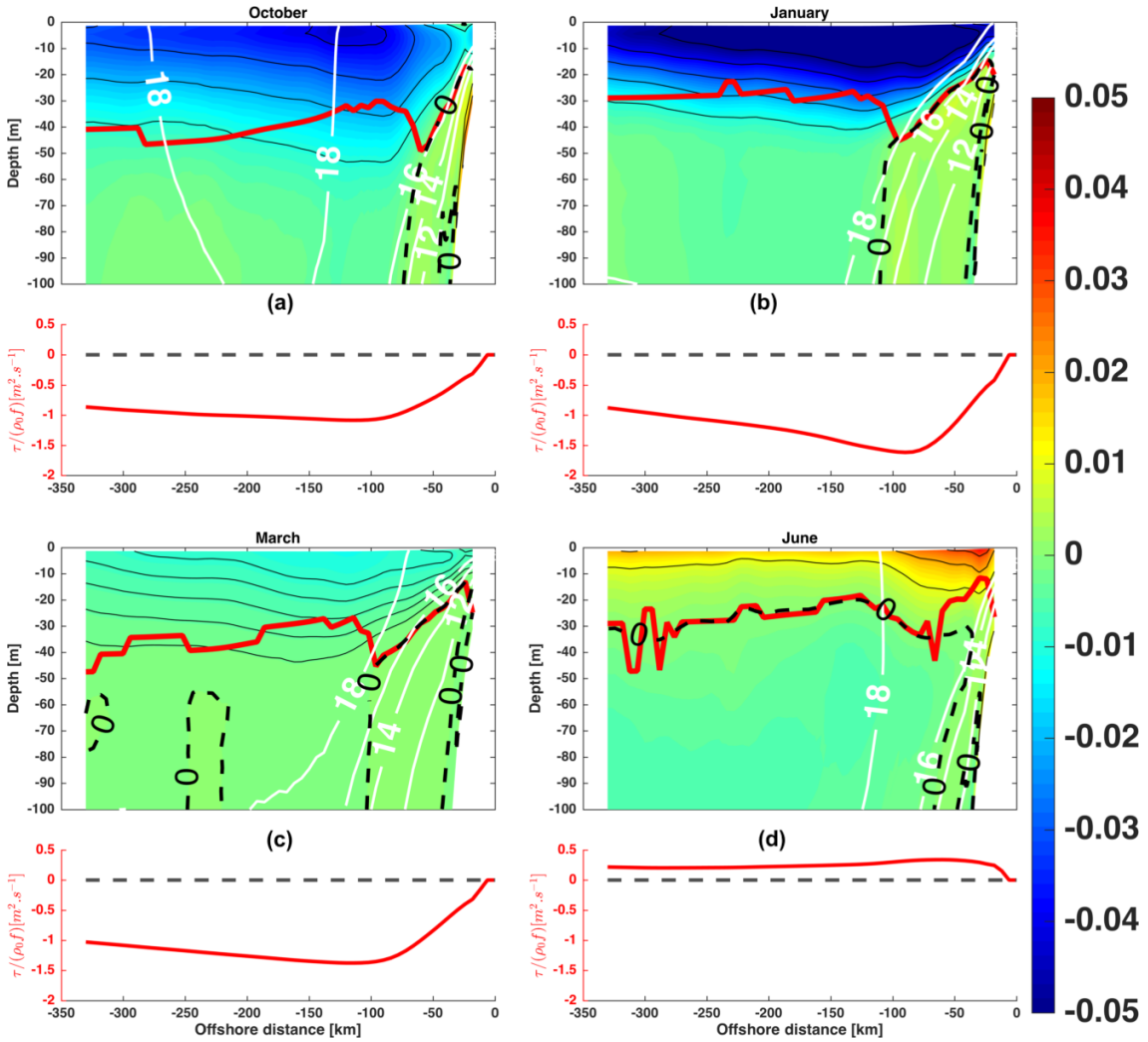

Figure 4.13: (Top): Grotto Bay vertical transect of across-shore ageostrophic velocities (color in m s^{-1}) and isotherms (white contours with contour spacing of 2°C). Contours of the current intensity are superimposed (black) with a contour spacing of 1 cm s^{-1} (zero contour in thick). The depth of the Ekman layer (m), computed after matching the vertical integration of the ageostrophic velocity with the total across-shore Ekman transport ($\tau_{alongshore}/(\rho f)$) is also superimposed in red. (Bottom): The across-shore Ekman transport along each across-shore transect (red) , with the zero line (black dashed). Quantities are the monthly climatologies for: (a) October; (b) January; (c) March; (d) June.

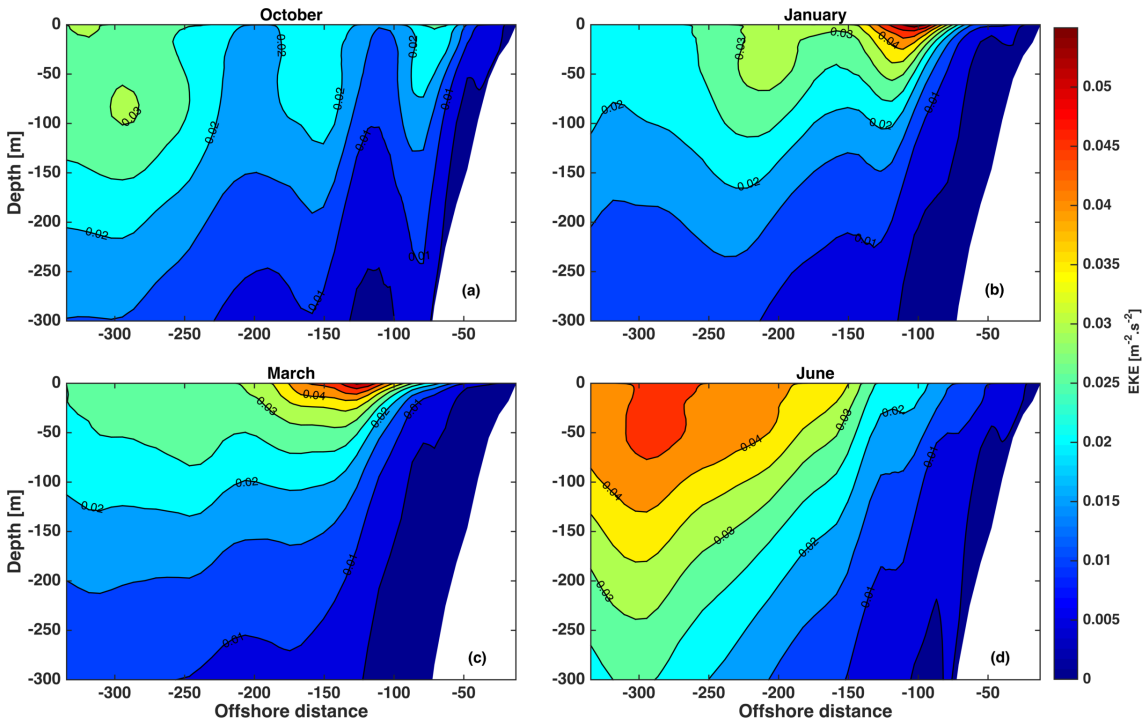

Figure 4.14: Grotto Bay vertical transect of monthly climatology of EKE (color in m^2 s^{-2}) for: (a) October; (b) January; (c) March; (d) June.

coherent intense nearshore branch. At this time of the year, transport success between Cape Point and St Helena Bay is at its highest rate (30%), and mainly involves particles initially released within the nearshore band delimited by the 300 m isobath: 90% of these latter particles are successfully transported to St Helena Bay in less than 15 days following a laminar route with little across-shore dispersion.

When the prevailing upwelling favourable winds start blowing consistently, transport success decreases continuously until it reaches its lowest value (15%) at the end of the upwelling season (March). Previous studies have attributed this decrease to an offshore loss of particles induced by a peak in the offshore wind induced Ekman drift. Our study shows that a reduced transport success can also be linked to a change in the structure of the equatorward jet. This occurs when the jet is shifted offshore towards a region of higher EKE, and particles are then more likely to fall within mesoscale features such as eddies or filaments and to get dispersed offshore. At this time of the year, the fast inshore successful route still exists, but becomes less likely than other offshore routes. Particles

taking these offshore routes have a longer journey towards the target area (> 20 days).

This study confirms that the offshore deviation of the Benguela Jet is linked to the poleward undercurrent intensification and shoaling (*Veitch et al.*, 2017). During the upwelling season, the wind drop-off within the first 100 km coastal band (due to the contrast in the land/sea drag coefficient) induces injection of negative cyclonic wind stress curl within the water column. The core of the poleward undercurrent thickens and outcrops to the surface, inducing the branching of the surface jet and/or a surface counter current in the nearshore band. This branching directly impacts the transport success, as successful particles follow the inshore branch. To do so, they must already be located within the inshore cyclonic side of the jet's core at the latitude of the jet's bifurcation. We have also shown that wind-induced Ekman surface drift acts on the particles either to keep them within the inshore side of the current in winter or to push them further offshore in summer. In summary, our simulations identified an efficient inshore pathway taken by particles in spring. This period is the optimal window, as the jet is in its intensified state, close to the shore, and relatively stable. At this time of the year, offshore Ekman transport is still low enough to allow particles to remain on the inshore side of the jet. The core of the poleward undercurrent remains located deeper than 100 m depth and therefore does not trap any particles.

One may question the limitations of this work in terms of realism of the ocean circulation model, and argue about the robustness of our results if carried out with a higher resolution model. Increasing the model resolution may certainly lead to a better representation of the bathymetry, in particular in regions with steep slopes, which may in turn modify the jet's positions and intensity, and therefore impacts the absolute values of transport success. However, we believe that the seasonal cycle of transport success and the processes that lead to it would still hold.

The characteristics of the jet in the 7.5 km interannual simulation, with the bifurcation and branching into multiple cores, are consistent with observations. The separation of the jet off Cape Columbine was pointed out in *Fowler and Boyd* (1998). *Shannon and Nelson* (1996) (their fig. 20) found a double-core jet off Cape Point. The two cores were

respectively located over the 100 m and 300 m isobath and separated by the shoaling of a poleward undercurrent. Additionally, the seasonal cycle of transport success is intimately related to the seasonal cycle of the Benguela Jet itself. The latter is in thermal wind-balance with the across-shore temperature gradient. Coarser simulations, forced with a monthly seasonal climatology wind, already had the ability to reproduce the seasonal cycle of this gradient just because they could reproduce the seasonality of the coastal upwelling (*Penven et al.*, 2001; *Veitch et al.*, 2017). Lagrangian studies based on these simulations found a seasonal cycle of transport success similar to ours (*Parada et al.*, 2003; *Huggett et al.*, 2003; *Mullon et al.*, 2005). The main difference concerned the winter particles that had a higher chance of reaching St Helena Bay than in our simulations (*Huggett et al.*, 2003), probably because inshore Ekman transport kept particles within the inshore jet, and the latter had less seasonal variability.

Lagrangian experiments based on a higher resolution simulation are expected to provide new insights on the role of (sub-)mesoscale turbulence on the dispersion of particles. Future studies should analyse this variability in detail using a higher resolution ($\preceq$ 3 km) nested simulation embedded within the 7.5 km simulation described here. Combining a better resolution of the innershelf dynamics together with a high-frequency atmospheric forcing should also lead to a more subtle nearshore dynamics made of thin jets (*Gan and Allen*, 2002b,a) and inertial waves (*Simpson et al.*, 20021; *Lucas et al.*, 2014).

This study has helped us identify some of the physical processes important for the dispersal of fish larvae in the SBUS. Our results show that being entrained within the fast inshore route taken by the Benguela Jet and avoiding being carried offshore when the jet splits into several branches are two major drivers of the connectivity between the spawning and nursery grounds. They must be considered as two important components of the fish reproductive strategy in the Southern Benguela. Finally, this study shows that successful transport from the Agulhas Bank to the west coast upwelling region cannot be attributed to only a simple wind induced modulation of the jet, as mentioned in previous studies. The seasonal characteristics of transport success result from the complex interactions of the Benguela Jet, the poleward undercurrent and the offshore Ekman transport together

with the turbulent off-shelf eddy field.

To conclude, it is important to recall that if the Lagrangian particles used for this study were to be considered as living larvae, transport success to the nursery grounds by the oceanic currents is only one of the factors that contribute to their survival. Other physical properties such as water temperature, vertical stratification, small-scale turbulence also strongly influence the growth rate of larvae, as well as their survival by affecting the availability, distribution and composition of the prey and predator field.

Chapter 5

The impact of downscaling on SBUS circulation and Langrangian pathways

5.1 Introduction

Chapter 4 underlined the importance of the Benguela Jet for the northward along-shore transport of particles from Cape Point to St Helena Bay. It also suggested that the presence of mesoscale eddies, mostly located offshore, beyond the 500 m isobath, could have a negative effect on this northward transport success. However, these results relied on a mesoscale eddy-permitting simulation with a horizontal resolution of 7 km. In the Southern Benguela Upwelling System (SBUS), the first baroclinic Rossby deformation radius is of the order of 35 km offshore and becomes as low as a few kilometers on the shelf. Therefore, many of the fine-scale dynamics that constitute the inertia range of the energy spectra (*Capet et al.*, 2008b) were not properly resolved in the reference simulation. The 7 km horizontal resolution was not sufficient to accurately represent the mesoscale eddies generated through the barotropic/baroclinic instabilities of the Benguela Jet (*Veitch et al.*, 2009), nor the complex structure of the innershelf circulation in depths less than 100 m.

In Eastern Boundary Upwelling Systems during the upwelling season, surface currents

are predominantly directed equatorward in thermal wind balance with the cross-shore density front resulting from the inshore upwelling of cold waters. Nevertheless, current reversals occur when the prevailing equatorward upwelling favourable winds relax. Usually, episodes of upwelling favourable winds and relaxation occur with a 2 to 4 day period. These events have been extensively documented for the California mid-shelf region characterised with depths beyond 100 m (*Send et al.*, 1987; *Winant et al.*, 1987; *Huyer and Kosro*, 1987; *Kosro*, 1987; *Largier et al.*, 1993; *Dever et al.*, 1998). They lead to strong poleward flows of tens of cm s^{-1} (*Cudaback et al.*, 2005; *Roughan et al.*, 2006). Inner-shelf current reversals have also been reported along the Iberian coast (*Relvas*, 2002) and in the SBUS (*Fawcett et al.*, 2008) where they can lead to increases of temperature up to $5°C$ day^{-1} in the very near-shore region in depths less than 50 m depth. The forcing mechanism for these nearshore poleward flows can either be the presence of a strong cyclonic wind stress curl due to the coastal wind drop-off or along shore pressure gradients that form in the presence of headlands, inside bays, during episodes of prevailing upwelling favourable winds (*Gan and Allen*, 2002a). When the equatorward along-shore wind stress relaxes, these pressure gradients are no longer balanced, which results in a poleward jet that flows around the headlands and transport some warm waters (*Gan and Allen*, 2002b; *Melton et al.*, 2009; *Washburn et al.*, 2011).

In this chapter, our goal is to study the differences in the coastal circulation and mesoscale turbulence that emerge when the model resolution is increased, and to highlight how a finer representation of the dynamics may affect the alongshore connectivity between Cape Point (34°S) and St Helena Bay (32°S). Our analysis focuses more specifically on the particles initialised in the nearshore coastal band (depth less than 200 m), where gains in the representation of the fine-scale coastal circulation are expected to be most significant when increasing the model resolution. We follow the same approach as in chapter 4. Lagrangian particles are released every 12 hours along a cross-shore transect off Cape Point and then followed for 30 days. However, the currents advecting the particles are now the outputs a 3-km horizontal resolution simulation nested into the reference configuration (7-km horizontal resolution: "BENGR15"). Like in chapter 4, we first focus on the physical processes that control the seasonal cycle of the along-shore northward

transport of particles. The analysis of the interannual variability is left to chapter 6. Sec-

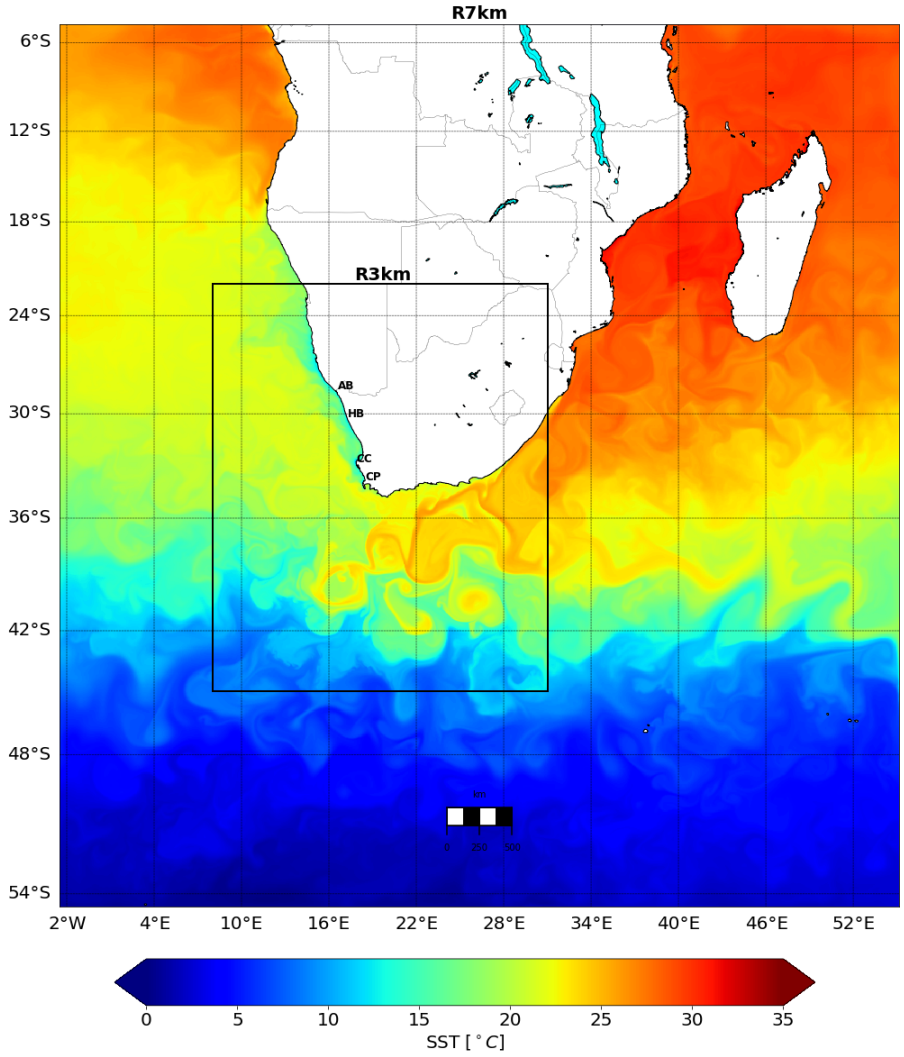

Figure 5.1: Snapshot of SST (Year 2005, 1st of January). The black box delineates the boundaries of the nested 3-km child grid. Within the box, the SST of the 3-km simulation is superimposed upon the one of the 7-km simulation.

tion 5.2 describes the new 3-km horizontal resolution nested simulation. Increasing the horizontal resolution improves the realism of the ocean circulation in the SBUS. The impact of model resolution on the mean circulation features and its variability are presented in section 5.3. The impact of model resolution on the Lagrangian pathways are then presented in section 5.5. Lagrangian experiments of particles advected with currents of the two simulations are carried out to investigate the impact of downscaling on transport success.

5.2 A 3-km resolution simulation of the SBUS

5.2.1 The design of an offline nested grid:

A new grid with a horizontal resolutions of 3-km and 75 vertical levels ($850 \times 691 \times 75$ grid points) is designed to encompass most of the coastal shelf waters of South Africa and to include the region of the Agulhas Current retroflection. This new domain is embedded within our reference 7-km grid (Fig. 5.1). It extends from 45°S to 22.5°S and from 8°E to 30°E. Due to computational cost, the number of vertical levels of the 3-km resolution simulation is reduced to 75 sigma levels, instead of 100 in the 7-km reference simulation (Fig. 5.3).

Bathymetry

The bathymetry of our new configuration is built following the same methodology as for our reference simulation (Chapter. 3). The 1-min global dataset provided by the Shuttle Radar Topography Mission (*Smith and Sandwell*, 1997) is interpolated on the new 3-km grid, and smoothed out so that the steepness of the topography ($r = \frac{\delta h}{2h}$) does not exceed 0.2 (*Beckmann and Haidvogel*, 1993). Because the smoothing is dependent on the model grid resolution, the 3-km nested grid allows for some fine scale features to be better represented (Fig. 5.2), both along the shelf edge and offshore. In the 7-km configuration, the Cape Canyon which extends south-west of Cape Columbine was almost completely smoothed out. In the 3-km configuration, it has a clear signature. Cross-shore transects off Cape Point also show some serious impact on the shelf slope. Two shelf breaks can be distinguished in the 3-km simulation at 30 km and 80 km offshore respectively, whereas in the 7-km configuration, the continental slope plunges smoothly towards depth (Fig. 5.3). Because along-slope jets are usually constrained by the iso-contours of constant planetary potential vorticity (f/h contours), these modifications of the across-shore shelf slope are expected to impact strongly the positions of the along-slope jets. In addition, isolated seamounts between the Agulhas bank and Agulhas ridge, the west-southwest/east-northeast orientated ridge that bounds the Cape Basin at southern latitudes, do not get smoothed out within the 3-km resolution grid. The latter are expected to play a large role in the leakage of Agulhas waters into the Cape Basin because of they

are on the main trajectory of the Agulhas rings (*Arhan et al.*, 1999; *Schouten et al.*, 2000).

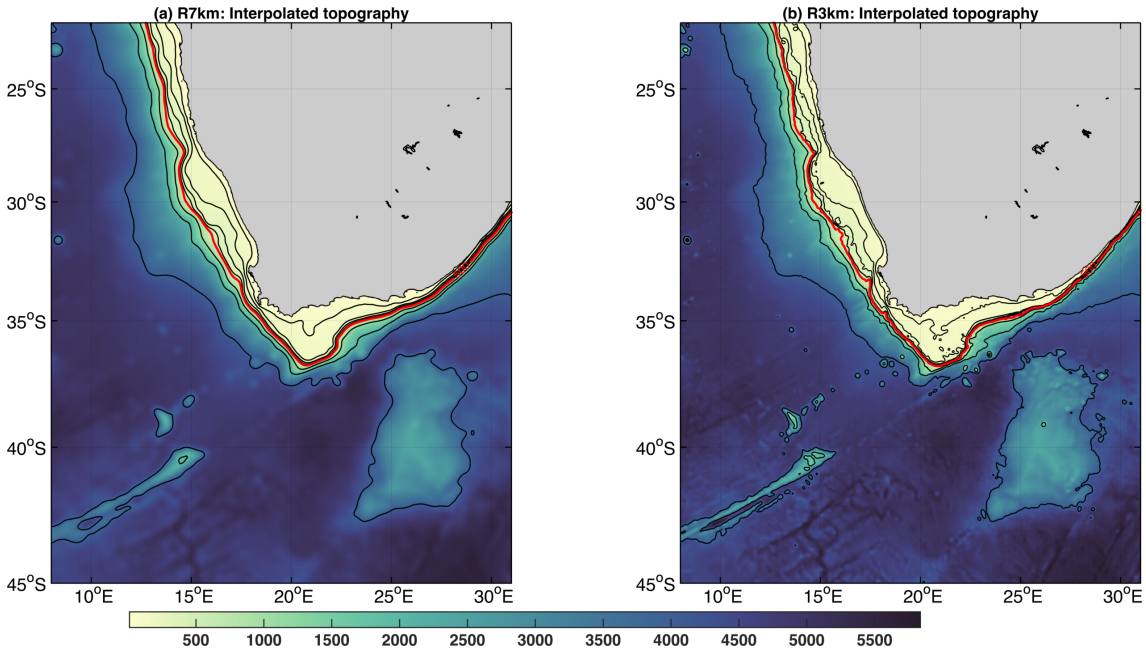

Figure 5.2: Model bathymetry for the reference configuration (R7km) and the nested domain (R3km)

One way nesting at the lateral boundaries:

A one-way nested approach is employed using the roms2roms algorithm (*Mason et al.*, 2010). While the lower resolution parent grid supplies boundary conditions to the higher resolution child domain, there is no feedback from the child to the parent. In the following, we use a daily-average archive of all prognostic variables (u, v, η, T, S) from the R7km reference simulation (Chap. 3) to specify the momentum, heat and fresh-water fluxes at the boundaries of the 3-km resolution simulation.

Surface forcing

For consistency, both simulations were identically forced at the surface with the same 6-hourly atmospheric forcing (heat, fresh and momentum fluxes) provided by CFSR at 0.3°horizontal resolution (*Saha*, 2010).

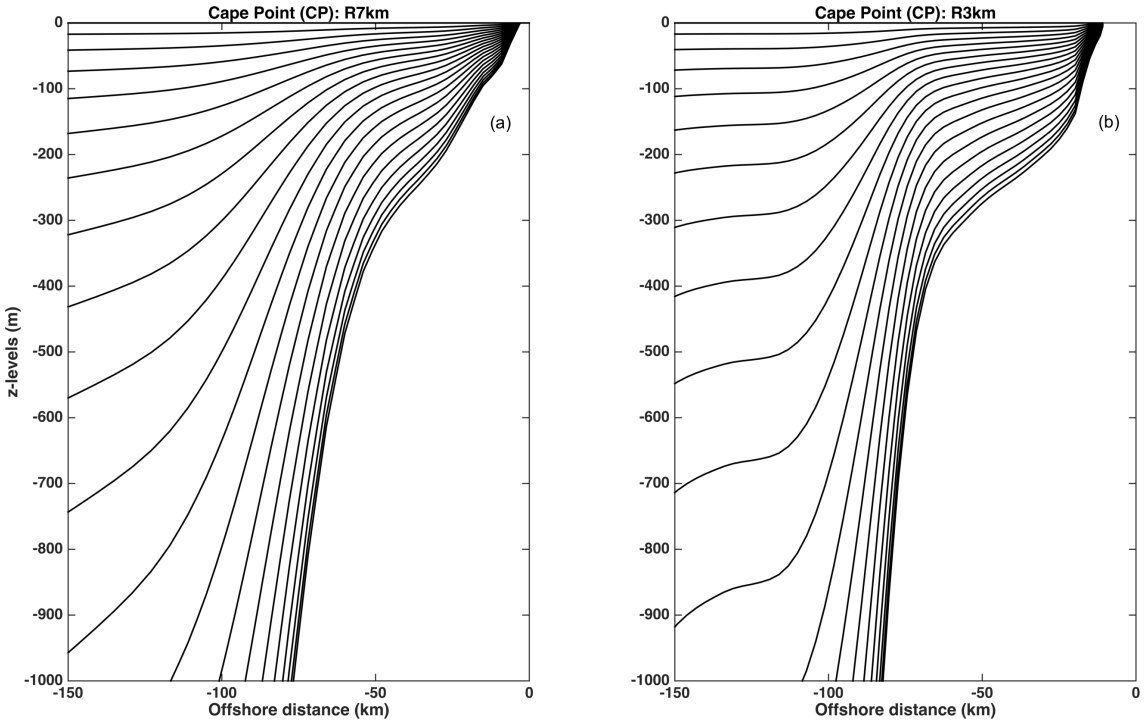

Figure 5.3: Cross-shore transects of vertical levels off Cape Point in the (a) R7km and (b) R3km model, plotted for every fifth level.

Initial condition and time integration

To have a coherent set of simulations, the R7km was run again and saved at a daily rate instead of 3 days. The 3-km resolution simulation is initialised on 1st January 1990 after interpolating the daily average archive of the 7-km simulation onto the new grid. The new simulation is run from 1989 to 2011, and daily averages of all variables of interest are archived. Our analysis focuses on the 1992-2011 period after discarding the first three years to avoid spurious dynamics related to adjustment processes. A three years spin-up phase was considered to be long enough to reach a statistical equilibrium. Some of the key parameters of the two simulations are summarised in table 5.1. Hereafter, these two simulations are referred to as R7km for the reference 7-km resolution simulation, and R3km for the new 3-km resolution simulation.

5.3 Impacts of the horizontal resolution on the circulation

Before testing the impact of the horizontal resolution on the Lagrangian pathways of particles in the SBUS, it is necessary to assess the differences in the representation of

Simulations	**R7km**	**R3km**
Domain	54°S-6°S; 2°W-54°E	45°S-22.5°S; 8°E-30°E
Grid points	909x866	850x691
σ-levels	100	75
Output frequency	Daily	Daily
Run period	1989-2011	1992-2011
Surface forcing	CFSR 6h 0.3°	CFSR 6h 0.3°
Lateral forcing	SODA 2.3.2	R7km
Bathymetry	SRTM 30 plus	SRTM 30 plus

Table 5.1: Summary of model configuration for the R7km and R3km simulations.

circulation between the R7km and R3km simulations. This section therefore compares the SST, SSH, surface currents and EKE between the two simulations and some observations.

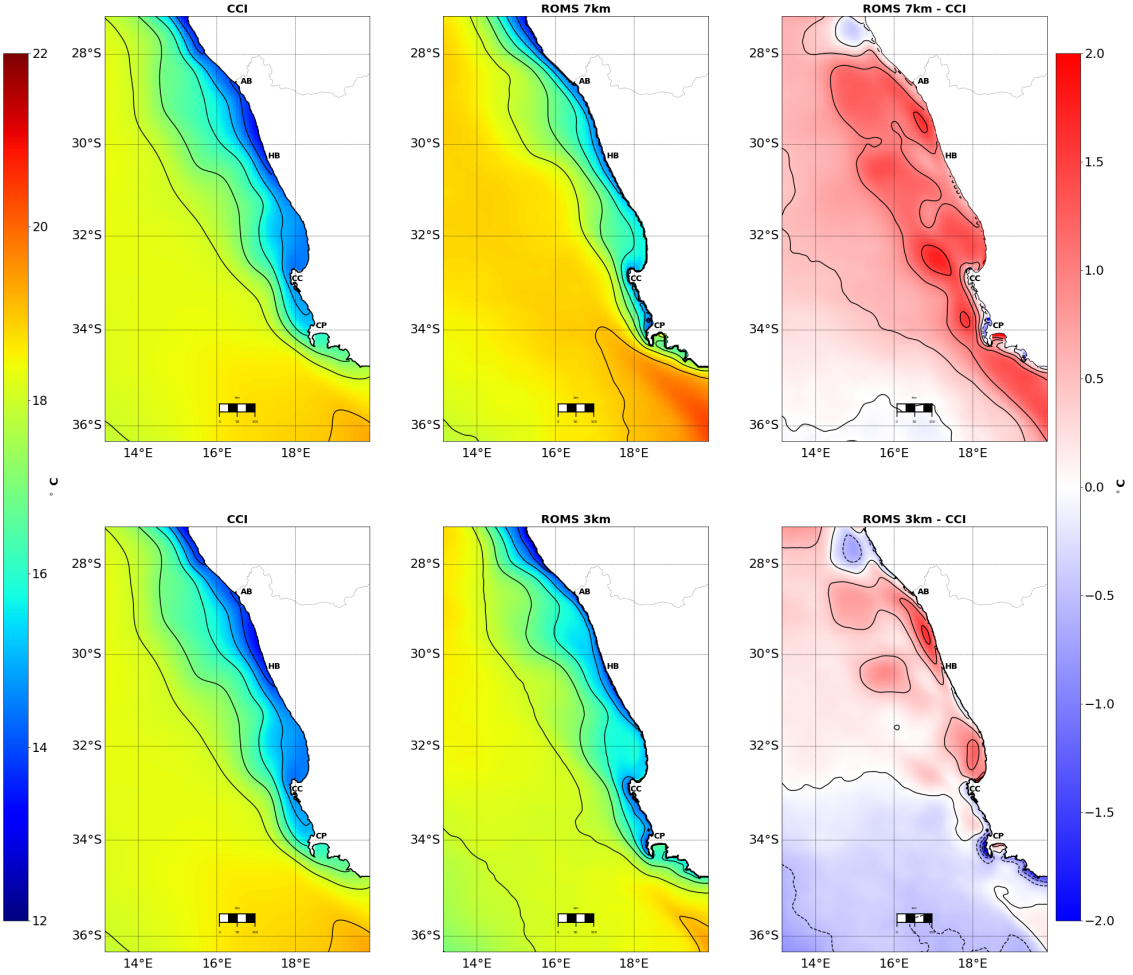

Figure 5.4: Annual average (2005-2012) of merged satellite CCI SST (left), model SST (centre), and SST bias [SST_{model} - SST_{CCI}] (right). SST contours are superimposed (black solid) with a 1°C contour interval. Top panels are for the R7km simulation whereas bottom panels are for the R3km simulation.

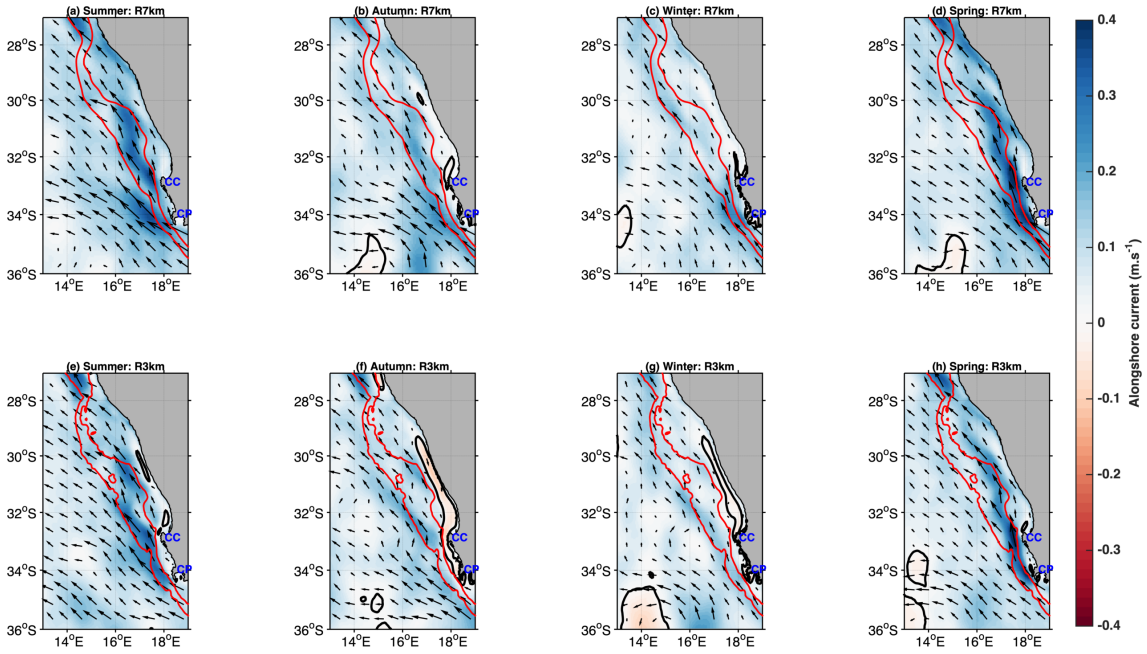

Figure 5.5: Maps of the seasonally averaged alongshore component of surface currents for the R7km simulation (Top panel a-d) and R3km simulation (Bottom panel e-h). The colorbar represents the magnitude of the alongshore component of the velocity vector in m s^{-1}. Current vectors are superimposed, as well as the 200 m and 500 m isobaths (red solid line).

5.3.1 Reduction in the warm bias of the coastal waters

The warm bias of the modelled SST is significantly reduced both in amplitude and spatial extension in the finer resolution R3km simulation (Fig. 5.4). It is now mostly confined to an innershelf coastal band over depths less than 200 m, and does not exceed 0.5°C in the offshore domain. Note that this warm bias is also reduced for the coastal sub-surface waters located off the continental slope (not shown). The tongue of warm water (>19°C) from the southern boundary is located further south in the R3km simulation as in the satellite observation than in the R7km simulation where it extends to 34°S. This suggests that there is a reduction in the warm Agulhas water influx in the higher resolution which could explain the reduction the warm bias in the offshore domain.

5.3.2 A narrower and smaller Benguela Jet

The simulated mean surface currents look quite similar in the two simulations (Fig. 5.5) and compare well with the surface currents derived from altimetry. The Benguela Jet that played a key role in the advection of particles from Cape Point to Cape Columbine in the R7km simulation is also present in the R3km simulation. However, it is narrower and more confined over the shelf-edge. This confinement of the jet over the 200 m - 500 m isobaths is even more pronounced in summer, between Cape Point and Cape Columbine. In the R3km simulation, the jet follows the shelf edge whereas, in the R7km simulation, it veers offshore and splits into two branches. At the seasonal time scale, the core of the jet coincides with the location of the maximum across-shore SST gradient in both of our simulations as observed in the satellite data (Fig. 5.6). This is in accordance with the findings of *Veitch and Penven* (2017) and shows that the main dynamical ingredients that control the seasonal cycle of the Benguela Jet are likely to be correctly reproduced in both simulations. In addition, in both simulations, the jet exhibits a similar seasonal cycle coherent with the observations. Its intensity peaks at 0.45 m s^{-1} in spring and summer and weakens to 0.1 m s^{-1} in winter.

Some clear differences between the two simulations can be observed in the across-shore and vertical structure of this equatorward jet (Fig. 5.7). In the R7km simulation, the Benguela Jet is characterised by higher speeds than in the R3km simulation. Its core extends further offshore (200 km in R7km versus 100 km in R3km) and deeper (-300 m in R7km versus -100 m in R3km). Note that this confinement of the Benguela Jet closer to the surface is accompanied by an the uplift of the isotherms, which reduces the sub-surface warm bias to almost zero below -30 m.

5.3.3 The presence of poleward jets

Maps of surface currents reveal the existence of a nearshore poleward flow in the R3km simulation only (Fig. 5.5) in agreement with insitu measurements (*Nelson*, 1989). This poleward surface countercurrent is evident all along the coast up to 29°S during summer and autumn. Its speed peaks at 0.1 m s^{-1} at the locations of the upwelling cells. Vertical transects off Cape Point show that this surface countercurrent results from the surfacing of

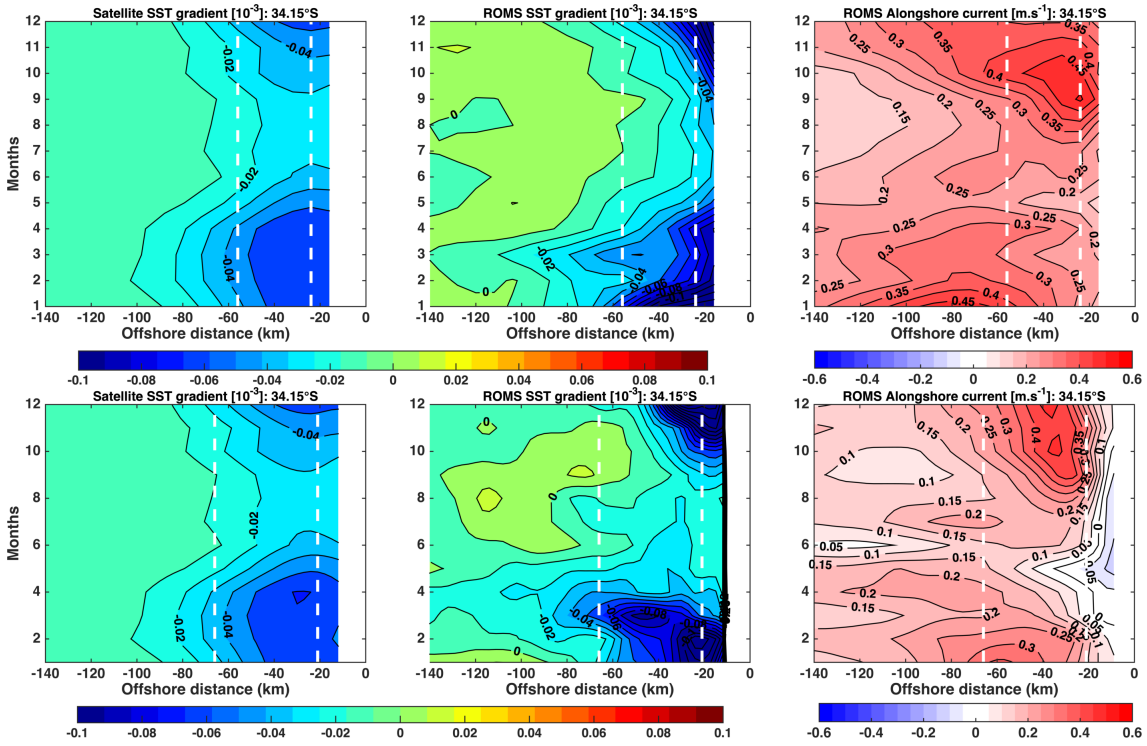

Figure 5.6: Hovmller plot of: satellite (left), model (middle) across-shore climatological mean SST gradient off Cape Point (34.15°S), and model monthly climatological mean of surface alongshore current (right panel) for the 7-km (top) and 3-km (bottom) simulations. The contour interval for the SST gradient and model velocity are 0.01°C km^{-1} and 0.05 m s^{-1} respectively. The location of the 200 m and 500 m isobaths are shown as white dashed lines.

a subsurface poleward jet (Fig. 5.7). The core of this poleward flow is located in between -50 m and -100 m depth (within 50 km offshore), which distinguishes it from the all year round persistent poleward undercurrent located on the shelf slope around -500 m depth. The physical mechanisms driving this poleward nearshore current were not studied in this thesis. Additional analysis would be required to disentangle the role of the cyclonic wind stress curl associated with the coastal wind drop-off, bottom friction, and modified bottom topography. Across-shore transects of alongshore currents (Fig. 5.7) show that this subsurface poleward flow is also present in the lower resolution R7km simulation. However, it is weaker than in the R3km simulation. Its core is also narrower and never shallows enough to reach the surface.

5.3.4 Impacts of the horizontal resolution on the mesoscale turbulence in the SBUS

Two different mechanisms for the offshore and inshore oceanic turbulence

Despite some differences, the large scale patterns of surface EKE (Fig. 5.8) look similar in both simulations. The offshore region is characterised by large EKE values, a testament to the passage of Agulhas rings and eddies. In the vicinity of the shelf-edge, some pockets of large EKE values can still be observed in the R3km simulation. Nevertheless, they tend to be more localised to the lee of Cape Point and Cape Columbine and mainly occur during summer and autumn. These large EKE values observed over the shelf-edge are likely to be generated by a different mechanism, *i.e.* the barotropic/baroclinic instabilities of the across-shore density front reinforced during the upwelling season. Therefore, the phenomenology of the mesoscale turbulence is likely to be different between the offshore and nearshore region. Snapshots of surface relative vorticity[1] ξ (Fig. 5.9) and temperature (not shown) show that offshore eddies are much larger than nearshore eddies. The former are a mixed of large ($R_v \simeq 100$ km) anticyclonic eddies associated with a warm signature in SST and smaller ($R_v \simeq 50$ km) cyclonic eddies (Fig. 5.9), both kinds originating predominantly from the Agulhas retroflection. On the other hand, the more inshore located mesoscale eddies originate from the shelf-edge.

[1] $\xi = \delta_x v - \delta_y u$

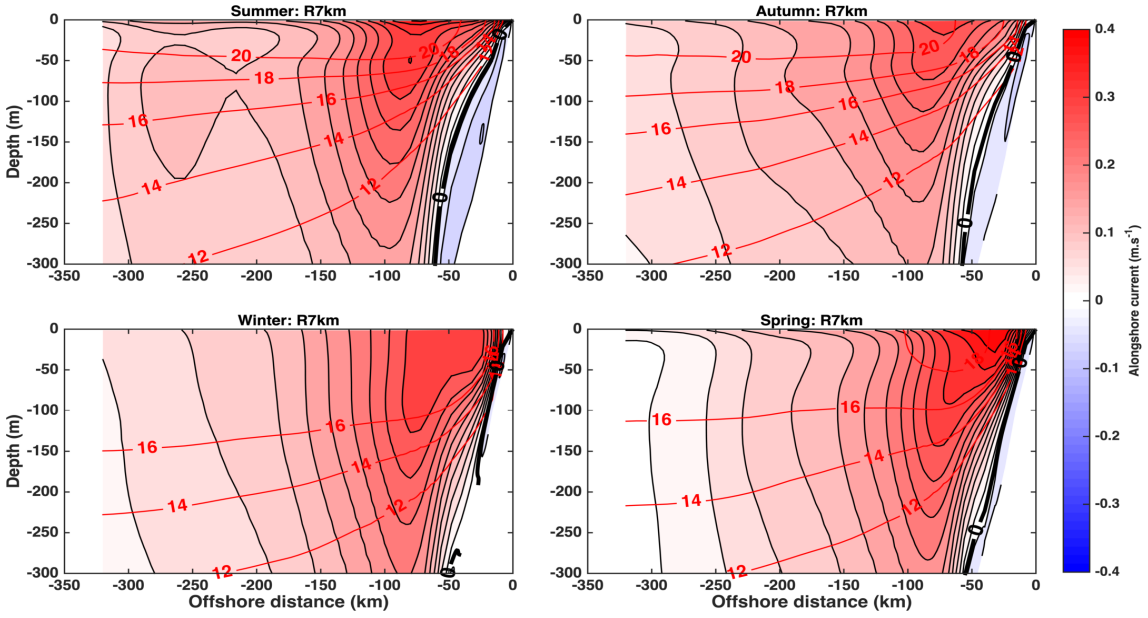

(a)

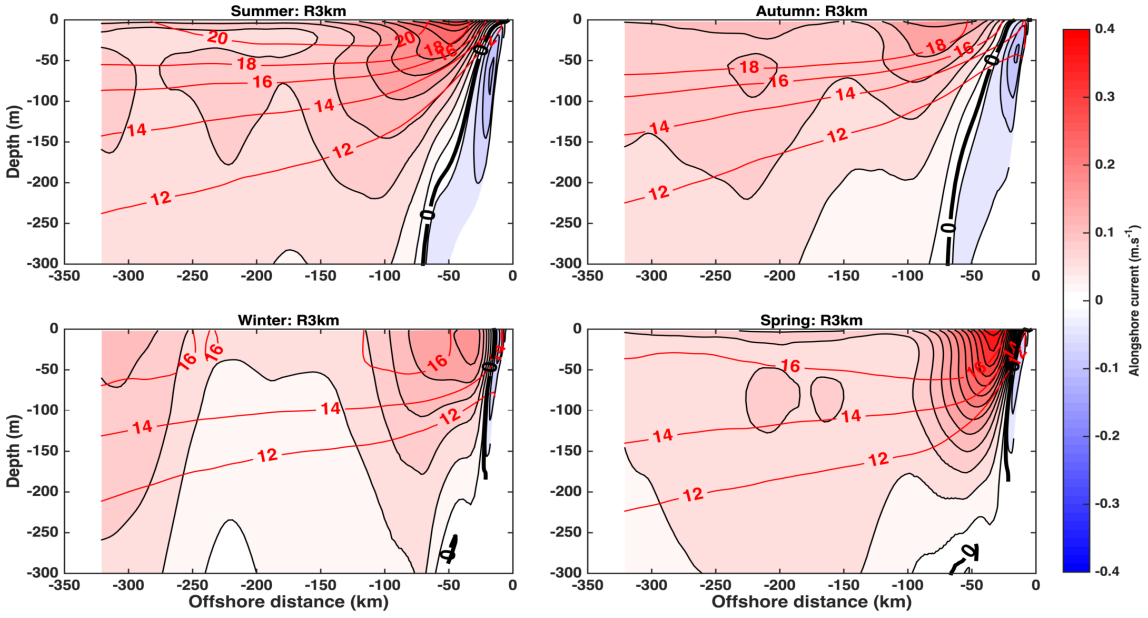

(b)

Figure 5.7: Vertical across-shore transects off Cape Point of the seasonally averaged alongshore component of the model current vector (colorbar in m s^{-1}) from the R7km (a) and R3km (b) simulation. Velocity/temperature iso-contours (black thin/red solid)are superimposed with a 0.1 m s^{-1}/2°C contour spacing.

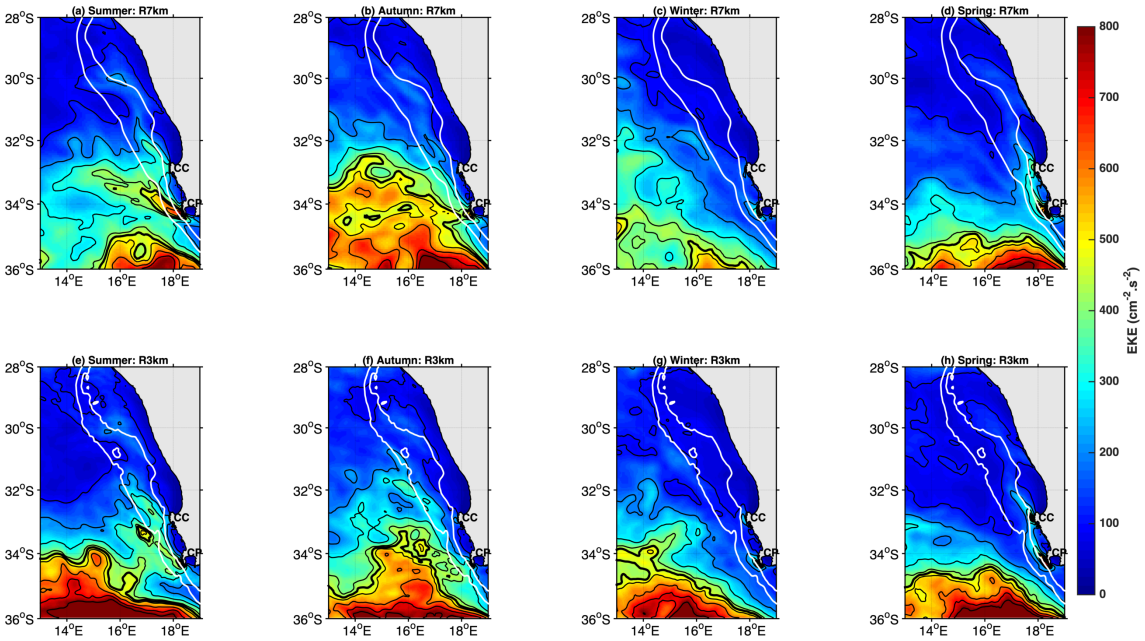

Figure 5.8: Comparison of seasonally averaged surface Eddy Kinetic Energy (EKE) for the: R7km simulation (Top panel a-d) and R3km simulation (Bottom panel e-h). The 450 cm^2 s^{-2} contour is shown in black bold line to delimit the extension of the high values of EKE typically found in region affected by the Agulhas Current retroflection. The 200 m and 500 m isobaths are shown as white lines.

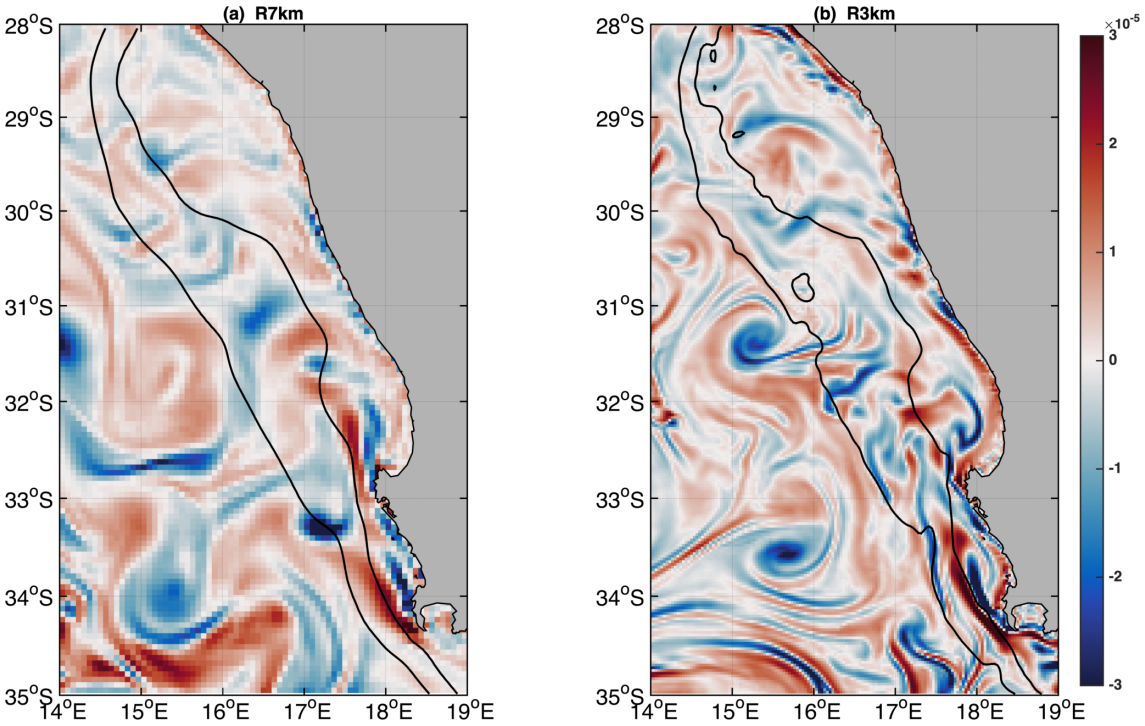

Figure 5.9: Snapshots of surface relative vorticity anomaly in the (a) R7km and (b) R3km simulation on the 1st of October 2010.

Vertical across-shore transects of EKE also reveal some striking differences between the vertical extension of inshore and offshore eddies. The offshore EKE patch extends much deeper than the inshore EKE patch as shown by the 300 $cm^2\ s^{-2}$ EKE contour (Fig. 5.10). In the R3km simulation, the latter contour is found as deep as -300 m offshore whereas as it is confined to the first 150 m of the water column on the shelf edge. In addition, the position of the inshore patch coincides with the very localised region situated at the interface between the core of the Benguela Jet and the core of nearshore sub-surface poleward current. This area is likely to be favourable for the occurrence of barotropic/baroclinic instabilities. In the following, we choose the 450 $cm^2\ s^{-2}$ surface EKE contour (Fig. 5.8) to delineate the region directly influenced by the very energetic turbulence originating from the Agulhas Current retroflection (*Loveday et al.*, 2014) from the inshore region impacted by the instabilities of the along-shore coastal jets. The two regions appear more clearly separated in the higher resolution simulation: the isoline gets much closer to the shelf in the R7km simulation than in the R3km simulation, in particular during summer and autumn when large EKE values are also found nearshore.

The presence of finer and more intense mesoscale eddies

As expected, the intensity of the mesoscale eddies increases when the resolution is increased from 7-km to 3-km, especially in the offshore turbulent region, referred to in the literature as the 'Cape Cauldron' (*Boebel et al.*, 2003) (Fig. 5.8b). This intensification is visible both in the mean EKE values observed offshore and the absolute values of relative vorticity found within these eddies. It could be attributed to the enhancement of the dynamical potential vorticity barrier that surrounds mesoscale eddies and prevents them from being deformed and/or destroyed by other neighbouring eddies. Consequently, eddies become more coherent and live longer (*Lévy et al.*, 2010, 2012).

As expected, spatial spectrum of vorticity and EKE (not shown) show that the slope of spectrum in the inertia range decreases as the spatial resolution increases, with cut-off wave number shifting towards larger values (20 km in R3km versus 50 km in R7km) confirming the presence of finer scale circulation features.

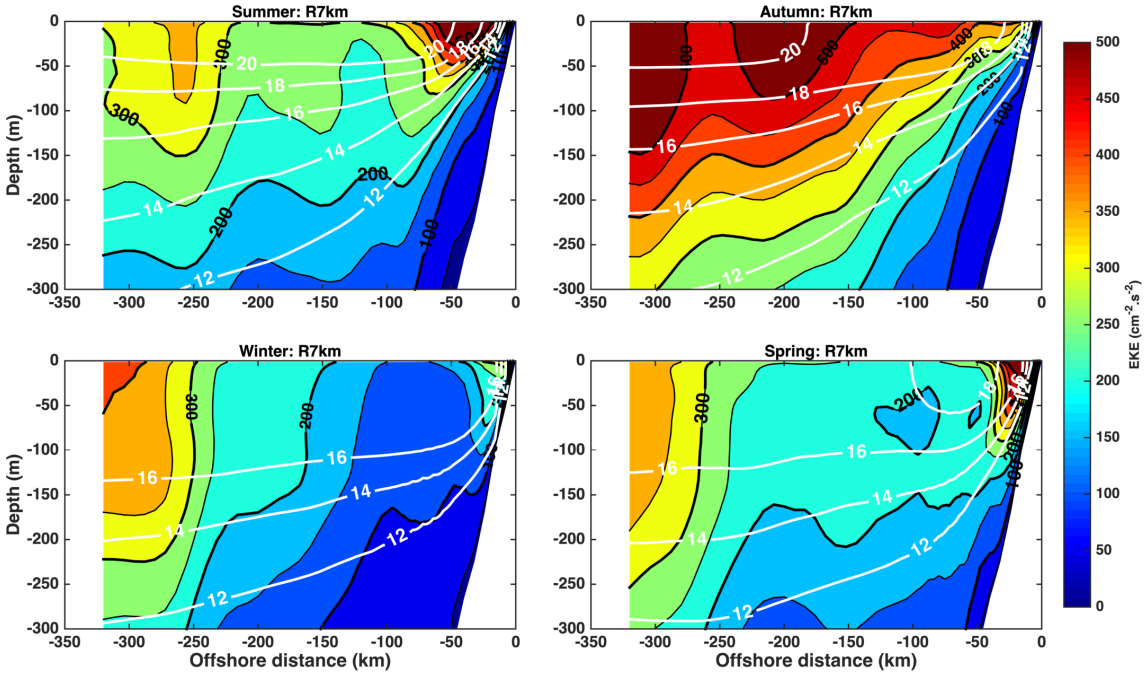

(a)

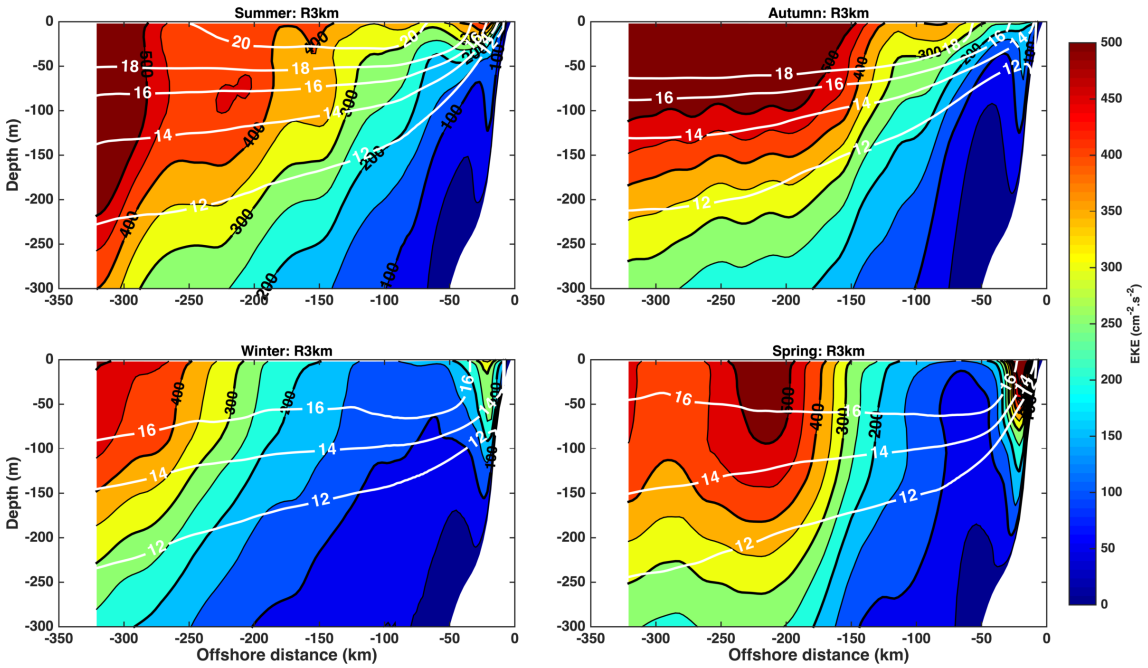

(b)

Figure 5.10: Same as Figure 5.7 but for EKE. Units in $cm^{-2}.s^{-2}$ and the contour interval is 50 cm^2 s^{-2}. Temperature contours are also superimposed in white with contour interval of 2°C.

5.3.5 An unexpected impact on the Agulhas leakage

Increasing the model resolution from 7-km to 3-km has led to a better representation of the cross-shelf temperature gradient and has reduced the warm bias between simulated and observed temperature both for surface and sub-surface waters (Fig. 5.4). The following section intends to show that a reduction of the volume of Agulhas waters leaking into the Cape Basin in the higher resolution simulation could explain the presence of colder water offshore.

Quantifying the Agulhas leakage into the Cape Basin is challenging due to its turbulent nature. The latter occurs predominately through the shedding of Agulhas rings at a rate of 5-6 per year (*Schouten et al.*, 2000; *van Aken et al.*, 2003; *Doglioli et al.*, 2006). In fact, each eddy transports large volumes of Indian Ocean waters, typically 0.5-1.5 Sv per eddy. Numerous attempts have been made to estimate this leakage using both Lagrangian (*Donners and Drijfhout*, 2004; *Doglioli et al.*, 2006; *Speich et al.*, 2006; *Richardson*, 2007; *van Sebille et al.*, 2010; *Durgadoo et al.*, 2013; *Rhüs et al.*, 2013) and Eulerian (*Gordon*, 1986; *Gordon et al.*, 1987; *Garzoli and Goni*, 2000; *Boebel et al.*, 2003; *Reason et al.*, 2003; *Treguier et al.*, 2003; *van Sebille et al.*, 2009, 2010; *Loveday et al.*, 2014) methods. Estimations vary from 10 Sv to 41 Sv, but mostly fall in the range of 10-20 Sv with a large uncertainty.

Here, the Agulhas Current leakage into the SBUS is estimated by calculating the volume transport using the monthly climatological mean meridional velocities across a zonal transect taken at 35°S hereafter referred to as the southern boundary line (SBL). The velocities are integrated over the top 1000 m of the water column between 12°E and 18°E. The estimated value of the meridional transport is relatively higher in the 7-km reference simulation where it is 18.3 Sv and 16.3 Sv in the 3-km resolution simulation. Both estimates fall within the mostly observed 10-20 Sv range (*Gordon*, 1986; *Gordon et al.*, 1987; *Garzoli and Goni*, 2000; *Boebel et al.*, 2003; *Reason et al.*, 2003; *Treguier et al.*, 2003; *van Sebille et al.*, 2009, 2010; *Loveday et al.*, 2014).

The heat transport is also estimated across the SBL transect and Fig 5.12 shows the

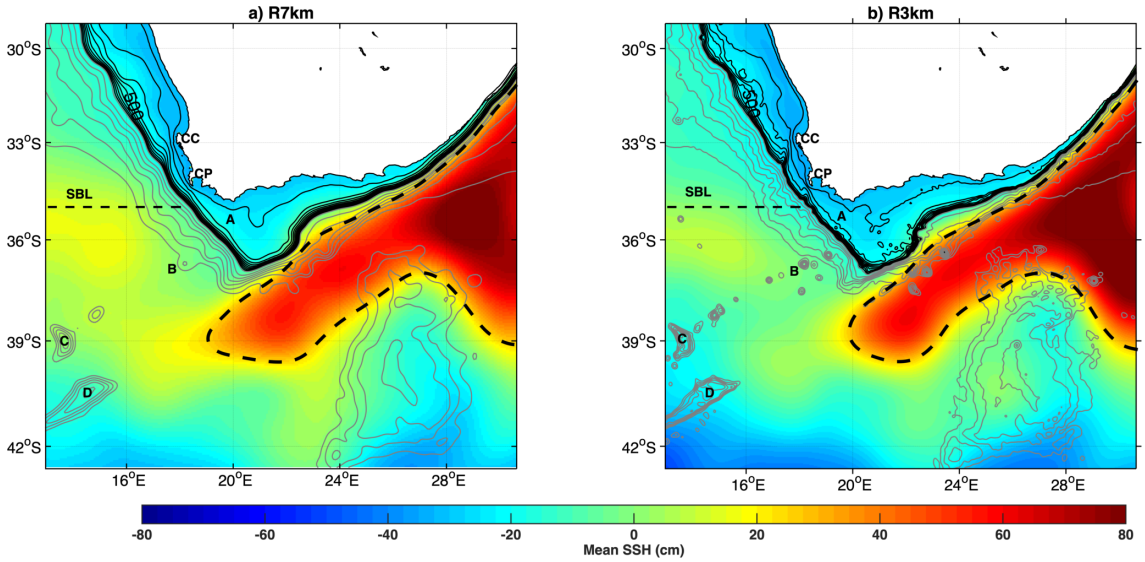

Figure 5.11: Mean annual SSH (color, in metres) over the 2005-2012 period for a) R7km and b) R3km simulation. The bold dashed line show the model retroflection path of the Agulhas Current derived from the annual mean of the same period. The dashed black transect shows the SBUS southern boundary line (SBL) over which the meridional heat fluxes are estimated. CC stands for Cape Columbine and CP for Cape Point, the southernmost tip of the Cape Peninsula. the Black contours represent bathymetry shallower than 1000 m at 100 m depth intervals, with the grey lines representing bathymetry deeper than 1000 m at 500 m depth intervals. Letters label the main bathymetric features namely: **A**-Agulhas Bank, **B**-Protea and Argentina Seamounts, **C**-Erica Seamount and **D**-Agulhas Ridge.

vertically integrated meridional heat transport Q estimated as follows:

$$Q(lon, lat) = \iint_{z=-1000\ \mathrm{m}}^{z=0} \rho_o C_p \overline{v}(lon, lat) \overline{\theta}(lon, lat) \partial z \partial x' \tag{5.1}$$

where ρ_o is the potential density of seawater, C_p the specific heat capacity, $\overline{v}(lon, lat, z)$ the annual mean meridional velocity and $\overline{\theta}(x, y, z, t)$ the annual mean potential temperature. At the SBL, the across-shore dependency of heat transport is very different in the two simulations (Fig. 5.12). In the reference simulation, it is much more intensified in the eastern part of the transect between 16°E and 18°E. Using altimetry data, *Dencausse et al.* (2010c) identified three routes followed by the Agulhas rings through the Agulhas corridor (Fig. 5.11): i) a northern route between the Agulhas Bank (**A**) and the Erica seamount **C**; ii) a central route between the Erica Seamount (**C**) and the Agulhas Ridge (**D**); iii) a southern route for eddies that initially track south and then pass over the Agulhas

Ridge. Our estimated transports at the SBL suggest that there is an overestimation of the transport of Agulhas waters into the Cape basin through the northern route in our reference simulation.

The high fluxes near 14°E and 17°E in the R7km (Fig. 5.12) could be due to a lack of topographical shielding by a group of isolated seamounts extending south-west of the Agulhas Bank (Fig. 5.11). In fact, increasing the resolution results in a much better representation of some important topographic features such as the Erica Seamount and a group of seamounts (**B**) south-west of the Agulhas Bank (**A**). These isolated seamounts disseminated along the Agulhas Rings corridor in the R3km simulation may block the northwestward propagation of Agulhas rings, and in turn reduce the inflow of warm waters into the Cape Basin (*Arhan et al.*, 1999).

In addition, the position of the Agulhas Current retroflection is located further east in the R3km simulation than in the R7km simulation (Fig. 5.11), in accordance with satellite sea surface height observations showing that a more westward (eastward) position of the

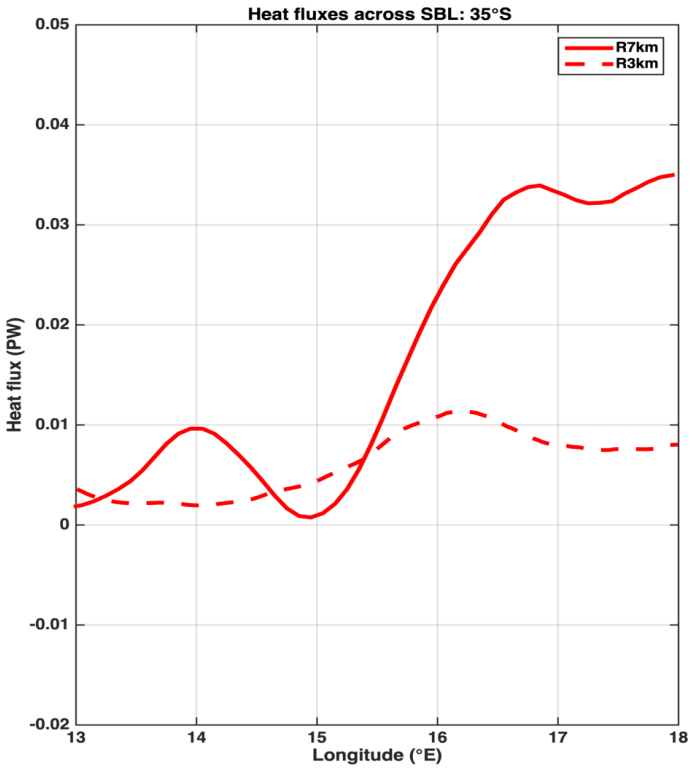

Figure 5.12: Mean annual depth-integrated (upper 1000 m depth) heat fluxes (PW) across SBL (35°S) transect for the R7km (solid red line) and R3km (dashed red line) simulations. 1 PW=10^{15}W.

Agulhas retroflection results in an enhanced (reduced) Agulhas leakage (*van Sebille et al.*, 2009). This improvement of the position of the Agulhas retroflection could also be linked to the presence of a more realistic bathymetry such as the Agulhas Bank in the high resolution simulation (*Speich et al.*, 2006).

5.4 Coastal circulation in the R3km simulation: summary

Increasing the ocean model horizontal resolution from 7 km (R7km) to 3 km (R3km) results in a net decrease of the SBUS warm SST bias in the simulation. The reduction in the offshore warm SST bias in the R3km could be explained by the reduced heat flux into the Cape basin due to a reduced Agulhas leakage of warm Indian ocean waters. The increased resolution also allows finer details of the coastal topography to be represented, and this leads to a coastal jet that is narrower and more confined towards the shelf-edge. Moreover, an increase in inner shelf poleward flow is evident in the higher resolution simulation. Further improvements of the mesoscale eddy structures increased the EKE associated with the passage of Agulhas rings and eddies. However, this high offshore EKE activity is separated from the inshore region in the R3km. There is also a difference in the magnitude of inshore EKE associated with the shear instabilities of the Benguela Jet and poleward current.

The changes in the mean circulation are expected to have an impact on the alongshore and cross-shore transport of Lagrangian particles, and thus transport success. The robustness of seasonal characteristics of transport success of particles advected by velocity fields from the R7km simulation (Chapter 4) is tested in the next section. The transport success in the two simulations is compared.

5.5 Sensitivity of the Lagrangian transport success to the downscaling

Given the importance of the oceanic circulation on the alongshore and cross-shore transport of Lagrangian particles, the impact of downscaling on the Lagrangian pathways is investigated in this section. Here, we study how the changes of the underlying Eulerian

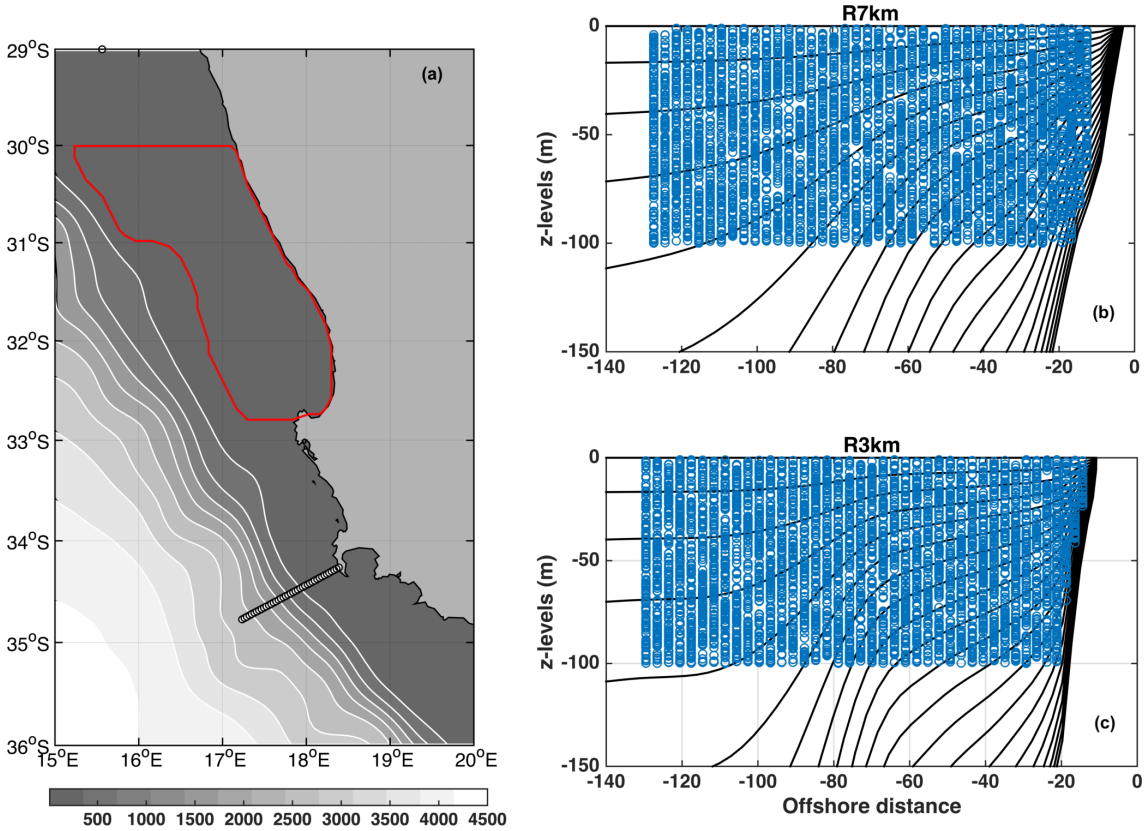

Figure 5.13: a): Set-up of the Lagrangian experiments: particles are released every 12 hours over the SARP line (white circles), a cross-shore transect off Cape Point. They are counted as successfully transported particles if they reach, within 30 days, the St Helena Bay target area delineated by the red polygon. The bathymetry of the R7km model (in grey with white contours every 500 m) is also superimposed. (b,c): Initial distribution of particles over the SARP line for a given release event for R7km and R3km, respectively. σ layers are superimposed (black solid).

fields impact the Lagrangian trajectories between Cape Point and St Helena Bay. To be coherent with the previous chapter, the focus will be on the seasonal pattern.

5.5.1 The Lagrangian setup

The same methodology as in Chapter 4 is used. The particles were released every 12 hours from 1992 to 2011 at a transect off Cape Point (SARP line) over 108 vertical profiles distributed every 3 km in horizontal distance (Fig. 5.13a). For each vertical profile, particles are randomly distributed over the first 100 m depth with a density of 1.125 particles per metre. This resulted in a total of 4976 for the R7km simulation (Fig. 5.13b) and 4840 for the R3km simulation (Fig. 5.13c). The lower number of particles in R3km is attributed to the shape of the shelf which is wider and shallower than in R7km and thus less particles are released over the inner shelf region. The particles are advected for 30 days by daily velocity fields provided by the R7km and R3km simulations. Transport success is given by the ratio of the number of particles reaching St Helena Bay target area over the total number released. This area is defined as a polygon that extends from the coast to the 300 m isobath and from 32.8°S to 30°S (Fig. 5.13a).

5.5.2 Comparison of the alongshore connectivity between R7km and R3km

Transport success in both simulations exhibits the same seasonal cycle, which is highest from August to December (Fig. 5.14a,b). Transport success is generally higher in the R3km with the exception of May. The largest differences in transport success between the two simulations occurs during the peak season (September-November). The lowest transport success in the R7km occurred in June whereas it occurred in May in the R3km. In the R7km, the standard deviation is lowest during spring (Fig. 5.14b) and in autumn (March-May) in the R3km (Fig. 5.14c).

Figure 5.15 compares the seasonal age of arrival in the target area. There is a peak in the age distribution between five to ten days for particles released between July and December in the R7km (Fig. 5.15a), while it peaked during September-December in the R3km (Fig. 5.15b). For the R3km, the oldest particles (20-30 days) have better probability

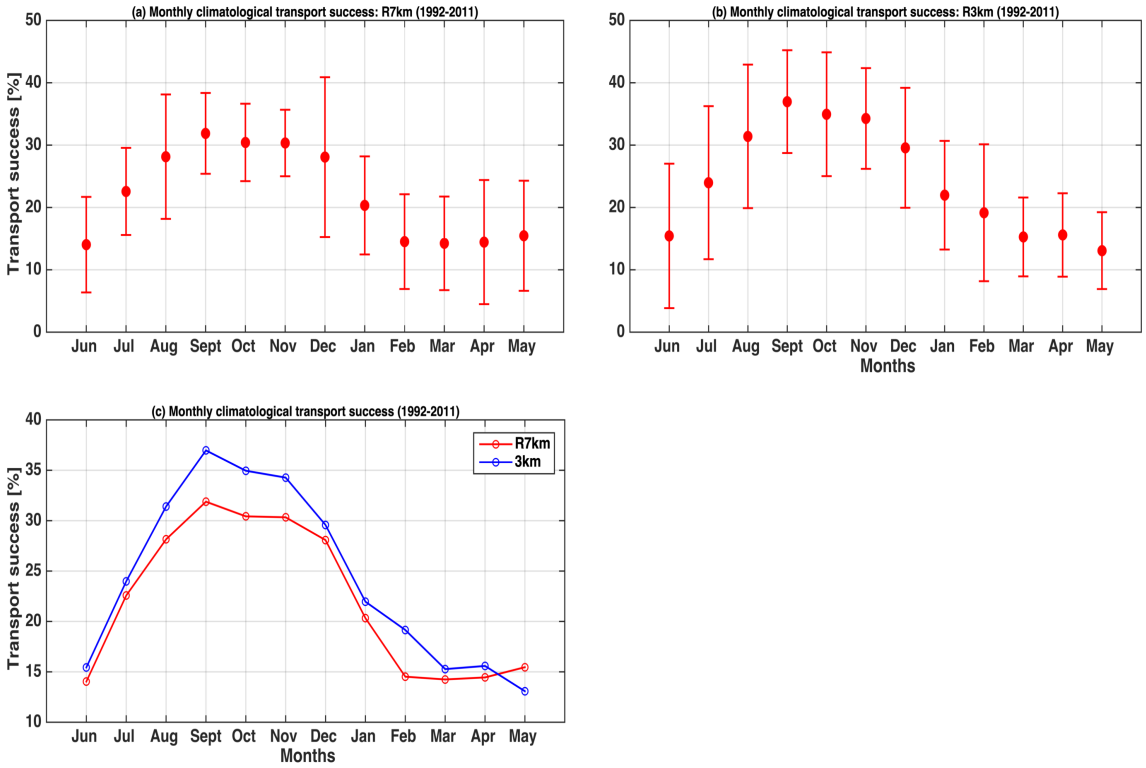

Figure 5.14: Monthly climatology of transport success TS_m (red dots) and standard deviation of TS_m superimposed as error bars for a) R7km and b) R3km. c) Monthly climatology of transport success for R7km (red line) and R3km (black line).

of transport success from the late upwelling season to winter (January to July).

Particles are then grouped according to the isobath on which they have been released, and this was done by grouping them as inshore and offshore particles. The 500 m isobath is used as the border between the inshore and offshore region. For both simulations, Figure 5.16a reveals that most of the successful particles originate from the inshore region, and their seasonal pattern is similar to that of the total transport success. In the R3km, this proportion is much smaller during autumn and early winter (March-July).

To evaluate the influence of the coastal poleward current on transport success, the inshore transport success was further divided into groups of inner shelf (<200 m isobath) and mid-shelf (>200 m-500 m isobaths). Their seasonal probability distribution (black and red lines) is superimposed on Fig. 5.16a). There are less successful inner shelf particles in the R3km than R7km throughout the year particularly during winter and spring. This result suggests that it is the mid-shelf particles rather than the inner shelf particles that contribute significantly to the inshore transport success in the R3km simulation during this period.

The opposite is observed in the offshore region, where the particles originating from this region have a relatively low chance of reaching St Helena Bay throughout the year, the probability being relatively lower in the R7km than in the R3km (Fig. 5.16b). Moreover, the seasonal cycle of the offshore transport success is different to the inshore particles as it peaks in November to February.

The most distinguishable impact of increasing the model resolution on the alongshore connectivity is that transport success increases when increasing the model resolution but only between August and February for inshore particles. The contribution of this inshore transport success mainly comes from the particles from the mid-shelf region under the influence of the Benguela Jet. In R7km, there is a high inner shelf transport success during autumn and winter. There is an increase in transport success of offshore particles in the R3km which resulted in the high total transport success from March to July despite the low inshore transport success during this period. This could explain why there is an increase in the proportion of old particles (20-30 days) because offshore particles are expected to take longer than those travelling over the shelf in the Benguela Jet. The effect

of the model resolution on the patterns of Lagrangian trajectories is presented next.

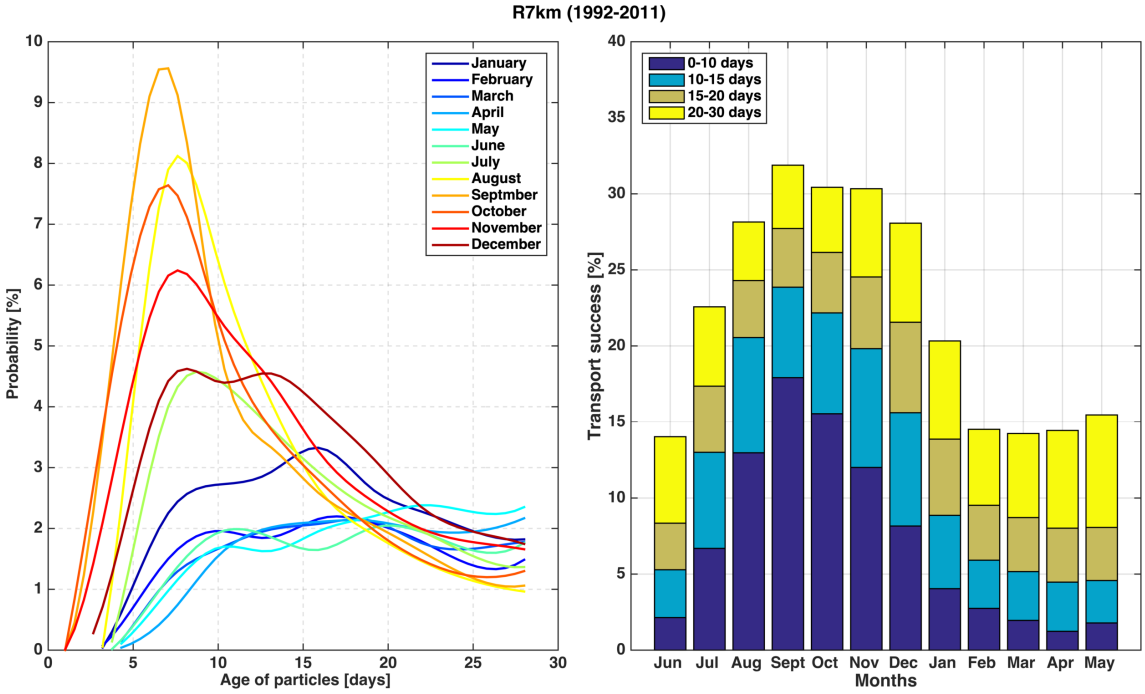

(a)

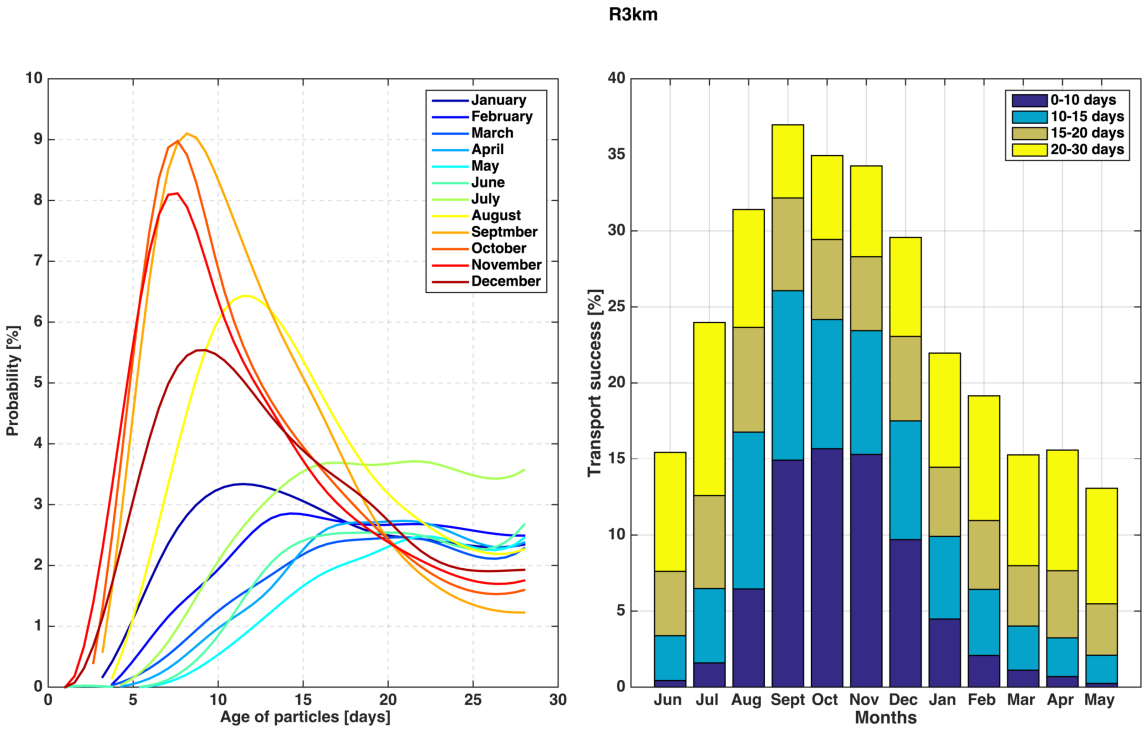

(b)

Figure 5.15: Left: Monthly distribution of successful particles by age when entering the target area. Right: Cumulative histogram of monthly climatology transport success with clusters of particles built according to their age of arrival: group I (age<10 days); group II (10<age≤15 days); group III: (15<age≤20 days); group IV: (20<age≤30 days). For R7km (a) and R3km (b). Probability have been normalised by the total number of particles released for each month m ($m = 1, \cdots, 12$) over the 20 years of the model run.

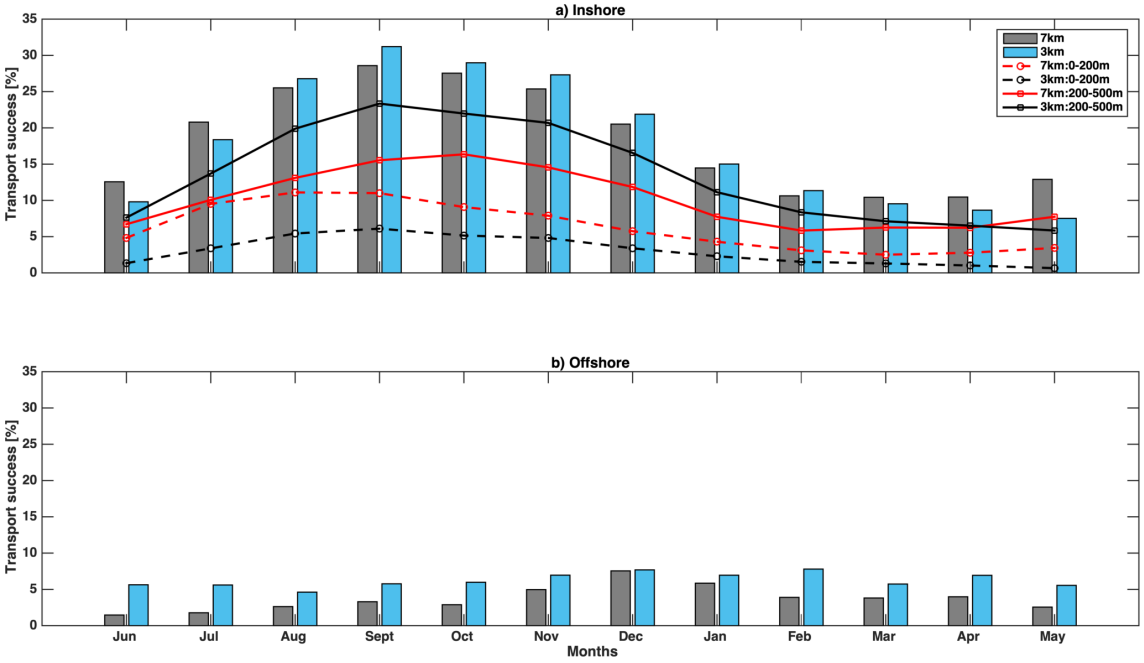

Figure 5.16: Monthly cumulative contribution of the (a): inshore particles and (b): offshore particles to transport success for the R7km (grey bars) and R3km (cyan bars). The monthly transport success of the particles originating over the inner shelf (0-200 m isobath) is also superimposed on (a) for the R7km (red dashed line) and R3km (black dashed line). The red and black lines respectively represent the transport success for particles from the mid-shelf (200-500 m isobaths) in the R7km and R3km.

5.6 Horizontal dispersion

The sensitivity of particle horizontal dispersion to the differences in the structure of the alongshore currents and in the mesoscale variability between the two simulations is analysed. To characterise the horizontal dispersion of particles, the maps of particles' spatial distribution (plumes) are plotted according to their age τ (in days) on the horizontal grid of the R7km and R3km simulations.

All particles aged τ found within the water column of the grid cell located at position (x, y) in Cartesian coordinates are counted. Particle density is calculated by dividing the total number of particles within each grid cell by the grid cell surface area. The seasonality of the dispersion patterns is considered by averaging the monthly climatology according to the four austral seasons: summer (December-February), autumn (March-May), winter (June-August) and spring (September-November). To study the differences in the evolution of the plume, maps of particles' spatial distribution are shown at 6 days and at 12 days after their release for unsuccessful particles (Fig. 5.17) and successful particles (Fig. 5.18).

Unsuccessful particles

The north-westward wide spread of the highest plume density (>4.5 m^{-2}) of unsuccessful particles into the open ocean in summer and autumn is greatest in the R7km (Fig. 5.17, panel a-b) and greater than in the R3km (Fig. 5.17, panel e-f). At 6 days, this plume of particles had travelled further westward across 16°E in the R7km (Fig. 5.17a, panel a-b) than in the R3km (Fig. 5.17a, panel e-f), although it appears more clustered during the other seasons (winter and spring). The size difference in the plume between summer-autumn (bigger) and winter-spring (smaller) is more apparent in R3km than in the R7km. A reference contour (blue line) of 3.5 m^{-2} is also superimposed on the distribution maps to estimate the spreading of particles in the two simulations. Figure 5.17b shows that the north-westward spreading that is enhanced at 12 days is minimised with increasing resolution. It is also apparent that increased resolution leads to the plume exhibiting more variability characterised by thinner filamentary structures suggesting that smaller structures are resolved by the R3km simulation. Closer to the coast, a poleward transport

of particles can also be noticed in both simulations with the largest transport occurring in summer and autumn. There are more particles advected south in the R3km simulation, and this explains why transport success of the inner shelf particles (Fig. 5.16a) is much smaller in the R3km simulation than in R7km. Interestingly, the high resolution also allows for the effective transport of high density plume into False Bay (east of Cape Point) throughout the year except in spring, this indicates that the poleward flow enters the bay rather than passing offshore of it.

Successful particles

In both simulations, the highest density of successful particles shaped like a alongshore filament is confined between the 200 m and 2000 m isobaths (Fig. 5.18). At 6 days, the plume is located between Cape Point and Cape Columbine (Fig. 5.18a). In winter and spring, the plume travels along shelf with some of the particles located in the inner shelf region and less particles offshore of the 2000 m isobath. On the other hand, there are less particles located in the inner shelf in autumn and summer, likely due to the increased southward transport seen in Figure 5.17a (panel a-b and e-f); more so in the R3km simulation (Fig. 5.17a, panel e-f). Also, there is a plume of $<3.5\ m^{-2}$ particles travelling offshore of the 2000 m isobath at 6 days that moves back towards the shelf at 12 days during summer. This implies that successful particles take a more offshore route during summer during the first 6 days hence the long travel time. At 12 days, the plume has been advected north past Cape Columbine (Fig. 5.18b), and it has propagated northward much faster in the R7km in autumn and winter (Fig. 5.18b, panel b-c) related to a much stronger Benguela Jet than in the R3km (Fig. 5.18b, panel f-g).

In conclusion, successful particles tend to travel between 200 m and 500 m isobaths but the north-westward dispersion at early ages during summer and autumn results in some successful particles travelling offshore. Hence, the particles are characterised by a longer connection time (20-30 days). However, there are relatively more offshore particles that become successful in the R3km because they do not get advected long distance offshore into the turbulent region. In the R3km, there is also a reduced transport success of inshore

1790 particles in summer and autumn due to the southward transport on the shelf.

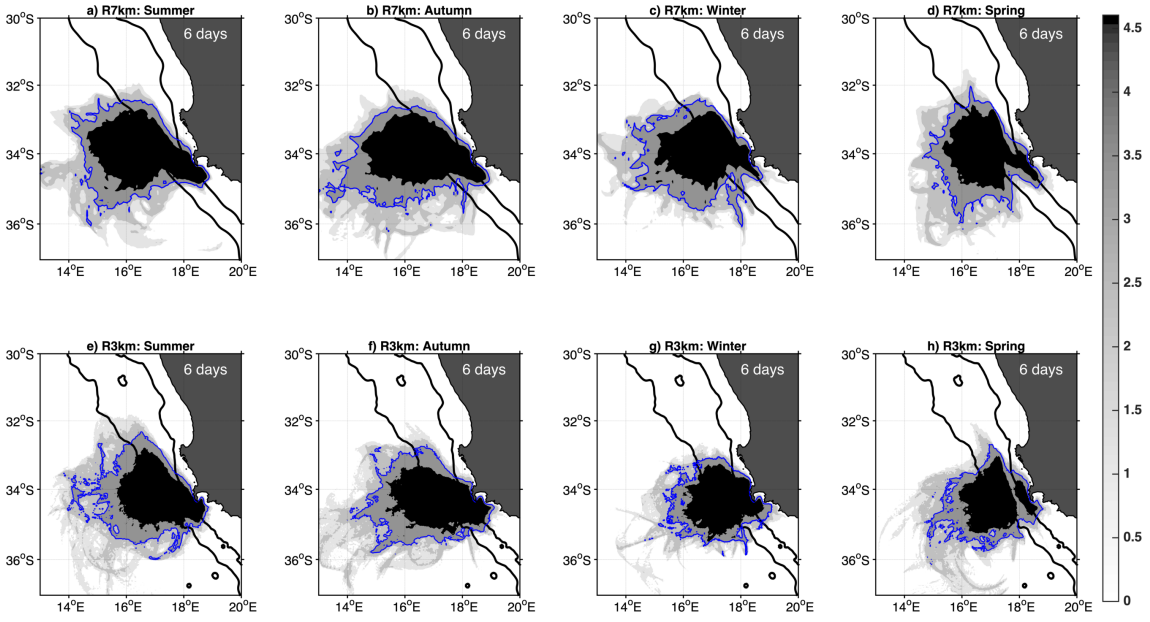

(a)

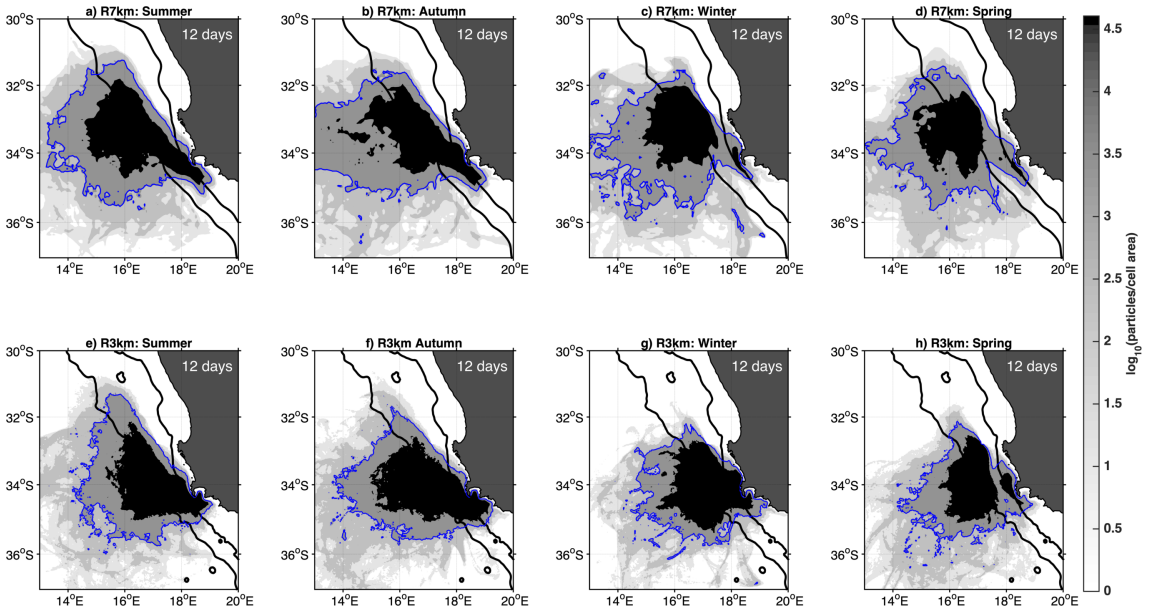

(b)

Figure 5.17: Seasonal plume dispersion pattern of unsuccessful particles at a) 6 days and b) 12 days after their release for 7 km (panel a-d) and 3 km (panel e-h). The density (colorbar) is obtained by dividing the sum of particles located in a defined grid box by their respective grid box area. The density of particles is shown in log scale to capture the large dispersion of particles in the higher resolution and a reference contour (blue line) of 3.5 m^{-2} is superimposed. The 200 m and 2000 m isobaths are also superimposed.

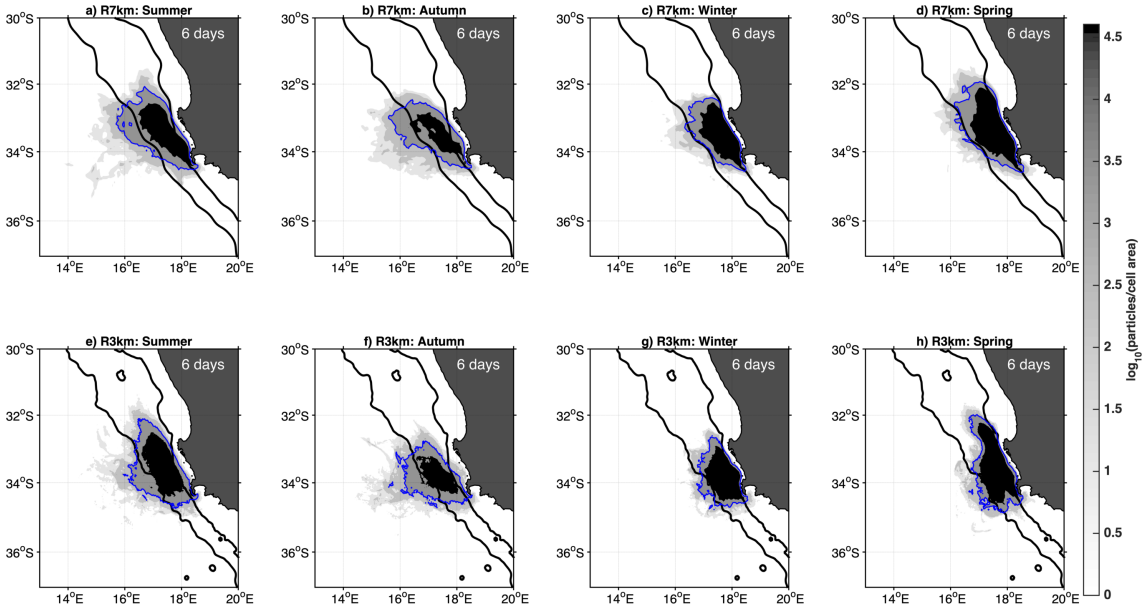

(a)

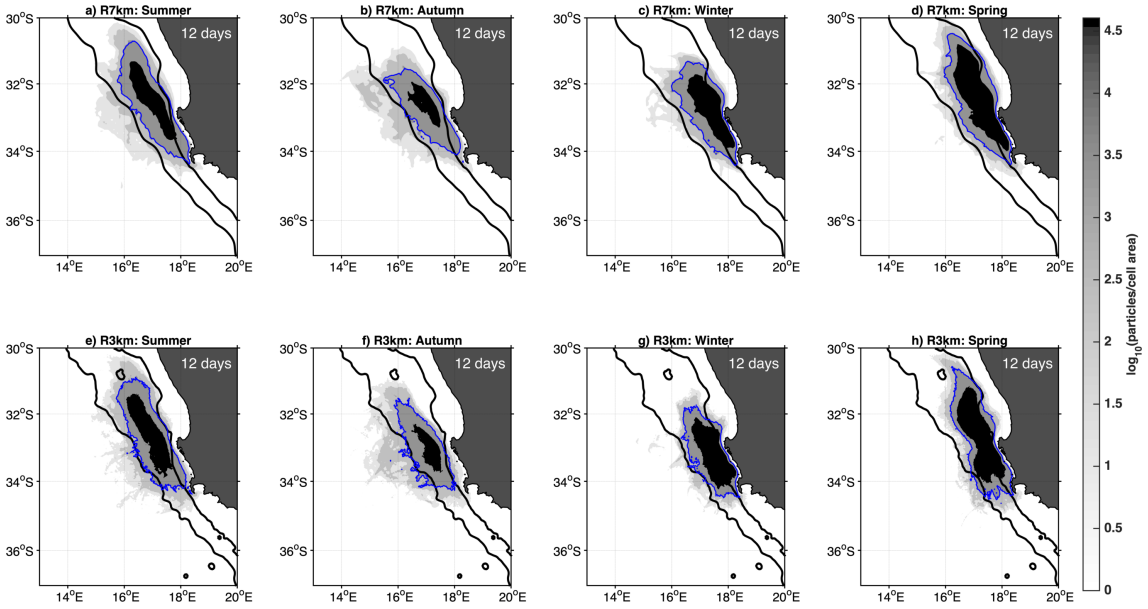

(b)

Figure 5.18: Same as in Figure 5.17 but for successful particles.

5.6.1 Lagrangian pathways and Eulerian oceanic circulation

The differences in inshore and offshore transport success in the two simulations is an indication of a difference in the ocean circulation influencing their transport. To relate the seasonality of the different Lagrangian transports to the contrasting ocean circulation features previously described, the cross-shore profiles of normalised: i) particles' distribution; ii) depth-integrated (top 100 m) alongshore velocity; iii) depth-integrated (top 100 m) EKE at the Cape Point transect are presented in Figure 5.19. Generally, the peak in the cross-shore distribution of all particles coincides with the peak of the jet in both simulations (Fig. 5.19). The probability of all particles that travel within the 50 km offshore distance is significantly smaller in the R3km simulation, and this due to the poleward current. On the other hand, successful particles tend to travel in the inshore side of the jet.

In the two simulations, the differences in inshore transport success is related to both the intensity and structure of the Benguela Jet and the inner shelf poleward flow. In summer and spring, inshore particles in the R3km leave Cape Point in a jet that is closer to the coast and confined between the 200 m and 500 m isobaths thus resulting in high inshore transport success. In winter and autumn, there are less inshore particles in the R3km due to low inner shelf transport success attributable to the nearshore poleward flow at Cape Point driving a southward transport.

Offshore particles were found to mainly be influenced by eddy activity at the shelf-edge. However, in the R7km, the proximity of high EKE signal to the shelf-edge exerts an enhanced turbulence dispersive effect (Fig. 5.8a). Thus, there is less transport success for the offshore particles. Furthermore, more particles are exposed to this high EKE in summer and autumn in the R7km (Fig. 5.19a,b) because of the north-westward transport of particles off Cape Point and hence a longer travel time during this period. Particles are also transported in the offshore direction in autumn in the R3km, however this had a small impact on transport success since the offshore EKE is relatively weaker than in the R7km run. Hence, the offshore particles in the R3km have higher probability of transport success during this period. The increase in transport success for the offshore particles in the R3km contributed significantly to the total transport success.

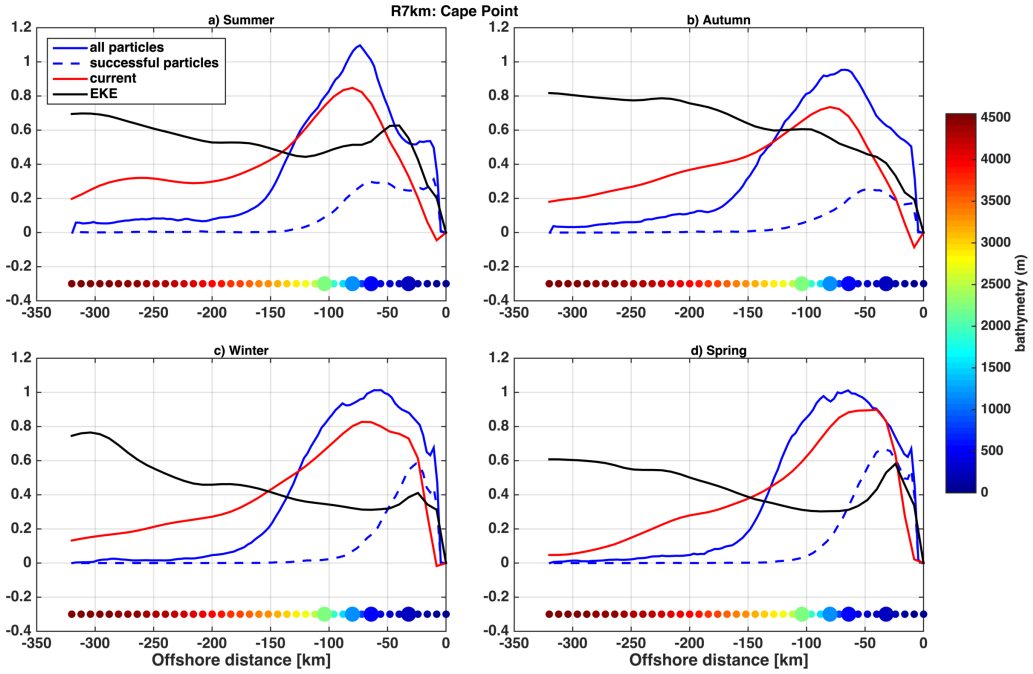

(a)

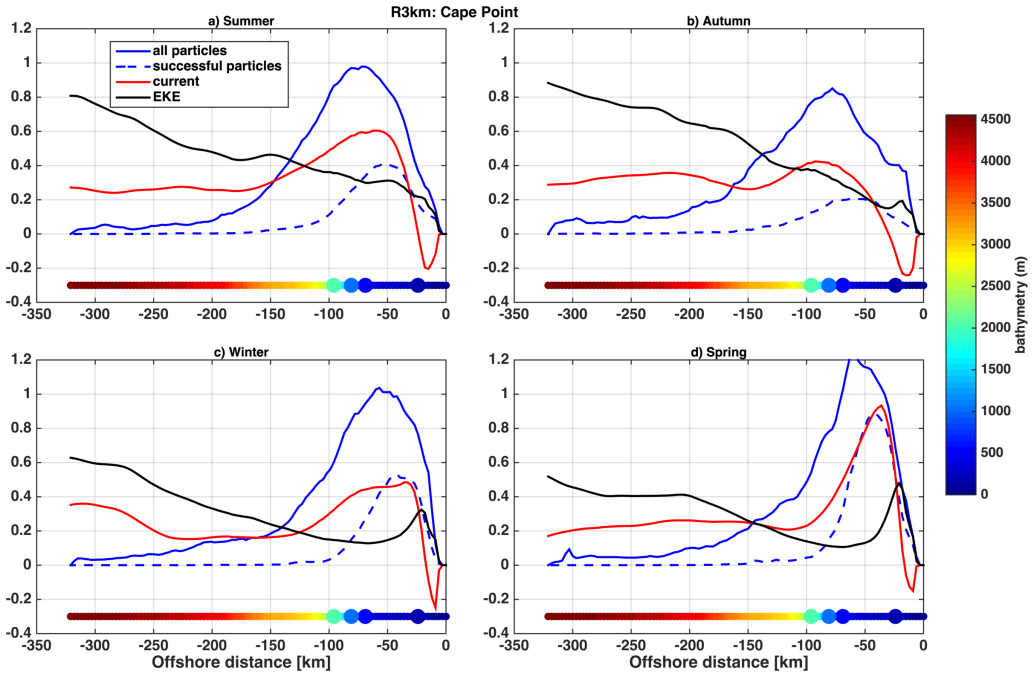

(b)

Figure 5.19: Seasonal cross-shore profile of normalised depth-integrated alongshore current (red), EKE (black), and probability of particles' occurrence (blue solid) at Cape Point for (a) R7km and (b) R3km. The histogram of successful particles is also superimposed (blue dashed). The enlarged circles mark the location of the 200 m, 500 m, 1000 m and 2000 m isobaths, respectively.

Finally, the increase in the long travelling time observed in the R3km could be explained by the significant offshore transport success and the fact that particles travel in a weaker jet during summer, autumn and winter in particular.

5.7 Summary and Conclusion

This chapter investigated how increasing the model resolution from 7-km to 3-km impacts the coastal circulation and therefore the alongshore connectivity between Cape Point and St Helena Bay. Despite some changes in the circulation, the seasonal cycle of the alongshore connectivity remains more or less the same. This is a highly unexpected result considering that increasing the resolution has significantly affected the across-shelf structure of the alongshore jets observed over the mid-shelf as follows:

- The Benguela Jet is narrower and less intense in the higher resolution simulation. It is also more confined towards the shelf edge and the surface.
- A poleward surface and sub-surface flow is enhanced inshore of the Benguela Jet.

Both of these impacts are expected to decrease the transport success of particles from Cape Point to St Helena Bay. In fact, the coastal poleward current contributes to the southward transport of inshore particles. Furthermore a weaker Benguela Jet results in a slower northward advection of particles. However, these negative effects are compensated by a much lower offshore loss of particles in the higher resolution simulation due to a more coherent Benguela Jet confined over the shelf-edge. The latter follows the 200-500 m isobaths, and its northwest-ward veering is reduced in the higher resolution simulation. These changes in the oceanic circulation may be linked to:

- a better representation of the fine scale dynamics when the resolution is being increased. Some fine scale structures smoothed out by the numerical viscosity at a resolution of 7-km may be more persistent with a resolution of 3-km. These effects might lead to a better representation of the along-shore jets and their instabilities. They might also play a role on the growth of the very nearshore poleward surface and sub-surface flow.

- a better representation of the coastal topography, in particular around capes and canyons. This would also lead to the enhancement of the across-shore shelf slope, which in turn could contribute to confine the along-shore jets over some specific isobaths.

- a reduction of large-scale biases, here the leakage of warm Agulhas waters into the Cape Basin. This result was largely unexpected. A better representation of the Agulhas Ridge and the isolated seamounts disseminated in between the eastern flank of this ridge and the continent seems to have blocked partly the leakage of warm Agulhas waters into the Cape basin, and pushed the route of turbulent eddies trapping these waters more offshore. As a result: i) the warm bias observed in the reference 7-km simulation is significantly reduced in the 3-km simulation, which contributes to change the characteristics of the Benguela Jet; ii) the mesoscale eddy turbulence in the offshore coastal transition zone is reduced in the 3-km simulation, which reduces the offshore loss of particles.

However, the main finding of this chapter is that the Benguela Jet is the main driver of the seasonal alongshore connectivity in the SBUS. Since the Benguela Jet is present in both simulations, there are little differences in the simulated transport success at the seasonal time-scale. In fact, the seasonal cycle of the Benguela Jet does not seem to be affected by the influx of Agulhas waters into the Cape basin that differed between the two simulations. To confirm this result, two nested 1 km simulations have been run over the 2005-2011 period. One was nested within the 3-km [R1km_EXP1] (Fig. 5.20a) and therefore had a reduced Agulhas water influx in comparison to the R7km simulation. The other was nested within the 7-km simulation [R1km_EXP2] (Fig. 5.20b) and therefore had an enhanced Agulhas waters influx in comparison to the R3km simulation. As expected, preliminary results show that increasing the resolution to 1 km leads to a stronger and more coherent surface and sub-surface nearshore poleward flow. Finer scale eddies can also be observed in the 1 km resolution simulations. Nevertheless, despite some small changes in its across-shore position, width and vertical extension, the seasonal cycle of the Benguela Jet is very similar in the two simulations, and coherent with our findings from previous lower 3-km and 7-km simulations. Therefore, the characteristics of the

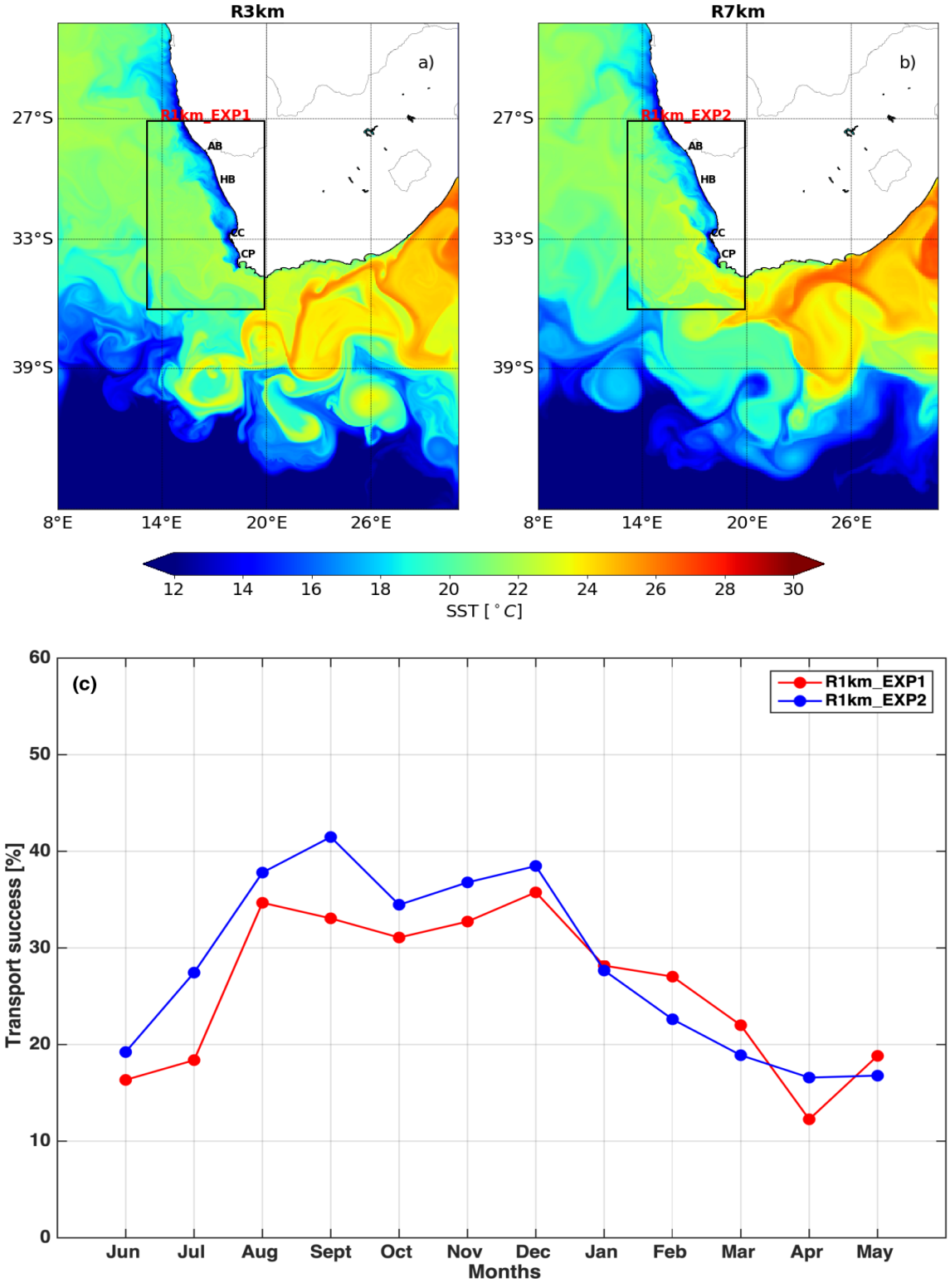

Figure 5.20: Snapshot of SST (Year 2005, 1st of January) for the (a) 7-km and (b) 3-km simulation. The black box delineates the 1-km simulation boundaries and the SST of the 1-km is superimposed within the box. (c) Monthly climatological transport success of R1km_EXP1 (red line) and R1km_EXP2 (blue line) over the 2005-2011 period.

alongshore connectivity and the seasonal cycle of the northward transport success is very similar (Fig. 5.20c). Nevertheless, differences between the two simulations are expected at intraseasonal and interannual time-scales.

Chapter 6

Interannual variability of transport success

6.1 Introduction

In Eastern Boundary Upwelling Systems (EBUS), the variability in small pelagic fish populations abundance depends on fish recruitment success which is influenced by a set of both environmental and biological factors (*Bakun*, 1996; *Painting et al.*, 1998). Small pelagic fish spawn in a stable (non-turbulent) environment, and their eggs and larvae must be transported almost as passive tracers towards a region of food availability (*Parrish et al.*, 1983). In the southern Benguela upwelling system (SBUS), sardines and anchovies spawn on the Agulhas Bank (Fig. 6.1a) located off the south-west and south coast of South Africa from October to March (*Painting et al.*, 1998; *van der Lingen and Huggett*, 2003). The northward advection of the eggs and larvae towards the food-rich nursery area off the west coast in St Helena Bay (located just to the northeast of Cape Columbine in Fig. 6.1a) is facilitated by a shelf-edge jet named the Benguela Jet (*Shelton and Hutchings*, 1982; *Hutchings et al.*, 1998). Those larvae that get successfully transported into the nursery area are considered as recruits.

Abundant catches of anchovy begun in the 1960s after the collapse of sardine fishery (*Hutchings et al.*, 1998), and continue to drive an essential socio-economic activity. Small

pelagic fish account for 20-25% of total South African fisheries catch value and contribute less than 1% of the country's total gross domestic product (GDP), but create substantial employment locally (*Brick and Hasson*, 2017). Analysis of repeated hydro-acoustic surveys of anchovy biomass done since 1984 over the entire area occupied by the anchovy adult population (Fig. 6.1b) shows a large interannual variation of recruitment and spawner stock size (*Huggett et al.*, 2003). This variability presents a challenge to fisheries management and has led to a large number of studies investigating how this variability is linked to changes in the environmental conditions (*Boyd et al.*, 1998; *Hutchings et al.*, 1998; *Huggett et al.*, 2003; *Mullon et al.*, 2003; *Parada et al.*, 2003; *Lett et al.*, 2006; *Parada et al.*, 2008; *Koné et al.*, 2013).

There are multiple variables linked to both the environment (e.g. wind-induced turbulence, temperature, food availability) and biological factors (e.g. egg abundance, spawning conditions, mortality due to predation, cannibalism and starvation) that can impact recruitment success (*Painting et al.*, 1998; *Shannon et al.*, 1996; *Hutchings et al.*, 1998). This complexity makes it difficult to evaluate the relative impact of these variables (which may act on different temporal and spatial scales) on recruitment, as they can act simultaneously or independently from one year to another (*Mullon et al.*, 2002). However, there has been an attempt in previous studies to understand the relationships between environmental fluctuations such as the wind and transport, enrichment processes and year-class recruitment strength, but with inconsistent findings (*Bloomer et al.*, 1994; *Boyd et al.*, 1998; *Shannon et al.*, 1996; *van der Sleen et al.*, 2018).

Empirical studies have shown a negative relationship between strong south-easterly winds and recruitment during the transport phase due to increased offshore loss of eggs and larvae and anchovy (*Boyd et al.*, 1998). On the other hand, *van der Sleen et al.* (2018) found a positive relationship between recruitment and a cumulative upwelling index which improves when the effect of upwelling is integrated over multiple spawning seasons. They suggest that high offshore loss that occurs in the summer of a particular year (year_t) could lead to low recruits and thus low spawners for the following year (year_{t+1}), whereas low

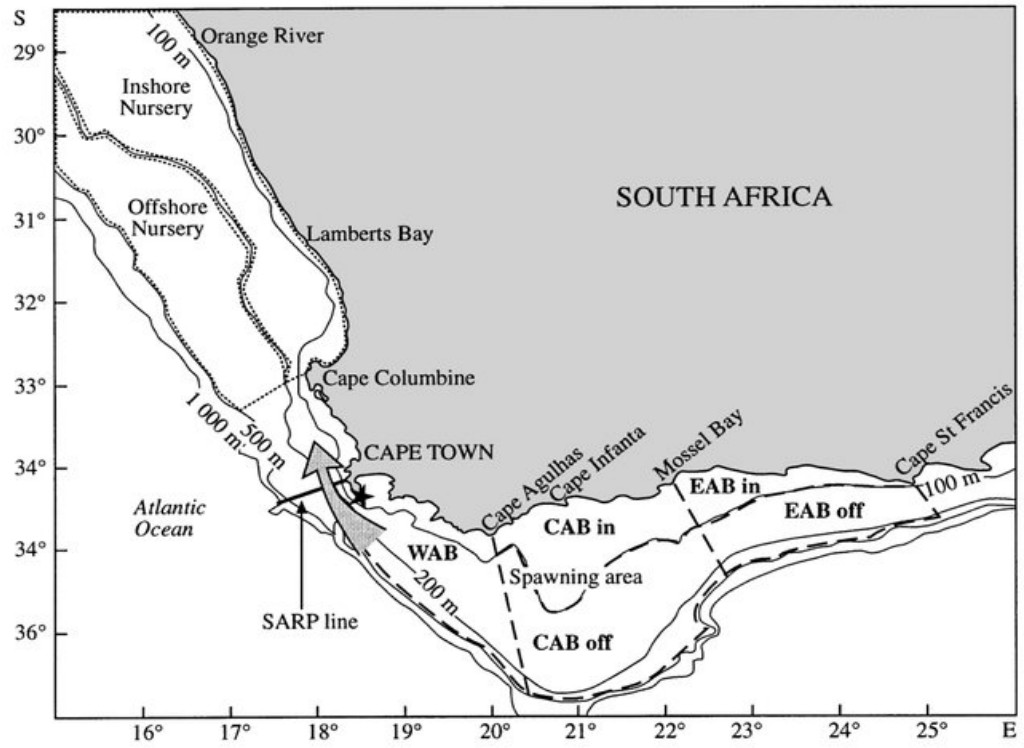

(a)

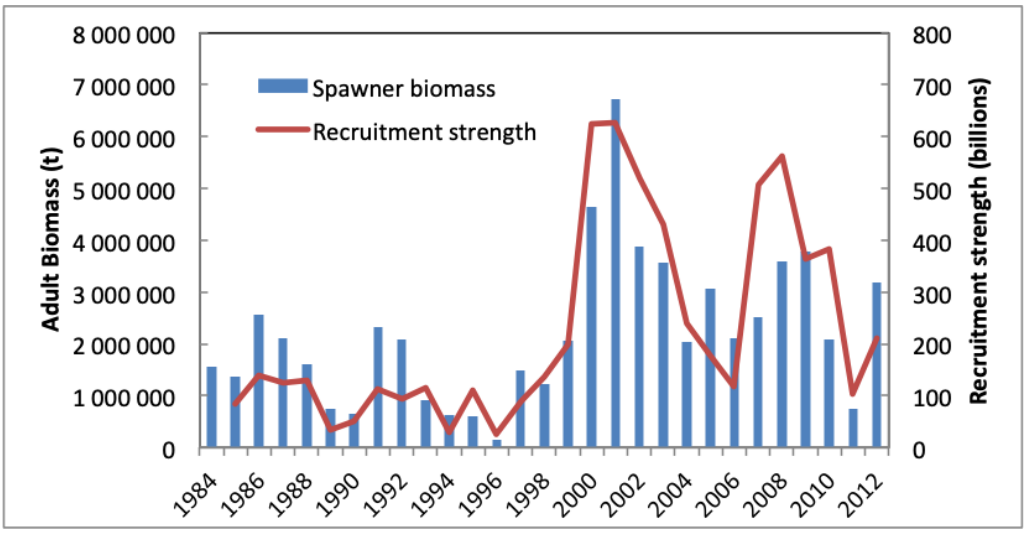

(b)

Figure 6.1: (a): Map showing anchovy spawning area on the Agulhas Bank (dashed lines) that extends from 18°E to 26°E and the nursery area located off the west coast between Cape Columbine and the Orange River on the west coast (dotted lines). The arrow indicates the approximate location of the shelf-edge jet current (Benguela Jet), the star indicates the location of Cape Point. The SARP monitoring line is represented by the cross-shore transect (black solid line) off Cape Point. The map has been adapted from *Huggett et al.* (2003). (b): SBUS recruitment strength of anchovies in billions (1985-2012) (black line) and adults biomass (bar graph) in tons (1984-2012). Updated from *van der Lingen and Huggett* (2003).

offshore loss could be beneficial for population growth during a period of low spawning activity.

Moreover, the early 2000s was characterized by a large increase in the mean level of both spawner biomass and recruitment (Fig. 6.1b) (*van der Lingen and Huggett*, 2003; *Roy et al.*, 2007). Figure 6.1b shows that the 1990s were characterised by moderate recruitment levels and that the 2000-2010 period experienced two periods of exceptionally high recruitment levels separated by low values during in the mid 2000's. Long-term observational studies of the Benguela upwelling system (BUS) suggest that these changes might be related to upwelling index variability (*Blamey et al.*, 2012; *Lamont et al.*, 2018). Previous studies (*van der Lingen et al.*, 2002; *van der Lingen and Huggett*, 2003; *Roy et al.*, 2007) indicate that in the early 1990s there was an eastward shift of the spawning region, attributed to coastal cooling east of Cape Agulhas Bank (Fig. 6.1a). This result is consistent with the findings of *Blamey et al.* (2012) based on in-situ wind measurements (1960-2010) and *Lamont et al.* (2018) who used reanalysis wind data (1979-2015). From about 1995 to 1999, the SBUS experienced a dominance of south-easterlies and strong upwelling together with WAB cooling which led to relatively low anchovy recruitment during this period (*Howard et al.*, 2007; *Blamey et al.*, 2012).

Variability in the passive transport of eggs and larvae from the spawning ground to the nursery on the west coast is also considered one of the critical factors influencing recruitment variability (*Hutchings*, 1992; *Hutchings et al.*, 1998; *Shannon et al.*, 1996). As a result, several numerical Lagrangian transport studies have focused on oceanic currents forced by monthly seasonal climatology of wind-stress, freshwater and heat fluxes (*Huggett et al.*, 2003; *Mullon et al.*, 2003; *Parada et al.*, 2003, 2008) thus excluding any externally forced interannual variability. The importance of using a realistic, time-varying surface forcing was highlighted by *Blanke et al.* (2005) who found that a daily wind product is more efficient in simulating the observed nearshore interannual variability of SST anomalies (warm and cold events) than a weekly product (*Blanke et al.*, 2002).

Oceanic mesoscale eddies can also play a significant role in transporting eggs and larvae by either retaining or dispersing them (*Hutchings et al.*, 1998). Moreover, eddies and their associated recirculation patterns can also play an essential role in advecting larvae back inshore into a retention area (*Penven et al.*, 2000). The impact of eddies on the alongshore connectivity between the Agulhas Bank and the SBUS shelf was demonstrated by *Blanke et al.* (2009). They found that if a cyclonic eddy (anti-cyclonic) eddy is generated on the western edge of the Agulhas Bank, the northward transport is reduced (enhanced). Nevertheless, the effect of the shelf-edge eddies in our domain between Cape Point and St Helena Bay has not been investigated.

This chapter aims to investigate the interannual variability of transport success between Cape Point and St Helena Bay and evaluate how it is related to variability of (i) wind-driven coastal circulation (Ekman transport, Benguela Jet, poleward current) and, (ii) the presence of mesoscale eddy activity at the coastal transition zone defined as the area from the continental slope to offshore. Analysis of transport success is based on Lagrangian particles trajectories advected by ocean currents provided by the 3-km resolution (R3km) interannual simulation described in chapter 5, for the 1992-2011 period. As it has been discussed in chapter 5, the R3km simulation is skilful at reproducing realistic Agulhas leakage (section 4.6) and captures well the shelf circulation of the Benguela Jet and poleward current (section 4.4). Given that this simulation is forced with realistic rather than climatological surface forcing, it allows us to investigate the role of interannual variability and locally forced episodic events, rather than just seasonal and intrinsic variability.

The rest of this chapter is structured as follows: section 6.2 presents the interannual transport success anomalies. Section 6.3 explores the relationship between these transport success anomalies and the anomalies of local dynamics such as the Benguela Jet, upwelling (wind field) and the oceanic turbulence (EKE). The contribution of the particles' initial cross-shore position to transport success anomalies and their relation to the oceanic circulation is presented in section 6.4. Analyses of the cross-shore transport variability of particles and the description of the role played by mesoscale eddies is found in section 6.6.

Finally, the main findings of this work are summarised in section 6.7.

6.2 Transport success variability

The interannual variability of transport success is investigated from 1992 to 2011 using Lagrangian experiments in which particles were randomly released every 12 hours at a cross-shore section off Cape Point (34°S) (Fig. 6.2a) over the upper 100 m of the water column (Fig. 6.2b) and followed for a duration of 30 days. The particles were released over 108 defined vertical profiles, 3 km apart, with a density of 1.125 particles per meter which resulted in a total of 4840 particles for each release event. The particles were then advected by daily 3-D velocity fields (u, v, w) provided by the R3km model simulation described in chapter 5 (section 5.2.1).

For each release event e, transport success TS_e (Eq. 6.1) is given by the ratio of the number of particles reaching St Helena Bay (n_e) over the total number of particles released (4840).

$$\mathrm{TS}_e = \frac{n_e}{4840}. \tag{6.1}$$

The monthly climatology ($\overline{TS}_m$) of transport success and its standard deviation σTS_m (Eq. 6.2a) shown in Fig. 6.3 exhibit a strong seasonal variability. Transport success is higher during late austral winter to austral spring (August-November) when particles have >30% probability of reaching St Helena Bay. The lowest transport success occurs during austral autumn (March-May) reaching as low as 13% in May and the standard deviation is also lowest at this time of the year. The highest standard deviation of transport success occurs during the winter season (June-August).

To analyse the interannual variability, anomalies TS'_m were defined by subtracting monthly climatology $\overline{TS_m}$ (shown in Fig. 6.3) from monthly mean patterns of transport success from 1992 to 2011 (240 months) and normalised by monthly climatological standard deviation σTS_m (shown in Fig. 6.3) as follows:

$$TS'_m = \frac{TS_m - \overline{TS_m}}{\sigma TS_m} \tag{6.2}$$

The time-series of normalised transport success anomalies is shown in Fig. 6.4 which

reveals strong interannual variability. There are notable periods of positive and negative transport success. Positive anomalies of transport occurred from 1992 to end of mid-1993. This period was followed by one of positive transport success from 1998 to mid-2001. The period between 2002 and 2004 is more variable, being characterised by as many positive as negative events that appear to be random. There was another extended period of negative transport success from 2008 to 2011.

Over the entire period, the highest positive transport success occurred in April 1992 with a standard anomaly of 3.1 whereas the lowest negative transport success happened during September 2002 with a standard anomaly of -2 (Fig. 6.4).

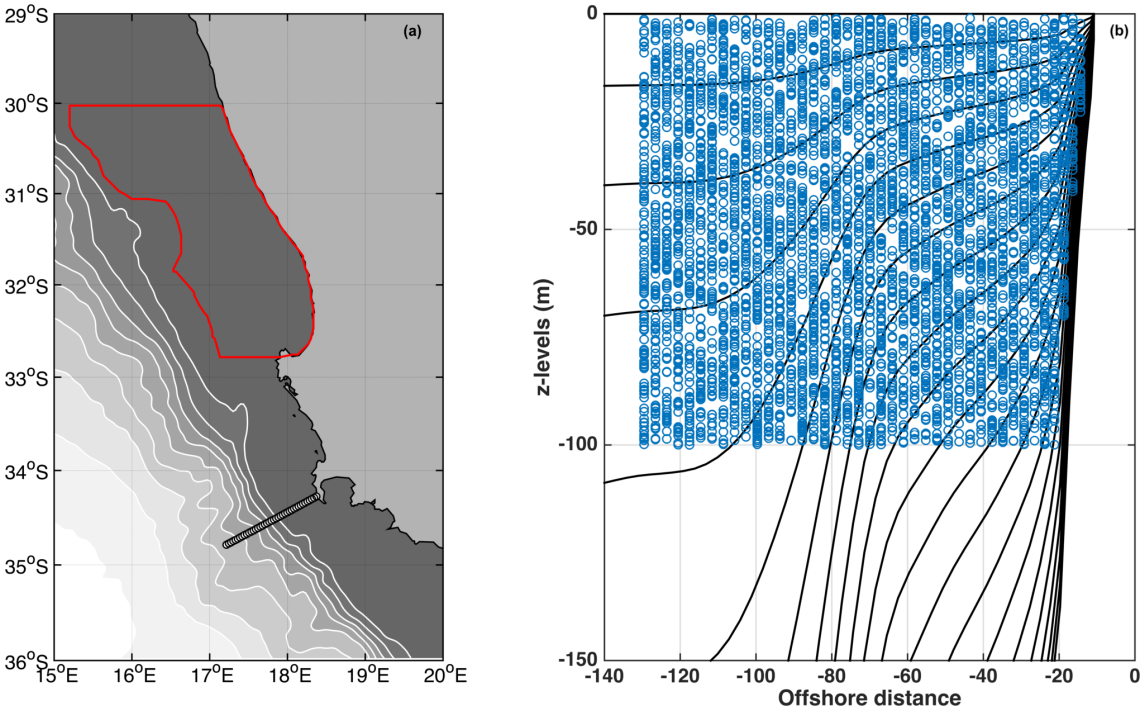

Figure 6.2: (a): Map of the R3km model simulation bathymetry (in grey with a contour interval of 500 m). Particles are released between the surface and -100 m along the across-shore transect off Cape Point (white circles). The target are is defined offshore St Helena Bay and is delineated by the red polygon. A particle is considered successful if it reaches the target area within 30 days (b): One random initial vertical distribution of particles off Cape Point during a release event (blue circles). Terrain following Sigma levels of the R3km model are superimposed in black.

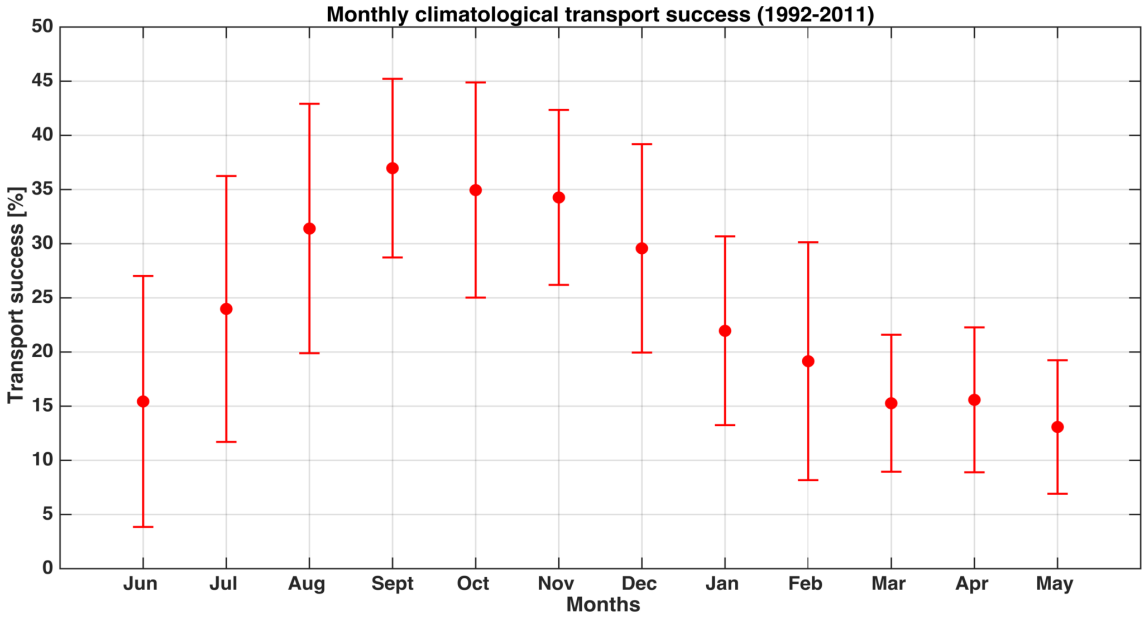

Figure 6.3: Monthly climatology of transport success $\overline{TS_m}$ (red dots) and their standard deviation σTS_m (error-bars)

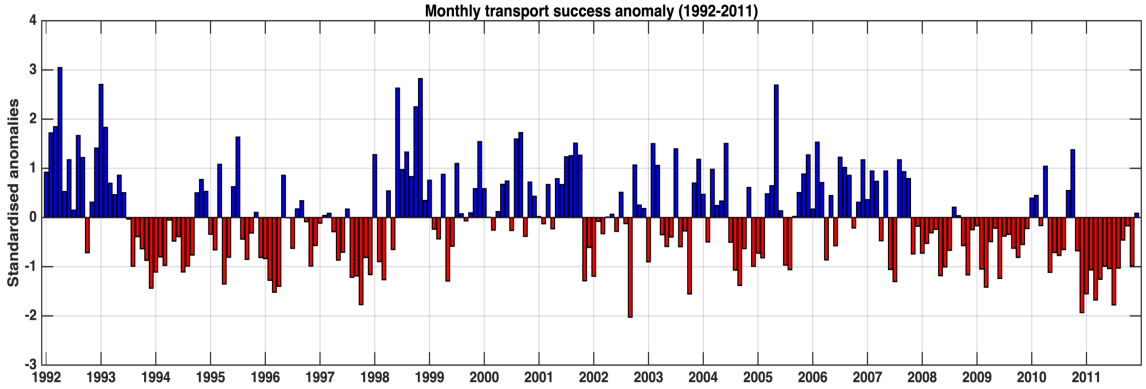

Figure 6.4: Normalised monthly transport success anomalies (TS′) over the 1992-2011 period.

6.3 The role of local dynamics

To understand the relationship between the anomalies of transport success and the local dynamics, anomalies of the Benguela Jet, alongshore wind stress, and eddy kinetic energy (EKE) are computed. All anomalies were computed by the removing the mean monthly climatology from the monthly mean values and then normalised by the standard deviation of the monthly mean values.

The annual mean surface alongshore current velocities (Fig. 6.5a) show that the Benguela jet is found between the 200 m and 500 m isobaths extending from Cape Point (34°S) to offshore St Helena Bay (32°S) consistent with *Veitch et al.* (2017). To investigate the relationship between the Benguela Jet variability and transport success variability, the surface alongshore current velocity anomalies are averaged over the 200-500 m isobaths from Cape Point to north of Cape Columbine at 32°S to form an index of the intensity of the Benguela Jet. The scatterplot in Fig. 6.5b shows normalised monthly anomalies in transport success and the Benguela Jet index. A significant positive correlation ($r = 0.49$, $p < 0.05$) is found indicating that positive (negative) transport success anomalies are attributed to a stronger (weaker) Benguela Jet intensity. Despite the relatively strong correlation, there are still some substantial positive (negative) events associated with negative (positive) Benguela Jet anomalies.

Equatorward alongshore winds (Fig. 6.6a) which are upwelling-favourable drive an offshore Ekman transport and could contribute to the cross-shelf transport of surface particles. Therefore, the interannual variability of upwelling-favourable winds strength could have an impact on the retention or offshore transport of particles. A weak, but still a significant negative relationship ($r = -0.22$, $p < 0.05$) is found between monthly alongshore wind stress anomalies and transport success anomalies (Fig. 6.6b). This correlation implies that strong equatorward wind stress (positive anomalies) and associated offshore Ekman transport tend to not be favourable for transport success. The low correlation could be because the correlations are done on monthly mean winds which filters out fluctuations of the upwelling favourable winds that induces alternating periods of intense and reduced upwelling (reduces offshore loss).

Another phenomenon in the SBUS is the presence of intense mesoscale eddy activity just off the shelf edge (*Veitch et al.*, 2009; *Veitch and Penven*, 2017). This eddy activity may affect particles that originate offshore as well as inshore particles that get advected into this domain of high mesoscale activity (Fig. 6.7a). To examine the relationships with transport success anomalies, anomalies of EKE averaged between Cape Point (34°S) and Cape Columbine (33°S) from the shelf edge (500 m isobath) to the 3000 m isobath are

computed (Fig. 6.7a). The anomalies of transport success and EKE are shown in Fig. 6.7b and are significant negatively correlated (r = -0.35, p < 0.05). This correlation suggests that anomalously positive EKE (high mesoscale turbulence) drives a dispersion of particles and thus contributes to negative transport success. However,it is unclear as to whether the high EKE is associated with cyclonic or anti-cyclonic eddies which are both prevalent in this region.

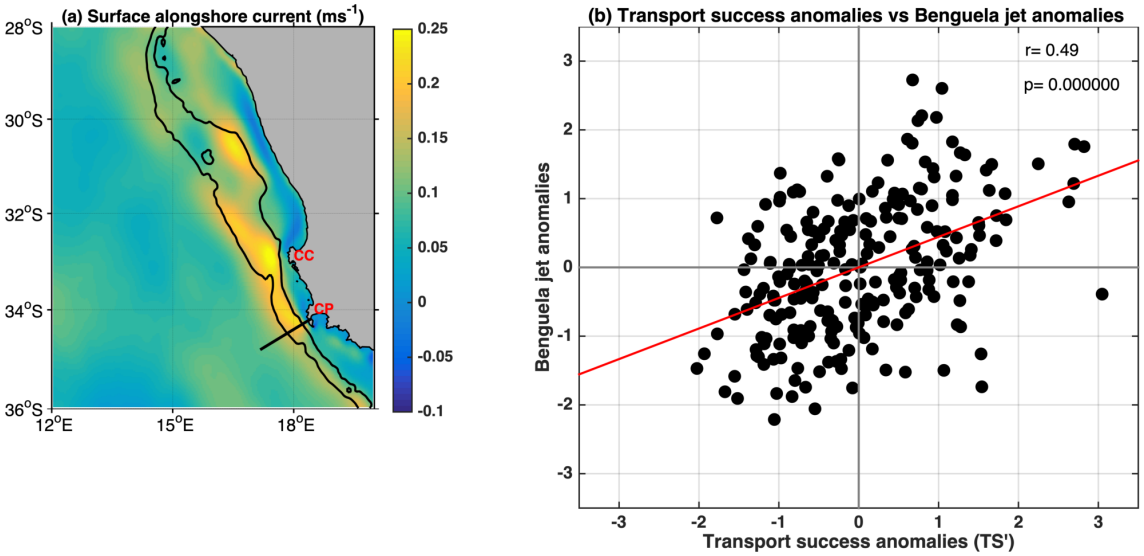

Figure 6.5: (a) Annual mean sea surface alongshore current velocities (m s^{-1}) of the R3km simulation. 200 m and 500 m isobaths are shown in black. (b) Scatterplots of normalised transport success anomalies against the Benguela Jet index anomalies averaged between Cape Point (34°S) and St Helena Bay (32°S) over the 200-500 m isobaths. A positive (negative) Benguela Jet anomaly suggests a stronger (weaker) than average northward jet

.

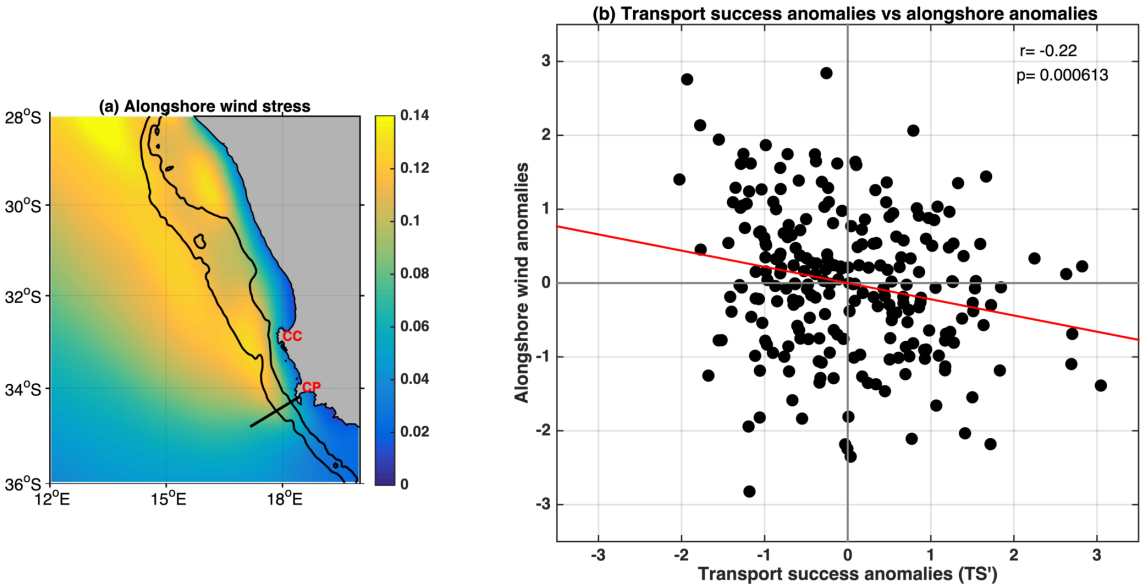

Figure 6.6: (a) January alongshore wind stress (m s^{-1}) climatological mean of the R3km simulation. 200 m and 500 m isobaths are shown in black. Same as in Fig. 6.5b but for transport success anomalies against alongshore wind stress anomalies averaged over at the transect off Cape Point (black line on the map (a)). A positive (negative) alongshore wind anomaly suggests a stronger (weaker) equatorward winds.

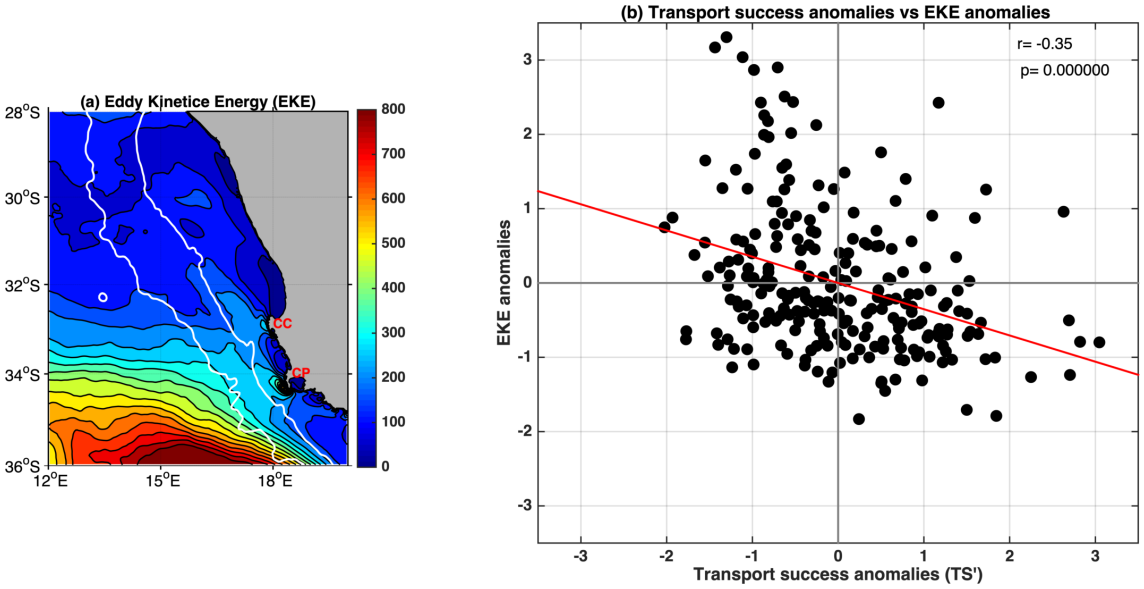

Figure 6.7: Annul mean surface EKE (c$m^{-2}s^{-2}$) of the R3km simulation. 500 m and 3000 m isobaths are superimposed in white. (b) Same as in Fig. 6.5b and Fig. 6.6b, but for normalised transport success anomalies against EKE anomalies. The EKE anomalies are averaged between Cape Point (34°S) and Cape Columbine (33°S), from the shelf edge (500 m isobath) to the 3000 m isobath. A positive (negative) EKE anomaly suggests a stronger (weaker) mesoscale turbulence.

6.4 Inshore and offshore transport success

The normalised transport success anomalies (TS′) shown in Fig. 6.4 were further separated into inshore (particles released inshore of the 500 m isobath) and offshore (particles released offshore of the 500 m isobath) particles to quantify their relative contribution of their successful transport anomalies to the total transport success anomaly. The monthly climatological means of inshore and offshore transport success are denoted as $\overline{TSI}$ and $\overline{TSO}$ with their standard deviations as σTSI and σTSO, respectively. Note that the seasonal cycle of inshore and offshore transport success is described in the previous chapter (Fig. 5.16) under section 5.5.

Monthly standardised anomalies are calculated as:

$$TSI'_m = \frac{TSI_m - \overline{TSI_m}}{\sigma TS_m} \tag{6.3a}$$

$$TSO'_m = \frac{TSO_m - \overline{TSO_m}}{\sigma TS_m} \tag{6.3b}$$

Both inshore TSI′ and offshore TSO′ are strongly correlated with the total transport mean TS′ (respective r = 0.83, 0.84 $p < 0.05$). Figure 6.8 indicates that although total negative transport is generally related to both negative inshore and offshore transport anomalies, notably the negative anomalies associated with inshore particles (blue bars) have a more significant role to play when there is negative total transport success. In contrast, it is the offshore particles (orange bars) that contribute more to transport during positive total transport success particularly for the largest values of positive transport success that are stronger than those inshore (Fig. 6.8). However, there is a weaker relationship between inshore TSI′ and offshore TSO′ transport success anomalies (r = 0.4, $p < 0.05$) which suggests that their variability might have different or independent physical drivers.

Similarly, the inshore and offshore transport success anomalies are related to the variability in the local dynamics. Fig. 6.9a suggests that inshore transport is positive (negative) when the Benguela Jet is stronger (weaker) than average, and indeed they are strongly correlated (r = 0.6, $p < 0.05$). Weaker upwelling favourable wind stress (offshore

Ekman transport) tends to favour positive TSI′ (r = -0.21, p < 0.05) (Fig. 6.9b). In addition, a coastal poleward flow driven by negative wind stress curl is likely to drive a southward transport of particles located inshore as previously discussed in Chapter 5. The poleward current is derived by averaging only negative velocities (v <0) over the 50 km coastal band and integrated over the top 100 m depth at a transect off Cape Point. Considering that the mean poleward current is negative, negative (positive) anomalies indicate a stronger (weaker) than average current. There is a significant positive correlation (r = 0.5, p < 0.05) between inshore transport success and the coastal poleward flow anomalies (Fig. 6.9c). The southward transport was determined by calculating the number of particles advected south from the inshore domain (<200 m isobath) which crosses 35°S. Indeed, the southward transport of these particles shows that positive southward transport anomalies are related to stronger poleward current (r = -0.34, p < 0.05) (Fig. 6.9c). However, there are some occurrences when this relationship does not hold, such as during mid-1998 where there was a stronger than usual poleward flow (negative anomalies) that drove a southward transport but positive anomalies in inshore transport. Furthermore, 2011 showed a stronger than usual poleward flow but negative anomalies of south transport did not occur.

Offshore mesoscale turbulence (EKE) might have an impact on inshore transport success if the particles become advected offshore into this turbulent region. Indeed, a significant negative correlation exists (r = -0.28, p <0.05) (Fig. 6.9d). Correlation maps of

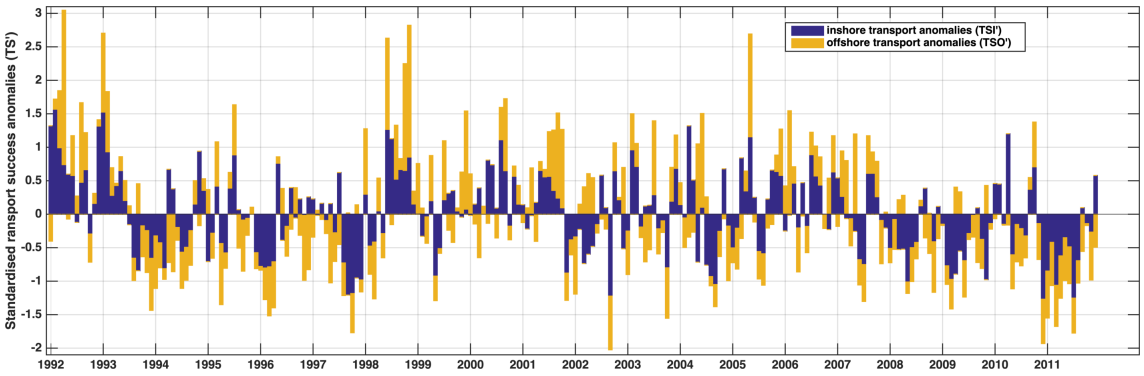

Figure 6.8: Same as in Fig. 6.4 but it is plotted in cumulated bars of inshore (TSI′: blue) and offshore (TSO′: orange) transport anomalies such that TSI′ + TSO′ = TS′

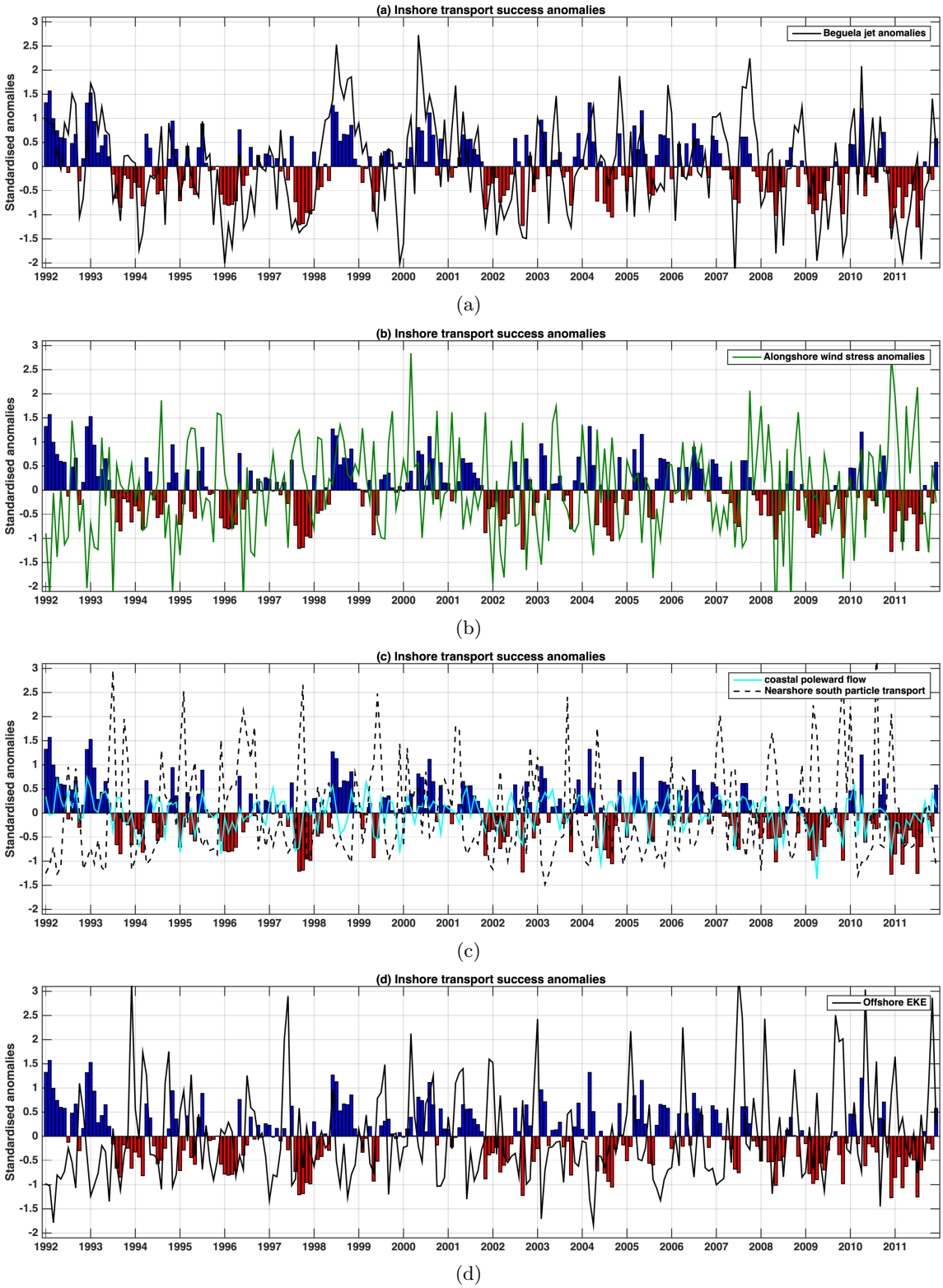

Figure 6.9: Standardised time-series of monthly inshore transport anomalies (bar graph) and superimposed is: (a) Benguela Jet anomalies (black line), (b) Alongshore wind stress anomalies (green line), (c) Coastal poleward flow (cyan) plus the nearshore southward transport of particles (dashed black line) and, (d) the offshore EKE anomalies.

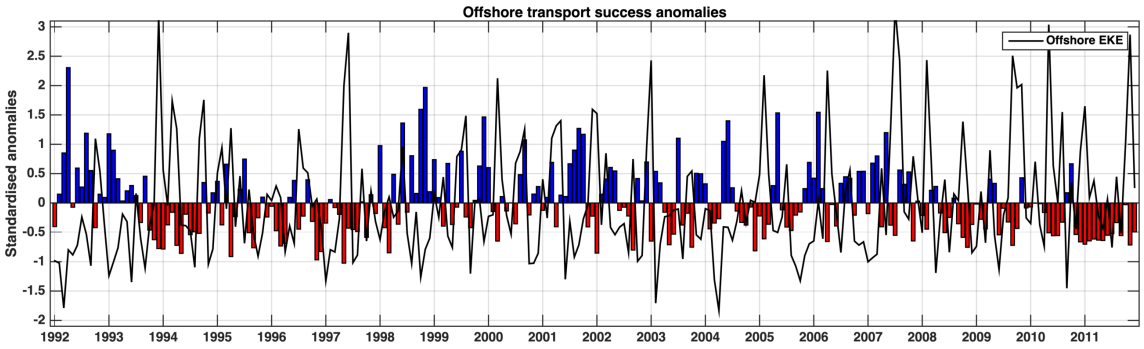

Figure 6.10: Standardised time-series of monthly offshore transport anomalies (bar graph) and EKE anomalies are superimposed as a black line.

EKE and inshore transport success anomalies further reveal that this negative correlation extends shoreward indicating that TSI′ becomes negative when the high turbulence is located closer to the shelf-edge.

The anomalies of offshore transport success and EKE are shown in Fig. 6.10 with a significant negative correlation (r=-0.31, $p < 0.05$) between them. As expected increased mesoscale turbulence leads to more dispersion which is unfavourable for offshore transport success. However, it is essentially the increased EKE case that is important as when reduced EKE events are considered, there is no obvious impact on transport success. There are also cases such as during late 1994 and early 1997 when negative offshore transport was associated with a negative offshore EKE.

Our analysis reveals that the transport success variability cannot be described by only one individual physical driver. Future work should preferably use the combinations of multiple drivers. Although multiple drivers are typically responsible for inshore transport success anomalies, it appears that particles must remain inshore where they can transported northward by the Benguela Jet for positive transport success. Also, periods (*i.e.* late-1993,late-1997, mid-2004, early 2008 and mid-2010 to mid-2011) with anomalously strong upwelling winds result in the removal of particles away from the shelf via offshore Ekman transport. This offshore loss can be counteracted to some extent when the Benguela Jet is anomalously strong and thus able to act as a barrier. On the other hand, a weak Benguela Jet does not necessarily mean negative inshore transport, espe-

cially if there is no offshore or southward loss of particles. Coastal poleward flow driven by negative wind stress curl, can lead to southward advection of particles. It is the offshore region which experiences strong mesoscale turbulence. Consequently, anomalously high mesoscale turbulence which if sufficiently large may leads to the dispersion of offshore particles or those inshore particles that have become advected offshore.

6.5 Cross-shore transport

Cross-shore transport determines the extent to which particles are impacted by the offshore mesoscale dynamics. In this section, we investigate whether particles have drifted further offshore away from the influence of the coastal Benguela Jet and how this offshore advection may have affected transport success. Furthermore, we consider how this offshore transport could be linked to the influence of mesoscale eddies.

To determine the cross-shore displacement (Δx) of successful particles, the distance (x) of an individual particle trajectory is calculated from the 500 m isobath at their point of release (t_l =1) to a time before their entry into the target area. Δx is calculated as follows:

$$\Delta x_i(t_l) = x_i(t_l) - x_i(t_{l=1}) \tag{6.4}$$

where i is the individual Lagrangian particle, x is the distance of the particle trajectory from the 500 m isobath at time t_l (12 hourly intervals). For the purpose of this analysis, four cases of cross-shore displacements are considered: two are for successful inshore particles, and the other two are for successful offshore particles.

6.5.1 Inshore particles

A first group of particles was selected by identifying those having, at any time, a distance (x) lower than 50 km. Each particle belonging to this inshore group was never displaced during its journey more than 50 km west (offshore) of its initial distance from the 500 m isobath. These particles are considered to have travelled inshore (TSII). Anomalies (TSII$'$) were standardised as follows:

$$TSII'_m = \frac{TSII_m - \overline{TSII_m}}{\sigma TS_m} \tag{6.5}$$

The second inshore group are defined as those that were displaced at any time, more than 50 km west of their initial position from the 500 m isobath and are considered to have travelled offshore (TSIO). Anomalies (TSIO$'$) are again standardised as follows:

$$TSIO'_m = \frac{TSIO_m - \overline{TSIO_m}}{\sigma TS_m} \tag{6.6}$$

An example of typical trajectories considered as belonging to the TSII (cyan) and TSIO (magenta) groups are presented in Fig. 6.11. The trajectory associated with TSIO group is characterised by a long-distance offshore loop and it is more likely that this particle has been impacted by offshore mesoscale turbulence.

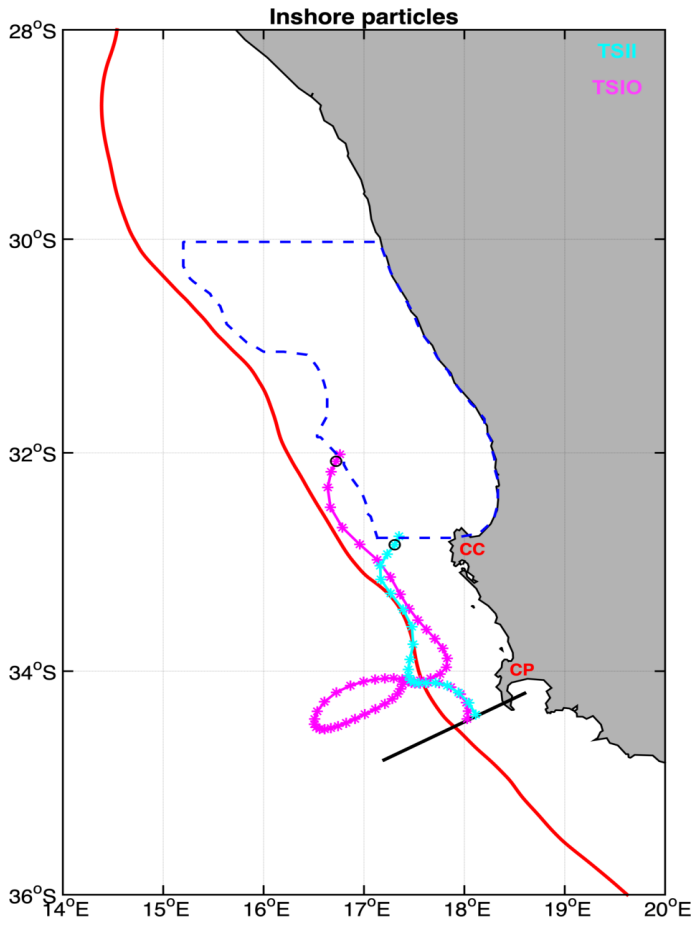

Figure 6.11: An example of the two individual trajectories plotted from their initial position on the SARP line (black line) to their entry into the target area (blue dashed polygon) corresponding to the groups of cross-shore displacement of particles originating from the inshore section: TSII in cyan and TSIO in magenta.

Figure 6.12a shows time-series of normalised anomalies of inshore transport (black line) and of successful particles that did not go further than 50 km west of their initial distance from the 500 m isobath (TSII′). Inshore transport success anomaly is significantly correlated with TSII′ ($r = 0.85$, $p < 0.05$). The two time-series appear to be highly coherent. It means that a majority of the successful particles that were released inshore did not extend at any time more than 50 km west of their initial distance from the 500 m isobath. The significant positive ($r = 0.59$, $p < 0.05$) correlation of TSII′ with the Benguela Jet anomalies suggest that the jet entrainment of the inshore particles is important for their success. On the other hand, negative anomalies of TSII′ are impacted by their removal (loss) from the shelf via offshore Ekman transport and southward transport. There is a weak but still significant negative correlation ($r = -0.17$, $p < 0.05$) between TSII anoma-

lies and alongshore wind anomalies suggesting that positive wind anomalies are relatively important. A stronger relationship (positive) exists between TSII′ and the poleward flow ($r = 0.41$, $p < 0.05$) but that with EKE is relatively weak and negative ($r = -0.25$, $p < 0.05$).

On the other hand, there is no correlation ($r = 0.07$) between inshore transport success anomalies (particles that were released inshore) and successful inshore particles that were once displaced during their journey more than 50km west of their initial position from the 500m isobath (TSIO′) (Fig. 6.12b). Their anomalies have little impact on TSI′, most of whose variability comes from TSII′ group. This further suggests that for successful transport of inshore particles, the particles have to remain on the shelf under the influence of the Benguela Jet and that they have low a chance of returning if they become transported out into the turbulent offshore domain.

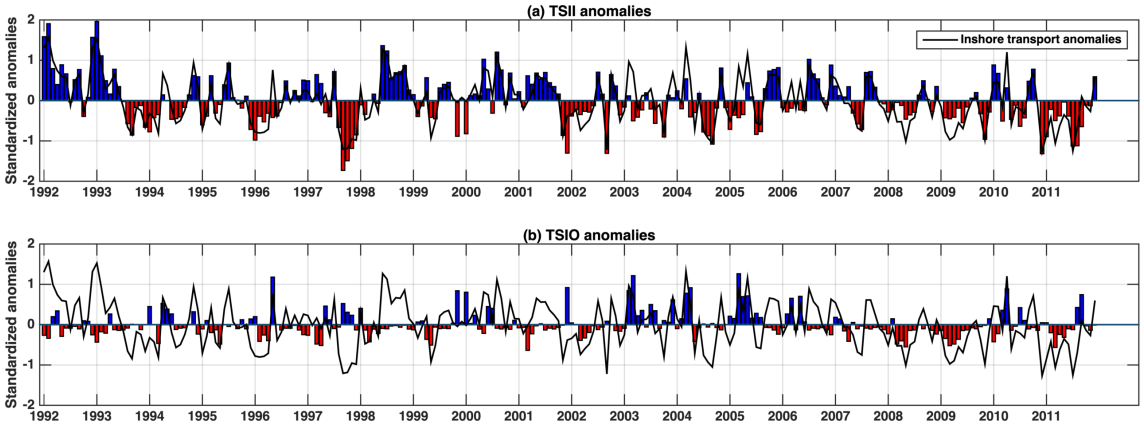

Figure 6.12: Standardised time-series (bar graph) of monthly successfully transported: (a) inshore particles that were displaced less than 50 km offshore from their initial distance from the 500 m isobath (TSII′) and, (b) inshore particles that were displaced more than 50 km offshore from their initial distance from the 500 m isobath (TSIO′) anomalies. Anomalies of inshore transport success (TSI′) are superimposed in a black line.

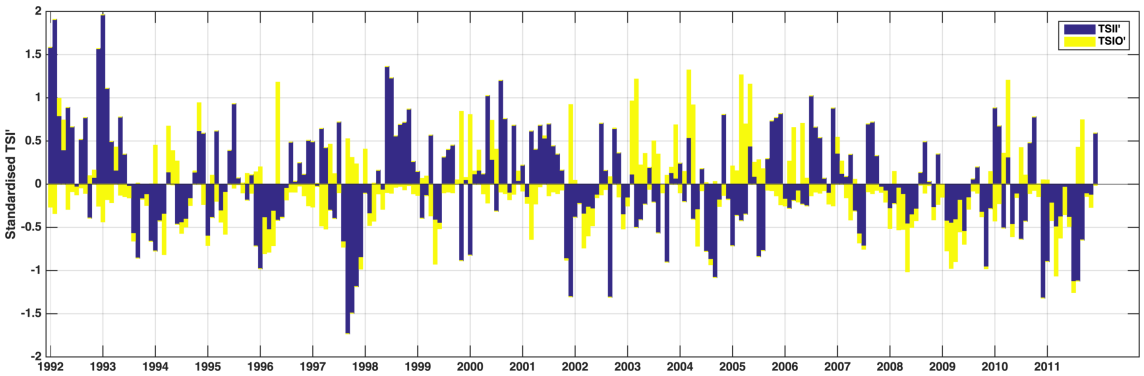

Figure 6.13: Inshore transport success anomalies (TSI′) shown as cumulative bars of successful particles that were not displaced beyond 50 km of their initial distance from the 500 m isobath (TSII′: blue) and inshore particles that were displaced more than 50 km of their initial distance from the 500 m isobath (TSIO′: yellow) such that $TSI' = TSII' + TSIO'$.

6.5.2 Offshore particles

Similarly, the offshore displacement of particles originating in the offshore section is analysed. The TSOI group is associated with successful offshore particles that did not get displaced more than 50 km west (offshore) of their initial distance from the 500 m isobath and are considered to have followed the shelf-edge. An example of such a trajectory is shown as a purple line in Fig. 6.14. Their normalised anomalies were calculated as follows:

$$TSOI'_m = \frac{TSOI_m - \overline{TSII_m}}{\sigma TS_m} \tag{6.7}$$

The second offshore group (TSOO) is associated with successful offshore particles that were displaced, at least once, to a distance greater than 50 km west (offshore) of their initial distance from the 500 m isobath. These particles were advected away from the shelf-edge and further into the open ocean. An example of their trajectory example is shown as the green line in Fig. 6.14. Their normalised anomalies were calculated as follows:

$$TSOO'_m = \frac{TSOO_m - \overline{TSII_m}}{\sigma TS_m} \tag{6.8}$$

For offshore particles, there is a positive correlation ($r = 0.9$, $p < 0.05$) between off-

shore transport success anomalies and TSOI anomalies (Fig. 6.15a). A significant negative correlation ($r = -0.31$, $p < 0.05$) exists with offshore EKE anomalies.

There is a significant but relatively weak positive relationship ($r = 0.24$, $p < 0.05$), between TSOO anomalies and offshore transport success anomalies (Fig. 6.15b). This result suggests that particles from the offshore section that become displaced further offshore can return somehow and contribute significantly to offshore transport success. However, no relationship was found between this group and EKE (mesoscale turbulence).

In summary, positive transport success of offshore particles is significantly related to particles that don't get advected too far from the shelf-edge, and their success is linked to low mesoscale turbulence. Interestingly, some offshore particles that get transported further into the open ocean do manage to come back inshore and contribute to positive offshore transport success. However, these offshore particles were found not to be linked to the general EKE turbulence. Thus, cross-shore transport mechanism could be better explained by the circulation patterns associated with mesoscale eddies rather than EKE associated with their turbulence.

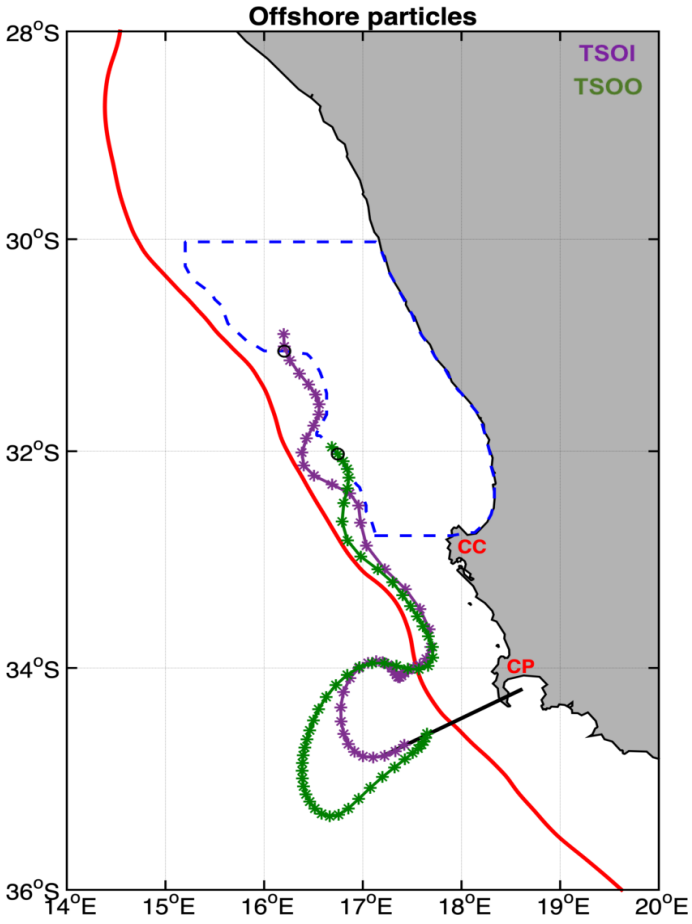

Figure 6.14: Same as Fig. 6.11 but corresponding to the groups of cross-shore displacement of particles originating from the offshore section: TSOI in purple and TSOO in green

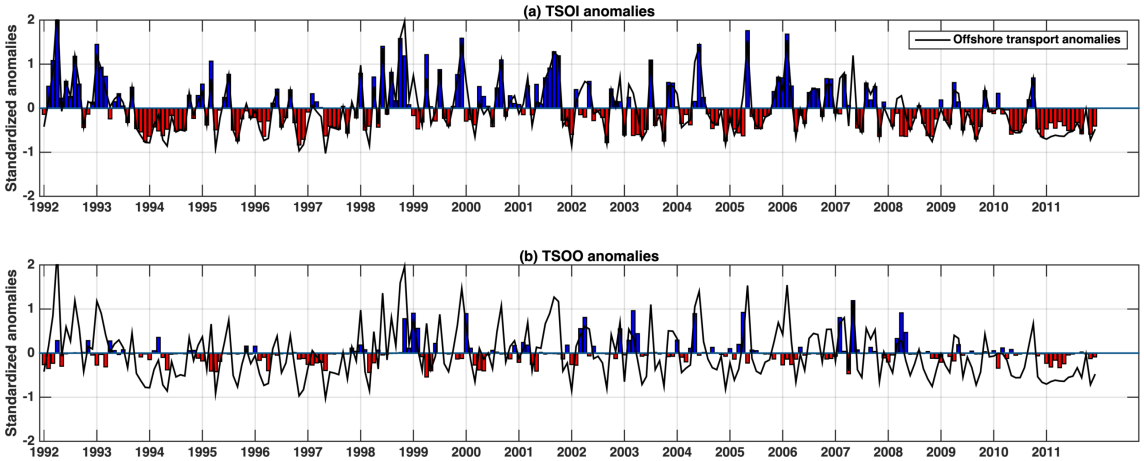

Figure 6.15: Normalised time-series (bar graph) of monthly: (a) offshore particles that were never displaced during their journey more than 50 km offshore from their initial distance from the 500 m isobath (TSOI′) and, (b) offshore particles that were displaced at least once, more than 50 km offshore from their initial distance from the 500 m isobath (TSOO′) anomalies. Anomalies of offshore transport success (TSO′) are superimposed in a black line.

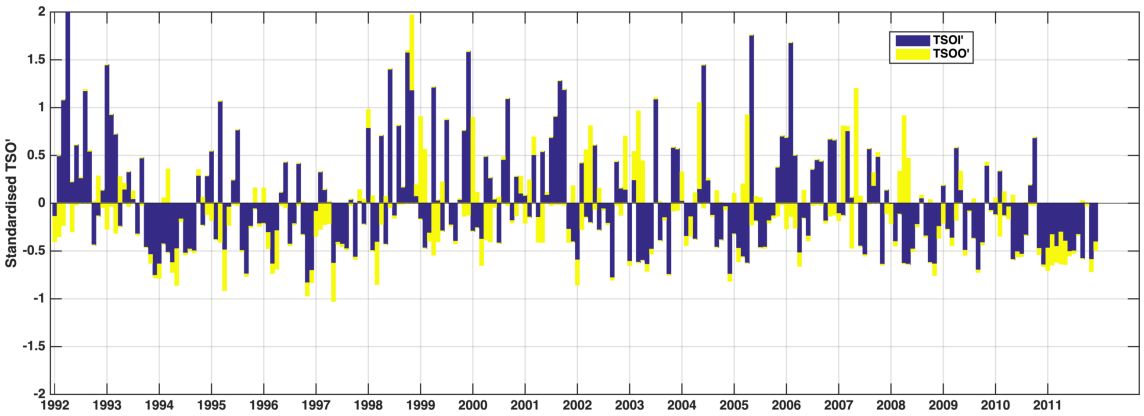

Figure 6.16: Offshore transport success anomalies (TSO′) shown as cumulative bars of successful particles that were not displaced beyond 50 km of their initial distance from the 500 m isobath (TSOI′:blue) and inshore particles that were displaced more than 50 km of their initial distance from the 500 m isobath (TSOO′:yellow) such that $TSO' = TSOI' + TSOO'$

6.6 The role of mesoscale eddies

As previously noted, particles need to be retained over the shelf region in order to achieve transport success, whereas the offshore particles need to be advected onshore into the Benguela Jet away from the turbulent eddy field to become successful. It is suggested that Ekman dynamics can play a role in the cross-shore displacement of the inshore particles.

Offshore loss of inshore particles can be attributed to strong offshore Ekman transport whereas retention is favoured by a weak offshore Ekman transport. Although that might be true in general, there are also some events where the loss of inshore particles was not related to offshore Ekman transport or to southward transport. Thus wind alone does not generate the cross-shelf transport, so other mechanisms must be responsible. However, it is also unknown as to which mechanism is responsible for the onshore transport of particles that do not get dispersed into the open ocean.

One possible mechanism could be a temporary localised cross-shore current induced by mesoscale eddies. Indeed, visual analysis of the particle trajectories reveals that the trajectories of particles found in the offshore domain are very chaotic and characterised by large loops indicative of mesoscale eddy structures. It is also evident that offshore (westward) transport is associated with anticyclonic eddies that pass north-westward in the vicinity

of offshore Cape Point. On the other hand, shoreward (eastward) transport occurs from the circulation associated with shelf-edge cyclonic eddies in a region between just north of the SARP line and offshore of St Helena Bay.

However, before investigating the role of mesoscale eddies, it is useful to first characterise the eddy mean properties such as their sign, radius, amplitude, duration and their point of origin in the SBUS. An eddy detection and tracking algorithm was applied to the daily SSH fields from the R3km simulation for the 1992-2011 period for this purpose. The details of this algorithm may be found in Appendix B.

Table 6.1 shows the mean eddy properties that were detected and tracked in the SBUS between 36°S - 32°S and 14°E - 20°E. A total of 2923 mesoscale eddies were tracked within the region with the vast majority of them being cyclonic (73.8%). The cyclonic eddies mostly originate over the shelf and along the shelf-edge (Fig. 6.17a), tend to have a smaller mean diameter (39.9 km) and amplitude of 3.1 cm and have a shorter duration (11 days). These small eddies could be associated to the barotropic/baroclinic instabilities of the upwelling front (*Hall and Lutjeharms*, 2011; *Rubio et al.*, 2009). The most massive cyclonic eddy detected was 160 km in diameter and generated north-east of the Agulhas retroflection. The predominance of cyclones is consistent with the findings of *Rubio et al.* (2009); however, these authors were not able to resolve the smaller cyclonic structures between the coast and the 500 m isobath due to their coarse resolution model (1/10°).

The slightly larger (diameter ∼30 km and amplitude ∼2 cm) anticyclonic eddies mostly originate over the deep ocean, with the largest eddies (>150 km) originating further south in the region of the Agulhas Current retroflection (Fig. 6.17b). Their larger size and less frequent occurrence are consistent with what is expected of Agulhas rings. The largest anticyclonic eddy detected was 230 km, again consistent with a Agulhas ring (*Lutjeharms and Van Ballegooyen*, 1988; *Boebel et al.*, 2003).

Anticyclonic eddies

Anticyclones with diameters that range from 20 km to 230 km were tracked, and it was found out that there was some indication that the passage of large anticyclones near the

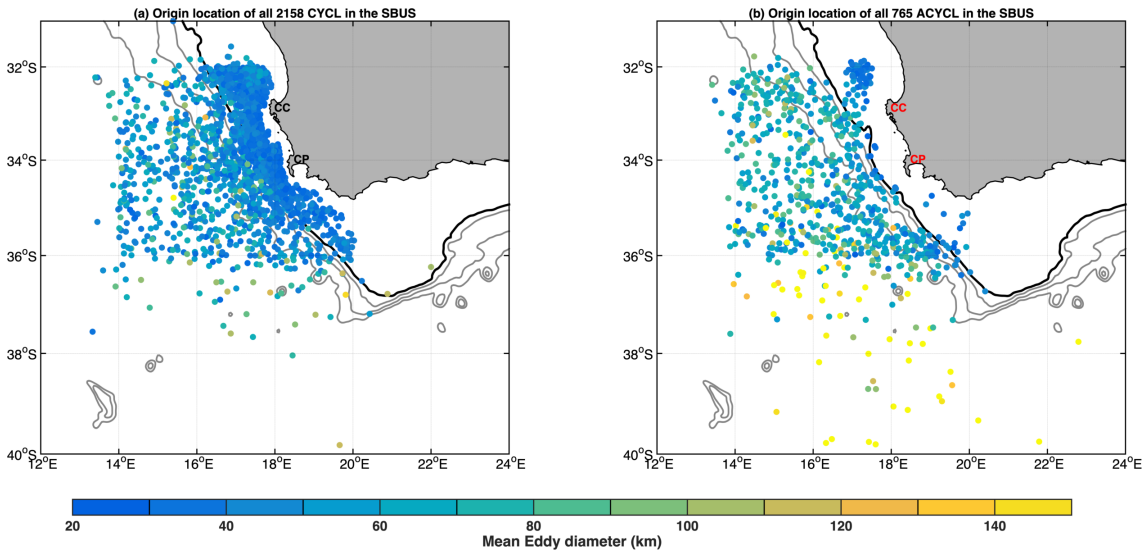

Figure 6.17: A map showing the distribution of eddies by their generation site indicated by the circles and their mean diameter (in color) during their duration in the region 36°S - 32°and 14°E - 20°E for: (a) cyclonic eddies and, (b) anti-cyclonic eddies. The background contours are the 500 m isobath in black and in grey is the 1000 m, 2000 m and 3000 m isobaths

SARP line can result in the offshore transport of particles. *Duncombe-Rae et al.* (1992) has documented the effects of an Agulhas Ring interacting with the Benguela upwelling front which generated a long filament of cold water extending further offshore (*Payne et al.*, 1992). It has been suggested that these filaments can entrain coastal biota a long distance offshore because of their associated offshore volume transport which *Lutjeharms et al.* (1991) estimated to be about 1.5 Sv.

To evaluate the possible influences of a Agulhas ring on the region, large anticyclones with a radius (R_{eddy}) greater than 100 km (200 km diameter) were identified and assumed to be Agulhas rings from their origin point and trajectories. A total of 38 Agulhas rings

	Cyclones	**Anticyclones**
Total number	2158 (73.8%)	765 (26.2%)
Duration (days)	11	18
Diameter (km)	39.9 (max = 160)	65.6 (max = 230)
Amplitude (cm)	3.1	5.2

Table 6.1: Summary of mean (1992-2011) cyclonic and anticyclonic eddy properties in the R3km simulation in the region 36°S - 32°and 14°E - 20°E.

were identified in the region 36°S - 32°and 14°E - 20°E between January 1992 and December 2011, their trajectories are shown in Fig 6.18a. These trajectories represent rings that follow the northern route (Fig 6.18b) defined by *Dencausse et al.* (2010a). However, only Agulhas rings whose paths were close to the SARP line (34°S-35°S) are considered below. Their closeness implies the interaction and influence of these rings on the distribution of particles.

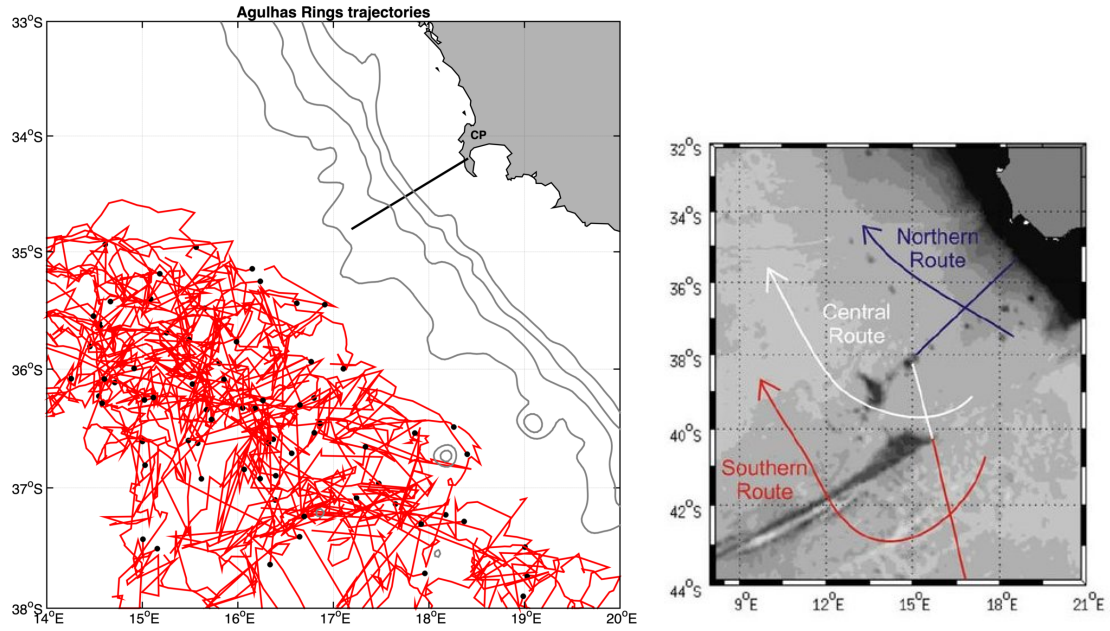

Figure 6.18: Left: trajectories of Agulhas rings (different colors) tracked into the south-eastern Cape Basin following the Northern route (blue) defined by *Dencausse et al.* (2010a) between January 1992 and December 2011. The black solid circles indicate where the rings were first detected. The black across-shore line off Cape Point represents the SARP line and grey lines are the 500 m, 1000 m, 2000 m and 3000 m isobaths. Right: the three routes - Northern, Central and Southern defined by *Dencausse et al.* (2010a)

An Agulhas Ring was considered to be in the range of influence in the region if the distance of its centre is less than $1.5\times R_{eddy}$ from the 3000 m isobath and less than $1.5\times R_{eddy}$ south of the SARP line. Out of the 38 Agulhas rings, 18 of them interacted with the 3000 m isobath for a total of 177 days with 8 of these interacting with the shelf-edge (500 m isobath). The interaction duration with the shelf is relatively brief, a total of 36 days. Due to their brevity and infrequent interaction with the shelf-edge, the rings were found not to affect the inshore transport success anomalies. Therefore only the results of their offshore influence are discussed below.

For each offshore interaction with the rings, their influence is evaluated through their duration, minimum and mean distance during their interaction (Table 6.2) with their associated offshore transport success anomalies. The results indicate that not all interactions lead to the effect of offshore transport success. The level of impact is independent but is also influenced by the minimum distance, mean distance and most importantly, its position relative to the SARP line (offshore or south). Out of the 18 Agulhas ring interactions, only 5 (28%) resulted in positive offshore transport success anomalies, with the vast majority (72%) led to negative transport success.

Years	**Months**	**Days of influence**	**Minimum distance (km)**	**Mean distance (km)**	**Offshore transport anomaly**
1992	January*	12	58	91	negative (-0.40)
1993	March	10	102	115	positive (0.41)
	September*	3	86	90	positive (0.45)
1994	October	20	95	116	positive (0.35)
	November	7	120	139	negative (-0.17)
1996	November	10	121	136	negative (-0.94)
1997	April	1	105	105	negative (-0.19)
2000	January*	5	74	82	positive (0.60)
	February*	7	61	83	negative (-0.15)
2001	January	13	124	159	negative (-0.12)
	December*	7	77	98	negative (-0.22)
2002	January	5	116	127	negative (-0.85)
2004	November*	19	42	75	negative (-0.07)
	December*	7	86	102	negative (-0.82)
2008	September*	8	63	80	negative (-0.35)
	October*	31	51	77	negative (-0.56)
	November	9	83	119	negative (-0.75)
2011	October	3	91	99	negative (-0.03)

Table 6.2: A summary of the occurrence of an Agulhas Ring interaction with the 3000 m isobath in the vicinity of the SARP in terms of years, months, days of influence, its minimum distance (km) and mean distance (km). Their associated offshore transport success anomaly is also presented. The instances when the ring had a interaction with the shelf-edge (500 m isobath) is denoted by *.

The difference in the influence of Agulhas rings on the offshore displacement of particles can be inferred by looking at different scenarios of trajectories. Fig. 6.19 (top row) represents a scenario associated with the passage of an Agulhas Ring that occurred in January 2000, which had less impact on the offshore displacement of particles or on offshore transport success. Although the ring was located close to the 3000 m isobath, its centre

was situated well south of the SARP line. Hence, this ring had minimal impact on the cross-shore transport of particles and thus, on offshore transport success. Moreover, the presence of a cyclonic eddy indicated by negative SSH anomaly on the shelf-edge between Cape Point and Cape Columbine (Fig. 6.19a) favoured the onshore transport of offshore particles (Fig. 6.19d).

On the other hand, the January 2002 shows how the combination of the closeness of the Agulhas ring to the SARP line and its short interaction resulted in a large number particles being entrained and thus transported offshore (Fig. 6.19: bottom row).

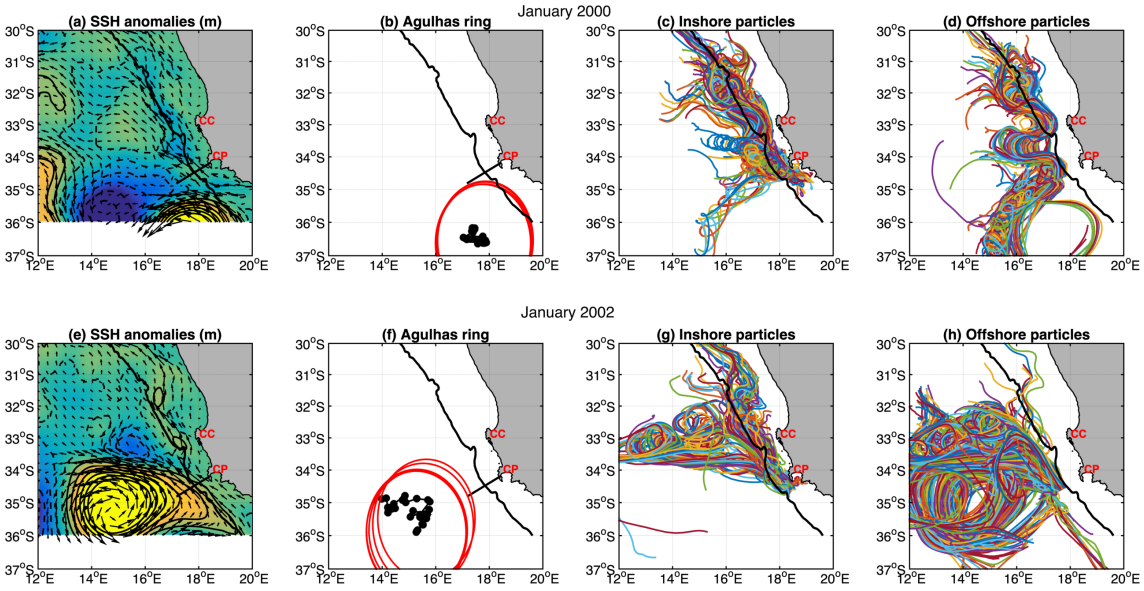

Figure 6.19: (a) Monthly mean SSH anomalies (m) in color and vectors superimposed corresponds to monthly mean surface current velocities. (b) The location of the detected Agulhas ring (black circles) during their interaction duration and the red circle represents size of the eddy at $1.5 \times R_{eddy}$. (c-d) shows the trajectories of inshore particles and offshore particles characteristic of the anticyclonic circulations. The black contour represents the 500 m isobath. The top row represents the scenario which is associated with an Agulhas ring was passed further south (January 2000) and whereas, the bottom row represents the scenario associated an Agulhas ring passing north near the SARP line (January 2002).

Cyclonic eddies

There is evidence that positive offshore transport anomalies (*i.e.* particles that were release on the offshore side of the SARP line) are influenced mainly by shelf-edge cyclonic eddies since these eddies transport offshore particles shoreward. The crucial feature favouring the on-shelf transport of particles is the small size of the cyclonic eddies, their short duration

and their clockwise circulation. However, despite their frequent occurrence at the shelf-edge, their influence is difficult to quantify, as particles are also affected by anticyclonic eddies at the SARP line. Fig. 6.20 shows an example (April 1992) illustrating how a shelf-edge cyclonic eddy can affect the cross-shelf transport of particles. Note the onshore transport of particles in the blue box (Fig. 6.20c,d) and their coincidence with the location of shelf-edge eddies (Fig. 6.20b). This month had the highest positive offshore transport success.

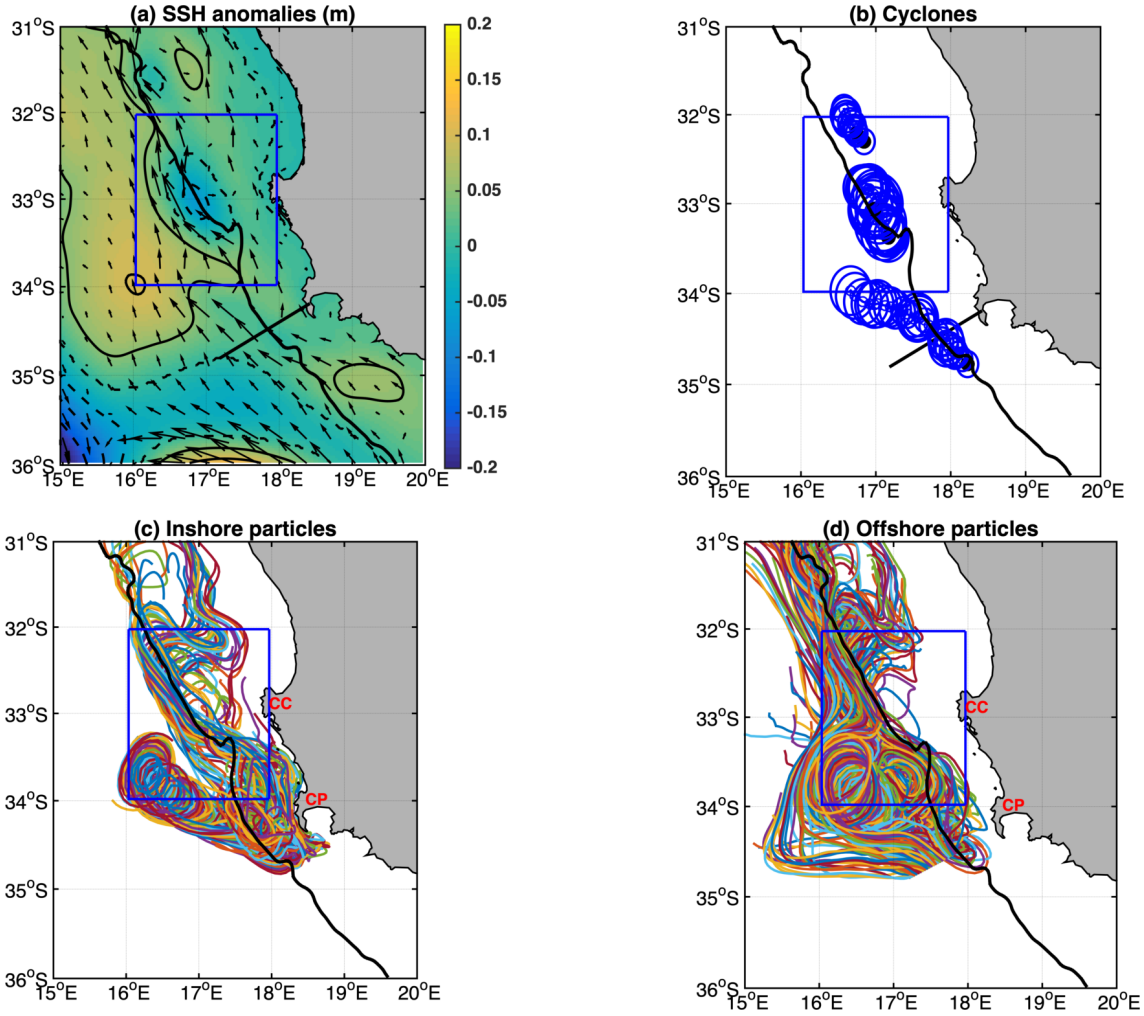

Figure 6.20: (a) April 1992 monthly mean SSH anomalies (m) in color and vectors superimposed corresponds to monthly mean surface current velocities. (b) The number of cyclonic eddies (blue circles) detected between Cape Point and Cape Columbine with their position at each time-step during their life-time is indicated by individual circles. (c-d) shows the trajectories of inshore particles and offshore particles characteristic of the cyclonic circulations.

In summary, the results suggest that mesoscale eddies play a role in the cross-shore

transport of particles. However, the relationship is ambiguous because the characteristics of coherent eddy structures are very variable in terms of their different polarities (circulation patterns), life-time, sizes, intensity and their proximity to the shelf or slope. Nevertheless, transport success variability of the offshore particle is strongly linked to the propagation of Agulhas rings, especially the north-westward propagating rings. The large size, long occupation, a strong associated anti-clockwise circulation of the rings leads to a more westward distribution of particles and negative offshore transport. However, these rings may have less impact if their passage occurs further south of the SARP line.

These results suggest that shelf-edge cyclonic eddies found between Cape Point and Cape Columbine can lead to favourable offshore transport success by transporting particles inshore into the Benguela Jet. However, since these eddies are present almost all the time, it is not easy to individually link them to specific events of transport success. Thus their influence is dependent on whether the initial conditions at the SARP are favourable for the northward transport instead of offshore.

The quantification of the impact of mesoscale eddies is further complicated by the coexistence of both cyclonic and anticyclonic eddies. Fig. 6.21 shows that there is a positive correlation between anomalies of transport success and nearshore EKE between north of Cape Point and offshore off St Helena where Fig. 6.17a indicate cyclonic eddies are prevalent.

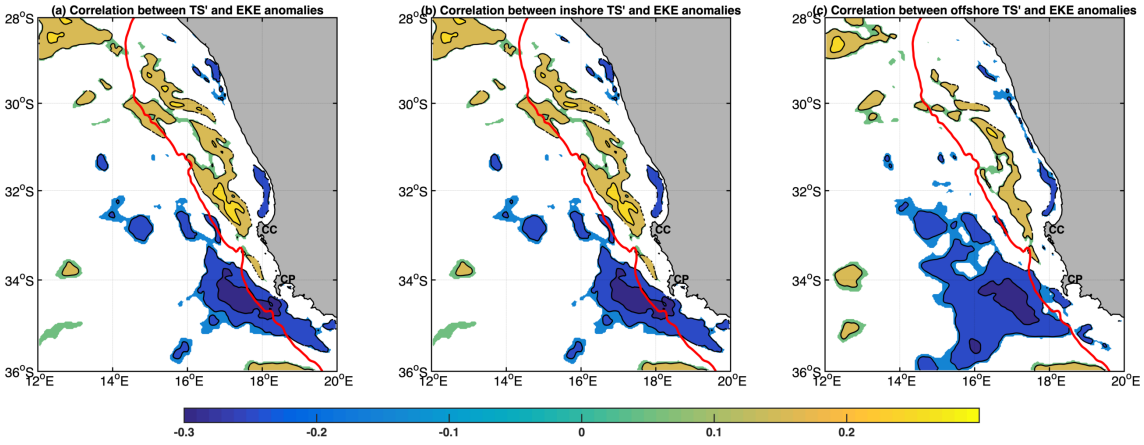

Figure 6.21: Correlation map showing only the significant correlation at 95% confidence level between monthly transport success time-series and EKE anomalies: (a) total transport success anomalies (TS′), (b) inshore transport success anomalies (TSI′) and, (c) offshore transport success anomalies (TSO′). The 500 m isobath separating the inshore and offshore region is superimposed as the red line.

This result supports the positive impact of these eddies on transport success. Note that the nearshore negative correlation off Cape Point to the south of it seen in Fig. 6.21b corresponds to cyclonic eddies whose presence here was observed to transport particles southward, and thereby contributing to negative inshore transport success. Whereas the region of negative correlation offshore coincides with the north-westward propagation of anticyclonic eddies with the offshore influence limited to 15°E. This impact of the anticyclonic eddies (Agulhas rings) depends on their closeness to the SARP line.

6.7 Discussion and conclusions

In the southern Benguela upwelling system, variability in annual recruitment of small pelagic fish has long been a significant concern to fisheries oceanographers. Successful advection is one of the factors required for the survival of fish larvae, and this chapter was aimed at relating anomalous transport success events to local physical processes such as i) wind surface forcing (Ekman transport, Benguela Jet, poleward current) and ii) mesoscale dynamics. The interannual variability in physical transport processes is investigated using a 3 km high-resolution simulation forced with 6-hourly atmospheric CFSR data provided for 20 years (1992-2011). The approach consisted of computing monthly transport success anomalies and characterising their wind-driven ocean circulation and mesoscale turbulence.

In the absence of mesoscale eddy influence (especially anticyclones), the Benguela Jet was found to play a pivotal role in the successful transport variability of particles originating inshore. If inshore particles remain entrained in the coastal Benguela Jet, they have a higher probability of being successfully transported. More importantly, it was shown that mesoscale eddies also contribute significantly to the variability of successful transport for particles originating offshore in particular. There is a difference in the role of cyclonic shelf-edge eddies off Cape Point that cause negative transport success and the cyclonic shelf-edge eddies off Cape Columbine and St Helena Bay that lead to more positive transport success.

In contrast, the passage of large anticyclonic eddies (Agulhas rings) in the vicinity of Cape Point can have a negative effect if they pass close enough to interact with the particles originating offshore.

Over the shelf, most of the variability in the transport success of particles originating from inshore is associated with a coherent Benguela Jet between the 200 m and 500 m isobath. Negative events of transport success could be related to their removal by wind-driven shelf circulation such as strong offshore Ekman transport and by a poleward current. However, the influence of Ekman transport is relatively small because a strong Benguela Jet can inhibit the offshore transport of inshore particles by the wind. Hence, the impact of large-scale interannual climate modes perturbations such as ENSO and SAM which influence wind forcing over the region was found to be small (not shown) and was therefore not discussed in this chapter.

For particles originating offshore to have positive transport success, the particle should not get advected offshore into the open ocean away from the influence of the shelf-edge cyclonic eddies. The passage of large anticyclonic eddies close to the SARP line was found to have a negative impact on transport success as they are associated with westward surface velocities, which advect particles away from the shelf-edge. This impact is limited to being only likely near Cape Point (35°S-34°S). This is not surprising, since the region is located in the vicinity of the 'Cape Cauldron' (*Lutjeharms et al.*, 2003) where there is high turbulence associated with the north-westward passage of Agulhas rings and other eddies (*Veitch et al.*, 2009; *Veitch and Penven*, 2017). Interaction of an Agulhas ring with the southern Benguela shelf-edge was found to be relatively infrequent since only 18 interactions occurred over the 20 years model simulation.

This study investigates in detail how physical processes can impact transport success between Cape Point and St Helena Bay. The next step is to investigate whether our results can help to explain and understand anchovy recruitment variability. This will require the incorporation of biological properties such as egg density, diel vertical motion, mortality

due to starvation and predation (*Huggett et al.*, 2003; *Mullon et al.*, 2003; *Parada et al.*, 2003, 2008; *Koné et al.*, 2013). This is however out of scope of this thesis but we are convinced that the physical processes we identified and the interannual variability of their contribution to transport success could be used to bring some light on the processes governing small pelagic fish recruitment variability in the SBUS.

This study confirms that the variability Benguela Jet is a primary driving mechanism the alongshore transport success and thus can help to explain some of the variability observed in recruitment strength of small pelagic fish. Therefore, it is essential to study response of the jet to large-scale influences such as Agulhas leakage, modes climate of variability as well as its long-term trends in order to anticipate changes that might occur in the light of climate change. It is known for example that the Agulhas leakage itself is sensitive to both the mid-latitudes westerlies and the trade winds over the South Indian Ocean (*Durgadoo et al.*, 2013; *Loveday et al.*, 2014). A better understanding of the Benguela Jet would help in the management of the marine ecosystem in the area.

This chapter also showed that the cross-shore transport contributes to the variability in transport success through the activity of mesoscale eddies. It is therefore critical to understand the dynamics of the cross-shore transport due to its importance for variability of regional ecosystems. Mesoscale eddies were found to exert a stronger influence of transport success than the local winds.

It is important to note that the results presented may be sensitive to model resolution and to the ability of the model to adequately capture the Agulhas leakage. Overestimation of the Agulhas leakage and their associated mesoscale turbulence which often occurs in coarse resolution models is likely to lead to unrealistic estimates of transport success. Moreover, underestimation of the abundance of small cyclonic sheld-edge eddies in such models could also lead to the underestimation of the inshore advection of offshore particles and associated transport success.

Chapter 7

Summary and future research

There have been numerous previous works interested in the alongshore Lagrangian connectivity in the southern Benguela upwelling system (SBUS) for fisheries related applications (*Boyd et al.*, 1998; *Hutchings et al.*, 1998; *Huggett et al.*, 2003; *Mullon et al.*, 2003; *Parada et al.*, 2003; *Lett et al.*, 2006; *Miller et al.*, 2006; *Parada et al.*, 2008; *Koné et al.*, 2013). In those studies, transport success was investigated as one of the factors modulating recruitment success and used as proxy for the Western Agulhas Bank/southern Benguela connectivity. These studies were based on the advection of Lagrangian particles by ocean currents produced by regional ocean circulation models. They discussed the sensitivity to spawning depth, the spawning area and some biological parameters like mortality (below a given temperature threshold and time-threshold to reach the recruitment area) (*Huggett et al.*, 2003; *Mullon et al.*, 2003; *Parada et al.*, 2003; *Lett et al.*, 2006; *Miller et al.*, 2006; *Parada et al.*, 2008; *Koné et al.*, 2013). However, none of this previous work analysed in detail the characteristics of the ocean dynamics that led to the simulated transport success and variability. In addition, most of these studies used outputs from ocean models with a coarse horizontal resolution (9 km for the finest one), which is not sufficient to accurately represent the mesoscale structures associated with the Benguela Jet and even less the inner shelf (less than 100 m depth) flows. Moreover, the ocean models were forced with atmospheric seasonal monthly climatology precluding studies of externally forced interannual variability of transport success.

In this thesis, numerical model simulations of the SBUS coupled with particle tracking

experiments were used to investigate Lagrangian pathways in the SBUS and their link to the oceanic circulation. This work is motivated by questions arising from the effect of ocean currents on fish eggs and larvae during their journey from the spawning to nursery grounds in the southern Benguela ecosystem. We used newly developed 20-year realistic simulations of the Benguela upwelling system and a series of Lagrangian experiments to identify the pathways connecting the spawning and nursery grounds as well as important processes impacting the connectivity between the two regions.

In **Chapter 3**, a mesoscale eddy resolving (1/15°, 'BENGR15') numerical simulation of the Benguela system the Regional Ocean Modelling System (ROMS) used as a reference simulation is described. The simulation spans from 1989 to 2010 (22 years) with bulk surface forcing (wind, heat and freshwater fluxes) that used CFSR atmospheric reanalysis and a seasonal monthly climatology extracted from SODA at the lateral open boundaries. In contrast to previous studies, our ocean model is forced by 6-hourly variable surface forcing. The aim is to build a robust model with realistic mesoscale eddy field, Agulhas leakage and the coastal circulation.
The BENGR15 configuration is able to capture the general mean circulation patterns and the seasonal variability typical of an upwelling system such as the equatorward jet (Benguela Jet), a slope-edge poleward undercurrent (>400 m depth) and shelf-edge instabilities related to the jet. The model was also able to capture the strong eddy kinetic energy (EKE) associated with the Agulhas Current and the Agulhas retroflection. However, the simulated retroflection overestimates the leakage of warm and saline Agulhas waters into the South Atlantic Ocean. This overestimation resulted in the model exhibiting a warm bias and strong cross-shore temperature gradients that drive an associated strong Benguela Jet. Although the simulated jet is much stronger than observed, the model adequately represents the characteristic seasonal variability of the jet. This provided the confidence in using this simulation to study the seasonal variability of the alongshore connectivity.

In **Chapter 4**, the BENGR15 configuration is used to characterise the seasonal alongshore connectivity between Cape Point (34°S) and St Helena Bay (32°S) and to also

identify important physical processes impacting this connectivity. We show that transport success has a strong seasonal cycle related to the structure of the alongshore currents and their characteristic variability, including the wind-driven Ekman transport.

It was found that transport success peaks in spring (September-November) when there is an efficient fast inshore pathway taken by particles reaching St Helena Bay within 15 days. This period is the optimal window, as the jet is in its intensified state, closer to the shore, and relatively stable (coherent). At this time of the year, offshore Ekman transport is still low enough to allow particles to remain on the inshore side of the jet.

However in summer, during the peak upwelling season, the jet veers offshore which is attributable to the intensification and the broadening of the slope-edge poleward undercurrent induced by negative wind stress curl. When this happens, particles follow the offshore route where they experience an increased dispersion with less successful rate due to offshore increasing EKE values. Also, there is a decrease in transport success of inshore particles as they are advected offshore by Ekman transport. Particles taking the offshore route were found to take longer (20-30 days) to reach St Helena Bay.

These results highlight some of the physical processes essential for the dispersal of fish eggs and larvae in the SBUS. For favourable transport between the spawning and nursery grounds, fish eggs and larvae have to be entrained within the fast inshore route taken by the Benguela Jet and avoid being carried offshore into the turbulent region when the jet splits into several branches. The latter was also found to be linked to wind induced offshore Ekman transport.

In **Chapter 5**, the sensitivity of physical transport processes to increasing model resolution is discussed by nesting a 3-km resolution child grid (R3km) within the 7-km parent grid (R7km). The new simulation was run for 22 years from 1989 to 2011 with 3 years considered a spin-up time. For consistency, the simulation was also forced with 6-hourly CFSR reanalysis surface forcing, and the STRM bathymetry was interpolated on the R3km grid. The high resolution was used to study the impact of increased resolution on the fine scale shelf dynamical features and their effect on transport success. There is some impact on the dispersion of particles associated with the differences in mesoscale

variability and the poleward coastal current. However, there is not much change in the seasonal cycle of transport success because the Benguela Jet which is the a primary driver of the alongshore connectivity is always present in both simulations.

It was found that increasing the resolution results in topographically controlled features specifically over the shelf region. With the R3km, the Benguela Jet is confined between 200 m and 500 m isobaths, whereas the lower resolution R7km grid resulted in a broader offshore jet particularly in summer. An inner shelf (<200 m isobath) poleward flow emerges that is most intense in autumn in the R3km, and this poleward flow was found to be responsible for the southward transport of particles located on the shelf. Consequently, the strongest southward transport occurred in autumn. A shelf-edge constrained jet in R3km was found to be beneficial for transport of inshore particles (originating <500 m isobath) during spring and summer, whereas the intensification of the poleward flow reduced inshore transport success in autumn and winter.

Surprisingly, there was also an unexpected impact on the quantity of warm Agulhas Current leakage into the SBUS by the increase of model resolution. There is a reduction in the Agulhas leakage in the higher resolution model. As a consequence, the stratification and the cross-shore density gradient were impacted. There were differences in the intensity of the jet related to the quantity of warm Agulhas water influx in two simulations. Topographical smoothing in the lower resolution R7km simulation led to an Agulhas retroflection that occurs more westward with more leakage of warm and salty Agulhas waters into the south Atlantic Ocean. Moreover, without the topographical blockage of the shallow sea-mounts located south-east of the Agulhas Bank, most of the leakage estimated at 18.3 Sv entered close to the shelf-edge of SBUS extending north to Cape Columbine in R7km. This enhanced the cross-shelf temperature gradient driving a more intense jet in the R7km simulation. However, increasing the resolution reduced this leakage by 2 Sv to 16.3 Sv due to a better representation of topography resulting in a weaker jet and particles taking longer to reach St Helena Bay in the R3km. Notably, offshore particles (originating >500 m isobath) had a better probability of transport success in the higher resolution due to a reduction of EKE along the shelf-edge. On the other hand, offshore particles in R7km are exposed to higher EKE and tend to be largely dispersed into the open ocean with low

probability of successful transport. However, although the Agulhas leakage was different in the two simulation, this did not have much impact on the seasonal cycle of alongshore connectivity as it is mostly driven by the Benguela Jet present in both simulations.

Having identified the physical drivers (*i.e.* the Benguela Jet, Ekman transport, poleward current and shelf-edge mesoscale turbulence) of the seasonal cycle of advective pathways and transport success, in **Chapter 6** we explore interannual variability of these drivers on the interannual variability of transport success. The interannual variability of transport success is investigated using Lagrangian experiments with particles being advected by velocity fields from the R3km simulation described in previous **Chapter 5**. This study found that in addition to the Benguela Jet, mesoscale eddies also play a role in the interannual variability of transport success.

It was found that there is an interaction between competing processes that impact transport success variability. However, we find that transport success is predominately influenced by the Benguela Jet variability such that particles must either remain over the shelf in the jet or are advected towards the shelf into it. In an event that particles are removed away from the shelf and from the influence of the jet either by offshore Ekman transport or by the poleward current, this can lead to a reduced contribution of inshore particles to transport success.

The results also showed that transport success of offshore particles can contribute significantly to total transport success anomalies especially strong positive anomalies. Nevertheless, their contribution is dependent on cross-shore displacement and mesoscale eddies are able to impact on the cross-shore distance that particles are able to reach through their ability to drive a cross-isobath flow. The presence of an anti-cyclonic eddy either nearshore, south or offshore of the SARP line leads to an enhanced offshore transport of particles and negative anomalies of offshore transport success. However, the extent of their impact is related to their close proximity to the SARP line whereas, cyclonic eddies located between Cape Point and Cape Columbine can favour onshore transport leading to positive transport success. Moreover, the results suggest that the size of the eddy structures is also important. Circulations associated with large eddies such as an Agulhus ring can drive

a more pronounced offshore long-distance advection of particles than small eddies. This is consistent with the effect of shelf-cyclonic eddies, where particles can undergo a small loop offshore and back inshore.

7.1 Key Findings

The key findings of Chapter 4, 5 and 6 are summarised by addressing the scientific questions and their conclusions.

Chapter 4: What are the spatio-temporal variability and the drivers of the alongshore connectivity between Cape Point and Cape Columbine?

Two clear main Lagrangian pathways are identified. The results show that there is a very efficient inshore route that is characterised by a short connection time (<15 days). This route is mostly efficient during spring and facilitated by a nearshore and coherent (one branch) equatorward along-shelf jet. Weaker upwelling enables particles to remain over the shelf and within the jet. An offshore route is predominant during peak and late upwelling season when the jet splits into multiple branches linked to the poleward undercurrent intensification. There is increased dispersion in the offshore region with less successful rate due to offshore increasing EKE values, and particles take longer (20-30 days) to reach St Helena Bay. The successful transport from the Agulhas Bank to St Helena is attributed to wind induced modulation of the jet including the full three dimensional structure of the oceanic circulation and to its inherent turbulent nature.

Chapter 5: What is the influence of the ocean model spatial resolution on the shelf circulation features of the SBUS shelf?

Increasing the model resolution led to a better representation of the bathymetry, in particular in regions with steeper slopes and also in the shallow inner shelf region, which in turn modified the cross-shore positions and intensities of the jet including the emergence of an inner shelf poleward flow. Furthermore, the higher resolution configuration allows

reproduction of a realistic pathway of the Agulhas Rings and thus of the Agulhas leakage into the South Atlantic. This is particularly true for the central route which is defined as eddies that flow between the Agulhas Ridge and the Schmitt-Ott Seamount and Erica Seamount (*Dencausse et al.*, 2010b). There is a reduced leakage of warm Agulhas water influx into the southern Atlantic as the leakage is blocked by these bathymetric features, which are smoothed out resolved in the coarser resolution. This has an impact on the intensity of the Benguela Jet, and as such, on the absolute values of transport success. However, the seasonal cycle of transport success and the physical processes responsible remain the same. The equatorward jet that is narrower and located between the 200 m and 500 m isobaths in the higher resolution R3km simulation is favourable for transport success of inshore particles in spring and summer. Moreover, the intensity of the Benguela Jet is weaker due to the reduced Agulhas leakage and thus the EKE associated with the baroclinic/barotropic instabilities is much lower. This led to the offshore particles experiencing less dispersion and having a higher probability of transport success which contributed significantly to the total transport success.

Chapter 6: How are anomalous transport events related to the local wind forcing and the turbulent eddy field?

Interestingly, the variability of wind had little influence on the interannual variation of transport success, in contrast to previous studies. This is because offshore transport due to strengthened upwelling could be prevented by a strong Benguela Jet. On the other hand mesoscale eddies have an influence on the cross-shore displacement of offshore particles. The interaction of large anti-cyclonic such as Agulhas ring with the shelf-edge at the SARP line could lead to an offshore advection of particles originating from the outer shelf into a region of high turbulence. This offshore advection can contribute to negative anomalies of transport success. However, in the case where these particles don't get advected offshore away from the shelf-edge, shelf-cyclonic eddies can advect them inshore into the Benguela Jet.

7.2 Future work

The findings obtained from this work provide us with a better understanding of Lagrangian transport dynamics and their association with the seasonal and interannual variability of ocean circulation. The high resolution model configuration of the SBUS was found to reproduce the main characteristics of the currents in the region and their long-term fluctuations. There are several ways in which these results can be extended or applied:

- Retention of larvae in the area of high productive area is one the key factors proposed by Bakun's fundamental triad processes (*Bakun*, 1996) that determines the variability in the stock of small pelagic fishes. In this study, the retention of particles in the target area after their arrival was not considered. Since the particles have to remain in the target area for specified time to be considered as successful recruits, it is important to also study cross-shore transport and retention processes in St Helena Bay. The consideration of retention time is expected to have an impact on the present transport success probabilities.

- The occurrence of inner shelf poleward flows is believed to be very important in the SBUS for the generation, propagation and dissipation of harmful algal blooms in St Helena Bay and on the Namaqua shelf (*Pitcher and Nelson*, 2006). Thus the high resolution model (R3km) of the SBUS shelf region could provide a temporally and spatially cohesive dataset for other investigations of the small-scale and high frequency dynamics that contribute to often catastrophic harmful algal bloom events. The R3km resolution can also be used indirectly to provide lateral boundary conditions to have a more higher resolution nested model (i.e. 1 km).

- Several other processes, that were not investigated in this thesis, may lead to intraseasonal variability of the inner shelf circulation. These processes include submesoscale eddy dynamics generated by frontogenesis events in the mesoscale eddy field of the coastal transition zone (*Capet et al.*, 2008b), the role of inertial waves generated by the diurnal cycle of the wind forcing (*Fawcett et al.*, 2008), Stokes drift transport, and bolus transport from internal tides (**?**). The former enhances the presence of high vertical velocities, which may impact the structure of primary

production (*Gruber et al.*, 2011). These events occur on a time scale of a few days and on spatial scales of a few kilometres. Unfortunately, the available computing resources prevented the study of such fine scales. These scales could be responsible for large amplitude pycnocline fluctuations (*Orlić and Pasarić*, 2011), enhanced diapycnal mixing, and trigger the occurrence of harmful algal blooms (*Lucas et al.*, 2014). However, these processes are challenging to model in a realistic configuration of the southern Benguela shelf, and would require a spatial and time resolution that is beyond our available computing resources.

- Mesoscale eddies, particularly anti-cyclonic eddies located near the shelf were found to have an impact on the distribution of particles by advecting them offshore. However, a field survey can be carried out to quantify the role of these eddies in the cross-shelf transport of biota. Comparing larval fish and plankton biomass entrained in a cyclonic and anti-cyclonic eddy that interacted with the shelf can help us to contrast and understands the ecological consequences associated with these features. Finding juveniles in an eddy that has travelled farther in the open ocean could also determine whether eddies can maintain the survival of late-stage larvae.

- Available satellite altimetry data can be used to detect eddies in the region going back in time to determine if anomalous fish recruitment events can be linked to the effect of mesoscale eddies transport.

- Our findings suggest that particles on the SARP line off Cape Point are likely to be more affected by the turbulent mesoscale eddy field than particles located further north. Thus, the SARP line may not be the best transect to survey larvae in order to estimate their subsequent recruitment. This possibility needs to be investigated by carrying out a sensitivity study releasing particles at different offshore transects all along the northward route.

- Our model set-up considers a monthly climatology at lateral boundaries which filters out the interannual signal such as equatorial coastal Kelvin waves generated by Atlantic Ninã and Benguela Ninõ. Some assessment of the relative roles of local forcing *vs* forcing at the lateral boundaries should be considered in future efforts

2686 that studies the interannual variability in physical transport processes.

2687 • Finally, the Benguela Jet has been suggested as to play a key role in carrying fish eggs
2688 and larvae from their food-poor Agulhas Bank spawning grounds to the nutrient-
2689 rich inshore nurseries on the west coast (*Hutchings et al.*, 1998). Our results provide
2690 robust evidence that this jet does indeed modulate alongshore transport success at
2691 both seasonal and interannual time-scales. Due to its importance in recruitment of
2692 small pelagic fishes, it is therefore important to establish a long-term monitoring (a
2693 mooring array) of the jet. This will provide the ocean modelling community with
2694 temporally coherent data that can be used to evaluate the simulated characteristics
2695 of the jet and to track long-term trends associated with it.

Appendix A

Abbreviations used for the description of the ROMS model

- x, y, z - are the zonal, meridional and vertical directions (m) in the Cartesian coordinate system.
- u ,v, w - are the components of the vector velocity $\vec{v}$ (m s^{-1}) in x,y,z respectively.
- t - is the time in seconds (s).
- f - is the Coriolis parameter (s^{-1}).
- ϕ - is the dynamic pressure (m^2 s^{-2}).
- D_u, D_v, D_T, D_S - are the dissipative terms.
- T - is the potential temperature (°C).
- S - is the salinity (psu)
- $\vec{g}$ - is the acceleration of gravity (m s^2).
- ρ - is the seawater density (kg m^{-3}).
- ρ_o - is the mean seawater density (kg m^{-3}).
- P - is the total pressure (N m^{-2} or Kg m^{-2}).
- ζ - is the sea surface variation (m).
- τ_s^x, τ_s^y - are the surface wind stress (N m^{-2}), in x and y directions respectively.
- τ_b^x, τ_b^y - are the bottom wind stress (N m^{-2}), in x and y directions respectively.
- Q_{net} - is the surface heat flux (W m^{-2}).
- K_{Mv} - is the coefficient of vertical eddy viscosity (m^2 s^{-1}).

- K_{Tv}, K_{Sv} - are coefficients of vertical eddy diffusivity ($m^2\ s^{-1}$).
- K_{Mh} - is the coefficient of horizontal eddy viscosity ($m^2\ s^{-1}$).
- K_{Th}, K_{Sh} - are coefficients of horizontal eddy diffusivity ($m^2\ s^{-1}$).
- E_r - is the evaporation rate (cm day^{-1}).
- P_r - is the precipitation rate (cm day^{-1}).
- C_p - is the heat capacity of seawater (J kg^{-1} °C).
- H - is the total ocean depth (m).
- u_{10}, v_{10} - are the horizontal components of the wind vector in x and y respectively, measured at 10 m above sea level.
- C_D surface is a non-dimensional wind-drag coefficient.
- C_D bottom is a non-dimensional bottom-drag coefficient.
- ρ_{air} - is the density of atmospheric air (kg m^{-3}).
- r - is the coefficient of linear bottom friction.
- γ_2 - is the coefficient of quadratic bottom friction.

Appendix B

Eddy detecting and tracking algorithm

An automatic eddy tracking algorithm developed by *Penven et al.* (2005) in Matlab is used to detect and study mesoscale eddy structures in the SBUS. Generally, there are two methods used to detect eddies in the ocean based on geometric criteria (*Chelton et al.*, 2011) and the dynamical method (*Isern-Fontanet et al.*, 2006; *Chelton et al.*, 2007) using local minima SSH, maxima SSH and Okubo-Weiss. The geometric method typically applied to altimetry data (*Halo et al.*, 2013) is based on detecting closed loops by first identifying local minima and maxima SSH fields as eddy centre points. Eddy boundaries corresponds to the largest closed loop SSH contour, however, a maximum eddy length-scale threshold is defined to exclude large close loops structures such as gyres (*Chelton et al.*, 2011).

On the other hand, the dynamical method is based on the local dynamical properties of the flow which compares relative vorticity to strain (deformation); where a negative Okubo-Weiss ($W < 0$) parameter indicates that relative vorticity dominates over strain and this is true for the inner region of an eddy (*Isern-Fontanet et al.*, 2006; *Chelton et al.*, 2007). The Okubo-Weiss parameter which measures the relative importance of strain tensor and vorticity (*Okubo*, 1970; *Weiss*, 1991) (Equation B) has to be assessed against a threshold value.

$$W = S_n^2 + S_s^2 - \xi^2 \tag{B.1}$$

where the components are:

$$S_n^2 = \frac{\partial u}{\partial x} - \frac{\partial v}{\partial y}, \qquad S_s^2 = \frac{\partial v}{\partial x} - \frac{\partial u}{\partial y}, \qquad \xi^2 = \frac{\partial v}{\partial x} - \frac{\partial u}{\partial y} \tag{B.2}$$

where S_n (S_s) is the normal (shear) strain component of the strain tensor; ξ is the vertical component of relative vorticity; u and v are respective zonal and meridional components of geostrophic velocity computed from SSH fields.

In our analysis, the combination of two methods is used, such that an eddy feature is considered as a feature that is characterised by a closed loops of SSH and a negative Okubo-Weiss parameter in our ocean model. The detailed description of this combined method is found in *Halo et al.* (2013, 2014) and has been proven to be more robust in consistent eddy detection. Firstly, using the Okubo-Weiss parameter, only regions dominated by vorticity (i.e. negative W) are considered. To avoid the detection of basin-scale gyres, detection of eddies is limited to a radius of less than 400 km. Next, the inner regions are detected by using SSH contour lines, and a 2 cm contour interval was used. Although, we use the same algorithm as *Halo et al.* (2013, 2014), some of the tunable parameters such as the maximum size of a closed loop (Halo = 600 km, chosen = 400 km), the number of the Hanning filter on W was set as zero (Halo = 2) in our analysis.

After an eddy structure is detected, it is tracked using the methodology of *Penven et al.* (2005), where changes are tracked over time. An eddy is detected in the first frame and is considered the same eddy if there is a minimum generalised change of some of their properties in the subsequent frames:

$$W_{e_1,e_2} = \sqrt{\left(\frac{\Delta X}{X_0}\right)^2 + \left(\frac{\Delta R}{R_0}\right)^2 + \left(\frac{\Delta \xi}{\xi_0}\right)^2} \tag{B.3}$$

Where

- ΔX is the spatial distance between two eddy centres e_1 and e_2

- ΔR is the variation in diameter between e_1 and e_2

- $\Delta\xi$ is the variation in relative vorticity between e_1 and e_2

- X_0 is the typical eddy length scale: 30 km

- R_0 is a typical eddy radius scale: 30 km

- ξ_0 is a typical eddy vorticity scale: 10^{-5} s^{-1}

In addition, for an eddy to be tracked as the same eddy between frames, it must retain its polarity. In the case where this condition is violated, $W_{e_1,e_2} = \infty$. A unique identifier is assigned to all eddies tracked which the eddy retains through its lifetime. Where an eddy splits, a new identifiers are assigned for each child eddy. The track gets terminated if no subsequent eddy is found.

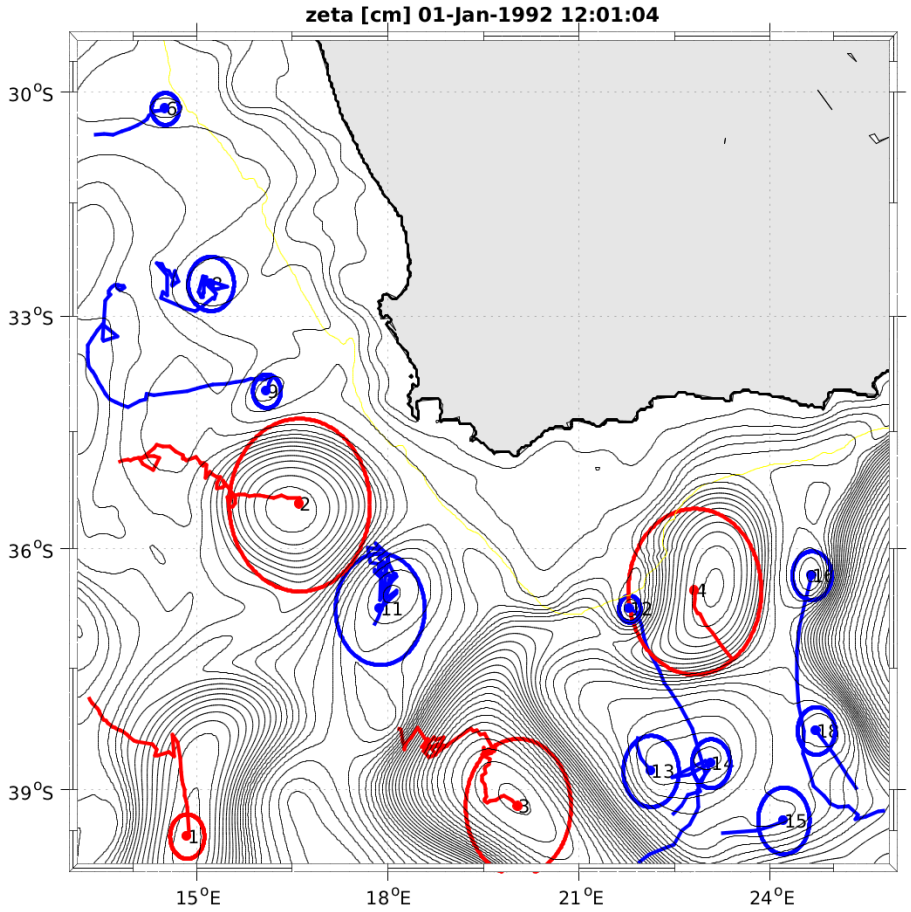

Figure B.1: Snapshot (01 January 1992) of eddies detected by the eddy detection algorithm in the R3km SSH field, contoured at 5 cm. Red (blue) circles indicate anti-cyclones (cyclones) and their trajectories throughout their lifetime are shown by red and blues lines, respectively. All eddies are tracked irrespective of their lifetime and the number shown on each eddy represents their identifiers (ID numbers). The yellow line traces the 500 m isobath.

Bibliography

Alves, J. M. R., and P. M. A. Miranda (2013), Variability of Iberian upwelling implied by ERA-40 and ERA-interim reanalyses, *Tellus, Series A: Dynamic Meteorology and Oceanography*, *65*(1), 1–12, doi:10.3402/tellusa.v65i0.19245.

Arakawa, A., and V. R. Lamb (1977), Computational design of the basic dynamical processes of the ucla general circulation model, in *General Circulation Models of the Atmosphere*, *Methods in Computational Physics: Advances in Research and Applications*, vol. 17, edited by J. CHANG, pp. 173 – 265, Elsevier, doi:https://doi.org/10.1016/B978-0-12-460817-7.50009-4.

Arhan, M., H. Mercier, and J. R. E. Lutjeharms (1999), The disparate evolution of three agulhas rings in the south atlantic ocean, *Journal of Geophysical Research: Oceans*, *104*(C9), 20,987–21,005, doi:10.1029/1998JC900047.

Armstrong, D. A., B. A. Mitchell-Innes, F. Verheye-Dua, H. Waldron, and L. Hutchings (1987), Physical and biological features across an upwelling front in the southern Benguela, *S. Afr. J. Mar. Sci.*, *5*, 171–190, doi:10.2989/025776187784522559.

Bakun, A. (1996), *Patterns in the ocean: ocean processes and marine population dynamics*, California Sea Grant, in cooperation with Centro de Investigaciones Biologicas del Noroeste, La Paz, Mexico.

Bakun, A. (2001), 'School-mix feedback': a different way to think about low frequency variability in large mobile fish populations, *Prog. Oceanog.*, *49*(1-4), 485–511, doi:10.1016/S0079-6611(01)00037-4.

Bakun, A., and C. Nelson (1991), The seasonal cycle of wind-stress curl in subtropical

eastern boundary current regions, *Journal of Physical Oceanography*, *21*(12), 1815–1834, doi:10.1175/1520-0485(1991)021⟨1815:TSCOWS⟩2.0.CO;2.

Bang, N., and W. Andrews (1974), Direct-current measurements of a shelf-edge frontal jet in southern benguela system, *J. Mar. Res.*, *32*(3), 405–417.

Beckmann, A., and D. B. Haidvogel (1993), Numerical simulation of flow around a tall isolated seamount. part i: Problem formulation and model accuracy, *J. Phys. Oceanogr.*, *23*(8), 1736–1753.

Blamey, L. K., J. A. Howard, J. Agenbag, and A. Jarre (2012), Regime-shifts in the southern benguela shelf and inshore region, *Progress in Oceanography*, *106*, 80 – 95, doi:https://doi.org/10.1016/j.pocean.2012.07.001.

Blamey, L. K., et al. (2015), Ecosystem change in the southern benguela and the underlying processes, *Journal of Marine Systems*, *144*, 9 – 29, doi:https://doi.org/10.1016/j.jmarsys.2014.11.006.

Blanke, B., C. Roy, P. Penven, S. Speich, J. McWilliams, and G. Nelson (2002), Linking wind and interannual upwelling variability in a regional model of the southern benguela, *Geophys. Res. Lett.*, *29*(24), 2188–2191, doi:10.1029/2002GL015718.

Blanke, B., S. Speich, A. Bentamy, C. Roy, and B. Sow (2005), Modeling the structure and variability of the southern Benguela upwelling using QuikSCAT wind forcing, *Journal of Geophysical Research: Oceans*, *110*(C7), n/a—-n/a, doi:10.1029/2004JC002529.

Blanke, B., P. Penven, C. Roy, N. Chang, and F. Kokoszka (2009), Ocean variability over the agulhas bank and its dynamical connection with the southern benguela upwelling system, *Journal of Geophysical Research: Oceans*, *114*(C12), doi:10.1029/2009JC005358.

Bloomer, S. F., K. L. Cochrane, and J. G. Field (1994), Towards predicting recruitment success of anchovy Engrauus capensis Gilchrist in the southern Benguela system using environmental variables: a rule-based model, *South African Journal of Marine Science*, *14*(1), 107–119, doi:10.2989/025776194784286897.

Boebel, O., J. Lutjeharms, C. Schmid, W. Zenk, T. Rossby, and C. Barron (2003), The cape cauldron: a regime of turbulent inter-ocean exchange, *Deep Sea Research Part II: Topical Studies in Oceanography*, *50*(1), 57 – 86, doi:https://doi.org/10.1016/S0967-0645(02)00379-X, inter-ocean exchange around southern Africa.

Boyd, A., L. Shannon, F. Schulein, and J. Taunton-Clark (1998), Food, transport and anchovy recruitment in the southern Benguela upwelling system of South Africa, *Global Versus Local Changes in Upwelling Systems*, pp. 195–209.

Brick, K., and R. Hasson (2017), Socio-Economic Contribution of Fisheries and other Marine Uses in South Africa.

Brown, P. C., and L. Hutchings (1987), The development and decline of phytoplankton blooms in the southern Benguela upwelling system. 1. Drogue movements, hydrography and bloom development, *South African Journal of Marine Science*, *5*(1), 357–391, doi:10.2989/025776187784522801.

Burls, N., and C. Reason (2008), Modelling the sensitivity of coastal winds over the southern benguela upwelling system to different sst forcing, *Journal of Marine Systems*, *74*(1), 561 – 584, doi:https://doi.org/10.1016/j.jmarsys.2008.04.009.

Capet, X., F. Colas, P. Penven, P. Marchesiello, and J. C. McWilliams (2008a), Eddies in eastern boundary subtropical upwelling systems, in *Ocean Modeling in an Eddying Regime*, vol. 177, edited by M. W. Hecht and H. H. Hasumi, Washington, D. C.

Capet, X., J. C. McWilliams, M. J. Molemaker, and A. F. Shchepetkin (2008b), Mesoscale to Submesoscale Transition in the California Current System. Part I: Flow Structure, Eddy Flux, and Observational Tests, *J. Phys. Oceanogr.*, *38*(1), 29–43, doi:10.1175/2007JPO3671.1.

Capet, X. J. (2004), Upwelling response to coastal wind profiles, *Geophysical Research Letters*, *31*(13), L13,311, doi:10.1029/2004GL020123.

Carton, J. a., and B. S. Giese (2008), A Reanalysis of Ocean Climate Using Simple Ocean Data Assimilation (SODA), *Mon. Weather Rev.*, *136*(8), 2999–3017, doi:10.1175/2007MWR1978.1.

Castelao, R. M., and J. A. Barth (2007), The Role of Wind Stress Curl in Jet Separation at a Cape, *J. Phys. Oceanogr.*, *37*(11), 2652–2671, doi:10.1175/2007JPO3679.1.

Chelton, D. B., M. G. Schlax, R. M. Samelson, and R. A. de Szoeke (2007), Global observations of large oceanic eddies, *Geophysical Research Letters*, *34*(15), doi:10.1029/2007GL030812.

Chelton, D. B., M. G. Schlax, and R. M. Samelson (2011), Global observations of nonlinear mesoscale eddies, *Progress in Oceanography*, *91*(2), 167 – 216, doi:https://doi.org/10.1016/j.pocean.2011.01.002.

Colas, F., J. C. McWilliams, X. Capet, and J. Kurian (2011), Heat balance and eddies in the Peru-Chile current system, *Climate Dynamics*, *39*(1-2), 509–529, doi:10.1007/s00382-011-1170-6.

Colas, F., X. Capet, J. C. McWilliams, and Z. Li (2013), Mesoscale Eddy Buoyancy Flux and Eddy-Induced Circulation in Eastern Boundary Currents, *Journal of Physical Oceanography*, *43*(6), 1073–1095, doi:10.1175/JPO-D-11-0241.1.

Colberg, F., C. J. C. Reason, and K. Rodgers (2004), South atlantic response to el niño southern oscillation induced climate variability in an ocean general circulation model, *Journal of Geophysical Research: Oceans*, *109*(C12), doi:10.1029/2004JC002301.

Cudaback, C. N., L. Washburn, and E. Dever (2005), Subtidal inner-shelf circulation near Point Conception, California, *Journal of Geophysical Research C: Oceans*, *110*(10), 1–12, doi:10.1029/2004JC002608.

Debreu, L., P. Marchesiello, P. Penven, and G. Cambon (2012), Two-way nesting in split-explicit ocean models: Algorithms, implementation and validation, *Ocean Model.*, *49-50*(April), 1–21, doi:10.1016/j.ocemod.2012.03.003.

Dencausse, G., M. Arhan, and S. Speich (2010a), Spatio-temporal characteristics of the agulhas current retroflection, *Deep Sea Research Part I: Oceanographic Research Papers*, *57*(11), 1392 – 1405, doi:https://doi.org/10.1016/j.dsr.2010.07.004.

Dencausse, G., M. Arhan, and S. Speich (2010b), Spatio-temporal characteristics of the agulhas current retroflection, *Deep Sea Research Part I: Oceanographic Research Papers*, *57*(11), 1392 – 1405, doi:https://doi.org/10.1016/j.dsr.2010.07.004.

Dencausse, G., M. Arhan, and S. Speich (2010c), Routes of agulhas rings in the south-eastern cape basin, *Deep Sea Research Part I: Oceanographic Research Papers*, *57*(11), 1406 – 1421, doi:https://doi.org/10.1016/j.dsr.2010.07.008.

Dever, E. P., M. C. Hendershott, and C. D. Winant (1998), Statistical aspects of surface drifter observations of circulation in the santa barbara channel, *Journal of Geophysical Research: Oceans*, *103*(C11), 24,781–24,797, doi:10.1029/98JC02403.

Doglioli, A. M., M. Veneziani, B. Blanke, S. Speich, and A. Griffa (2006), A lagrangian analysis of the indian-atlantic interocean exchange in a regional model, *Geophysical Research Letters*, *33*(14), doi:10.1029/2006GL026498.

Donners, J., and S. S. Drijfhout (2004), The lagrangian view of south atlantic interocean exchange in a global ocean model compared with inverse model results, *Journal of Physical Oceanography*, *34*(5), 1019–1035, doi:10.1175/1520-0485(2004)034⟨1019:TLVOSA⟩2.0.CO;2.

Ducet, N., P. Y. Le Traon, and G. Reverdin (2000), Global high-resolution mapping of ocean circulation from TOPEX/Poseidon and ERS-1 and -2, *Journal of Geophysical Research*, *105*(C8), 19,477, doi:10.1029/2000JC900063.

Dufois, F., P. Penven, C. Peter Whittle, and J. Veitch (2012), On the warm nearshore bias in Pathfinder monthly SST products over Eastern Boundary Upwelling Systems, *Ocean Modelling*, *47*, 113–118, doi:10.1016/j.ocemod.2012.01.007.

Duncombe-Rae, C., F. Shillington, J. Agenbag, J. Taunton-Clark, and M. Gründlingh (1992), An agulhas ring in the south atlantic ocean and its interaction with the benguela upwelling frontal system, *Deep Sea Research Part A. Oceanographic Research Papers*, *39*(11), 2009 – 2027, doi:https://doi.org/10.1016/0198-0149(92)90011-H.

Durgadoo, J. V., B. R. Loveday, C. J. C. Reason, P. Penven, and A. Biastoch (2013),

Agulhas leakage predominantly responds to the southern hemisphere westerlies, *Journal of Physical Oceanography*, *43*(10), 2113–2131, doi:10.1175/JPO-D-13-047.1.

Ezer, T., H. Arango, and A. F. Shchepetkin (2002), Developments in terrain-following ocean models: intercomparisons of numerical aspects, *Ocean Modelling*, *4*(3), 249 – 267, doi:https://doi.org/10.1016/S1463-5003(02)00003-3.

Fairall, C. W., E. F. Bradley, J. S. Godfrey, G. A. Wick, J. B. Edson, and G. S. Young (1996), Cool-skin and warm-layer effects on sea surface temperature, *J. Geophys. Res.*, *101*(C1), 1295–1308, doi:10.1029/95JC03190.

Fawcett, A. L., G. Pitcher, and F. Shillington (2008), Nearshore currents on the southern Namaqua shelf of the Benguela upwelling system, *Cont. Shelf Res.*, *28*(8), 1026–1039, doi:10.1016/j.csr.2008.02.005.

Fennel, W. (1999), Theory of the Benguela Upwelling System, *J. Phys. Oceanogr.*, *29*(2), 177–190, doi:10.1175/1520-0485(1999)029⟨0177:TOTBUS⟩2.0.CO;2.

Fennel, W., T. Junker, M. Schmidt, and V. Mohrholz (2012), Response of the Benguela upwelling systems to spatial variations in the wind stress, *Cont. Shelf Res.*, *45*, 65–77, doi:10.1016/j.csr.2012.06.004.

Fowler, J. L., and A. J. Boyd (1998), Transport of anchovy and sardine eggs and larvae from the western agulhas bank to the west coast during the 1993/94 and 1994/95 spawning seasons, *S. Afr. J. Mar. Sci.*, *19*(1), 181–195, doi:10.2989/025776198784127006.

Gan, J., and J. S. Allen (2002a), A modeling study of shelf circulation off northern California in the region of the Coastal Ocean Dynamics Experiment: Response to relaxation of upwelling winds, *J. Geophys. Res.*, *107*(C9), 6–31, doi:10.1029/2000JC000768.

Gan, J., and J. S. Allen (2002b), A modeling study of shelf circulation off northern California in the region of the Coastal Ocean Dynamics Experiment 2. Simulations and comparisons with observations, *J. Geophys. Res.*, *107*(C11), 1–21, doi:10.1029/2001JC001190.

Garavelli, L., a. Grüss, B. Grote, N. Chang, M. Smith, P. Verley, E. K. Stenevik, D. M. Kaplan, and C. Lett (2012), Modeling the dispersal of Cape hake ichthyoplankton, *Journal of Plankton Research*, *34*(8), 655–669, doi:10.1093/plankt/fbs039.

Garzoli, S. L., and G. J. Goni (2000), Chapter 5 combining altimeter observations and oceanographie data for ocean circulation and climate studies, in *Satellites, oceanograghy and society*, *Elsevier Oceanography Series*, vol. 63, edited by D. Halpern, pp. 79 – 97, Elsevier, doi:https://doi.org/10.1016/S0422-9894(00)80006-9.

Gordon, A. (1985), Indian-Atlantic transfer of thermohaline water at the Agulhas retroflection, *Science*, *227*, 1030–1033.

Gordon, A. L. (1986), Interocean exchange of thermocline water, *Journal of Geophysical Research: Oceans*, *91*(C4), 5037–5046, doi:10.1029/JC091iC04p05037.

Gordon, A. L., J. R. Lutjeharms, and M. L. GrÃŒndlingh (1987), Stratification and circulation at the agulhas retroflection, *Deep Sea Research Part A. Oceanographic Research Papers*, *34*(4), 565 – 599, doi:https://doi.org/10.1016/0198-0149(87)90006-9.

Gruber, N., Z. Lachkar, H. Frenzel, P. Marchesiello, M. Münnich, J. C. McWilliams, T. Nagai, and G.-K. Plattner (2011), Eddy-induced reduction of biological production in eastern boundary upwelling systems, *Nature Geoscience*, *4*(11), 787–792, doi:10.1038/ngeo1273.

Gula, J., M. J. Molemaker, and J. C. McWilliams (2014), Submesoscale Cold Filaments in the Gulf Stream, *J. Phys. Oceanogr.*, *44*(10), 2617–2643, doi:10.1175/JPO-D-14-0029.1.

Hall, A., and M. Visbeck (2002), Synchronous variability in the southern hemisphere atmosphere, sea ice, and ocean resulting from the annular mode, *Journal of Climate*, *15*(21), 3043–3057, doi:10.1175/1520-0442(2002)015⟨3043:SVITSH⟩2.0.CO;2.

Hall, C., and J. Lutjeharms (2011), Cyclonic eddies identified in the cape basin of the south atlantic ocean, *Journal of Marine Systems*, *85*, 1–10, doi:10.1016/j.jmarsys.2010.10.003.

Halo, I., B. Backeberg, P. Penven, I. Ansorge, C. Reason, and J. Ullgren (2013), Eddy properties in the mozambique channel: A comparison between observations and two numerical ocean circulation models, *Deep Sea Research Part II Topical Studies in Oceanography*, *100*, doi:10.1016/j.dsr2.2013.10.015.

Halo, I., B. Backeberg, P. Penven, I. Ansorge, C. Reason, and J. Ullgren (2014), Eddy properties in the mozambique channel: A comparison between observations and two numerical ocean circulation models, *Deep Sea Research Part II: Topical Studies in Oceanography*, *100*, 38 – 53, doi:https://doi.org/10.1016/j.dsr2.2013.10.015, the Mozambique Channel: Mesoscale Dynamics and Ecosystem Responses.

Hardman-Mountford, N. J., a. J. Richardson, J. J. Agenbag, E. Hagen, L. Nykjaer, F. a. Shillington, and C. Villacastin (2003), Ocean climate of the South East Atlantic observed from satellite data and wind models, *Progress in Oceanography*, *59*(2-3), 181–221, doi:10.1016/j.pocean.2003.10.001.

Hedstrom, K. (1997), User's manual for an s-coordinate primitive equation ocean circulation model (scrum) version 3.0, *Institute of Marine and Coastal Sciences, Rutgers University Contribution*, pp. 97–10.

Hedström, K. S. (2009), Technical Manual for a Coupled Sea-Ice / Ocean Circulation Model (Version 3), *Circulation*, (Version 3), 158.

Hernández-Carrasco, I., V. Rossi, E. Hernández-García, V. Garçon, and C. López (2014), The reduction of plankton biomass induced by mesoscale stirring: A modeling study in the Benguela upwelling, *Deep Sea Research Part I: Oceanographic Research Papers*, *83*, 65–80, doi:10.1016/j.dsr.2013.09.003.

Hill, a. E. (1998), Diel vertical migration in stratified tidal flows: Implications for plankton dispersal, *Journal of Marine Research*, *56*(5), 1069–1096, doi:10.1357/002224098765173464.

Hollmann, R., et al. (2013), The esa climate change initiative: Satellite data records for essential climate variables, *Bulletin of the American Meteorological Society*, *94*(10), 1541–1552, doi:10.1175/BAMS-D-11-00254.1.

Howard, J., A. Jarre, A. Clark, and C. Moloney (2007), Application of the sequential t-test algorithm for analysing regime shifts to the southern benguela ecosystem, *African Journal of Marine Science*, *29*(3), 437–451, doi:10.2989/AJMS.2007.29.3.11.341.

Huggett, J., P. Fréon, C. Mullon, and P. Penven (2003), Modelling the transport success of anchovy Engraulis encrasicolus eggs and larvae in the southern Benguela: The effect of spatio-temporal spawning patterns, *Marine Ecology Progress Series*, *250*(Linnaeus 1758), 247–262, doi:10.3354/meps250247.

Hutchings, L. (1992), Fish harvesting in a variable, productive environment — searching for rules or searching for exceptions?, *S. Afr. J. Mar. Sci.*, *12*(1), 297–318, doi:10.2989/02577619209504708.

Hutchings, L., et al. (1998), Multiple factors affecting South African anchovy recruitment in the spawning, transport and nursery areas, *S. Afr. J. Mar. Sci.*, *19*(1), 211–225, doi:10.2989/025776198784126908.

Hutchings, L., et al. (2009), The Benguela Current: An ecosystem of four components, *Progress in Oceanography*, *83*(1-4), 15–32, doi:10.1016/j.pocean.2009.07.046.

Huyer, A., and P. M. Kosro (1987), Mesoscale surveys over the shelf and slope in the upwelling region near Point Arena, California, *Journal of Geophysical Research*, *92*(C2), 1655, doi:10.1029/JC092iC02p01655.

Illig, S., M.-L. Bachèlery, and E. Cadier (2018), Subseasonal coastal-trapped wave propagations in the southeastern pacific and atlantic oceans: 2. wave characteristics and connection with the equatorial variability, *Journal of Geophysical Research: Oceans*, *123*(6), 3942–3961, doi:10.1029/2017JC013540.

Isern-Fontanet, J., E. Garcá-Ladona, and J. Font (2006), Vortices of the mediterranean sea: An altimetric perspective, *Journal of Physical Oceanography*, *36*(1), 87–103, doi:10.1175/JPO2826.1.

Junker, T., M. Schmidt, and V. Mohrholz (2015), The relation of wind stress curl and meridional transport in the benguela upwelling system, *Journal of Marine Systems*, *143*, 1 – 6, doi:https://doi.org/10.1016/j.jmarsys.2014.10.006.

Jury, M., C. Macarthur, and C. Reason (1990), Observations of trapped waves in the atmosphere and ocean along the coast of southern africa, *South African Geographical Journal*, *72*(2), 33–46, doi:10.1080/03736245.1990.10586373.

Jury, M. R., and G. B. Brundrit (1992), Temporal organization of upwelling in the southern Benguela ecosystem by resonant coastal trapped waves in the ocean and atmosphere, *South African Journal of Marine Science*, *12*(1), 219–224, doi:10.2989/02577619209504704.

Koné, V., C. Lett, and P. Fréon (2013), Modelling the effect of food availability on recruitment success of cape anchovy ichthyoplankton in the southern benguela upwelling system, *African Journal of Marine Science*, *35*(2), 151–161, doi:10.2989/1814232X.2013.796893.

Kosro, P. M. (1987), Structure of the coastal current field off the northern California during the Coastal Ocean Dynamics Experiment, *J. Geophys. Res.*, *92*(C2), 1637–1654.

Kundu, P. K., D. R. Dowling, G. Tryggvason, and I. M. Cohen (2015), Fluid mechanics.

Lamont, T., L. Hutchings, M. A. van den Berg, W. S. Goschen, and R. G. Barlow (2015), Hydrographic variability in the st. helena bay region of the southern benguela ecosystem, *Journal of Geophysical Research: Oceans*, *120*(4), 2920–2944, doi:10.1002/2014JC010619.

Lamont, T., M. G. a Reyes, S. Bograd, C. van der Lingen, and W. Sydeman (2018), Upwelling indices for comparative ecosystem studies: Variability in the benguela upwelling system, *Journal of Marine Systems*, *188*, 3 – 16, doi:https://doi.org/10.1016/j.jmarsys.2017.05.007, benguela: Opportunity, Challenge and Change.

Large, W. G., J. C. McWilliams, and S. C. Doney (1994), Oceanic vertical mixing: A review and a model with a nonlocal boundary layer parameterization, *Reviews of Geophysics*, *32*(4), 363–403, doi:10.1029/94RG01872.

Largier, J. L., B. a. Magnell, and C. D. Winant (1993), Subtidal circulation over the northern California shelf, *Journal of Geophysical Research*, *98*(C10), 18,147, doi:10.1029/93JC01074.

Lemarié, F., J. Kurian, A. F. Shchepetkin, M. J. Molemaker, F. Colas, and J. C. McWilliams (2012), Are there inescapable issues prohibiting the use of terrain-following

coordinates in climate models?, *Ocean Modelling*, *42*(Supplement C), 57 – 79, doi:10.1016/j.ocemod.2011.11.007.

Lett, C., C. Roy, A. Levasseur, C. van de Lingen, and C. Mullon (2006), Simulation and quantification of enrichment and retention processes in the southern Benguela upwelling ecosystem, *Fisheries Oceanography*, *15*(5), 363–372, doi:10.1111/j.1365-2419.2005.00392.x.

Lévy, M., P. Klein, A.-M. Tréguier, D. Iovino, G. Madec, S. Masson, and K. Takahashi (2010), Modifications of gyre circulation by sub-mesoscale physics, *Ocean Modelling*, *34*(1), 1 – 15, doi:https://doi.org/10.1016/j.ocemod.2010.04.001.

Lévy, M., R. Ferrari, P. J. S. Franks, A. P. Martin, and P. Rivière (2012), Bringing physics to life at the submesoscale, *Geophysical Research Letters*, *39*(14), doi:10.1029/2012GL052756.

Locarnini, R. A., et al. (2013), World Ocean Atlas 2013. Vol. 1: Temperature., *S. Levitus, Ed.; A. Mishonov, Technical Ed.; NOAA Atlas NESDIS*, *73*(September), 40, doi:10.1182/blood-2011-06-357442.

Loveday, B. R., J. V. Durgadoo, C. J. Reason, A. Biastoch, and P. Penven (2014), Decoupling of the Agulhas leakage from the Agulhas Current, *Journal of Physical Oceanography*, p. 140411151744003, doi:10.1175/JPO-D-13-093.1.

Lucas, A. J., G. C. Pitcher, T. A. Probyn, and R. M. Kudela (2014), The influence of diurnal winds on phytoplankton dynamics in a coastal upwelling system off southwestern Africa, *Deep Sea Res., Part II*, *101*, 50–62, doi:10.1016/j.dsr2.2013.01.016.

Lutjeharms, J., F. Shillington, and C. Duncombe Rae (1991), Observations of extreme upwelling filaments in the southeast atlantic ocean, *Science (New York, N.Y.)*, *253*, 774–6, doi:10.1126/science.253.5021.774.

Lutjeharms, J. R. E., and R. C. Van Ballegooyen (1988), The retroflection of the agulhas current, *Journal of Physical Oceanography*, *18*(11), 1570–1583, doi:10.1175/1520-0485(1988)018⟨1570:TROTAC⟩2.0.CO;2.

Lutjeharms, J. R. E., O. Boebel, and H. T. Rossby (2003), Agulhas cyclones, *Deep-sea research ii*, *50*(1), 13–34, doi:10.1016/S0967-0645(02)00378-8.

Marchesiello, P., J. C. McWilliams, and A. Shchepetkin (2001), Open boundary conditions for long-term integration of regional oceanic models, *Ocean Modell.*, *3*(1-2), 1–20.

Marchesiello, P., A. F. Shchepetkine, and J. C. McWilliams (2003), Equilibrium structure and dynamics of the California Current System., *J. Phys. Oceanogr.*, *126*, 753–783.

Marchesiello, P., L. Debreu, and X. Couvelard (2009), Spurious diapycnal mixing in terrain-following coordinate models: The problem and a solution, *Ocean Modelling*, *26*(3-4), 156–169, doi:10.1016/j.ocemod.2008.09.004.

Marshall, G. J. (2003), Trends in the southern annular mode from observations and reanalyses, *Journal of Climate*, *16*(24), 4134–4143, doi:10.1175/1520-0442(2003)016⟨4134:TITSAM⟩2.0.CO;2.

Mason, E., J. Molemaker, A. F. Shchepetkin, F. Colas, J. C. McWilliams, and P. SangrÃ (2010), Procedures for offline grid nesting in regional ocean models, *Ocean Modelling*, *35*(1), 1 – 15, doi:https://doi.org/10.1016/j.ocemod.2010.05.007.

Melton, C., L. Washburn, and C. Gotschalk (2009), Wind relaxations and poleward flow events in a coastal upwelling system on the central California coast, *Journal of Geophysical Research: Oceans*, *114*(11), C11,016, doi:10.1029/2009JC005397.

Miller, D. C., C. L. Moloney, C. D. van der Lingen, C. Lett, C. Mullon, and J. G. Field (2006), Modelling the effects of physical–biological interactions and spatial variability in spawning and nursery areas on transport and retention of sardine Sardinops sagax eggs and larvae in the southern Benguela ecosystem, *J. Mar. Sys.*, *61*(3-4), 212–229, doi:10.1016/j.jmarsys.2005.03.007.

Mullon, C., P. Cury, and P. Penven (2002),) in the southern Benguela, *Can. J. Fish. Aquat. Sci.*, *59*(5), 910–922, doi:10.1139/f02-064.

Mullon, C., P. Fréon, C. Parada, C. Van Der Lingen, and J. Huggett (2003), From particles to individuals: Modelling the early stages of anchovy (Engraulis capensis/encrasicolus)

in the southern Benguela, *Fish. Oceanogr.*, *12*(4-5), 396–406, doi:10.1046/j.1365-2419.2003.00240.x.

Mullon, C., P. Fréon, and P. Cury (2005), The dynamics of collapse in world fisheries, *Fish and Fisheries*, *6*(2), 111–120, doi:10.1111/j.1467-2979.2005.00181.x.

Nelson, G. (1989), *Poleward motion in the Benguela area, in Poleward Flows Along Eastern Ocean Boundaries*, Springer, New York.

Nelson, G., and L. Hutchings (1983), The Benguela upwelling area, *Prog. Oceanog.*, *12*(3), 333–356, doi:10.1016/0079-6611(83)90013-7.

Okubo, A. (1970), Horizontal dispersion of floatable particles in the vicinity of velocity singularities such as convergences, *Deep Sea Research and Oceanographic Abstracts*, *17*(3), 445 – 454, doi:https://doi.org/10.1016/0011-7471(70)90059-8.

Orlić, M., and Z. Pasarić (2011), A simple analytical model of periodic coastal upwelling, *Journal of Physical Oceanography*, *41*(6), 1271–1276, doi:10.1175/JPO-D-10-05000.1.

Pagès, F., H. M. Verheye, J. M. Gili, and J. Flos (1991), Short-term effects of coastal upwelling and wind reversals on epiplanktonic cnidarians in the Southern Benguela ecosystem, *South African Journal of Marine Science*, *10*(1), 203–211, doi:10.2989/02577619109504632.

Painting, S. J., L. Hutchings, J. A. Hugget, J. L. Korrûbel, A. J. Richardson, and H. M. Verheye (1998), Environmental and biological monitoring for forecasting anchovy recruitment in the southern benguela upwelling region, *Fisheries Oceanography*, *7*(34), 364–374, doi:10.1046/j.1365-2419.1998.00086.x.

Parada, C., C. D. Van Der Lingen, C. Mullon, and P. Penven (2003), Modelling the effect of buoyancy on the transport of anchovy (Engraulis capensis) eggs from spawning to nursery grounds in the southern Benguela: An IBM approach, *Fish. Oceanogr.*, *12*(3), 170–184.

Parada, C., C. Mullon, C. Roy, P. Fréon, L. Hutchings, and C. D. Van Der Lingen (2008), Does vertical migratory behaviour retain fish larvae onshore in upwelling ecosystems?

A modelling study of anchovy in the southern Benguela, *African Journal of Marine Science*, *30*(3), 437–452, doi:10.2989/AJMS.2008.30.3.1.635.

Parrish, R. H., A. Bakun, D. M. Husby, and C. S. Nelson (1983), Comparative climatology of selected environmental processes in relation to eastern boundary current pelagic fish reproduction, *FAO Fisheries Report (FAO)*.

Payne, A. I. L., K. H. Brink, K. H. Mann, and R. Hilborn (1992), Benguela trophic functioning, *S. Afr. J. mar. Sci.*, *12*, 1108pp.

Penven, P., J. R. E. Lutjeharms, P. Marchesiello, C. Roy, and S. J. Weeks (2000), Generation of cyclonic eddies by the agulhas current in the lee of the agulhas bank, *Geophysical Research Letters*, *28*(6), 1055–1058, doi:10.1029/2000GL011760.

Penven, P., C. Roy, J. Lutjeharms, A. Colin de Verdière, A. Johnson, F. Shillington, P. Fréon, and G. Brundrit (2001), A regional hydrodynamic model of the Southern Benguela, *S. Afr. J. Mar. Sci.*, *97*, 472–476.

Penven, P., V. Echevin, J. Pasapera, F. Colas, and J. Tam (2005), Average circulation, seasonal cycle, and mesoscale dynamics of the Peru Current System: A modeling approach, *J. Geophys. Res.*, *110*(10), 1–21, doi:10.1029/2005JC002945.

Peterson, R. G., and L. Stramma (1991), Upper-level circulation in the South Atlantic Ocean, *Progress in Oceanography*, *26*(1), 1–73, doi:10.1016/0079-6611(91)90006-8.

Piollé, J., and E. Autret (2011), *Product user manual for l3 and l4 odyssea sst products over the global and north western shelves*, Myocean.

Pitcher, G., and S. Pillar (2010), Harmful algal blooms in eastern boundary upwelling systems, *Progress in Oceanography*, *85*(1–2), 1–4, doi:http://dx.doi.org/10.1016/j.pocean.2010.02.001.

Pitcher, G. C., and G. Nelson (2006), Characteristics of the surface boundary layer important to the development of red tide on the southern Namaqua shelf of the Benguela upwelling system, *Limnology and Oceanography*, *51*(6), 2660–2674.

Ragoasha, N., S. Herbette, G. Cambon, J. Veitch, C. Reason, and C. Roy (2019), Lagrangian pathways in the southern benguela upwelling system, *Journal of Marine Systems*, *195*, 50 – 66, doi:https://doi.org/10.1016/j.jmarsys.2019.03.008.

Reason, C., J. Lutjeharms, J. Hermes, A. Biastoch, and R. Roman (2003), Inter-ocean fluxes south of africa in an eddy-permitting model, *Deep Sea Research Part II: Topical Studies in Oceanography*, *50*(1), 281 – 298, doi:https://doi.org/10.1016/S0967-0645(02)00385-5, inter-ocean exchange around southern Africa.

Relvas, P. (2002), Mesoscale patterns in the Cape São Vicente (Iberian Peninsula) upwelling region, *J. Geophys. Res.*, *107*(C10), 1–23, doi:10.1029/2000JC000456.

Rhüs, S., J. V. Durgadoo, E. Behrens, and A. Biastoch (2013), Advective timescales and pathways of agulhas leakage, *Geophysical Research Letters*, *40*(15), 3997–4000, doi:10.1002/grl.50782.

Richardson, P. L. (2007), Agulhas leakage into the atlantic estimated with subsurface floats and surface drifters, *Deep Sea Research Part I: Oceanographic Research Papers*, *54*(8), 1361 – 1389, doi:https://doi.org/10.1016/j.dsr.2007.04.010.

Risien, C. M., C. J. C. Reason, F. A. Shillington, and D. B. Chelton (2004), Variability in satellite winds over the benguela upwelling system during 19992000, *Journal of Geophysical Research: Oceans*, *109*(C3), doi:10.1029/2003JC001880.

Roughan, M., N. Garfield, J. Largier, E. Dever, C. Dorman, D. Peterson, and J. Dorman (2006), Transport and retention in an upwelling region: The role of across-shelf structure, *Deep-Sea Research Part II: Topical Studies in Oceanography*, *53*(25-26), 2931–2955, doi:10.1016/j.dsr2.2006.07.015.

Roy, C., C. van der Lingen, J. Coetzee, and J. Lutjeharms (2007), Abrupt environmental shift associated with changes in the distribution of Cape anchovy Engraulis encrasicolus spawners in the southern Benguela, *African Journal of Marine Science*, *29*(3), 309–319, doi:10.2989/AJMS.2007.29.3.1.331.

Rubio, A., B. Blanke, S. Speich, N. Grima, and C. Roy (2009), Mesoscale eddy activity

in the southern Benguela upwelling system from satellite altimetry and model data, *Progress in Oceanography*, *83*(1-4), 288–295, doi:10.1016/j.pocean.2009.07.029.

Saha, e. a., Suranjana (2010), The ncep climate forecast system reanalysis, *Bull. Amer. Meteor. Soc.*, *91*(8), 1015–1057, doi:10.1175/2010BAMS3001.1.

Schouten, M. W., W. P. M. de Ruijter, P. J. van Leeuwen, and J. R. E. Lutjeharms (2000), Translation, decay and splitting of Agulhas rings in the southeastern Atlantic Ocean, *J. Geophys. Res.*, *105*(C9), 21,913–21,925, doi:10.1029/1999JC000046.

Send, U., R. C. Beardsley, and C. D. Winant (1987), Relaxation from upwelling in the coastal ocean dynamics experiment, *Journal of Geophysical Research: Oceans*, *92*(C2), 1683–1698, doi:10.1029/JC092iC02p01683.

Shannon, L., and G. Nelson (1996), The Benguela: large scale features and processes and system variability, in *The South Atlantic. Present and past circulation*, edited by G. Wefer, W. H. Berger, G. Shiedler, and D. Webb, pp. 163–210, Springer-Verlag, Berlin Heidelberg.

Shannon, L., G. Nelson, R. Crawdord, and A. Boyd (1996), Possible impacts of environmental change on pelagic fish recruitment: modelling anchovy transport by advective processes in the southern Benguela, *Global Change Biology*, *2*(5), 407–420, doi: 10.1111/j.1365-2486.1996.tb00091.x.

Shannon, L. V. (1985), The benguela ecosystem. i. evolution of the bengue]a, physical features and processes., *In Oceanography and Marine Biology*, pp. 105–182.

Shchepetkin, A. F., and J. C. McWilliams (1998), Quasi-monotone advection schemes based on explicit locally adaptive dissipation, *Mon. Weather Rev.*, *126*(6), 1541–1580, doi:10.1175/1520-049.

Shchepetkin, A. F., and J. C. McWilliams (2005), The regional oceanic modeling system (ROMS): A split-explicit, free-surface, topography-following-coordinate oceanic model, *Ocean Model.*, *9*(4), 347–404, doi:10.1016/j.ocemod.2004.08.002.

Shelton, P., A. Boyd, and M. Armstrong (1985), the Influence of Large-Scale Environmental Processes on Neritic Fish Populations in the Benguela Current System, *California cooperative oceanic fisheries investigations progress report*, *25*, 72–92.

Shelton, P. A., and L. Hutchings (1982), Transport of anchovy, engraulis capensis gilchrist, eggs and early larvae by a frontal jet current, *Journal du Conseil*, *40*(2), 185–198, doi: 10.1093/icesjms/40.2.185.

Shelton, P. A., and L. Hutchings (1990), Ocean stability and anchovy spawning in the southern benguela current region, *Fish. Bull.*, *88*(2), 323–338.

Shillington, F. A., C. J. C. Reason, C. M. Duncombe Rae, P. Florenchie, and P. Penven (2006), Large scale physical variability of the {Benguela Current Large Marine Ecosystem (BCLME)}, in {*Large Marine Ecosystems*}*: the* {*Benguela*}*: predicting a large marine ecosystem*, vol. 14, edited by V. Shannon, G. Hempel, P. Malanotte-Rizzoli, C. Moloney, and J. Woods, pp. 47–68, Elsevier, Amsterdam.

Simpson, J. H., P. Hyder, T. P. Rippeth, and I. M. Lucas (20021), Forced oscillations near the crtitical latitude for diurnal-inertial-resonnance, *J. Phys. Oceanogr.*, *32*, 177–187.

Skogen, M. D., L. J. Shannon, and J. E. Stiansen (2003), Drift patterns of anchovy engraulis capensis larvae in the southern benguela, and their possible importance for recruitment, *Afr. J. mar. Sci.*, *25*(1), 37–47, doi:10.2989/18142320309503999.

Smith, R., J. Dukowicz, and R. Malone (1992), Parallel ocean general circulation modeling, *Physica D: Nonlinear Phenomena*, *60*(1-4), 38–61, doi:10.1016/0167-2789(92)90225-C.

Smith, W. H. F., and D. T. Sandwell (1997), Global sea floor topography from satellite altimetry and ship depth soundings, *Science*, *277*(5334), 1956–1962, doi:10.1126/science.277.5334.1956.

Song, H., A. J. Miller, B. D. Cornuelle, and E. Di Lorenzo (2011), Changes in upwelling and its water sources in the California Current System driven by different wind forcing, *Dyn. Atm. Oceans*, *52*(1-2), 170–191, doi:10.1016/j.dynatmoce.2011.03.001.

Song, Y., and D. Haidvogel (1994), A semi-implicit ocean circulation model using a generalized topography-following coordinate system, *Journal of Computational Physics*, *115*(1), 228 – 244, doi:https://doi.org/10.1006/jcph.1994.1189.

Speich, S., L. J. R. E, P. Penven, and B. Bruno (2006), Role of bathymetry in agulhas current configuration and behaviour, *Geophysical Research Letters*, *33*, doi:10.1029/2006GL027157.

Strub, P. T., F. A. Shillington, C. James, and S. J. Weeks (1998), Satellite comparison of the seasonal circulation in the benguela and california current systems, *South African Journal of Marine Science*, *19*(1), 99–112, doi:10.2989/025776198784126836.

Tim, N., E. Zorita, and B. Hünicke (2015), Decadal variability and trends of the Benguela upwelling system as simulated in a high-resolution ocean simulation, *Ocean Science*, *11*(3), 483–502, doi:10.5194/os-11-483-2015.

Treguier, A.-M., O. Boebel, B. Barnier, and G. Madec (2003), Agulhas eddy fluxes in a 1/6 degrees atlantic model, *Deep Sea Research Part II: Topical Studies in Oceanography*, *50*(1), 251–280, doi:https://doi.org/10.1016/S0967-0645(02)00396-X.

Twatwa Mhlongo, N., C. van der Lingen, L. Drapeau, C. Moloney, and J. Field (2005), Characterising the spawning habitats of anchovy engraulis encrasicolus and sardine sardinops sagax in the southern benguela upwelling ecosystem, *Afr. J. mar. Sci.*, *27*, 487–500.

Vallis, G. K. (2006), *Atmospheric and oceanic fluid dynamics : fundamentals and large-scale circulation*, first ed., Cambridge University Press.

van Aken, H., A. van Veldhoven, C. Veth, W. de Ruijter, P. van Leeuwen, S. Drijfhout, C. Whittle, and M. Rouault (2003), Observations of a young agulhas ring, astrid, during mare in march 2000, *Deep Sea Research Part II: Topical Studies in Oceanography*, *50*(1), 167 – 195, doi:https://doi.org/10.1016/S0967-0645(02)00383-1, inter-ocean exchange around southern Africa.

van der Lingen, C., and J. Huggett (2003), *The role of ichthyoplankton surveys in re-*

cruitment research and management of South African anchovy and sardine, 301–343 pp.

van der Lingen, C., J. Coetzee, and L. Hutchings (2002), Temporal shifts in the spatial distribution of anchovy spawners and their eggs in the southern benguela: Implications for recruitment, *GLOBEC Report*, *16*, 46–48.

van der Sleen, P., et al. (2018), Non-stationary responses in anchovy (engraulis encrasicolus) recruitment to coastal upwelling in the southern benguela, *Marine Ecology Progress Series*, *596*, 155–164.

van Sebille, E., C. N. Barron, A. Biastoch, P. J. van Leeuwen, F. C. Vossepoel, and W. P. M. de Ruijter (2009), Relating agulhas leakage to the agulhas current retroflection location, *Ocean Science*, *5*(4), 511–521, doi:10.5194/os-5-511-2009.

van Sebille, E., L. M. Beal, and A. Biastoch (2010), Sea surface slope as a proxy for agulhas current strength, *Geophysical Research Letters*, *37*(9), doi:10.1029/2010GL042847.

van Sebille, E., et al. (2018), Lagrangian ocean analysis: Fundamentals and practices, *Ocean Modelling*, *121*, 49 – 75, doi:https://doi.org/10.1016/j.ocemod.2017.11.008.

Veitch, J., P. Florenchie, and F. Shillington (2006), Seasonal and interannual fluctuations of the angola-benguela frontal zone (abfz) using 4.5 km resolution satellite imagery from 1982 to 1999, *Int. J. Remote Sens.*, *27*, 987–998, doi:10.1080/01431160500127914.

Veitch, J., P. Penven, and F. Shillington (2009), The Benguela: A laboratory for comparative modeling studies, *Prog. Oceanog.*, *83*(1-4), 296–302, doi:10.1016/j.pocean.2009.07.008.

Veitch, J., P. Penven, and F. Shillington (2010), Modeling Equilibrium Dynamics of the Benguela Current System, *J. Phys. Oceanogr.*, *40*(9), 1942–1964, doi:10.1175/2010JPO4382.1.

Veitch, J., J. Hermes, T. Lamont, P. Penven, and F. Dufois (2017), Shelf-edge jet currents in the southern benguela: A modelling approach, *J. Mar. Sys.*, doi:10.1016/j.jmarsys.2017.09.003.

3299 Veitch, J. A., and P. Penven (2017), The role of the Agulhas in the Benguela Current
3300 system: A numerical modeling approach, *J. Geophys. Res.*, *122*(4), 3375–3393, doi:
3301 10.1002/2016JC012247.

3302 Washburn, L., M. R. Fewings, C. Melton, and C. Gotschalk (2011), The propagat-
3303 ing response of coastal circulation due to wind relaxations along the central Califor-
3304 nia coast, *Journal of Geophysical Research: Oceans*, *116*(12), C12,028, doi:10.1029/
3305 2011JC007502.

3306 Weeks, S., R. Barlow, C. Roy, and F. Shillington (2006), Remotely sensed variability
3307 of temperature and chlorophyll in the southern Benguela: upwelling frequency and
3308 phytoplankton response, *African Journal of Marine Science*, *28*(3-4), 493–509, doi:
3309 10.2989/18142320609504201.

3310 Weiss, J. (1991), The dynamics of enstrophy transfer in two-dimensional hydrodynam-
3311 ics, *Physica D: Nonlinear Phenomena*, *48*(2), 273 – 294, doi:https://doi.org/10.1016/
3312 0167-2789(91)90088-Q.

3313 Winant, C. D., R. C. Beardsley, and R. E. Davis (1987), Moored wind, temperature,
3314 and current observations made during Coastal Ocean Dynamics Experiments 1 and 2
3315 over the Northern California Continental Shelf and upper slope, *Journal of Geophysical*
3316 *Research*, *92*(C2), 1569, doi:10.1029/JC092iC02p01569.